Title
Novel Organizers of Signal Transduction Impact Cellular Processes

Permalink
https://escholarship.org/uc/item/2sq6v5b8

Author
Zhang, Jason Zhaoxing

Publication Date
2020

UNIVERSITY OF CALIFORNIA SAN DIEGO

Novel Organizers of Signal Transduction Impact Cellular Processes

A dissertation submitted in partial satisfaction of the
requirements for the degree Doctor of Philosophy

in

Bioengineering

by

Jason Zhaoxing Zhang

Committee in charge:

Professor Jin Zhang, Chair
Professor Yingxiao Wang, Co-Chair
Professor Silvio Gutkind
Professor Andrew McCulloch
Professor Susan Taylor

2020

The dissertation of Jason Zhaoxing Zhang is approved, and it is acceptable in quality and form for publication on microfilm and electronically:

Co-chair

Chair

University of California San Diego

2020

Table of Contents

List of Figures

Acknowledgments

I would like to acknowledge Professor Jin Zhang for her guidance throughout my doctoral degree and as chair of my committee. I have grown a lot professionally and academically with the guidance of Professor Zhang. I could not have asked for a better doctoral advisor as Professor Zhang has invested in many hours discussing interesting science and guided me in achieving my academic goals.

I also want to thank my collaborators Professor Susan Taylor, her graduate student Tsan-wen Lu, Professor Padmini Rangamani, and her postdoctoral scholar Lucas Stolerman for their tireless efforts in preparing our manuscript. The discussions with Professor Taylor and Professor Rangamani and their respective labs were truly illuminating.

I want to thank Professor Rati Fotedar for aiding me in my training as an academic educator. As I have assisted in her biotechnology lab class for over 4 years at Miramar College, I have gained both a teacher mentor and a great friend.

I would like to thank my lab mates for their camaraderie, especially as my PhD journey has had a lot of ups and downs. I appreciate their constructive criticism throughout my projects and the fun nights of trivia at Rock Bottom. I would especially like to thank Sohum Mehta for his keen mind and attention to detail, Brian Tenner for mentoring me and his lab antics, my desk mate and close friend Clara Posner, and my undergraduate assistants Andy Nguyen and Michelle Tong for both their their help in lab and their friendship.

I would also like to thank the various friends made along the way during PhD within the bioengineering and nanoengineering departments. Some to highlight include: One of my best friends who I literally met from day one: Carina Arboleda. My good friend and lockdown buddy: Yoon Choi. My friend who I remember we first talked at a bus stop 3 years ago: April Xing.

Finally, I would like to thank my parents for always being supportive. I am thankful for the plethora of advice from my brother and dad, both of whom have PhDs. I am also unendingly thankful for my mom who has been my biggest supporter; all of this would not be possible without her.

Chapter 1, in part, is currently being prepared for submission for publication of the material. Mehta, Sohum; Zhang, Jin. Jason Zhaoxing Zhang was the first-author of this paper.

Chapter 2, in part, has been submitted for publication of the material as it may appear in PLOS Biology 2020. Nguyen, Andy H; Miyamoto, Shigeki; Brown, Joan Heller; McCulloch, Andrew D; Zhang, Jin, PLOS Biology, 2020. Jason Zhaoxing Zhang was the first-author of this paper. We thank Yi Wu for the DORA RhoA construct; Alexandra Newton and Angela Van for the PMA and Gö6983 reagents; Silvio Gutkind and Justine Paradis for the $G\alpha_q$-DREADD construct and CNO reagent; Kim McCabe for help in the computational model; Maya Kunkel for critical reading of the manuscript.

Chapter 3, in part, has been submitted for publication of the material as it may appear in Cell 2020. Lu, Tsan-Wen; Stolerman, Lucas M; Tenner, Brian; Yang, Jessica; Zhang, Jin-Fan; Falcke, Martin; Rangamani, Padmini; Taylor, Susan S; Mehta, Sohum; Zhang, Jin, Cell 2020. Jason Zhaoxing Zhang was the first-author of this paper. We thank A. Hong, K.L. Guan, and S. Banerjee for their guidance with CRISPR; E. Griffis and D. Bindels for their confocal microscopy expertise; D.L. Schmitt for help with neuron and glial experiments; C. Brand for help with cardiomyocyte experiments; Y.L. Ma and M. Falcke for insightful discussion; and A. Nguyen and M. Tong for help with cloning.

Chapter 4, in part, is currently being prepared for submission for publication of the material. Tenner, Brian; Huang, Bo; Mehta, Sohum; Zhang, Jin. Jason Zhaoxing Zhang was the

co-first-author of this paper. The authors are grateful to W. Lin for their help in TIRF imaging. This work was supported by R01 DK073368 (to J.Z.); R21 EB022798, R01 GM124334, and R01 GM131641 (to B.H.); and a National Science Foundation predoctoral fellowship DGE-1650112 (to J.Z.Z.).

Vita

Education

PhD Candidate in Bioengineering, University of California San Diego, (September 2015-October 2020)
BS in Bioengineering, University of California Berkeley, (August 2012-December 2014)

Publications

Zhang J.Z., Lu T.W., Stolerman L.M., Tenner B., Yang J., Zhang J.F., Falcke, M., Rangamani P., Taylor S.S., Mehta S., Zhang J. (2020). Phase separation of a PKA regulatory subunit controls cAMP compartmentation and oncogenic signaling. Cell *182*, 1531-1544.e15.
Zhang J.Z., Nguyen A., Miyamoto S., McCulloch A.D., Brown J.H., Zhang J. (2020). Histamine-induced biphasic activation of RhoA allows for persistent RhoA signaling. PLoS Biology *18*, e3000866.
Zhang J.F., Liu B., Hong I., Mo A., Roth R.H., Tenner B., Lin W., **Zhang J.Z.**, Johnson R.C., Molina R.S., Drobizhev M., Taylor S.S., Hughes T.E., Tian L., Huganir R.L., Mehta S., Zhang J. (2020) A highly sensitive fluorescent biosensor for multi-modal kinase activity detection and high-resolution imaging in awake mice. *Nature Chemical Biology*. In press.
Tenner B.*, **Zhang J.Z.*,** Huang B., Mehta S., Zhang J. Fluorescent biosensors for monitoring compartmentalized signaling within endogenous microdomains. *Science Advances*. In revision.

Abstract of the Dissertation

Novel Organizers of Signal Transduction Impact Cellular Processes

by

Jason Zhaoxing Zhang

Doctor of Philosophy in Bioengineering

University of California San Diego, 2020

Professor Jin Zhang, Chair
Professor Yingxiao Wang, Co-Chair

Our bodies are highly dynamic and the cells within our bodies must continuously sense their ever-changing environment. To respond to extracellular stimuli, signaling pathways are tightly regulated to enable proper cellular function. Spatiotemporal regulation of signal transduction is an emerging theme that enables specificity in signaling. Throughout this dissertation, the spatiotemporal regulation of the RhoA and cAMP/PKA signaling pathways was explored by using various novel tools such as fluorescence-based biosensors. In Chapter 2, we characterized receptor-mediated biphasic RhoA activation and found “memory”-like behaviors in RhoA activity. In Chapter 3, we discovered liquid-liquid phase separation of the PKA regulatory subunit RIα as a novel organizer of the cAMP/PKA pathway. We further showed that these biomolecular condensates enable cAMP compartmentation and suppress tumorigenic signaling. In Chapter 4, we engineered a suite of FRET-based biosensors to measure signaling dynamics around a protein of interest that is expressed at endogenous levels and applied these biosensors to unveil unique cAMP dynamics at clathrin plaques. Altogether, this dissertation showcases new tools for investigating signal transduction and the application of these tools to reveal novel modes of spatiotemporal regulation in intracellular signaling.

Chapter 1: Introduction

Compartmentalizing cellular processes

Our environment is ever changing and the cells in our body must dynamically adapt to these changes. A network of dynamic molecules is responsible for orchestrating the appropriate responses by decoding the input signals and passing along the cellular information. Mechanistically, each molecule relays the signaling information downstream by altering the next molecule in the pathway through a cascade of biochemical reactions, a process termed signal transduction. Specificity in signal transduction is necessary for normal cellular function as any aberrations can lead to numerous pathological consequences.

Spatiotemporal regulation of intracellular signaling, which is the idea that signaling molecules are turned on and off at precise locations and times within the cell, is an emerging theme in enabling specificity in these biochemical activities. By segregating these biochemical reactions into separate sections within the cell, compartments enable spatiotemporal regulation and are thus necessary for specificity and efficiency in cellular processes. The typical intracellular compartments biologists think of are membrane-bound ones, which enclose biochemical activities within defined membrane walls. In the past decade though[1], the discovery of liquid-liquid phase separation has shifted our understanding of how compartmentation can be achieved through via membraneless organelles[2,3].

Liquid-liquid phase separation is the idea that a homogeneous solution of a certain biomolecule spontaneously de-mixes after a threshold concentration of said biomolecule is reached into two phases: one phase concentrated and the other phase dilute in the biomolecule of interest. The concentrated phase has many names such as biomolecular condensates[4], phase separated bodies[5], liquid droplets[2], granules[6], or assemblies[7], and they are used interchangeably in this review. Excitingly, there is a recent acceleration in discovering new phase separated systems within cells, many of which are involved in signal transduction[8]. With the specialized properties of phase-separated condensates (Box 1 describes the biophysical properties of condensates), it is possible that unique biochemical activities can arise by virtue of phase separating key components involved in signaling. Thus, this review will discuss how phase separation builds biochemical activity architectures and explore the biochemical, physiological, and pathological consequences of this phase separation.

Box 1: Formation and regulation of phase-separated bodies

Due to the unique liquid-like properties of deformability, fusion, and rapid exchange of molecules within these round condensates[9,10], these membraneless organelles allow for more flexibility in terms of reaction kinetics and regulation compared to membrane-bound ones. Thus, one immediate question in understanding how these assemblies work: what drives and influences phase separation? Understanding the principles underlying phase separation will also inherently allows us to understand how phase separation is regulated. One useful concept to utilize for understanding phase-separated systems is “scaffolds” and “clients”[5]. Scaffold molecules drive phase separation as they are necessary and sufficient for spontaneous droplet formation *in vitro* and in cells. Client molecules partition into scaffold-driven condensates and can influence the properties of the phase-separated system. There is growing evidence that phase separation is driven by a network of interactions between proteins and sometimes nucleotides[11–13], thus these multivalent interactions regulate the dynamics of phase separation by the scaffold molecule and determine which clients are sequestered into the condensate[4,14,15]. Stable multivalent interactions that are necessary for phase separation can be derived from the interaction between multiple folded domains and short linear motifs such as from Src homology domain 3 (SH3) and proline-rich motifs (PRMs), respectively[4,16]. In addition, phase separation can be driven by weak multivalent interactions from intrinsically disordered regions (IDRs) with multiple interaction motifs, commonly termed as "stickers" that are separated by "spacers" for flexibility, a classic example being interactions between RNA and RNA-binding proteins[17,18].

While it is still hard to predict which proteins can phase separate, finding common features of scaffold proteins and mutagenesis experiments have unveiled several amino acid interactions that contribute to the phase separation of scaffold proteins[17]. Cation-pi interactions from positively charged and aromatic residues and cation-cation interactions are necessary and sufficient for phase separation of certain systems[17,19]. Electrostatic forces also regulate phase separation by altering interdomain connections[20,21], and this may explain why some post-translational modifications (PTMs) such as phosphorylation can regulate condensation[22,23]. In addition, IDRs are enriched with glycines, serines, and glutamines[17]. While the cation-pi and cation-cation interactions can be considered as stickers in determining the propensity for condensation, the spacer regions within IDRs influence the phase behavior of droplets. Glycines enhance liquidity of condensates possibly due to glycine enhancing backbone flexibility or alter hydrophobicity, and glutamines and serines promote hardening[17].

Condensates shape the signaling landscape

What is the functional impact by concentrating signaling molecules and their effectors in these condensates (Box 1 gives a brief overview of the mechanisms underlying phase separation)? Condensation may enhance molecular interactions/collisions, which in turn will affect the kinetics of biochemical activities within and will influence the signaling outside the droplet. In this review, three examples are presented that highlight the functional impact of phase separation. Along with the examples, we will also highlight the innovative molecular tools developed and used to characterize the activity and function of signaling condensates.

Dynamic sequestration of key effector molecules in condensates

By sequestering clients, condensates can act as reservoirs. The recent discovery that a regulatory subunit of the cyclic AMP (cAMP)-dependent kinase (PKA), RIα, undergoes liquid-liquid phase separation demonstrates this principle[24]. Spatial compartmentation of the ubiquitous second messenger cAMP has been a key concept to explain specificity of cAMP signaling for more than three decades[25]. However, direct proof as well as plausible mechanisms of cAMP compartmentation have been lacking given that cAMP-degrading phosphodiesterases (PDEs) have modest catalytic properties[26,27] and cAMP diffusion has been found by several labs to be essentially unrestricted[28–30], thus raising the question of whether and how cAMP is compartmentalized. We address this question by showing that cAMP is dynamically sequestered in RIα phase separated bodies. Strikingly, *in vitro* experiments suggest that 99% of cAMP is sequestered into these RIα droplets[24], highlighting the buffering capabilities of phase separated systems.

To measure the cAMP and PKA dynamics inside native condensates inside cells, the fluorescent sensor targeted to endogenous proteins (FluoSTEP) platform was developed and several FluoSTEP probes were designed to specifically measure cAMP levels and PKA activities. FluoSTEPs are FRET-based sensors[31] that are split into two: one portion targeted to a protein of interest (POI) (e.g. scaffold) via CRISPR, the other portion being the remaining parts of the fluorescent sensor that is sensitive to a molecule of interest (e.g. kinase). Only when both components are present can the fluorescent sensor operate and measure the native signaling dynamics around the POI without affecting its endogenous expression[32,33]. FluoSTEPs are especially useful for phase separation studies as they measure the biochemical activities only around the POI and do not perturb the endogenous stoichiometry and expression level of the POI, which dictates droplet formation. FluoSTEP measurements for the endogenously tagged RIα indicated that the cAMP levels and PKA activities are higher inside the condensates compared to outside and that during the formation of RIα bodies, cAMP is recruited with commensurate substantial increases in PKA activity[24].

As RIα bodies are enriched with cAMP, we explored whether this enrichment limits the availability of cAMP outside RIα bodies, thus decreasing the effective cAMP in the cytosol and allowing for nanometer-sized cAMP sinks to exist[24]. When RIα bodies are either pharmacologically or genetically disrupted, PDEs can no longer compete with the new influx of cAMP and lose their ability to maintain local cAMP sinks. Essentially, RIα bodies act as a sponge in soaking up cAMP, thus restricting the availability of cAMP outside the condensate and allowing for fine-tuning of cAMP action. This example highlights the capabilities of signaling condensates to affect signaling both inside and outside its borders.

Phase transitions mediate non-linear amplification of signaling cascades

Bringing together key components of the same pathway can augment the signaling output. This has been seen in various signaling systems such as the Erk pathway where the Kinase Suppressor of Ras acts as a scaffold in binding to Erk and its directly upstream effectors Raf and MEK in a 1:1:1:1 stoichiometry[34]. Signaling condensates can also concentrate pathway components but is not restricted to a set stoichiometry, thus potentially allowing for more diverse signaling dynamics such as non-linear signal amplification as seen in clustering of the Linker for activation of T-cells (LAT)[35]. After activation of the T-cell receptor (TCR) such as through antigen presentation, a series of biochemical events leads to the phosphorylation of LAT[36]. Phosphorylated LAT interacts with and activates the Ras guanine exchange factor Sons of sevenless homolog 1 (Sos1) to signal downstream to the Ras/Raf/MEK/Erk pathway[36]. Recent studies have discovered that LAT undergoes phase transitions to form clusters and this compartment enhances Erk activation and actin polymerization by recruiting activators and excluding repressors (e.g. phosphatases) of this pathway[35]. Interestingly, while LAT clustering leads to 2x more Sos1 recruitment, Ras activation is increased 8-fold compared to no clustering[37]. To understand this amplification in signaling downstream of the pathway, biophysical modeling was used to understand the influence of protein condensation on signaling dynamics. Modeling of Sos1 activation kinetics revealed that LAT-mediated clustering of Sos1 supra-stoichiometrically enhances Ras activation due to increased Sos1 dwell times in the condensate, which allows for a higher probability of Sos1 to complete its rate-limiting step (release of Sos1 autoinhibition[38,39]) and thus substantially increasing Sos1 activation[37]. In these studies, *in vitro* experiments and computational modeling were instrumental in enhancing our understanding of how the signaling amplitude can be magnified in a non-intuitive manner within signaling bodies.

Substrate channeling within multienzyme, phase-separated complexes

Controlled condensation of the various substrates and enzymes involved in a complex pathway can dictate the kinetics of biochemical activities by acting as conduits in directing the flow of molecules within the droplet. Some higher-order assemblies that coordinate metabolic pathways called metabolons[40] form via phase separation and display the aforementioned feature. An example is the glucosome, which is a dynamic, multienzyme complex which was recently revealed to be formed by phase separation and plays a critical role in organizing glucose metabolism in channeling glucose flux between glyocolysis, serine biosynthesis, gluconeogenesis, and pentose phosphate pathway[41,42]. Another metabolon is the purinosome, which concentrates the 10-step, 6-enzyme-mediated de novo purine biosynthesis[43,44]. While the purinosome complex was identified a decade ago[45], revisiting the purinosome with the lens of phase separation revealed that this metabolon also forms via phase separation[46]. This macromolecular granule is formed in purine-depleted environments and once formed promotes substrate channeling in enhancing production of IMP, the pre-cursor to adenosine and guanine. Recently developed mathematical models of both the glucosome and purinosome suggested that enzyme clustering via phase separation allows for dynamic regulation of the direction and kinetics of metabolite flux within the condensate[47]. In corroboration with these computational predictions, the localized metabolite levels were directly measured via mass spectrometry imaging such as gas cluster ion beam secondary ion mass spectrometry (GCIB-SIMS), which allows for biomolecule profiling at subcellular locales[48]. GCIB-SIMS was used to profile the metabolites within intact purinosomes in frozen, hydrated HeLa cells with 1μm x 1μm x 400nm voxel resolution. Interestingly, GCIB-SIMS experiments showed that de novo production of the metabolites AICAR (300-1000x) and ATP is greatly increased and pathway flux is enhanced 7-fold in the purinosomes compared to the diffuse, cytosolic regions, demonstrating that purinosomes are active, purine-producing hotspots[49]. By selectively recruiting pathway components into a tight area, condensates can organize complex, muli-step processes that require coordination between various molecules and enzymes.

Pathological signaling arising from and therapeutic targeting of aberrant phase separation

From the previous section, it is clear that unique functions arise by virtue of concentrating key signaling molecules into phase-separated bodies. What happens then when the phase separation behavior becomes dysfunctional? Here, we discuss several examples where deviations in signaling condensates lead to disease, which give new insight into the mechanisms of these pathological processes. Moreover, there is immense interest in reverting these aberrant phase separation behaviors in the hopes of finding critical treatments.

Deviations in phase separation in cancer

Many cancer-related fusion oncoproteins induce aberrant signaling programs, but the mechanisms of how aberrant signaling occurs are unclear for many cases[50]. For instance, the fusion of DnaJB1's exon 1 with the last 9 exons of PKAcat (DnaJB1-PKAcat) is exclusively detected in patients with fibrolamellar carcinoma (FLC)[51], a rare liver cancer that has little similarities with other liver cancers[52]. While it is clear that this chimeric fusion enzyme drives FLC as it is sufficient to induce FLC-like tumors in mice[53], many biochemical and structural studies show little difference in either the activity or regulation between DnaJB1-PKAcat and wildtype PKAcat[54–56]. Recent work has brought new insight into the oncogenic mechanisms of this fusion oncoprotein by revealing that DnaJB1-PKAcat disrupts RIα phase separation by recruiting Hsp70 and losing myristoylation[24]. Furthermore, DnaJB1-PKAcat induces loss of cAMP signaling specificity and loss of functional RIα phase separation alone induces increased cell proliferation and transformation, suggesting that RIα phase separation has tumorsuppressive roles.

Another set of fusion oncoproteins, EML4-ALK and CCDC6-RET[57], contain the intracellular domains of RTKs and have recently been shown to form membrane-independent protein granules that aberrantly activate cytosolic Ras, as measured via fluorescent protein-tagged Ras effector proteins enriched in these RTK oncoprotein puncta[58]. Interestingly, the kinase function of EML4-ALK seems to be required for granule formation and cytosolic Ras activation as ALK inhibition abrogates the recruitment of binding partners such as GRB2. To evaluate the impact of condensation of intracellular RTKs on cellular signaling, Tulpule et al. utilized perturbative tools to artificially induce phase separation and then measured signaling outputs[58]. Homo oligomeric-tagging[59] RTK oncoproteins that cannot form granules on their own forced protein condensation by higher-order oligimerization. This forced condensation of mutant RTKs induced GRB2 co-phase separation and cytosolic Ras activation, suggesting that these aberrant structures are sufficient to induce membrane-independent RAS/MAPK signaling.

Phase transitions in neurodegenerative disease

Liquid-to-solid phase transition of protein condensates is a hallmark for various neurodegenerative diseases such as Amyotrophic lateral sclerosis (ALS), Frontotemporal dementia (FTD), Huntington's Parkinson's, and Alzheimer's[60]. The traditional viewpoint is that these protein-dense structures are precipitate-like aggregates, but emerging evidence now suggest that they are indeed phase separated bodies[61] that become more gel-like during disease progression[21,62]. Mutations and PTMs on disease-related, condensate-localized proteins such as Transactive response DNA-binding protein-43 (TDP-43) and Fused in sarcoma (FUS) facilitate the solidification of neurodegenerative protein bodies[61]. For instance, ALS and FTD-associated mutations in the nuclear localization sequence of FUS weaken the binding and folding by Transportin and decrease arginine methylation, which leads to increased FUS phase separation and association with stress granules[63]. In another example, TDP-43 or FUS binding to PolyADP ribose on many RNA binding proteins enhance the phase separation of TDP-43 and FUS[64,65]. Furthermore, inhibition of Poly ADP-ribose polymerase is neuroprotective in decreasing TDP-43-mediated toxicity[66].

Phosphorylation is another well studied PTM that contributes to the hardening of neurodegeneration-linked condensates[61]. Hyperphosphorylation of TDP-43 by CK1/2 and GSK3 lead to the formation of disease-related inclusion bodies in the brain and spinal cord of FTD and ALS patients[67]. In addition, recent work has shown that Tau can phase separate and hyperphosphorylation of Tau solidifies Tau bodies[22]. Tau is phosphorylated by various kinases such as GSK3B, CDK5, CDK1, Jnk, and MARK2[68,69]. As PTMs play an important regulatory role in the phase behavior, inhibiting PTM of neurodegenerative disease-related proteins is an ongoing clinical strategy to clear out pathological condensates[70–73].

A recent exploratory approach has identified new compounds that may act as laboratory and therapeutic tools in altering the phase behavior of Fused in Sarcoma (FUS)[74]. Through a drug screen on HeLa cells engineered to express fluorescently labeled FUS, lipoamide and lipoic acid were identified to specifically inhibit arsenite-induced FUS condensation[62] and did not affect other phase separated systems, and similar results were seen in C elegans. Importantly, these compounds also attenuated motor defects in Drosophila that were expressing mutant FUS proteins that cause motility issues and restored axonal transport in iPSC-derived neurons expressing the same mutant FUS. While the mechanisms of how these molecules affect FUS liquidity is unknown, Wheeler et al. showed that these effects are non-enzymatic and non-antioxidant[74]. Overall, this latest understanding of neurodegenerative plaques originating from phase-separated bodies provides new insight into this 3 decades old question in how we can clear these deleterious condensates in patients[75,76].

Acknowledgements

Chapter 1, in part, is currently being prepared for submission for publication of the material. Mehta, Sohum; Zhang, Jin. Jason Zhaoxing Zhang was the first-author of this paper.

Chapter 2: Histamine-induced biphasic activation of RhoA allows for persistent RhoA signaling

Abstract

The small GTPase RhoA is a central signaling enzyme that is involved in various cellular processes such as cytoskeletal dynamics, transcription, and cell cycle progression. Many signal transduction pathways activate RhoA, for instance $G\alpha_q$-coupled Histamine 1 Receptor signaling via $G\alpha_q$-dependent activation of RhoGEFs such as p63. While multiple upstream regulators of RhoA have been identified, the temporal regulation of RhoA and the coordination of different upstream components in its regulation have not been well characterized. In this study, live-cell measurement of RhoA activation revealed a biphasic increase of RhoA activity upon histamine stimulation. We showed that the first and second phase of RhoA activity are dependent on p63 and Ca^{2+}/PKC, respectively, and further identified phosphorylation of Serine 240 on p115 RhoGEF by PKC to be the mechanistic link between PKC and RhoA. Combined approaches of computational modeling and quantitative measurement revealed that the second phase of RhoA activation is insensitive to rapid turning off of the receptor and is required for maintaining RhoA-mediated transcription after the termination of the receptor signaling. Thus, two divergent pathways enable both rapid activation and longer-term "memory" in receptor-mediated RhoA signaling via intricate temporal regulation.

Introduction

The highly conserved small GTPase RhoA regulates various cellular processes such as cellular motility and transcription and is implicated in cancer[77]. RhoA regulates these processes by dynamically cycling between its active GTP-bound state and its inactive GDP-bound state. Activation of RhoA is regulated by guanine nucleotide exchange factors (GEFs) that facilitate the exchange of the bound GDP for GTP. RhoA has intrinsic GTPase activity to hydrolyze GTP to GDP, and GTPase activating proteins (GAP) accelerate this hydrolysis by 3 orders of magnitude[78]. Guanine dissociation inhibitors (GDI) further inhibit RhoA and preserve the GDP-bound RhoA state by inhibiting GDP dissociation. To ensure signaling specificity for achieving its many roles, RhoA is spatiotemporally regulated through these GTPase regulators, which are in turn specifically regulated. For instance, many RhoGEFs are activated by membrane recruitment[79,80] or by heterotrimeric G-proteins[81,82], including $G\alpha_q$-activatable p63 RhoGEF[83] and $G\alpha_{12/13}$-activatable p115 RhoGEF[84].

Characterization and understanding of the temporal regulation of RhoA is important as it has a huge impact on cellular processes[85,86]. In this study, we used a genetically encoded fluorescent biosensor DORA RhoA[79] to measure RhoA activation kinetics in single living cells and uncovered unique biphasic activation of RhoA stimulated by histamine. We then examined the molecular mechanisms and functional roles of the biphasic RhoA activation and discovered that the sustained second-phase of RhoA activation is regulated by Ca^{2+}-PKC-p115, can be decoupled from the receptor activity, and is required for maintaining RhoA-mediated transcription after the termination of the receptor signaling.

Results

Histamine induces biphasic activation of RhoA

To measure the dynamics of RhoA activation in response to histamine in cells, we used the FRET-based DORA RhoA biosensor in HeLa cells expressing the canonical Gα_q-activatable p63 RhoGEF (p63)[79,81,87]. The DORA RhoA sensor reports RhoA activation in single cells by converting changes in the RhoA nucleotide state to changes in FRET. This biosensor contains a FRET pair sandwiched between the Rho binding domain of Protein Kinase N1 (PKN1) and full-length RhoA. When RhoA is activated, the PKN1 domain binds to RhoA-GTP, inducing a conformational change and altering FRET, which is measured by an increase in the acceptor-to-donor (yellow/cyan or Y/C) emission ratio[79]. To test the sensitivity of the DORA RhoA sensor to RhoGEFs and RhoGAPs, the sensor was co-expressed with either p63 RhoGEF, p115 RhoGEF, or p190 RhoGAP and the basal emission ratio was measured. Co-expression with p190 RhoGAP decreased the basal emission ratio by 18% while co-expression with either p63 RhoGEF or p115 RhoGEF increased the basal emission ratio by 20% and 25% respectively, suggesting that the DORA RhoA sensor is sensitive to both RhoGEFs and RhoGAPs (Figure 2.1A). Upon stimulation with 100 μM histamine, HeLa cells expressing both p63 and DORA RhoA displayed a rapid increase in the Y/C emission ratio (22 ± 0.8% emission ratio increase, $t_{1/2,\text{Phase 1}} = 1.4 \pm 0.1$ min, n = 54 (mean ± SEM; n = number of cells)) (Figure 2.2A-C). This initial ratio increase was subsequently followed by an additional 26 ± 1.9% emission ratio increase ($t_{1/2,\text{Phase 2}} = 13 \pm 0.3$ min) (Figure 2.2A-C). Pretreatment with 100 μM H_1HR inverse agonist pyrilamine [88] abolished the histamine-induced response (Figure 2.1B). Control cells co-expressing p63 and DORA RhoA (L59Q), which contains a L59Q mutation in PKN1 to prevent RhoA binding[79], exhibited no detectable FRET changes in response to histamine stimulation (Figure 2.2A-C), suggesting that the observed responses were specific. This histamine-induced biphasic activation

Figure 2.1: Activation of Gα_q-coupled receptor induces biphasic activation of RhoA
(**A**) Average basal DORA RhoA emission ratio in HeLa cells with either nothing else coexpressed (red) or p190 RhoGAP (blue), p63 RhoGEF (orange), or p115 RhoGEF (purple) coexpression (nothing: *n* = 87 cells; +p190: *n* = 94 cells; +p63: *n* = 63 cells; +p115: *n* = 42 cells). ****$P < 0.0001$; ordinary one-way ANOVA followed by Dunnett's multiple comparisons test (versus nothing transfected). (**B**) Representative average time courses ± SEM of the Y/C emission ratio changes in HeLa cells coexpressing p63 and DORA RhoA. Pyrilamine (100 μM) and then histamine (100 μM) was added to cells (*n* = 9 cells). (**C**) Representative average time courses ± SEM of the Y/C emission ratio changes in HeLa cells coexpressing p63 and RhoA1G. Histamine (100 μM) was added to cells (*n* = 8 cells). (**D**) Representative average time courses ± SEM of the Y/C emission ratio changes in MEF cells expressing DORA RhoA. Histamine (100 μM) was added to cells (*n* = 9 cells). (**E**) Quantification and representative western blot images of MEF cells simulated with 100 μM histamine. Numbers in the middle refer to minutes post histamine stimulation. For the Rhotekin pulldown samples, cell lysates were precipitated via beads covered with GST-tagged Rhotekin-RBD. Immunoblotting of RhoA of both the Rhotekin pulldown and whole-cell lysate samples show activation of RhoA in two waves from histamine stimulation (*n* = 3). Asterisks are statistics in comparison to 0 min: 0 min versus 2 min: *P = 0.047; 0 min versus 20 min: **P = 0.0063; ordinary one-way ANOVA followed by Dunnett's multiple-comparisons test (versus 0 min). (**F**) Representative average time courses ± SEM of the Y/C emission ratio changes in HeLa cells coexpressing p63, DORA RhoA, and Gα_q-DREADD. Cells were stimulated with 1 μM CNO (*n* = 6 cells). (**G**) Representative average time courses ± SEM of the Y/C emission ratio changes in MEF cells expressing DORA RhoA, p63, and p190. Histamine (100 μM) was added to cells (*n* = 18 cells).

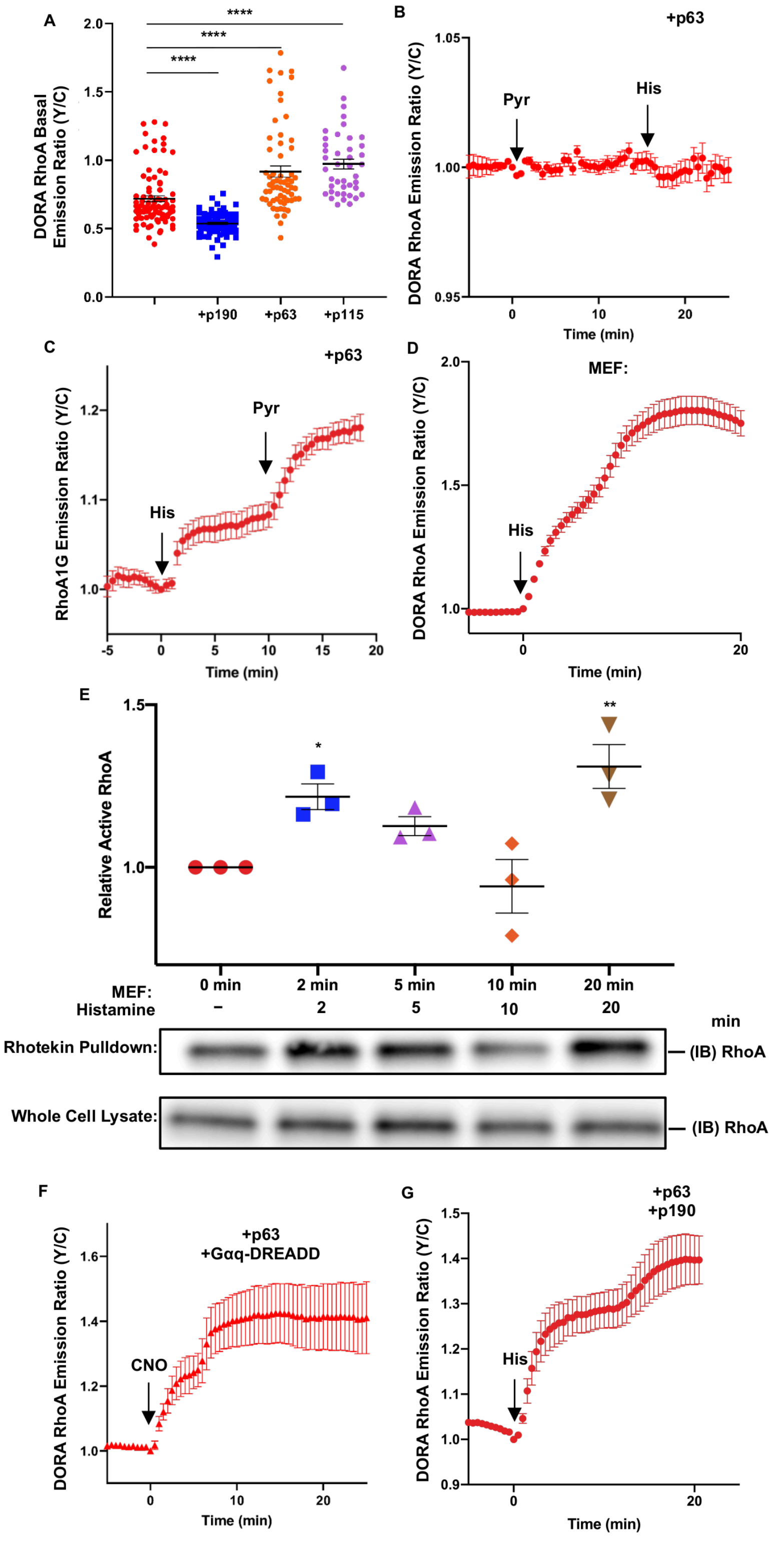
A
DORA RhoA Basal Emission Ratio (Y/C)
2.0
1.5
1.0
0.5
0.0
****
****
****
+p190
+p63
+p115
B
+p63
DORA RhoA Emission Ratio (Y/C)
1.05
1.00
0.95
Pyr
His
0
10
20
Time (min)
C
+p63
RhoA1G Emission Ratio (Y/C)
1.2
1.1
1.0
His
Pyr
-5
0
5
10
15
20
Time (min)
D
MEF:
DORA RhoA Emission Ratio (Y/C)
2.0
1.5
1.0
His
0
20
Time (min)
E
Relative Active RhoA
1.5
1.0
*
**
0 min
2 min
5 min
10 min
20 min
MEF:
Histamine
–
2
5
10
20
min
Rhotekin Pulldown:
(IB) RhoA
Whole Cell Lysate:
(IB) RhoA
F
+p63
+Gαq-DREADD
DORA RhoA Emission Ratio (Y/C)
1.6
1.4
1.2
1.0
CNO
0
10
20
Time (min)
G
+p63
+p190
DORA RhoA Emission Ratio (Y/C)
1.5
1.4
1.3
1.2
1.1
1.0
0.9
His
0
20
Time (min)

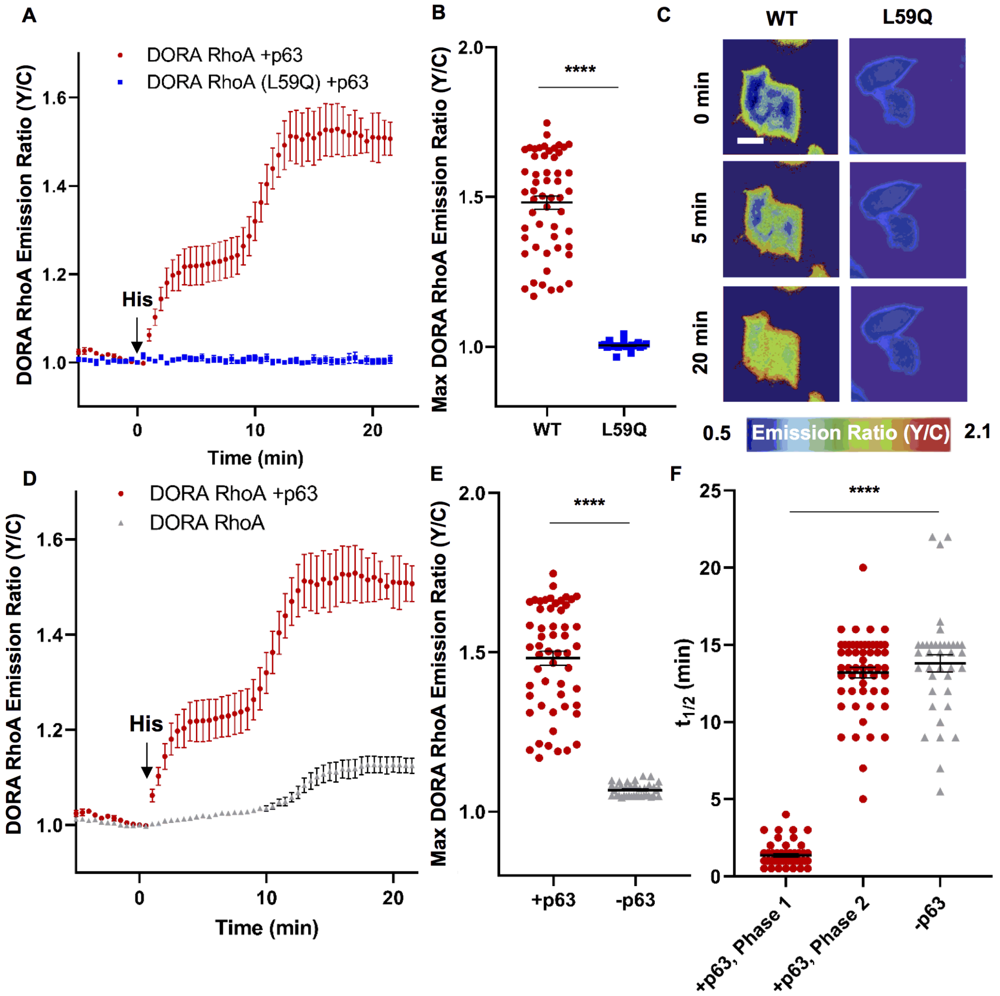

Figure 2.2: Histamine induces biphasic activation of RhoA

(**A-C**) Histamine (100 µM) stimulated responses in HeLa cells co-expressing mCherry-tagged p63 and either DORA RhoA (red) or DORA RhoA (L59Q) (blue). (**A**) Representative average time courses ± SEM of yellow/cyan (Y/C) emission ratio changes (DORA RhoA: n = 9 cells; DORA RhoA (L59Q): n = 5 cells). Error bars indicate ± SEM. (**B**) Maximum emission ratio changes upon histamine (DORA RhoA: n = 54 cells; DORA RhoA (L59Q): n = 23 cells). ****$P<0.0001$; unpaired two-tailed Student's t-test. Bars indicated mean, error bars indicate ± SEM. (**C**) Pseudocolored images show the Y/C emission ratio in representative cells expressing the indicated constructs at 0, 5, and 20 min after histamine stimulation. (**D-F**) Histamine (100 µM) stimulated DORA RhoA responses in HeLa cells transfected with DORA RhoA and p63 (red) or DORA RhoA alone (gray). (**D**) Representative average time courses ± SEM of yellow/cyan (Y/C) emission ratio changes (DORA RhoA alone: n = 9 cells). (**E**) Maximum emission ratio changes upon histamine (DORA RhoA alone: n = 38 cells). ****$P<0.0001$; unpaired two-tailed Student's t-test. (**F**) Time to half-maximal responses ($t_{1/2}$) after histamine stimulation for the first ($t_{1/2,\ \text{Phase 1}}$) and second ($t_{1/2,\ \text{Phase 2}}$) phases of the Y/C ratio increase in HeLa cells co-transfected with DORA RhoA and p63, and for the slow histamine-induced response ($t_{1/2}$) in HeLa cells transfected with DORA RhoA only (DORA RhoA + p63: n = 54 cells; DORA RhoA alone: n = 38 cells). ****$P<0.0001$; unpaired two-tailed Student's t-test. Scale bar, 10 µm.

of RhoA was also observed using another FRET-based RhoA sensor RhoA1G[89] (Figure 2.1C), suggesting that this biphasic behavior is characteristics of RhoA and independent of biosensors. In the absence of p63 overexpression, DORA RhoA-expressing MEF cells, which endogenously express p63 RhoGEF[90], also displayed biphasic increases in DORA RhoA emission ratio (Figure 2.1D), which is consistent with the biphasic RhoA activation measured using the Rhotekin pulldown assay which detects RhoA-GTP[91] (Figure 2.1E). Moreover, the biphasic response to $G\alpha_q$-coupled receptor stimulation is generalizable as CNO activation of the synthetic $G\alpha_q$-coupled receptor ($G\alpha_q$-DREADD)[92,93] also produced biphasic RhoA activation in cells co-expressing p63 (Figure 2.1F).

To explore whether these two phases of RhoA activation from histamine stimulation are both dependent on p63, we tested the histamine-induced RhoA response in HeLa cells lacking p63 overexpression. Interestingly, these cells exhibited a monophasic, slow increase in the DORA RhoA emission ratio (6.8 ± 3.3%, $t_{1/2} = 14 \pm 0.6$ min, n = 38) upon histamine stimulation (Figure 2.2D-E), the kinetics of which mirrored the second phase of the FRET response seen in p63-transfected cells ($P = 0.38$) (Figure 2.2D and 2.2F). These results suggest that histamine can induce biphasic increases in RhoA activity where the first phase appears to be dependent on p63. The amplitude of the response in the absence of p63 overexpression is lower than the 2nd phase (26 ± 1.9%) of the biphasic RhoA activation when p63 was overexpressed, suggesting that p63 may also enhance the second phase of RhoA activation. We also explored the effect of RhoGAPs in our system by expressing p63 and p190 in HeLa cells, which still exhibited a biphasic increase in DORA RHoA emission ratio, suggesting that p190 does not play a major role in RhoA activation timescale and kinetics in our system (Figure 2.1G).

Second phase of RhoA activation is dependent on the Ca^{2+}/PKC/p115 signaling axis

Like all $G\alpha_q$-coupled receptors, stimulation of the H_1HR increases intracellular Ca^{2+} levels and PKC activity by $G\alpha_q$-mediated activation of PLCβ[94]. Thus, we explored whether the second phase of this biphasic RhoA activation, which is still present when p63 is absent, is dependent on PLCβ, Ca^{2+}, and PKC. To probe the role of PLCβ, we utilized a dominant negative variant of PLCβ, C-terminus of PLCβ (PLCβ-Cterm), which binds to active $G\alpha_q$ but has no catalytic activity[95]. Expression of PLCβ-Cterm in in HeLa cells expressing p63 largely abolished the second histamine-induced increase in DORA RhoA emission ratio, suggesting that PLCβ-signaling regulates the second phase of RhoA activation (n = 25, Figure 2.3A). Next we probed the role of Ca^{2+}. In HeLa cells transfected with p63 and DORA RhoA and pretreated with 20 μM of the intracellular calcium chelator BAPTA, histamine increased the emission ratio rapidly by 13 ± 2.2% ($t_{1/2}$ = 0.7 ± 0.09 min, n = 18) with no subsequent second increase in emission ratio (Figure 2.4A). Addition of BAPTA 5 min after histamine stimulation also eliminated the second increase in DORA RhoA emission ratio (Figure 2.3B). In addition, BAPTA pretreatment eliminated the delayed increase but not the immediate increase in RhoA1G emission ratio upon histamine stimulation (Figure 2.5A), suggesting that the observed effect of chelating intracellular calcium on RhoA kinetics is independent of the RhoA sensor. Furthermore, in p63-expressing cells imaged in Ca^{2+} free media containing 1 mM EGTA to eliminate extracellular calcium, histamine stimulation again increased the DORA RhoA emission ratio rapidly by 14 ± 2.3% ($t_{1/2}$ = 0.8 ± 0.05 min, n = 18) with no subsequent increase (Figure 2.3C), suggesting that removal of Ca^{2+} abolishes the slow phase of RhoA activation from histamine. In contrast, increasing

Figure 2.3: Delayed activation of RhoA is dependent on the Ca^{2+}/PKC/p115 signaling axis (**A-E**) Representative average time courses ± SEM of the Y/C emission ratio changes in HeLa cells coexpressing p63 and DORA RhoA. Cells were either stimulated with 100 μM histamine and then 5 min afterwards with 20 μM BAPTA (**A**) (*n* = 15 cells), imaged in HBSS imaging media containing 1 mM EGTA and then stimulated with 100 μM histamine (**B**) (*n* = 8 cells), stimulated with 1 μM ionomycin and then stimulated with 100 μM histamine (**C**) (*n* = 3 cells), stimulated with 100 μM histamine and then 5 min afterwards with 1 μM Gö6983 (*n* = 11 cells) (**D**), or stimulated with 50 ng/mL PMA and then stimulated with 100 μM histamine (**E**) (*n* = 3 cells). (**F**) Representative average time courses ± SEM of the Y/C emission ratio changes in HeLa cells expressing DORA RhoA and stimulated with 50 ng/mL PMA and then 1 μM Gö6983 (*n* = 5 cells). (**G**) Representative western blot images of p115 knockdown in HeLa cells. HeLa cells were transfected with either shRNA p115 (p115) or shRNA Scrambled (Sc) via calcium phosphate methods. Immunoblotting of p115 (top) shows substantial knockdown of p115 when transfecting shRNA p115. (**H, I**) Representative average time courses ± SEM of the Y/C emission ratio changes in HeLa cells transfected with DORA RhoA and either shRNA p115 (**H**) or shRNA Scrambled (**I**). Cells were stimulated with 100 μM histamine and then 100 μM pyrilamine (sh p115: *n* = 3 cells; sh Scrambled: *n* = 5 cells). (**J**) Left: Representative average time courses ± SEM of the Y/C emission ratio changes in HeLa cells expressing DORA RhoA, p63, and with p115 (red) or without p115 (blue) overexpressed and stimulated with 100 μM histamine (+p63 +p115: *n* = 7 cells; +p63: *n* = 14 cells). Right: Maximum emission ratio changes upon histamine stimulation (+p63 +p115: *n* = 22 cells; +p63: *n* = 27 cells). $****P < 0.0001$; unpaired two-tailed Student's *t* test. (**K**) HeLa cells expressing either p63 and p115 or p63 only were stimulated with 100 μM histamine. Percentage of total increase in DORA RhoA Y/C emission ratio contributed from the first phase (Peak 1%) or from the second phase (Peak 2%) (+p63 + p115: *n* = 22 cells; +p63: *n* = 27 cells). $****P < 0.0001$; unpaired two-tailed Student's *t* test.

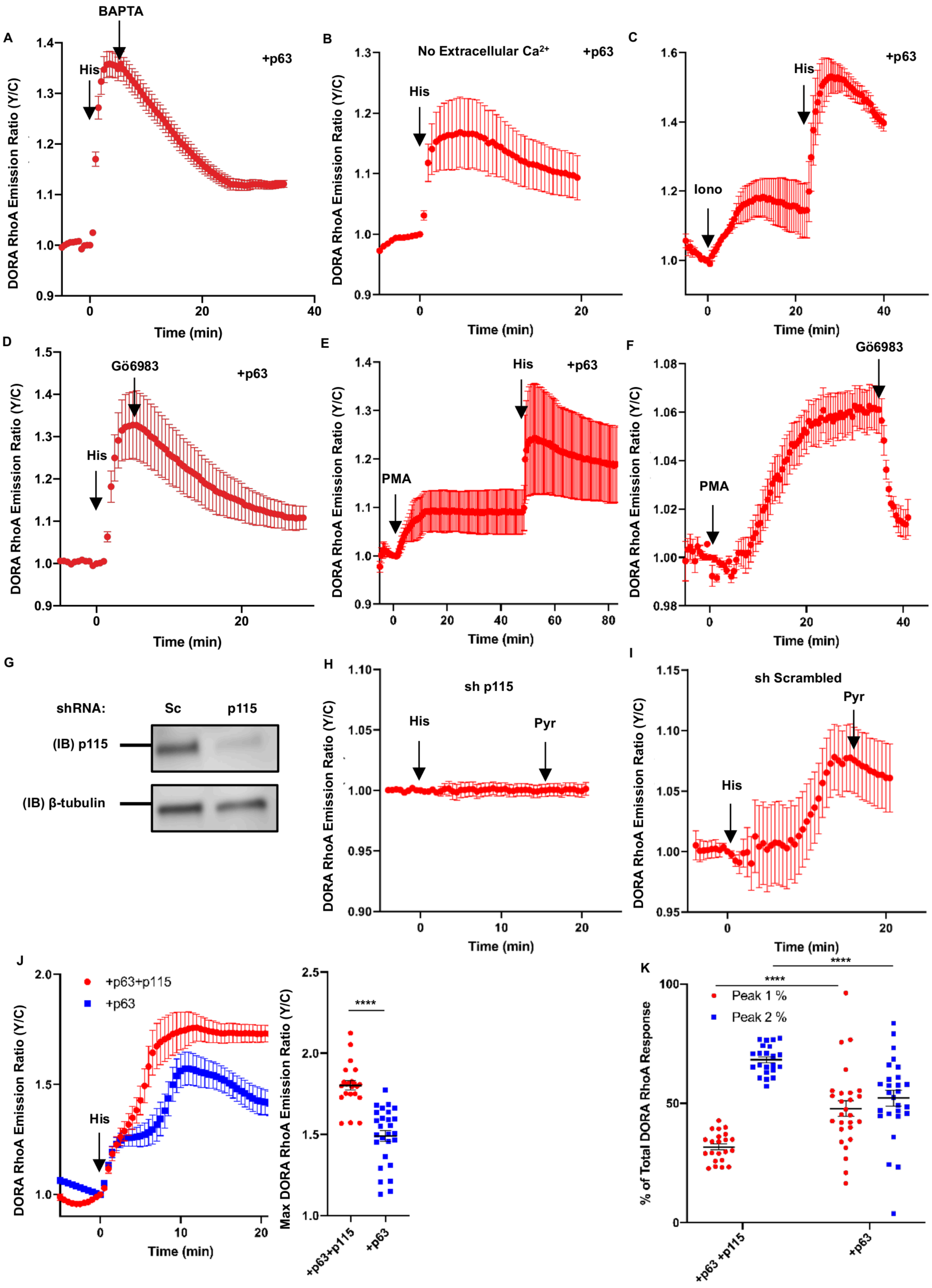
A
BAPTA
His
+p63
DORA RhoA Emission Ratio (Y/C)
Time (min)
B
No Extracellular Ca²⁺
+p63
His
DORA RhoA Emission Ratio (Y/C)
Time (min)
C
+p63
His
Iono
Time (min)
D
Gö6983
+p63
His
DORA RhoA Emission Ratio (Y/C)
Time (min)
E
His
+p63
PMA
DORA RhoA Emission Ratio (Y/C)
Time (min)
F
Gö6983
PMA
DORA RhoA Emission Ratio (Y/C)
Time (min)
G
shRNA:
Sc
p115
(IB) p115
(IB) β-tubulin
H
sh p115
His
Pyr
DORA RhoA Emission Ratio (Y/C)
Time (min)
I
sh Scrambled
Pyr
His
DORA RhoA Emission Ratio (Y/C)
Time (min)
J
+p63+p115
+p63
His
DORA RhoA Emission Ratio (Y/C)
Time (min)
Max DORA RhoA Emission Ratio (Y/C)
****
+p63+p115
+p63
K
Peak 1 %
Peak 2 %
****
****
% of Total DORA RhoA Response
+p63 +p115
+p63

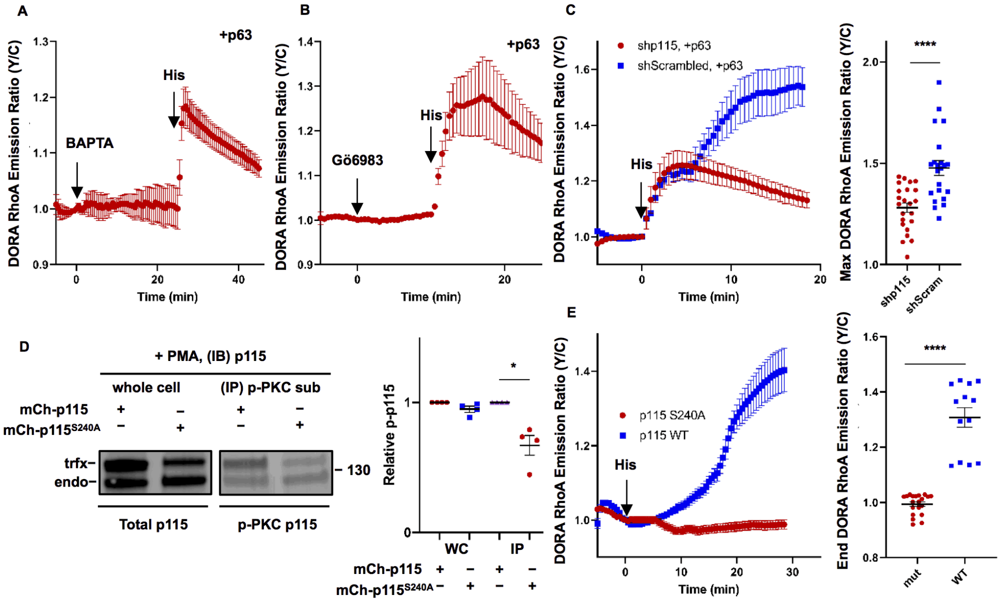

Figure 2.4: Second phase of RhoA activation is dependent on the Ca^{2+}/PKC/p115 signaling axis

(**A-B**) Representative average time courses ± SEM of the Y/C emission ratio changes in HeLa cells co-expressing p63 and DORA RhoA. Cells were stimulated with either 20 µM BAPTA (**A**) (n = 4 cells) or stimulated with 1 µM Gö6983 (**B**) (n = 7 cells). Then cells were subsequently stimulated with 100 µM histamine. (**C**) Left: Representative average time courses ± SEM of the Y/C emission ratio changes in HeLa cells expressing DORA RhoA, p63, and either shRNA p115 (red) or shRNA Scrambled (blue) and stimulated with 100 µM histamine (shp115: n = 5 cells; shScrambled: n = 4 cells). Right: Maximum emission ratio changes upon histamine (shp115: n = 23 cells; shScrambled: n = 22 cells). ****P<0.0001; unpaired two-tailed Student's t-test. (**D**) Left: Representative western blot images of HeLa cells show that PKC phosphorylates p115 on the Serine 240 residue. HeLa cells expressing either mCherry-tagged p115 or p115 S240A were stimulated with 50ng/mL PMA and subjected to immunoprecipitation with antibodies to phospho-PKC substrate. Whole cell samples and the immunoprecipitated (IP) samples were immunoblotted for p115. Right: Densitometry analysis of the immunoblot shown in blot calculating the percentage of PKC-phosphorylated p115 over total p115 for the endogenous p115 (endo, lower band) and transfected p115 (trfx, upper band). Average percentage ± SEM shown in bar graph amongst the various transfection conditions (n = 4 for each condition). Endogenous p115 vs p115 S240A: P = 0.1; Transfected p115 vs p115 S240A: *P = 0.02; unpaired two-tailed Student's t-test. (**E**) Representative average time courses ± SEM of the Y/C emission ratio changes in DORA RhoA-expressing HeLa cells co-expressing either mCherry-tagged p115 (blue) or mCherry-tagged p115 S240A (red) and stimulated with 100 µM histamine (p115: n = 5 cells; p115 S240A: n = 12 cells). Right: Maximum emission ratio changes upon histamine (p115: n = 13 cells; p115 S240A: n = 20 cells). ****P<0.0001; unpaired two-tailed Student's t-test.

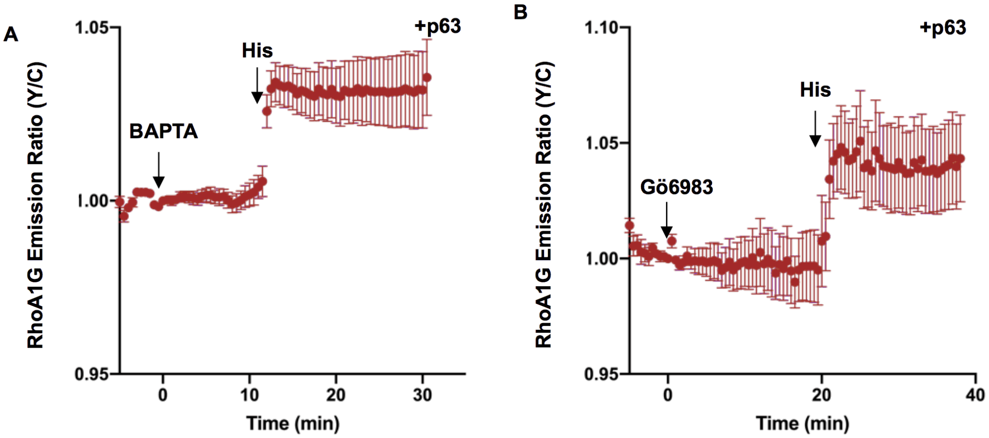

Figure 2.5: RhoA1G biosensor shows similar results to DORA RhoA sensor
(**A-B**) Representative average time courses ± SEM of the Y/C emission ratio changes in HeLa cells co-expressing p63 and RhoA1G. Cells were either pretreated with either 20 µM BAPTA (**A**) (n = 11 cells) or 1 µM Gö6983 (**B**) (n = 5 cells). 100 µM histamine was subsequently added to cells.

intracellular Ca^{2+} by addition of 1 μM ionomycin in p63-expressing cells led to a gradual increase the DORA RhoA emission ratio by 12 ± 2.6% (n = 12). Subsequent histamine stimulation again rapidly increased the emission ratio by an additional 30 ± 3.9% ($t_{1/2}$ = 1.2 ± 0.2 min, n = 12) (Figure 2.3D). These data suggest that the second phase of RhoA activation is dependent on Ca^{2+} and an increase in intracellular Ca^{2+} alone is sufficient to activate RhoA.

Given that PKC is activated by Ca^{2+} and has been implicated in activation of RhoA[96,97], we next assessed PKC's role in histamine-induced RhoA activation. When PKC is inhibited by 1 μM Gö6983, subsequent histamine stimulation of p63-expressing cells rapidly ($t_{1/2}$ = 0.9 ± 0.2 min) increased the DORA RhoA emission ratio by 34 ± 3.0% (n = 16) with no subsequent increase in emission ratio (Figure 2.4B), similar to what was observed in the BAPTA experiments. Addition of Gö6983 5 min after histamine stimulation also eliminated the second increase in DORA RhoA emission ratio (Figure 2.3E). In addition, Gö6983 pretreatment eliminated the delayed increase but not the immediate increase in RhoA1G emission ratio upon histamine stimulation (Figure 2.5B), suggesting that the observed effect of PKC inhibition on RhoA kinetics is independent of the RhoA sensor. On the other hand, activation of PKC by 50ng/mL PMA increased the DORA RhoA emission ratio of p63-expressing cells by 12 ± 2.6% (n = 13). Subsequent histamine stimulation rapidly increased the DORA RhoA emission ratio by an additional 13 ± 2.8% ($t_{1/2}$ = 0.6 ± 0.05 min, n = 13) (Figure 2.3F). Even when p63 was not expressed in cells, PMA treatment can lead to a gradual increase of the DORA RhoA emission ratio by 7.2 ± 0.8% (n = 15), suggesting that PKC can activate RhoA independent of p63. Subsequent PKC antagonism by Gö6983 decreased the DORA RhoA emission ratio to near pre-PMA stimulation emission ratio values (-4.7 ± 0.8%, n = 15) (Figure 2.3G). Overall, our data suggests that the second phase of RhoA activation induced by histamine is dependent on PKC and PKC activation alone is sufficient to activate RhoA.

Next we set out to identify the RhoGEF involved in Ca^{2+}/PKC mediated activation of RhoA. Among the potential links between PKC and RhoA, several studies report that PKC can increase RhoA activity by phosphorylating the $G\alpha_{12/13}$-activatable p115 RhoGEF (p115)[96,98]. To test the role of p115 in our system, we knocked down endogenous p115 in HeLa cells (Figure 2.3H) and measured the histamine induced RhoA activation. In cells expressing p115 shRNA and p63, histamine addition rapidly increased the DORA RhoA emission ratio (28 ± 2.4%, $t_{1/2}$ = 1.2 ± 0.1 min, n = 23) with no subsequent increase in emission ratio (Figure 2.4C). In contrast, cells with the scrambled shRNA control and p63 and stimulated with histamine displayed a biphasic increase (48 ± 3.1%, $P < 0.0001$) in the DORA RhoA emission ratio ($t_{1/2,\ \mathrm{Phase}\ 1}$ = 1.9 ± 0.3 min, $t_{1/2,\ \mathrm{Phase}\ 2}$ = 16 ± 1.5 min, n = 22) (Figure 2.4C), similar to the histamine-induced RhoA activation in cells with p63 and no shRNA (Figure 2.2A). In the absence of p63, histamine induced no increase in DORA RhoA emission ratio in the p115 shRNA-expressing cells (Figure 2.3I), in contrast to the delayed increase in the scrambled shRNA control (Figure 2.3J). When p115 was co-expressed with p63, the biphasic activation of RhoA from histamine stimulation was still present and the maximum DORA RhoA emission ratio was higher (80 ± 2.9%) compared to when only p63 was expressed (49 ± 3.4%, $P < 0.0001$) (Figure 2.3K). Moreover, this increase in DORA RhoA emission ratio in the p115 and p63 co-expression case is primarily contributed by the second phase of RhoA activation (Figure 2.3L). Together, these data suggest that p115 RhoGEF is required for the second phase of RhoA activation from histamine.

PKC phosphorylation on serine 240 as the critical link between PKC and RhoA

While several studies show that thrombin or tumor necrosis factor (TNFα) stimulation induces PKCα-mediated phosphorylation and activation of p115 to regulate endothelial cell permeability, the specific phosphorylation site has not yet been determined and it is not clear if this PKC dependent mechanism[96,98] occurs downstream of $G\alpha_q$. To determine if p115 is phosphorylated by PKC in response to histamine, we immunoprecipitated p115 from cells treated with PKC activator and/or inhibitor and examined its phosphorylation with an anti-phospho-PKC substrate antibody. PMA treatment increased PKC phosphorylation of p115 by 2 fold (2.1 ± 0.4, n = 5) compared with no drug treatment. Inhibition of PKC with Gö6983 abolished PMA-induced phosphorylation (1.1 ± 0.1, n = 4) (Figure 2.6A-B).

Serine 240 was predicted to be a PKC phosphorylation site based on Kinexus PhosphoNet[99] predictions using kinase consensus motif information (Figure 2.6C). We therefore mutated this serine 240 to an alanine (p115 S240A), tagged it with mCherry, and tested its phosphorylation by PKC. Due to technical reasons (see Materials and Methods), we modified the protocols for examining the phosphorylation of mCherry-tagged p115. We treated cells expressing either mCherry-tagged wildtype p115 or S240A mutated p115 with PMA to activate PKC, immunoprecipitated phosphorylated PKC substrates[100], and probed for p115. The amount of PKC-phosphorylated endogenous p115 (lower band) was similar between the two samples, while PKC phosphorylation of the mCherry-tagged p115 S240A (upper band) decreased by 1.6-fold (1.6 ± 0.2, n = 4) compared to mCherry-tagged wildtype p115 (Figure 2.4D), suggesting that PKC phosphorylation of p115 is at least partly through this site.

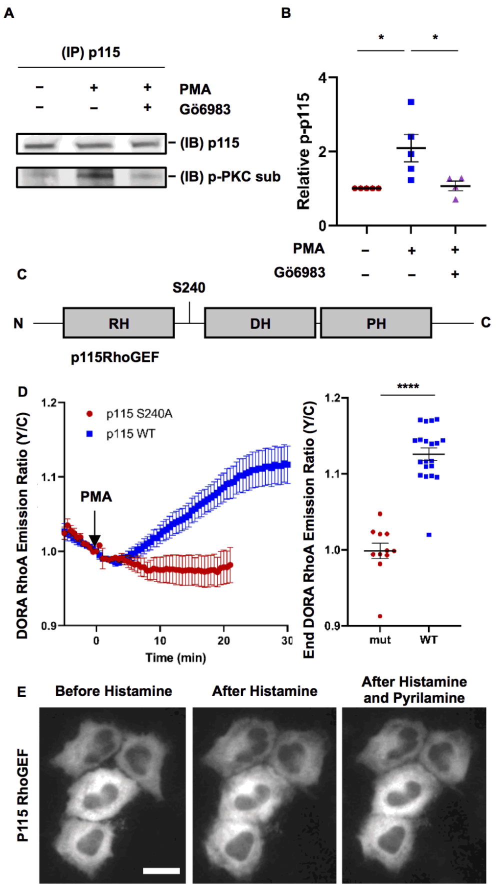

Figure 2.6: PKC phosphorylates p115 RhoGEF on Serine 240

(**A**) Representative western blot images of HeLa cells show that PKC phosphorylates p115. HeLa cells were either not stimulated, stimulated with 50ng/mL PMA, or stimulated with 50ng/mL PMA and 1 µM Gö6983. Afterwards, HeLa cell lysates were subjected to immunoprecipitation with antibodies to p115 and were immunoblotted for p115 (top) or phospho-PKC substrate (bottom) (**B**) Densitometry analysis of the immunoblot shown in (**A**) calculating the percentage of PKC-phosphorylated p115 over total p115. Average percentage ± SEM shown in bar graph amongst the various drug conditions (n = at least 4 for each condition). Nothing vs. +PMA: **P* = 0.04; +PMA vs. +PMA + Gö6983: **P* = 0.05; unpaired two-tailed Student's t-test. (**C**) Domain structure of p115 RhoGEF (RH: RGS homology domain, DH: Dbl homology domain, PH: pleckstrin homology domain) [101]. Line indicates location of Serine 240 residue. (**D**) Left: Representative average time courses ± SEM of the Y/C emission ratio changes in HeLa cells co-expressing DORA RhoA and either p115 WT (blue) or p115 S240A (red). 50ng/mL PMA was added to cells (p115 WT: n = 10 cells; p115 S240A: n = 4 cells). Right: Maximum emission ratio changes upon PMA and Gö6983 addition (p115 WT: n = 20 cells; p115 S240A: n = 11 cells). *****P* < 0.0001; unpaired two-tailed Student's t-test. (**E**) Representative fluorescence images of HeLa cells transfected with p115 tagged with mCherry. Shown are images before drug addition, after addition of 100 µM histamine, and subsequent addition of 100 µM pyrilamine. Scale bar, 10 µm.

To test whether Serine 240 plays a key role in PKC-mediated RhoA activation, we examined DORA RhoA responses in cells expressing either wildtype or S240A mutant of p115. Histamine stimulation led to a 31% ± 3.5% increase in DORA RhoA emission ratio in cells overexpressing wildtype p115 (increase of p115 protein by 2x based on Figure 2.4D), with kinetics consistent with the second phase ($t_{1/2} = 11 \pm 1.8$ min, n = 13) (Figure 2.4E). In contrast, histamine induced no change in DORA RhoA emission ratio in the presence of p115 S240A (0.01% ± 0.8%, n = 20) (Figure 2.4E), suggesting that the S240A mutation not only abolished the PKC-mediated RhoA activation but p115 S240A also exhibited some dominant negative effect. Similar results were seen in cells stimulated with PMA as p115 S240A abolished PMA-induced RhoA activation (Figure 2.6D). While membrane recruitment of p115 RhoGEF (most commonly through activation of $G\alpha_{12/13}$-coupled receptors) increases RhoA activity[102–108], neither histamine nor the histamine receptor antagonist pyrilamine affected p115 localization (Figure 2.6E), suggesting that histamine-induced PKC phosphorylation of p115 activates p115 in a non-canonical way that is independent of acute membrane recruitment. Overall, these data suggest that PKC phosphorylates serine 240 on p115 to activate its RhoGEF activity, which is responsible for the second phase of histamine-induced RhoA activation. These results also uncovered a critical mechanistic link between PKC and RhoA and provided the molecular mechanism underlying a non-canonical signaling axis that connects $G\alpha_q$-coupled GPCRs to RhoA.

The Ca^{2+}/PKC/p115 signaling axis enables RhoA memory

Given that stimulation of the histamine receptor activates RhoA in a biphasic manner via p63-dependent and p115-dependent pathways, we wondered whether active receptors are required to maintain the activation of RhoA. We tested this experimentally by applying the H_1HR inverse agonist pyrilamine after the biphasic activation reaches a plateau. As a metric for measuring the RhoA activity after receptor inactivation, we devised the residual RhoA activity metric, which is the ratio of the DORA RhoA emission ratio post-pyrilamine over the ratio post-histamine (Figure 2.7A-B and see Materials and Methods). In biphasic-responding cells overexpressing p63 (with endogenous p115), pyrilamine addition decreased the RhoA activity by 67%, leaving 33% ± 2.6% as residual RhoA activity (n = 54) (Figure 2.7A-B). In cells where flux into the Ca^{2+}/PKC/p115 signaling axis is largely reduced such as p63-expressing cells pretreated with either BAPTA or Gö6983, the residual RhoA activity was largely eliminated (BAPTA: residual RhoA activity= 2% ± 3.7%, n = 18; Gö6983: residual RhoA activity = 9.7% ± 2.6%, n = 16) (Figure 2.7B). In contrast, cells overexpressing p115 in the absence of p63 exhibited no decrease when pyrilamine was added post-histamine stimulation (residual RhoA activity = 99% ± 2.6%, n = 13) (Figure 2.7B). Testing various other conditions that either increase or decrease flux into the Ca^{2+}/PKC/p115 signaling axis showed a consistent trend that increasing Ca^{2+}/PKC/p115 signaling also increased residual RhoA activity (Figure 2.8A). Furthermore, PKC inhibition by Gö6983 after pyrilamine addition completely reversed the DORA RhoA emission ratio back down to basal levels (residual RhoA activity = 4.3% ± 2.9%, n = 19) (Figure 2.8B), suggesting that PKC remains active and plays an important role in maintaining the residual RhoA activity. Indeed, while histamine induces a transient increase in Ca^{2+} (Figure 2.9A), both PKC activity, detected by ExRai CKAR[109] (Figure 2.9B), and phosphorylation of p115 (Figure 2.9C) remain elevated even after pyrilamine treatment. Conceptually, these data suggest that the Ca^{2+}/PKC/p115 signaling pathway enables storage of "RhoA memory" where previous histamine-induced RhoA activation is retained even after

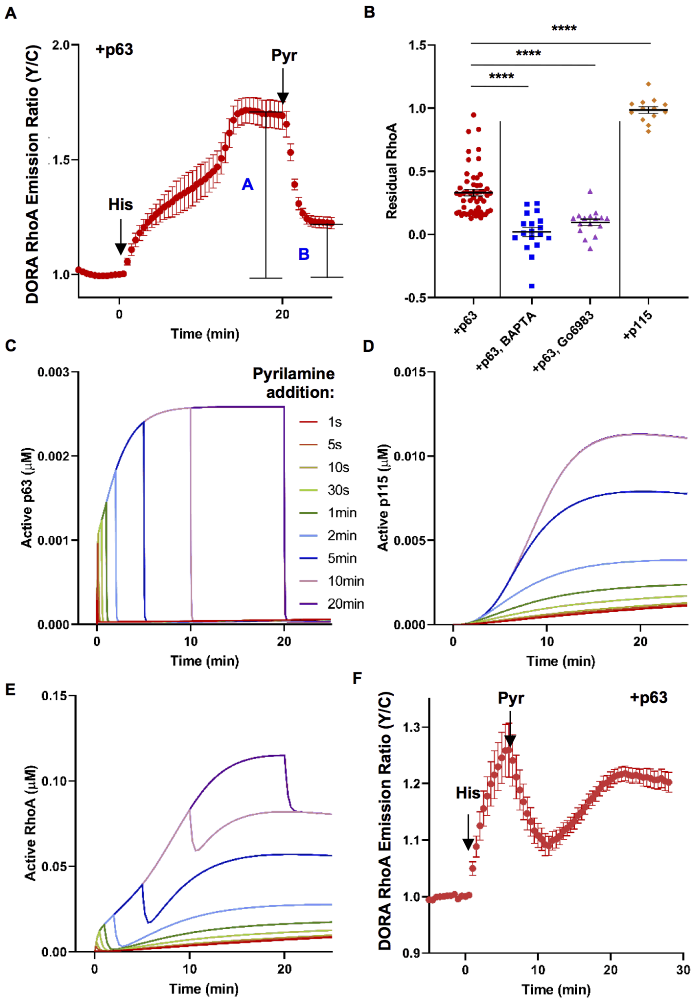

Figure 2.7: The Ca^{2+}/PKC/p115 signaling axis enables RhoA memory

(**A**) Residual RhoA activity is defined as the DORA RhoA Y/C emission ratio after addition (B) divided by the maximum increase of the DORA RhoA Y/C emission ratio after histamine stimulation (A). (**B**) Residual RhoA activity for various conditions to either increase (+p115, n = 13 cells) or decrease (+p63 with either BAPTA (n = 18 cells) or Gö6983 pretreatment (n = 16 cells)) flux into the Ca^{2+}/PKC/p115 signaling axis. Compared to the residual RhoA activity in cells expressing p63 (+p63, n = 54 cells) with no drug treatment, conditions with increased flux into the Ca^{2+}/PKC/p115 signaling axis also increased residual RhoA activity. For all comparisons to +p63 condition: *****P*<0.0001; unpaired two-tailed Student's t-test. (**C-E**) Computational simulations of adding pyrilamine at different time points after histamine stimulation and measuring concentrations of active p63 (**C**), active p115 (**D**), or active RhoA (**E**). (**F**) Average time course from multiple experiments ± SEM of the Y/C emission ratio changes in HeLa cells expressing DORA RhoA and p63. Cells were stimulated with 100 μM histamine and then 100 μM pyrilamine was added 5.5 min afterwards (n = 17 cells).

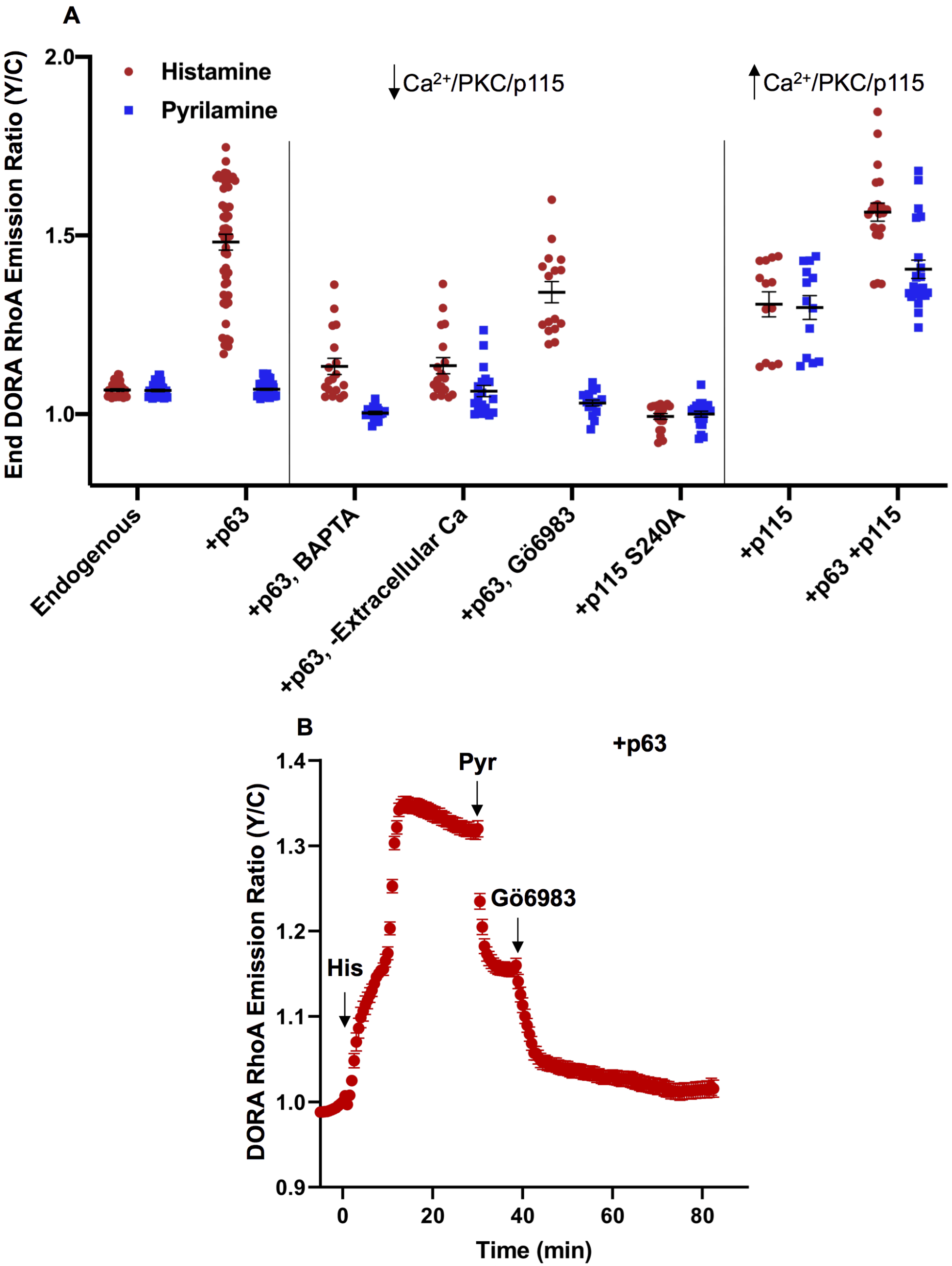

Figure 2.8: RhoA memory is dependent on Ca^{2+}/PKC/p115 signaling axis

(**A**) HeLa cells expressing various proteins and treated with various drugs to increase or decrease flux into the Ca^{2+}/PKC/p115 signaling axis. The Y/C emission ratio was measured after 100 µM histamine stimulation and then subsequently 100 µM pyrilamine addition (endogenous: n = 38 cells; +p63: n = 54 cells; +p63, BAPTA: n = 18 cells; +p63, -Extracellular Ca: n = 18 cells; +p63, Gö6983: n = 16 cells; +p115 S240A: n = 20 cells; +p63, ionomycin: n = 12 cells; +p63, PMA: n = 13 cells; +p115: n = 13 cells; +p63 +p115: n = 22 cells). (**B**) Representative average time courses ± SEM of the Y/C emission ratio changes in HeLa cells co-expressing p63 and DORA RhoA. Cells were stimulated with 100 µM histamine, 100 µM pyrilamine, and then 1 µM Gö6983 (n = 9 cells).

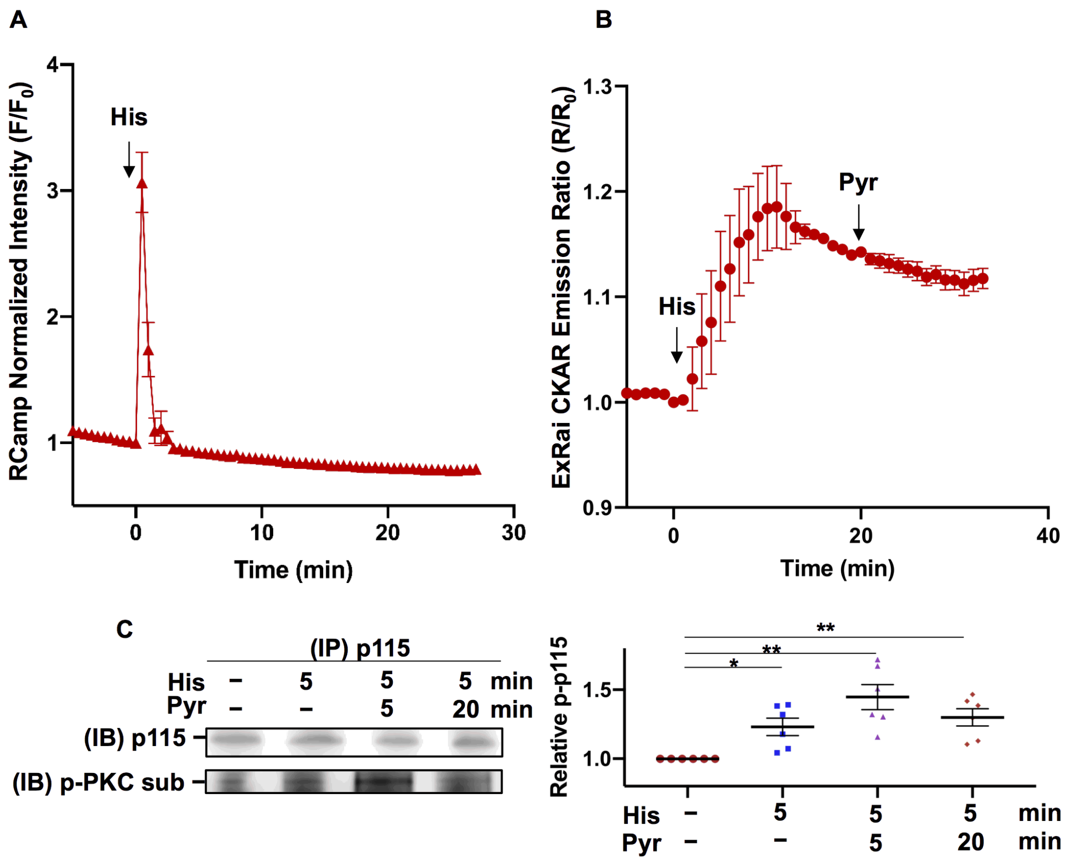

Figure 2.9: Calcium and PKC phosphorylation dynamics under histamine stimulation
(**A**, **B**) Representative average time courses ± SEM of the Y/C emission ratio changes in HeLa cells expressing either RCamp[110] (**A**) or ExRai CKAR [109] (**B**), to measure dynamics in calcium levels and PKC activity, respectively. HeLa cells were stimulated with either 100 µM histamine alone (**A**) or 100 µM histamine and then 100 µM pyrilamine (**B**) (RCamp: n = 8 cells; ExRai CKAR: n = 7 cells). This set of data was used to fit parameters in the computational model. (**C**) Left: Representative western blot images of HeLa cells simulated with either 100 µM histamine only or 100 µM histamine and then 100 µM pyrilamine. Numbers above refer to the number of minutes post histamine or pyrilamine addition. For all samples, cell lysates were immunoprecipitated with p115 antibody and immunoblotted for either p115 (top gel) or phospho-PKC substrates (bottom gel). Right: Densitometry analysis of the immunoblot shown on the left calculating the percentage of PKC-phosphorylated p115 over total p115. Average percentage ± SEM shown in bar graph amongst the various drug conditions (n = 6). Nothing vs. 5 min histamine: **P* = 0.015; Nothing vs. 5 min histamine + 5 min pyrilamine: ***P* = 0.0044; Nothing vs. 5 min histamine + 20 min pyrilamine: ***P* = 0.0048; unpaired two-tailed Student's t-test. The western blot results show prolonged PKC phosphorylation of p115 even after receptor antagonism.

histamine receptor inactivation. While the pyrilamine experiments gave hints into the differential regulation of the p63 and p115-dependent pathways by H_1HR, we constructed a computational model to more directly probe the impact of the receptor state on RhoA activity. By modeling binding events with mass action kinetics and enzyme-mediated events with Michaelis-Menten kinetics, the model captured the characteristics of the biphasic RhoA activation ($t_{1/2,\text{Phase 1}} = 1.9$ min, $t_{1/2,\text{Phase 2}} = 8.6$ min) when both p63 and p115 are present (Figure 2.10A-B). In addition, monophasic histamine activation is fast ($t_{1/2} = 1.4$ min) if only p63 is present and slow ($t_{1/2} = 9.4$ min) if only p115 is present (Figure 2.10B-C). In alignment with experimental data, the model predicts that upon pyrilamine addition RhoA activity goes down to pre-stimulation levels when only p63 is present, decreases by 35% when both p63 and p115 are present, and has no effect when only p115 is present in the simulation (Figure 2.10B).

To further probe the impact of the H_1HR state on RhoA activity, receptor inactivation by pyrilamine over a range of times post-histamine stimulation was simulated and the amount of active p63, active p115, and active RhoA was plotted (Figure 2.7C-E). While p63 activity was immediately turned off by pyrilamine treatment (Figure 2.7C) after histamine stimulation, p115 activity can still accumulate even if pyrilamine was added soon after histamine stimulation (Figure 2.7D). The overall RhoA activation kinetics and strength were altered depending on the duration of receptor activation. However, regardless of when pyrilamine was added after histamine stimulation and how transiently the receptor is activated, RhoA activity gradually increases after a transient decrease (Figure 2.7E), a prediction that was validated experimentally (Figure 2.7F). The computational predictions and experimental data suggest that the first, p63-dependent phase of RhoA activation requires continuously active receptor, while the second,

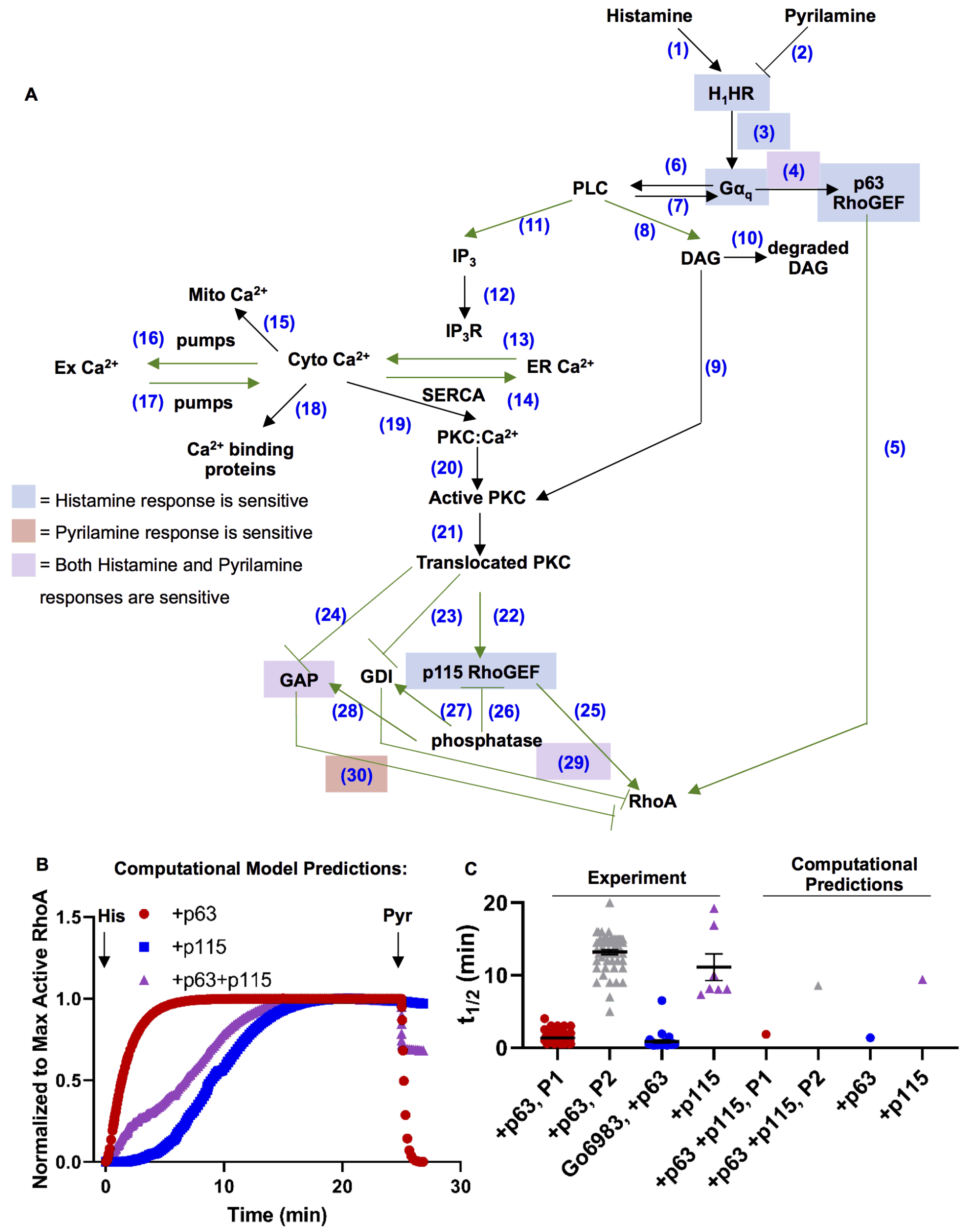

Figure 2.10: Computational model of biphasic RhoA activation

(**A**) Construction of the computational model. Enzyme-mediated reactions are modeled with Michaelis-Menten kinetics (green). Binding events are modeled with mass action kinetics (black). Sensitivity analysis shows that the histamine response (blue), pyrilamine response (red), or both responses (purple) are sensitive (sensitivity metric > 1) to the highlighted parameters. (**B**) Computational model predictions for RhoA kinetics under various RhoGEF conditions. (**C**) Computational model aligns with experimental data. $t_{1/2}$ comparison between computational predictions and experimental data (+p63, Phase 1 and Phase 2: n = 54 cells; +p63, Gö6983: n = 26 cells; +p115: n = 7 cells).

p115-dependent phase can be decoupled from the receptor activity, allowing for this persistent “RhoA memory”.

RhoA memory is important for transcriptional activity following transient receptor activation

To explore the functional role of this p115-dependent “RhoA memory”, we examined the downstream effects of RhoA activation. RhoA activates various transcription factors such as inducing the translocation of Myocardin-related transcription factor (MRTF-A/B) into the nucleus[77]. While in the nucleus, MRTF interacts with Serum Response Factor (SRF) to activate transcription of target genes[111]. Thus, to monitor RhoA-mediated transcriptional events, we first measured the nuclear localization of MRTF[112–114]. In p63-expressing cells that exhibited histamine-induced biphasic RhoA activation, nuclear translocation of MRTF-B was also biphasic (Figure 2.11A). In these cells, subsequent pyrilamine addition decreased RhoA activity and MRTF-B nuclear localization but not to pre-stimulation levels. Interestingly, the decrease in MRTF-B nuclear localization is smaller than the decrease in RhoA activity, suggesting that the “RhoA memory” is amplified downstream of RhoA (RhoA: residual RhoA activity = 30% ± 3.2%, n = 10; MRTF-B: residual MRTF-B nuclear localization = 49% ± 5.2%, n = 10, P = 0.0056) (Figure 2.11A and Figure 2.12A). In contrast, Gö6983-pretreated cells expressing p63 exhibited fast, monophasic RhoA activation and relatively transient MRTF-B nuclear translocation (Figure 2.11B and Figure 2.12B). In these monophasically-responding cells, the transient MRTF-B nuclear translocation almost completely reversed to pre-stimulation levels. In

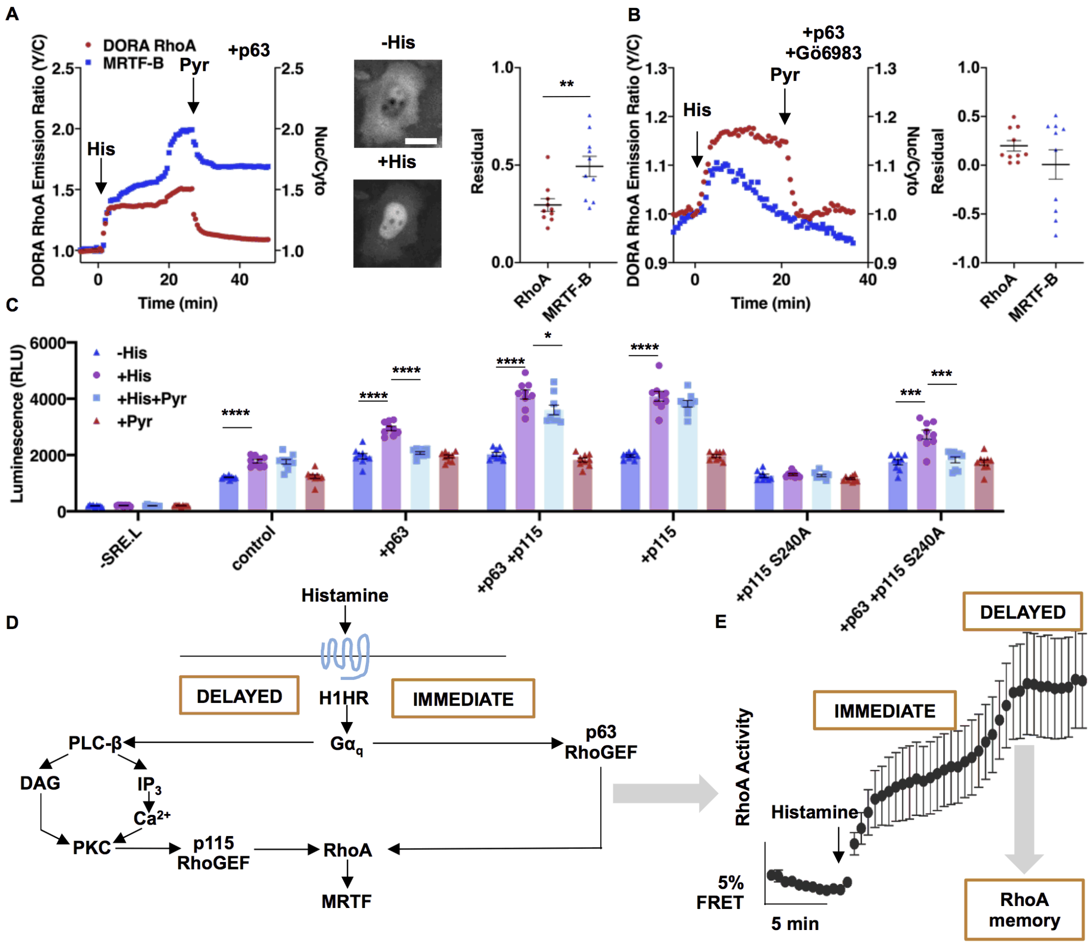

Figure 2.11: RhoA memory is important for transcriptional activity following transient receptor inactivation

(**A, B**) RhoA activation and MRTF-B nuclear translocation in HeLa cells expressing DORA RhoA, p63, and mTagBFP2-tagged MRTF-B stimulated with 100 µM histamine and then 100 µM pyrilamine, without (**A**) and with (**B**) Gö6983 pretreatment. (**A**) Left: Representative time course of biphasic-responding HeLa cells. DORA RhoA Y/C emission ratio changes on left axis and nuclear to cytosol ratio of MRTF-B on right axis. Middle: Representative BFP epifluorescence images of HeLa cells expressing mTagBFP2-tagged MRTF-B before and after histamine stimulation. Right: Residual RhoA activity and residual MRTF-B in the nucleus (n = 10 cells for each metric). Scale bar, 10 µm. (**B**) Left: Representative time course of monophasic-responding HeLa cells. Right: Residual RhoA activity and residual MRTF-B in the nucleus (n = 10 cells for each metric). (**C**) Average bioluminescence in cells with various transfection and drug stimulation conditions (n = 6 wells for each condition). **P*<0.05, ****P*<0.001, *****P*<0.0001; unpaired two-tailed Student's t-test. (**D**) Summary of findings. Histamine binding to the Gα_q-coupled H_1HR activates the Gα_q-activatable p63 RhoGEF to immediately activate RhoA. H_1HR activation also leads to the canonical Gα_q pathway where intracellular Ca^{2+} levels and PKC activities are increased. PKC phosphorylates p115 RhoGEF on the Serine 240 residue, which in turn activates p115 to activate RhoA during the delayed phase. Activation of RhoA leads to nuclear translocation of MRTF-A/B to increase transcriptionally activity. (**E**) The two phases of RhoA activation leads to different phenotypic responses, where the delayed phase leads to RhoA memory and persistent transcriptional activity.

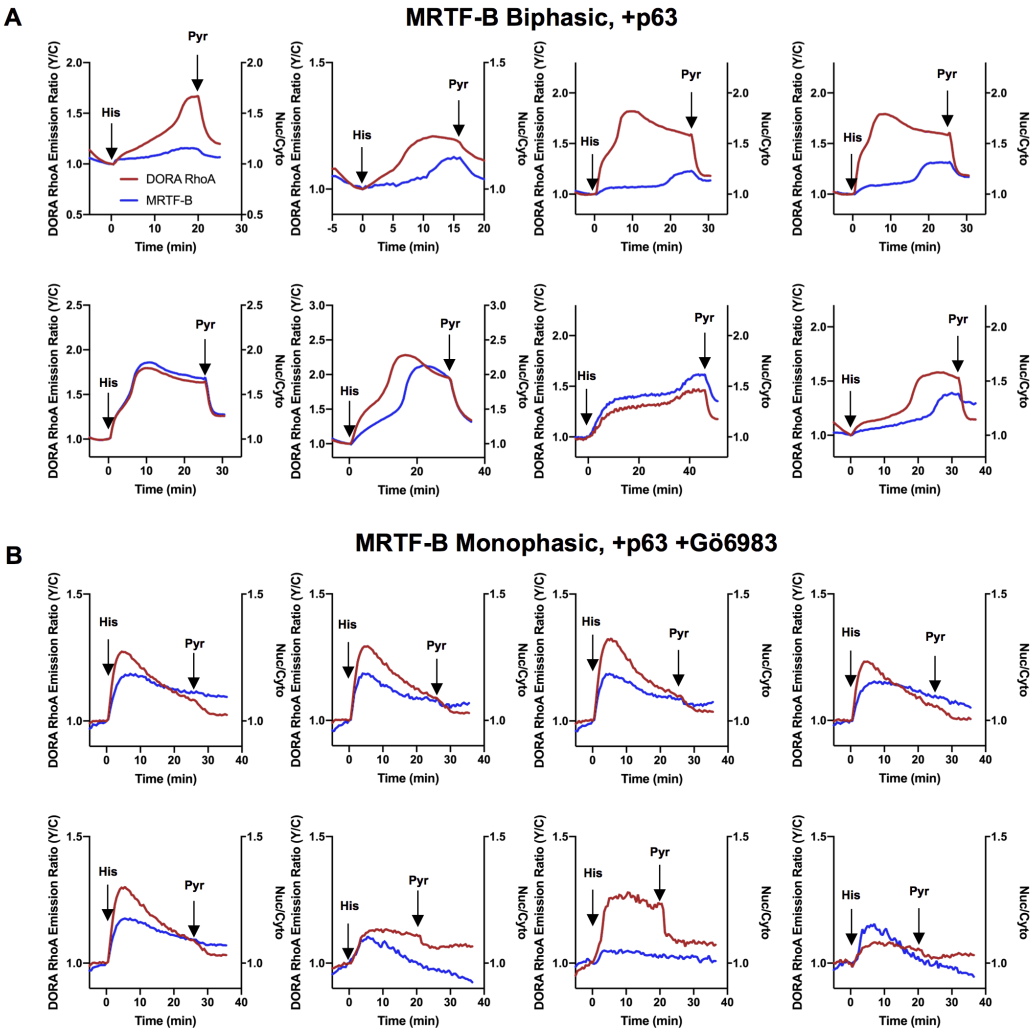

Figure 2.12: RhoA signaling kinetics direct MRTF-B nuclear translocation dynamics
(**A, B**) Individual cell traces of the DORA RhoA Y/C emission ratio changes (left axis) and the nuclear to cytosol ratio of MRTF-B (right axis) in HeLa cells expressing DORA RhoA, p63, and mTagBFP2-tagged MRTF-B. Cells were pretreated with Gö6983 to produce monophasic responders (**B**) with biphasic responders as controls (**A**).

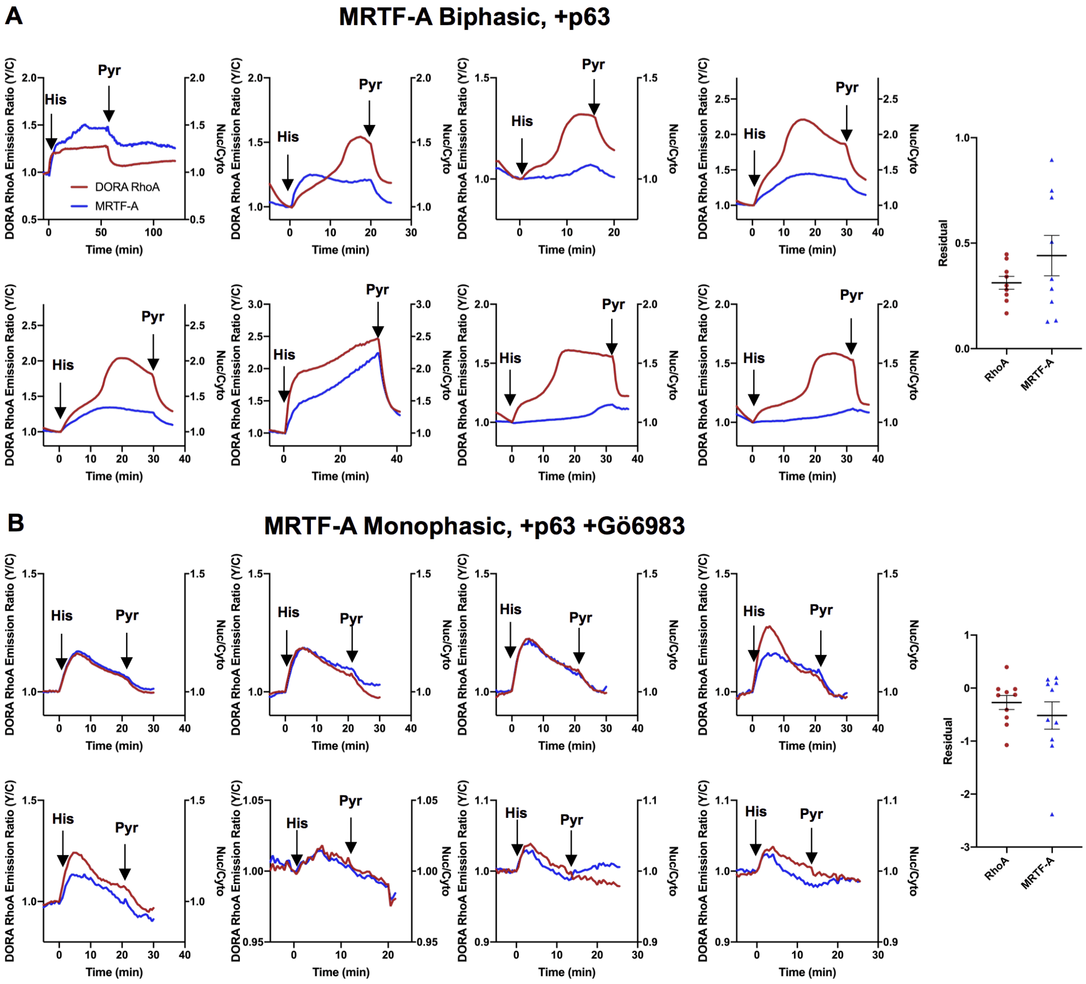

Figure 2.13: RhoA signaling kinetics direct MRTF-A nuclear translocation dynamics
(**A, B**) Left: Individual cell traces of the DORA RhoA Y/C emission ratio changes (left axis) and the nuclear to cytosol ratio of MRTF-A (right axis) in HeLa cells expressing DORA RhoA, p63, and mTagBFP2-tagged MRTF-A. Cells were pretreated with Gö6983 to produce monophasic responders (**B**) with biphasic responders as controls (**A**). Right: residual RhoA activity and residual nuclearly localized MRTF-A for biphasic responders (**A**) and monophasic responders (**B**) (biphasic: n = 9 cells; monophasic: n = 10 cells).

addition, pyrilamine had a small effect to further reduce nuclear localization of MRTF-B and MRTF-A (Figure 2.13). These data suggest that the biphasic behavior of RhoA activation after pyrilamine treatment there was essentially no residual nuclear localization (RhoA: residual RhoA activity = 20% ± 5.4%, n = 10 cells; MRTF-B: residual MRTF-B nuclear localization = 0.8% ± 15%, n = 10 cells, $P = 0.3$) (Figure 2.11B and Figure 2.12B). Similar results are seen for impacts MRTF-B and MRTF-A nuclear translocation kinetics and retention of nuclear localization after histamine receptor inactivation.

Looking further downstream, we measured MRTF/SRF-mediated transcription via the SRE.L luciferase reporter[115]. Basal RhoA-mediated transcriptional activity was increased compared to the endogenous condition (SRE.L) when wildtype p63 or p115 RhoGEFs were overexpressed ("–His" comparison in Figure 2.11C of control to either +p63 or +p115 conditions: $P < 0.0001$). Histamine stimulation (30 min) increased RhoA-mediated transcription, which was measured 24 hours later, when either wildtype p63 or p115 was overexpressed; the only case where histamine had no effect on RhoA-mediated transcription was when only the PKC-phosphorylation defective mutant of p115 (SRE.L + p115 (S240A)) was expressed (Figure 2.11C), consistent with the data showing that histamine does not activate RhoA when p115 S240A was expressed (Figure 2.4E). Pyrilamine incubation (30 min) after histamine stimulation (30 min) (+His +Pyr) decreased RhoA-mediated transcription compared to histamine alone stimulation (+His) when p63 was expressed, while expression of wildtype p115 attenuated pyrilamine's effect in decreasing RhoA-mediated transcription (Figure 2.11C). For instance, expression of only wildtype p115 (+ p115) abrogated the difference in RhoA-mediated transcription between histamine alone (+His) versus histamine and then pyrilamine (+His +Pyr) (Fig 2.11C) (+ p115 condition: +His, RLU = 4084 ± 175; +His +Pyr, RLU = 3823 ± 120, n = 9, $P = 0.24$). These data suggest that even though both p63 and p115 play a role in both basal and histamine-induced increases in RhoA mediated transcription, p115 plays a unique role in transducing "RhoA memory" into sustained transcriptional activity following transient receptor activation.

Discussion

By measuring signaling kinetics through FRET-based biosensors, we discovered that stimulation of $G\alpha_q$-coupled receptors such as the histamine receptor induces biphasic RhoA activation. We determined the mechanisms underlying these two activation phases to be attributed to two pathways that bifurcate at $G\alpha_q$ (Fig 2.11D). The immediate phase of RhoA activation is by $G\alpha_q$ activating p63 RhoGEF, which in turn activates RhoA. The delayed phase is through the canonical $G\alpha_q$ pathway to activate PLCβ to produce DAG and inositol trisphosphate, thereby increasing Ca^{2+} levels and PKC activity. Interestingly, the engagement of both p63 RhoGEF and PLCβ raise the possibility of near-simultaneous activation of both effectors. Following activation of PKC by DAG and Ca^{2+}, p115 RhoGEF is activated through PKC-mediated phosphorylation of serine 240, leading to further activation of RhoA. Furthermore, the immediate phase is tightly regulated by the histamine receptor while the delayed phase is decoupled from the receptor after initial activation, causing "RhoA memory" to allow for persistent RhoA signaling. This "RhoA memory" is also amplified and transduced into persistent transcriptional activity that is uncoupled from the activation state of the receptor (Fig 2.11E). Our data suggests that this observed "RhoA memory" is not encoded at the RhoA level but more upstream. Histamine-induced Ca^{2+} increases allow for Ca^{2+} binding and membrane recruitment of PKC[116]. Although Ca^{2+} increases are transient (Figure 2.9A) which would affect PKC activity, our computational model predicts that DAG levels are sustained even after pyrilamine addition, which allows for persistent PKC activity even after receptor inactivation. This persistent PKC activity and relatively slow phosphatase activity (Figure 2.9B-C) allow the sustained phosphorylation of p115 RhoGEF. Altogether, we postulate that the mechanism for the observed "RhoA memory" is through persistent PKC activity from sustained DAG levels and slow dephosphorylation on p115 RhoGEF. These findings are likely a general feature of RhoA signaling[117] as biphasic RhoA activation is not only seen by histamine stimulation but also other $G\alpha_q$-coupled receptors such as the synthetic $G\alpha_q$-DREADD (Figure 2.1F).

To reveal the impact of the upstream signaling pathways on RhoA kinetics, we combined computational modeling with live-cell fluorescence imaging. By measuring spatiotemporal signaling dynamics at single-cell resolution using fluorescent biosensors, we can obtain quantitative kinetic information and then incorporate these parameters to form a biologically accurate and relevant model. While other studies have also applied computational models to answer various questions in the signaling field[118,119], few studies have incorporated quantitative biosensor imaging to revise and validate their computational models[120,121]. Here, we computationally simulated the pathways responsible for RhoA activation to tease apart the impact of histamine receptor state on RhoGEF and RhoA activity. While the FRET-based biosensors measured RhoA activity one condition at a time, the computational modeling allowed us to test many conditions quickly and evaluate metrics that cannot be measured with current tools such as the activity state of specific RhoGEFs. Modeling predictions were then tested experimentally. Combining both computational and experimental approaches, we concluded that the PKC/p115 pathway is responsible for maintaining the RhoA memory after receptor inactivation. In the future, the computational model can be further expanded to address the role of other players in these complex pathways such as protein phosphatases in regulating RhoA kinetics.

In summary, our study identified a set of biochemical events to produce biphasic activation of RhoA from histamine stimulation. These two phases were regulated by the receptor differently and impacted transcription with different kinetics to allow both rapid kinetics and sustained signaling memory. These studies allow for greater appreciation of the intricate organization of RhoA signaling[117], providing mechanisms underlying RhoA signaling specificity.

Materials and Methods

Plasmid Construction

All assembly of constructs was performed using Gibson Assembly (NEB 2x High Fidelity Master Mix). mCherry-tagged p63 RhoGEF, DORA RhoA, and DORA RhoA (L59Q) were constructed previously[79]. To make mCherry-tagged p115 RhoGEF, Gibson assembly of PCR products (Q5 High-Fidelity Kit, New England BioLabs) amplified from mCh-p63 for mCherry using the forward primer (lowercase letters are Gibson assembly overhangs and uppercase letters are priming regions) 5'-cactatagggagacccgccaccATGGTGAGCAAGGGCGAGGA-3' and reverse primer 5'- GCATGGACGAGCTGTACAAG-3' and from pCEFL-p115 plasmid (gift of Silvio Gutkind, University of California San Diego, CA) for p115 using forward primer 5'-

gcatggacgagctgtacaagATGGAAGACTTCGCCCGAG-3’ and reverse primer 5’-GCCTGGCTGCACTTGAgaattctgcagatatccagc-3’. Assembly of S240A mutant of p115 was generated via Gibson assembly of PCR products that introduced the mutation in mCh-p115 using the forward primer 5’-aagaaggcaggtagaaatTTCTTCCGGAAAAAGGTGATG-3’ and the reverse primer 5’-gaagaaatttctacctgcCTTCTTGTCTCCACTCTTGGTC-3’. shRNA p115 and Scrambled were generated from Santa Cruz Biotech (sc-48363). Generation of mTagBFP2-tagged MRTF-A was through Gibson assembly of PCR products amplified from p3xFLAG-MKL1 (gift from Ron Prywes (Addgene plasmid # 11978; http://n2t.net/addgene:11978; RRID:Addgene_11978)) for MRTF-A using the forward primer 5’-aactggggcacaagcttaatggaggtactggtggaagtATGCCGCCTTTGAAAAGTCC-3’ and the reverse primer 5’-taaacgggccctctagactaCTACAAGCAGGAATCCCAGTG-3’ and from mTagBFP2-pBAD (gift from Michael Davidson (Addgene plasmid # 54572; http://n2t.net/addgene:54572; RRID:Addgene_54572)) for mTagBFP2 using the forward primer 5’-agacccaagctggctagcgtttaaacttaagcttgggccaccATGAGCGAGCTGATTAAGGAG-3’ and the reverse primer 5’-ACTGGGGCACAAGCTTAAT-3’. Generation of mTagBFP2-tagged MRTF-B was similar to MRTF-A but using pmVenus-C2-MmMKL2 (gift from Dorus Gadella (Addgene plasmid # 67894; http://n2t.net/addgene:67894; RRID:Addgene_67894)) for MRTF-B using the forward primer 5’-aactggggcacaagcttaatggaggtactggtggaagtATGATCGATAGCTCCAAGAAGC-3’ and the reverse primer 5’-GTTTAAACGGGCCCTCTAGACTAgtcccatggcagcg-3’. Generation of C-terminus of PLCβ-P2A-mCherry in the pcDNA3.1 backbone was via Gibson assembly of PCR products amplified from mCh-p63 for mCherry using the forward primer 5’-gagagtttgatactcctctgGCTACTAACTTCAGCCTGTTAAAGC-3’ and reverse primer 5’-

TCACTTGTACAGCTCGTCCA-3’ and from pCDN3-PLCβ-C-terminus (gift of Lynn Heasley, University of Colorado Anschutz Medical Campus, CO) [95] for PLCβ-C-terminus using forward primer 5’gagagtttgatactcctctgGCTACTAACTTCAGCCTGTTAAAGC-3’ and reverse primer 5’-ggaacatcatatcgatacatGGTGGCGGGTCTCCCTAT-3’. The RhoA1G plasmid was a gift from Klaus Hahn (Addgene plasmid #12150; http://n2t.net/addgene:12150; RRID:Addgene_12150). The pKH3-p190 GAP plasmid was a gift from Ian Macara (Addgene plasmid #15547; http://n2t.net/addgene:15547; RRID:Addgene_15547).

Cell Culture and Transfection

HeLa cells were cultured in Dulbecco modified Eagle medium (DMEM; Gibco) containing 1 g/L glucose and supplemented with 10% (v/v) fetal bovine serum (FBS, Sigma) and 1% (v/v) penicillin-streptomycin (Pen-Strep, Sigma-Aldrich). All cells were maintained in a humidified incubator at 37°C with a 5% CO_2 atmosphere. Prior to transfection, cells were plated onto sterile 35-mm glass-bottomed dishes and grown to 50–70% confluence. Cells were then transfected using Lipofectamine 2000 (Invitrogen) or Calcium Phosphate (for studies that involve shRNA) and grown an additional 24 h before imaging.

Bioluminescence Assay

HeLa cells seeded onto a 6-well plate (Falcon) were transfected with SRE.L and indicated plasmids. 24 h after transfection, cells were passaged onto a 96-well plate (Corning Costar) in triplicates. If indicated, cells were stimulated with either histamine for 30 min, pyrilamine for 30 min, or histamine for 30 min and then pyrilamine for 30 min. After drug addition, drug was washed away at least 3 times with fresh media. 24 hr later, media was replaced with PBS and

150µg/mL D-luciferin (Gold Biotechnology) was added to cells and bioluminescence was measured on the Tecan Spark 20M.

Immunoprecipitation and western blot

HeLa cells were washed 3x with 37°C HBSS and then indicated drugs were added for 30 min in 37°C non-CO_2 incubator. HeLa cells were subsequently lysed (1mM NaF, 1mM Na_3VO_4, 10nM Calyculin A, 1mM PMSF, 1mg Complete, EDTA-free protease inhibitor cocktail (Roche) in RIPA buffer), scraped, collected, and spun at 15,000*g* for 30 min at 4°C. Supernatant was collected and incubated with immunoprecipitating antibody (p115 (C-9) (sc-74565) (Santa Cruz)) or phospho-PKC substrate ((#2261) (Cell Signaling)) for 16-24 h at 4°C. The lysate-antibody mix was incubated with Protein A/G PLUS-Agarose beads (Santa Cruz), which were equilibrated in RIPA buffer beforehand, for 3 h. After 4 washes with ice-cold DPBS, bound protein was eluted by boiling for 10 min SDS sample buffer. Whole cell lysates, supernatant, and immunopreciptated samples were probed with antibodies to p115, phospho-PKC substrate, and β-tubulin (#2146S, Cell Signaling).

For probing serine 240 on p115 as the PKC phosphorylation site, we expressed mCherry-tagged wildtype and S240A mutant p115. After p115 immunoprecipitation, phospho-PKC substrates were immunoblotted. Unfortunately, there was a non-specific phospho-PKC substrate band with a size that coincided with mCherry-tagged p115 as it was seen when no plasmid was transfected. Thus, we swapped mCherry with a GFP and performed a GFP immunoprecipitation. However, the GFP pulldown was non-specific. Therefore, we pulled down phospho-PKC substrates and probed for p115, which is what is shown in the paper.

Rhotekin pulldown assay

RhoA activation was determined as described previously[122]. Briefly, cell lysates were incubated with the agarose-bound glutathione S-transferase-rhotekin-RhoA binding domain and then subjected to series of washes and centrifugations. 4 × Laemmli buffer was added and boiled for 5 min prior to SDS-PAGE analysis. Activated GTP-bound RhoA was detected by Western blotting for RhoA (#2117S, Cell Signaling) and normalized to total RhoA in cell lysate.

Time-lapse fluorescence imaging

Cells were washed twice with Hank's balanced salt solution (HBSS, Gibco) and subsequently imaged in HBSS in the dark at 37°C. Histamine (His; Sigma-Aldrich), Pyrilamine (Pyr; Sigma-Aldrich), 1,2-Bis(2-aminophenoxy)ethane-N,N,N′,N′-tetraacetic acid tetrakis (acetoxymethyl ester) (BAPTA; Cayman Chemical Company), Ethylene glycol-bis(β-aminoethyl ether)-N,N,N′,N′-tetraacetic acid (EGTA, Sigma-Aldrich), Ionomycin (Iono, LC Laboratories), 3-[1-[3-(Dimethylamino)propyl]-5-methoxy-1H-indol-3-yl]-4-(1H-indol-3-yl)-1H-pyrrole-2,5-dione (Gö6983, Calbiochem), Phorbol Myristate Acetate (PMA, Calbiochem), Clozapine N-Oxide (CNO, Fisher) were added as indicated.

Epifluorescence imaging was performed on a Zeiss Axiovert 200M microscope (Carl Zeiss) equipped with a xenon lamp, a 40x/1.3 NA objective and a cooled CCD controlled by METAFLUOR 7.7 software (Molecular Devices). For the Zeiss Axiovert 200M, the following excitation/emission filter combinations (maxima/bandwidths in nm) were used: BFP - EX380/10, EM475/25; CFP - EX420/20, EM475/25; YFP - EX495/10, EM535/25; RFP - EX568/55,

EM653/95; CFP/YFP FRET - EX420/20, EM535/25. Exposure times were either 50 (for yellow channel), 100 ms (for red channel), or 500 ms (for all other channels) and images were acquired every 30 s. All epifluorescence experiments were subsequently analyzed using MetaFluor software. Pseudocolor images were generated in Image J.

Time to Half Max Analysis

To calculate time to half max ($t_{1/2}$) in an unbiased manner, MATLAB code was generated to computationally calculate $t_{1/2}$. Briefly, monophasic responding curves were fit to the general exponential function:

$$A - Be^{-ct}$$

where c relates to $t_{1/2}$ by the relationship:

$$\frac{\ln(2)}{c}$$

Biphasic responding curves were fitted to a piece-wise exponential function. To divide the curve into two separate exponential functions, the second derivative was calculated and was fitted to a 4th order polynomial curve. The first local maximum of the curve fitted to the second derivative served as the time point for separating the first phase and second phase (t_c). The time frame for the first phase was defined as $0 < t < t_c$, while the time frame for the second phase was defined as $t_c < t < t_{max}$, where t_{max} is the time point corresponding to the max DORA RhoA emission ratio value post drug addition. The two phases were fitted to exponential curves similar to the analysis for the monophasic responding curves. The end emission ratio for the first peak $(Y/C)_{\text{Peak 1}}$ was calculated by the respective emission ratio value for time point t_c. An example biphasic curve fitted to 2 exponential curves based on our generated code is shown in Figure 2.14. The code for the aforementioned analysis is available upon request.

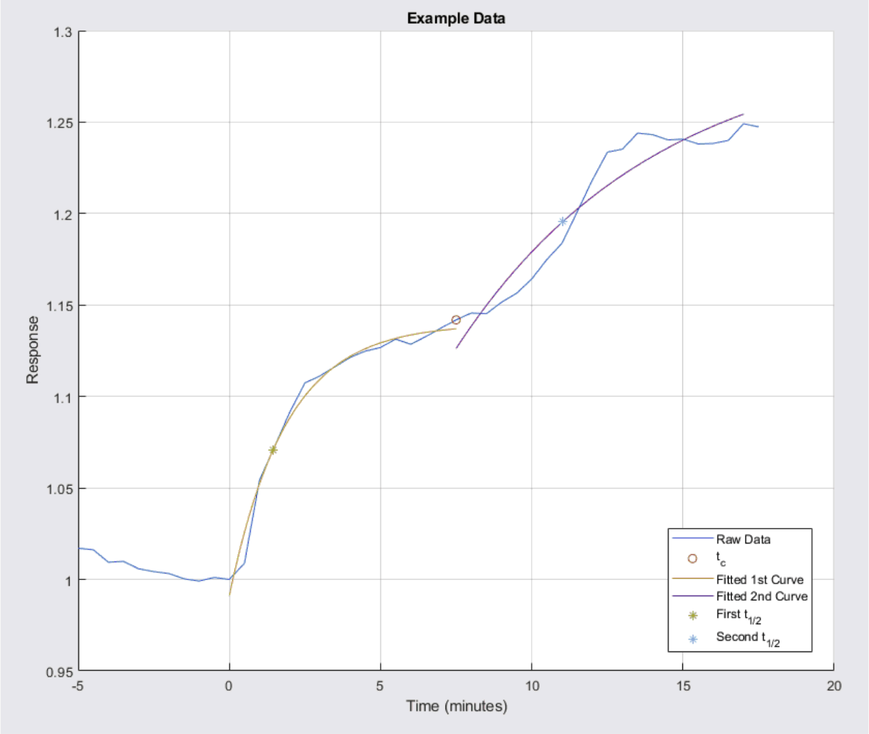

Figure 2.14: Example time-to-half maximum analysis for a biphasic curve
A representative biphasic curve which underwent time-to-half maximum analysis. Two exponentials are fit for different time periods. The dividing point (t_c) and its respective y-point on the curve, the two exponentials fitted to the separate phases, and the calculated $t_{1/2}$ for each phase are depicted in the graph.

Fluorescence analysis

For biosensor analysis, raw fluorescence intensities were corrected by subtracting the background fluorescence intensity of a cell-free region from the emission intensities of biosensor-expressing cells. Yellow/Cyan (Y/C) emission ratios were then calculated at each time point. For calculating normalized Y/C emission ratio, the raw ratios were normalized by dividing the emission ratio at each time point by the starting ratio value at time zero (R_0), which was defined as the emission ratio at the time point immediately preceding drug addition. For calculation of max Y/C emission ratio, the maximum changes from drug stimulation were reported for some of the bar graphs and were calculated as: $(R_{max}- R_0)/R_{0,}$ where R_{max} is the maximum emission ratio after the corresponding drug addition. For calculation of end R, the change in R after drug addition was reported for some of the bar graphs and were calculated as: (end $R_{drug} – R_0)/R_{0,}$ where end R_{drug} is the emission ratio at the end of the imaging period after the corresponding drug addition. Residual RhoA activity was calculated as the emission ratio after pyrilamine addition R_{Pyr} over the ratio after histamine addition R_{His}, R_{Pyr}/R_{His}. For biphasic responses, the peak percentage of total DORA RhoA response was calculated as the change in emission ratio from the indicated peak over the maximum ratio change, for peak 1 $(R_{peak\ 1} – R_0)/(\max R – R_0)$ and for peak2 $(R_{peak\ 2} – R_0)/(\max R – R_0)$, where $R_{Peak\ 1}$ is the end emission ratio for peak 1 and $R_{Peak\ 2}$ is the end emission ratio for peak 2.

When using the RCaMP sensor[110], the normalized RFP intensity was calculated by dividing the raw RFP intensity at each time point by the starting RFP intensity at time zero (F/F_0), which was defined as the RFP intensity at the time point immediately preceding drug addition. When using the ExRai CKAR sensor [109], the normalized excitation ratio was calculated by dividing the raw emission ratio (480 nm/400nm) at each time point by the starting ratio value at time zero (R/R_0), which was defined as the emission ratio at the time point immediately preceding drug addition. For MRTF nuclear to cytosol analysis, the normalized nuclear/cytosol ratio was calculated by dividing the BFP intensity ratio between nucleus and cytosol ($BFP_{nucleus}/BFP_{cytosol}$) at each time point by the starting ratio value at time zero (N/N_0), which was defined as the nuclear/cytosol ratio at the time point immediately preceding drug addition (N_0). Residual MRTF was calculated as the nuclear/cytosol ratio after pyrilamine addition (N_{Pyr}) over the ratio after histamine addition (N_{His}) (N_{Pyr}/N_{His}). All graphs were plotted using GraphPad Prism 7 (GraphPad).

Statistics and reproducibility

Statistical analyses were performed in GraphPad Prism 7 (GraphPad). All data were assessed for normality. For normally distributed data pairwise comparisons were performed using unpaired two-tailed Student's t-tests, with Welch's correction for unequal variances used as indicated. Statistical significance was set at $P < 0.05$. Average time courses shown in Figures 2.1B-D, 2.1F-G, 2.2A, 2.2D, 2.3A-G, 2.3I-K (curves), 2.4A-C (curves), 2.4E (curve), 2.5, 2.6D (curve), 2.7A, 2.7F, 2.8B, 2.9A-B, and 2.11E are representative of at least 3 independently repeated experiments. Time courses shown in Figures 2.11A (curve), 2.11B (curve), 2.12, and 2.13 (curve) are single-cell traces that are representative of at least 9 cells in total from 3 independently repeated experiments. Average time course from all experiments is shown in Fig 3F. Average bar graphs shown in Figures 2.1A, 2.2B, 2.2E, 2.2F, 2.3K-L (bar), 2.4C-E (bar), 2.6B, 2.6D (bar), 2.7B, 2.8A, 2.9C, 2.10C, 2.11A (bar), 2.11B (bar), 2.11C, and 2.13 (bar) depict combined data sets from at least 3 independent experiments.

Computational modeling

All computational modeling was performed using Virtual Cell version 7.1.0.3. Briefly, the biphasic RhoA activation was modeled using either mass action kinetics for binding events or irreversible Michaelis-Mentin kinetics for enzyme-mediated reactions (Figure 2.10A). Although RhoGDIs were not considered experimentally in this paper, PKC is known to phosphorylate and thus deactivate RhoGDIs, and this PKC regulation of RhoGDIs was considered in the computational model[123,124]. All components were assumed to be homogenous and no spatial components were considered. All concentration and kinetic parameters were either attained from the literature or approximated. Parameter approximation was done by inputting experimental data throughout the paper (including data from Figure 2.9) into Virtual Cell's parameter estimation module and fitted using the particle swarm COPASI method. The concentration for histamine and pyrilamine were those used in our experiments. Simulations were run using the IDA/CVODE method. A protocol where pyrilamine was added at indicated times was included in the simulations. The Virtual Cell BioModel "Histamine-RhoA Model_final" is available from the Public BioModels within the Virtual Cell software under the username "jzz002". Virtual Cell can be downloaded from http://vcell.org[125,126].

We performed a sensitivity analysis to investigate how each parameter affected the kinetics and shape, but not magnitude, of the RhoA activity curve. Each parameter was individually perturbed upwards and downwards by one order of magnitude compared with the value in the original model. The RhoA activity curve was simulated and the ratio between active RhoA for each time point was calculated as:

$$\frac{\text{active RhoA}_{\text{changed value}}(t)}{\text{active RhoA}_{\text{original value}}(t)}$$

The standard deviation of these ratios was calculated and used as a measure of the effect of each perturbation. If the RhoA activity curve changed in magnitude but not in overall kinetics, this sensitivity metric was close to 0. If the overall kinetics of the RhoA activity curve changed, then it will be higher. The sensitivity metric was calculated for the responses both to histamine (simulated as 100 μM histamine added at $t = 0$ and recorded for 20 min) and pyrilamine (simulated as 100 μM pyrilamine at $t = 20$ min post histamine addition, recorded for 30 min). Parameters where one order magnitude change in the original value resulted in sensitivity metric values for either histamine or pyrilamine response to be greater than 1 are highlighted in Figure 2.9A.

From the sensitivity analysis, the parameters that affected histamine-stimulated RhoA kinetics the most are either involved with H_1HR/Gα_q/p63 RhoGEF coupling or direct regulation of RhoA by p115 RhoGEF, GAP, and GDI (Figure 2.10A), consistent with the idea that direct effectors of RhoA have a key role in regulating RhoA activity dynamics. In addition, the results from the sensitivity analysis highlight key components (p63 and p115) of our mechanistic model, which proposes that histamine-stimulated biphasic activation of RhoA is due to p63-dependent and p115-dependent pathways.

Acknowledgements

Chapter 2, in part, has been submitted for publication of the material as it may appear in PLOS Biology 2020. Nguyen, Andy H; Miyamoto, Shigeki; Brown, Joan Heller; McCulloch, Andrew D; Zhang, Jin, PLOS Biology, 2020. Jason Zhaoxing Zhang was the first-author of this paper. We thank Yi Wu for the DORA RhoA construct; Alexandra Newton and Angela Van for the PMA and Gö6983 reagents; Silvio Gutkind and Justine Paradis for the Gα_q-DREADD construct and CNO reagent; Kim McCabe for help in the computational model; Maya Kunkel for critical reading of the manuscript.

Chapter 3: Phase separation of a PKA regulatory subunit controls cAMP compartmentation and oncogenic signaling

Abstract

The fidelity of intracellular signal transduction hinges on the organization of signaling molecule activities into a dynamic architecture. Spatial compartmentation was first proposed over 30 years ago to explain how diverse G-protein-coupled receptors can regulate specific cellular processes despite converging on the ubiquitous second messenger 3',5'-cyclic adenosine monophosphate (cAMP). Recent work has challenged the textbook model that cAMP compartmentation is achieved by its local degradation, yet the specific mechanisms responsible for spatially constraining this diffusible messenger remain elusive. We address this longstanding question by identifying the formation of biomolecular condensates of the type I regulatory subunit of cAMP-dependent protein kinase (PKA), RIα, as a key driver of cAMP compartmentation. RIα undergoes liquid-liquid phase-separation at endogenous levels as a function of dynamic cAMP signaling to form RIα bodies harboring high levels of cAMP and PKA activity. Importantly, we show that this active cAMP sequestration is critical for effective cAMP compartmentation in cells. The pathophysiological relevance of this compartmentation system is illustrated by its key role in the etiology of the atypical liver cancer fibrolamellar carcinoma (FLC). We show that an FLC-linked oncoprotein fusion between DnaJB1 and the PKA catalytic subunit (PKA_{cat}) potently blocks RIα phase separation and induces aberrant cAMP signaling. Furthermore, loss of RIα phase separation independent of the fusion oncoprotein in normal hepatocytes increased cell proliferation and resulted in cell transformation. Our work

reveals liquid-liquid phase separation as a principle organizer of signaling compartments and highlights the pathological consequences of dysregulating this activity architecture.

Introduction

3’,5’-cyclic adenosine monophosphate (cAMP) is a universal regulator of cellular function and behavior across evolution. In eukaryotes, cAMP production is canonically triggered in response to hormone signaling via the G protein-coupled receptor (GPCR)-mediated activation of transmembrane adenylyl cyclases (ACs), which catalyze the synthesis of cAMP from ATP. cAMP signals are transduced by a number of well-studied effector proteins, most prominently the cAMP-dependent protein kinase (PKA), a tetrameric holoenzyme consisting of a regulatory subunit dimer bound to a pair of catalytic subunits. Binding of cAMP to the PKA regulatory subunit unleashes the activity of the PKA catalytic subunit (PKA_{cat}), which then phosphorylates a myriad of targets throughout the cell. Together, cAMP and PKA exert tight control over numerous physiological processes, from cell growth and survival[127–129] to cardiac[130] and neuronal[131] functions.

The functional diversity of cAMP signaling is driven by hundreds of GPCR inputs[132] capable of elevating cAMP levels to produce distinct cellular responses[133]. This remarkable specificity may be achieved through compartmentation of cAMP, a concept first proposed over 35 years ago[25,134,135]. Indeed, cAMP gradients[30,136–138] and microdomains[139–141] have been observed experimentally in various contexts. While compartmentalized AC activity is involved in forming these cAMP microdomains[142,143], cAMP-hydrolyzing phosphodiesterases (PDEs) are widely considered the primary diffusional barrier responsible for fencing local cAMP pools[144–146].

However, this longstanding model of PDE-controlled cAMP compartmentation is at odds with reports describing almost unrestricted (e.g., 270-780 $\mu m^2/s$) cAMP diffusion in cells[28–30]. Indeed, various computational studies have failed to reproduce the formation of cAMP gradients through the sole action of PDEs[26,119,147–149], whose catalytic activity is insufficient to constrain such a rapidly diffusing messenger[26,119], suggesting that experimentally observed cAMP microdomains instead require substantially (~100- to 10,000-fold) slower cAMP diffusion. Notably, more recent investigations have in fact reported significantly lower cytosolic cAMP diffusion rates that are more conducive of cAMP compartmentalization than the original estimates[150,151]. However, the specific mechanisms responsible for spatially constraining this critical second messenger remain to be elucidated.

Here, we identify the formation of biomolecular condensates of the type I regulatory subunit of PKA, RIα, as a key driver of cAMP compartmentation. RIα undergoes liquid-liquid phase-separation at endogenous levels as a function of dynamic cAMP signaling to form RIα bodies harboring high levels of cAMP and PKA activity, and this active cAMP sequestration is required to spatially constrain cAMP in cells. Importantly, RIα phase separation is explicitly disrupted by a PKA_{cat} fusion oncoprotein present in the atypical liver cancer fibrolamellar carcinoma (FLC)[51], leading to aberrant cAMP signaling and cell transformation. Our work reveals liquid-liquid phase separation as an essential coordinator of signaling compartments and provides critical mechanistic clues into the etiology of FLC, highlighting the pathological consequences of dysregulating this activity architecture.

Results

RIα undergoes liquid-liquid phase separation at endogenous levels

Of the four non-redundant PKA regulatory subunits, only RIα is ubiquitously expressed and it is essential for proper regulation of PKA activity[152]. To visualize the dynamics of RIα expressed at endogenous levels, we introduced the 11th β-strand of GFP (FP_{11})[32] at the C-terminus of RIα via CRISPR/Cas9 in HEK293A cells, yielding the 293-RIα cell line. This small segment permits efficient knock-in and enables targeted reconstitution of intact GFP when the remaining strands ($GFP_{1\text{-}10}$) are co-expressed. By doing so in 293-RIα cells, we observed fluorescent puncta (Figure 3.1A) similar to those seen with overexpressed RIα[153,154]. These puncta are highly dynamic, with coalescence of dispersed puncta occurring on the minute scale (Figure 3.1B). Fluorescence recovery after photobleaching (FRAP) experiments indicated that labeled RIα can dynamically exhange between the puncta and diffuisble pools, as indicated by similar fluorescence recovery kinetics ($t_{1/2}$ of 7 s ± 0.44 s, mean ± SEM, n = 12 puncta vs. $t_{1/2}$ of 7.8 s ± 0.41 s, n = 5 cytosolic regions) (Figure 3.1C), although labeled RIα showed decreased mobility within puncta ($t_{1/2}$: 35 s ± 1.3 s, n = 9 regions inside RIα puncta; $P < 0.0001$; Figure 3.2A). In addition, treatment with 2.5% 1,6-hexanediol, which disrupts weak intermolecular forces present in liquid-like assemblies[62], reduced the number of endogenous RIα puncta per cell by 68% ± 8.6% (Figure 3.1D).

Figure 3.1: Endogenous PKA regulatory subunit RIα undergoes phase separation.
(**A**) Observing the localization of endogenously expressed RIα. The 11th β-strand of GFP (FP_{11}) was knocked-in at the C-terminus of RIα in HEK293A cells. Transfecting these 293-RIα cells with the remaining GFP β-strands ($GFP_{1\text{-}10}$) and imaging them in the GFP channel revealed the formation of fluorescent RIα puncta. (**B**) Representative GFP fluorescence images of 293-RIα cells transfected with $GFP_{1\text{-}10}$ show merging of endogenous RIα puncta. (**C**) Monitoring the dynamics of labeled RIα. FRAP of RIα puncta (blue curve) compared with diffuse RIα (red curve) in $GFP_{1\text{-}10}$-transfected 293-RIα cells. Curves show average time-course of normalized fluorescence intensity. Solid lines indicate the mean; shaded areas, SEM. (**D**) RIα puncta disrupted by 1,6-hexanediol. Representative GFP fluorescence images of $GFP_{1\text{-}10}$-transfected 293-RIα cells before (t = 0 min; left) and after (t = 10 min; middle) 2.5% 1,6-hexanediol addition. Quantification of the number of RIα puncta per cell at the indicated times with (Hex; red curve) or without (Control; blue curve) 1,6-hexanediol addition. Error bars indicate ± SEM. (**E**) Representative DIC images showing liquid droplet formation by purified RIα at the indicated concentrations *in vitro*. (**F**) Representative *in vitro* phase diagram of RIα liquid droplet formation at varying concentrations of PEG 4000. Each condition was assessed at least twice. Scale bars: (**A**) 30 µm (inset, 10 µm); (**B**) 30 µm; (inset, 1 µm); (**E**) 10 µm.

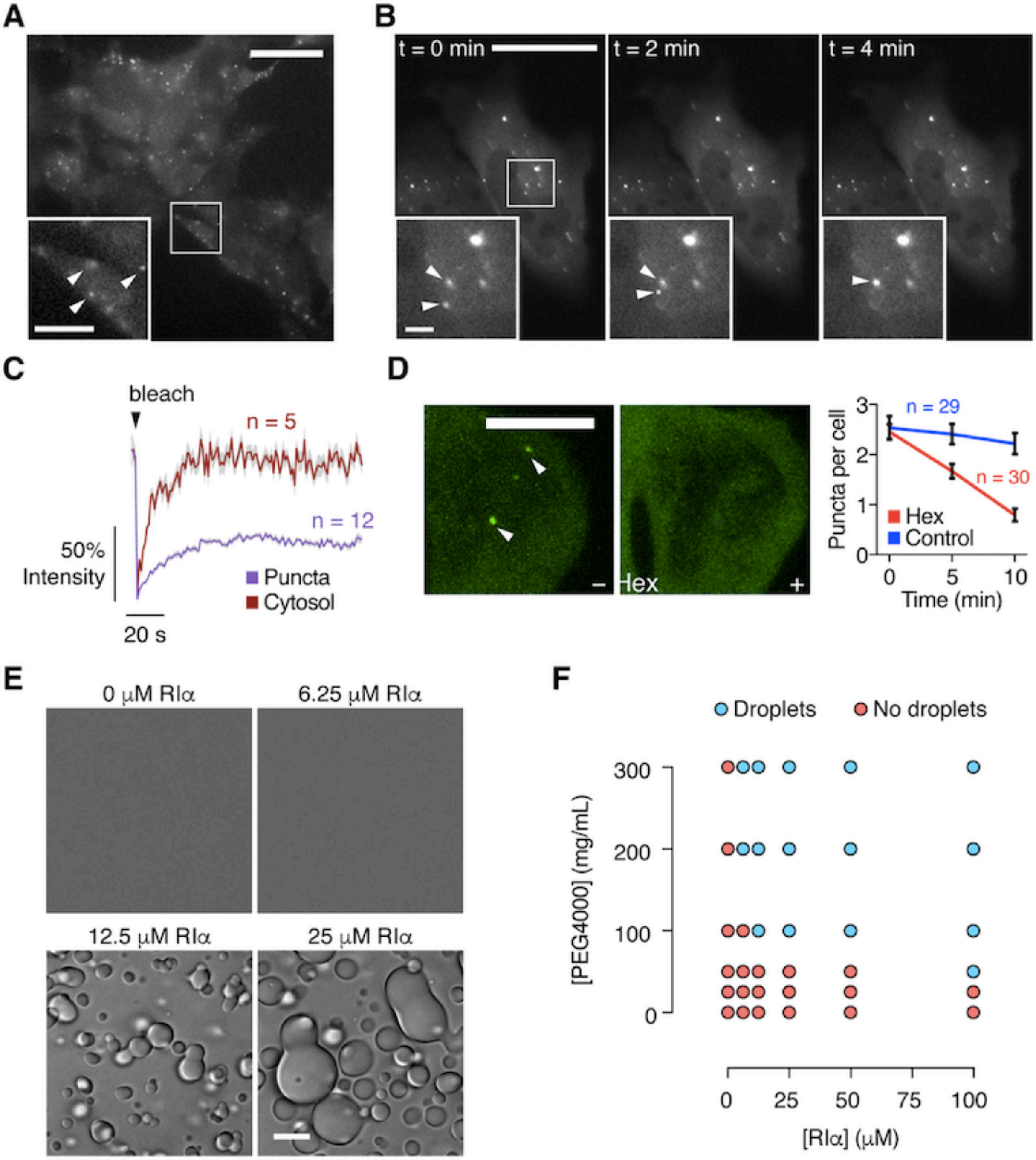
A
B
t = 0 min
t = 2 min
t = 4 min
C
bleach
n = 5
n = 12
50%
Intensity
20 s
Puncta
Cytosol
D
– Hex +
Puncta per cell
n = 29
n = 30
Hex
Control
0
1
2
3
0
5
10
Time (min)
E
0 μM RIα
6.25 μM RIα
12.5 μM RIα
25 μM RIα
F
Droplets
No droplets
[PEG4000] (mg/mL)
300
200
100
0
0
25
50
75
100
[RIα] (μM)

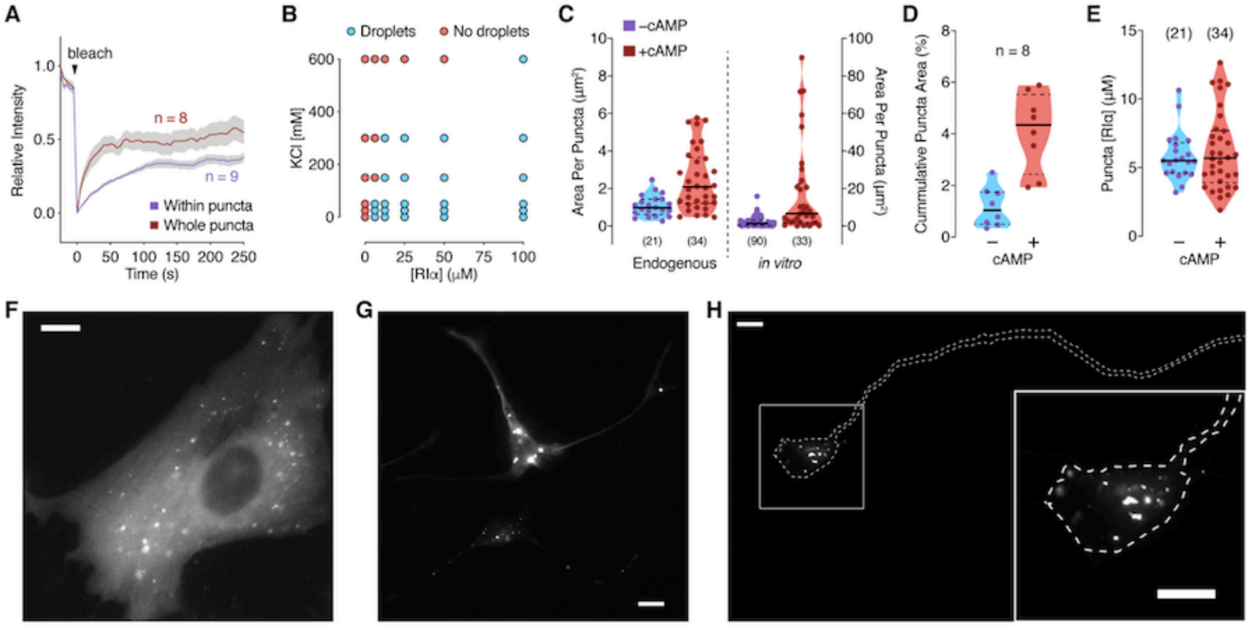

Figure 3.2: Additional characterization of RIα phase-separated bodies.
(**A**) FRAP of a region within an RIα puncta (blue curve) compared with an entire RIα puncta (red curve) in HEK293T cells transfected with RIα-EGFP. Curves show average time-course of normalized fluorescence intensity. Solid lines indicate the mean; shaded areas, SEM. (**B**) Representative *in vitro* phase diagram of RIα liquid droplet formation at varying concentrations of KCl. Each condition was assessed at least twice. (**C-E**) Average size of (**C**), percent area occupied by (**D**), and RIα concentrations inside RIα droplets (**E**) in 293-RIα cells transfected with $\text{GFP}_{1\text{-}10}$ (endogenous) or *in vitro* RIα droplets (in vitro) (50 μM RIα + 12.5 μM PKA_{cat}). Analyses were performed before and after 50 μM Fsk stimulation (endogenous) or 10 μM cAMP addition (in vitro) (endogenous: -cAMP: n = 21 puncta from 8 cells, +cAMP: n = 34 puncta from 8 cells; in vitro: -cAMP: 93 droplets, +cAMP: 34 droplets). Violin plots show the median and quartiles as solid and dashed lines, respectively. (**F-H**) RIα phase separation occurs in various tissues. Representative fluorescence images of EGFP-RIα-expressing (**F**) neonatal rat ventricular myocytes, (**G**) astrocytes, and (**H**) dissociated primary embryonic rat hippocampal neurons grown for 3 days *in vitro* (outline indicates cell shape; inset, zoomed image) showing RIα puncta formation. Scale bars, 10 μm.

Strikingly, purified RIα by itself formed liquid droplets *in vitro* (Figure 3.1E). Increasing molecular crowding with increasing concentrations of PEG decreased the concentrations of RIα needed for liquid droplet formation (Figure 3.1F), while increasing salt (KCl) concentrations increased the concentrations of RIα needed for liquid droplet formation (Figure 3.2B). RIα droplets varied in size both *in vitro* and in cells (Figure 3.2C), and while endogenous RIα puncta account for only 1.2% ± 0.27% of the entire cellular area, we estimated the RIα concentration inside these puncta to be about 5.5 μM (Figures 3.2D-E). We also observed similar fluorescent puncta in various other cell types expressing RIα-GFP, such as cardiomyocytes, astrocytes, and neurons (Figures 3.2F-H). Together, these data indicate that RIα is capable of forming biomolecular condensates and does so at endogenous expression levels.

RIα phase separation is inhibited by PKA catalytic subunit and enhanced by cAMP

RIα forms an obligate dimer via its N-terminal dimerization and docking (D/D) domain, which bridges its binding to A-Kinase Anchoring Proteins (AKAPs). Connecting the D/D domain and cAMP binding domains is a linker region that is relatively disordered (see Methods) and contains an inhibitory sequence that acts as a pseudosubstrate for PKA_{cat} (Figure 3.3A)[155]. To probe the role of these domains in RIα phase separation, we generated a panel of EGFP-tagged RIα truncation mutants and monitored their ability to form puncta when overexpressed in wild-type HEK293T cells. No phase separation was observed with mutants lacking the D/D domain or the linker region (Figures 3.3B and 3.4A-E), in contrast to the wild-type control, whereas fluorescent puncta were observed in cells expressing a truncation mutant containing only these two regions (Figure 3.3B). These data suggest that a segment containing the D/D

Figure 3.3: Regulation of RIα phase separation by PKA catalytic subunit and cAMP. (**A**) Domain structure of full-length, wild-type RIα. (**B**) Comparison of RIα puncta number in wild-type HEK293T cells expressing EGFP-tagged wild-type or mutant RIα. The D/D domain (residues 12-61), the linker region (62-113), or both (12-113) were either deleted or overexpressed. Horizontal lines indicate mean ± SEM. Representative fluorescence images of HEK293T cells transfected with the corresponding EGFP-tagged RIα constructs are shown above each bar. (**C-G**) cAMP enhances RIα phase separation in the presence of PKA_{cat}. (**C**) Representative *in vitro* phase diagram of RIα liquid droplet formation as a function of RIα and PKA_{cat} concentration in the presence (right) or absence (left) of 10 μM cAMP. Each condition was assessed at least twice. (**D**) Representative fluorescence images of $\text{GFP}_{1\text{-}10}$-transfected 293-RIα cells before (t = 0; top) and after (t = 10 min; bottom) addition of 50 μM Fsk. (**E**) Representative fluorescence images of wild-type HEK293T cells transfected with EGFP-RIα (left) and mTagBFP2-PKA_{cat} (right) shown before (t = 0; top) and after (t = 10 min; bottom) addition of 50 μM Fsk. (**F**) Average time-courses of the number of RIα puncta per cell in 293-RIα cells transfected with $\text{GFP}_{1\text{-}10}$ and treated with 50 μM Fsk (blue curve) or 10 μM isoproterenol (Iso) (red curve). Error bars indicate ± SEM. (**G**) Representative GFP (top) and DIC (bottom) images of 50 μM RIα mixed with 25 μM PKA_{cat} (1% GFP-tagged), showing PKA_{cat} in RIα liquid droplets without (left) and with (right) 10 μM cAMP. All scale bars, 10 μm.

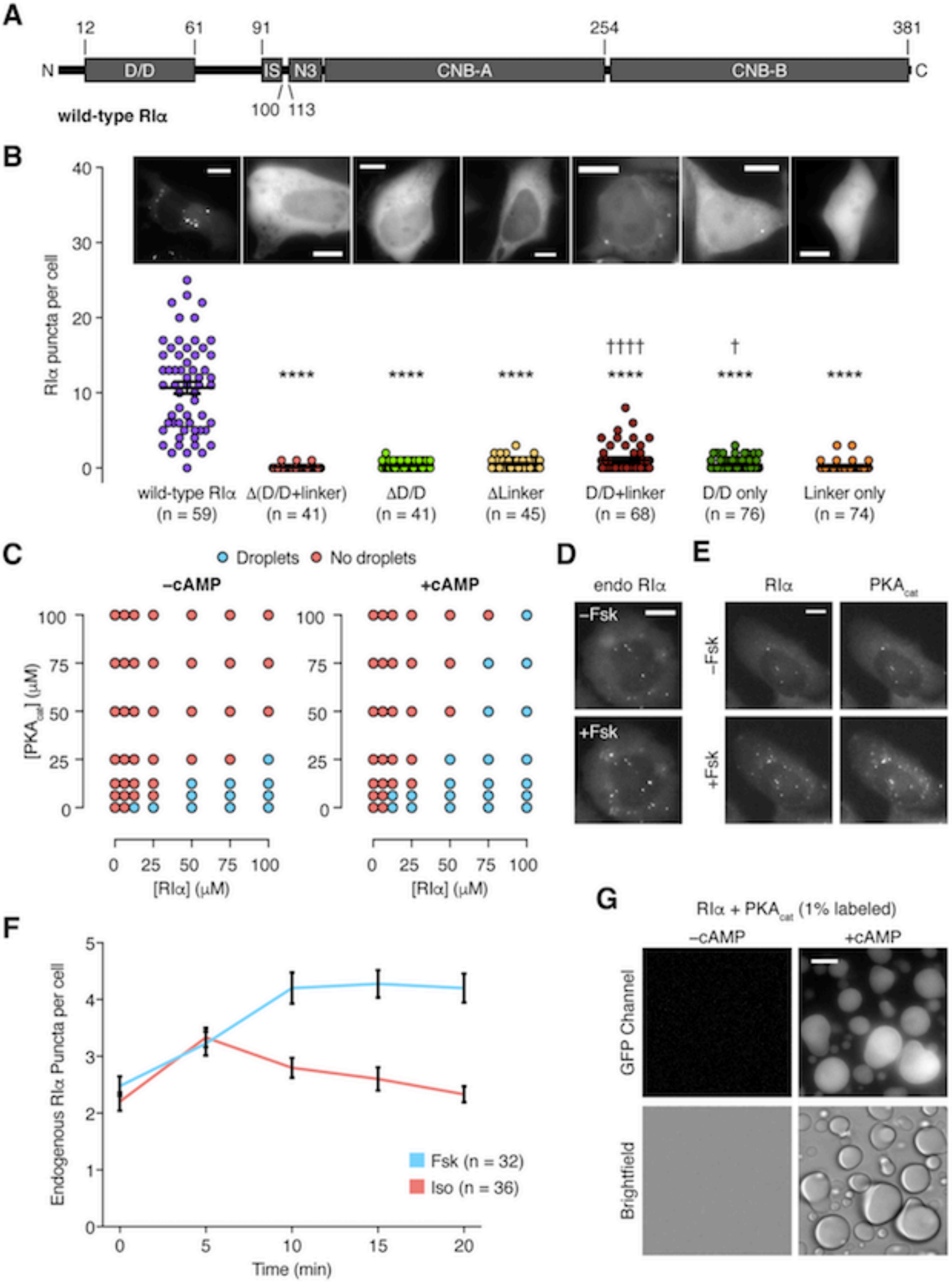
A
12
61
91
254
381
N
D/D
IS
N3
CNB-A
CNB-B
C
100
113
wild-type RIα
B
RIα puncta per cell
40
30
20
10
0
††††
†
****
wild-type RIα (n = 59)
Δ(D/D+linker) (n = 41)
ΔD/D (n = 41)
ΔLinker (n = 45)
D/D+linker (n = 68)
D/D only (n = 76)
Linker only (n = 74)
C
Droplets
No droplets
−cAMP
+cAMP
[PKAcat] (μM)
0
25
50
75
100
[RIα] (μM)
D
endo RIα
−Fsk
+Fsk
E
RIα
PKAcat
−Fsk
+Fsk
F
Endogenous RIα Puncta per cell
0
1
2
3
4
5
Time (min)
0
5
10
15
20
Fsk (n = 32)
Iso (n = 36)
G
RIα + PKAcat (1% labeled)
−cAMP
+cAMP
GFP Channel
Brightfield

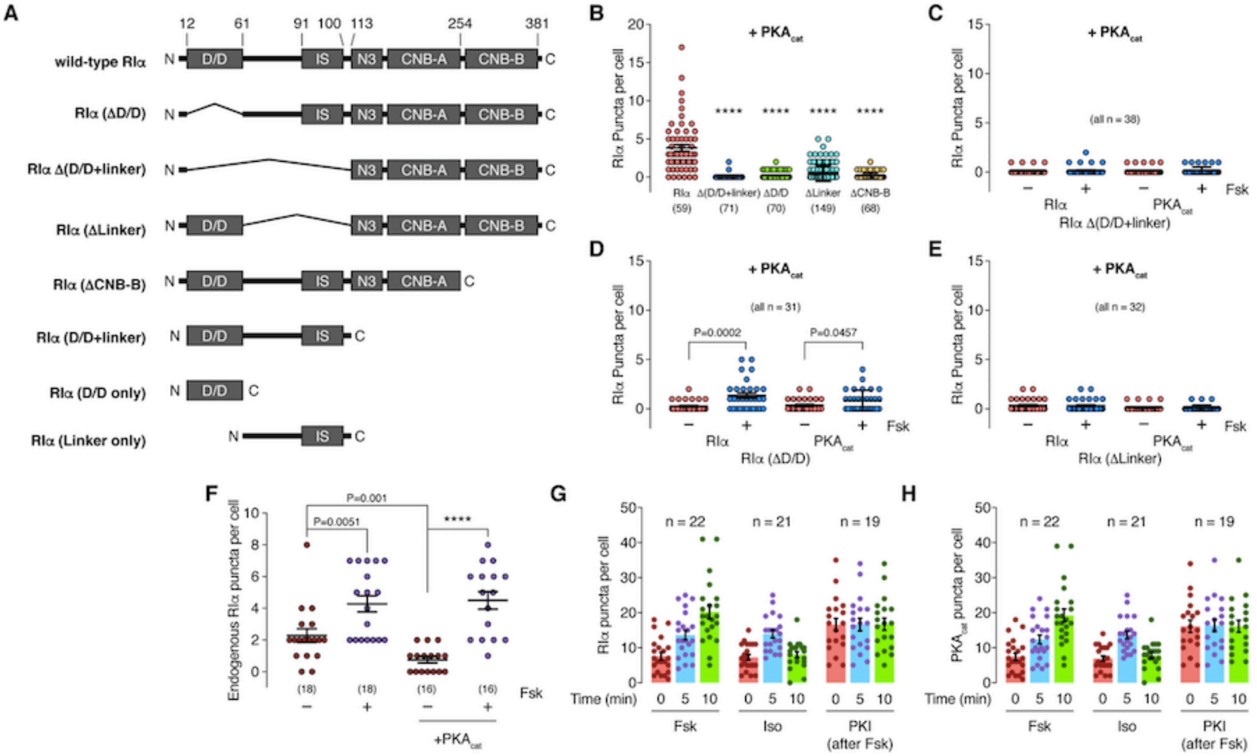

Figure 3.4: RIα phase separation requires the D/D domain and linker region and is regulated by PKA_{cat} and cAMP.

(**A**) Domain structure of RIα (D/D: docking/dimerization domain, IS: inhibitory sequence, CNB-A: cAMP binding domain A, CNB-B: cAMP binding domain B) and the various truncation mutants used in this study. (**B**) Comparison of the number of basal RIα puncta per cell in cells expressing PKA_{cat} plus either wild-type RIα or various RIα mutants. Deletion of either the D/D domain or linker region greatly reduced number of RIα puncta per cell. (**C-E**) Comparison of the number of basal and Fsk-stimulated RIα puncta in HEK293T cells expressing mCherry-tagged PKA_{cat} plus EGFP-tagged $\text{RI}\alpha_{\Delta\text{D/D+Linker}}$ (**C**), $\text{RI}\alpha_{\Delta\text{D/D}}$ (**D**), or $\text{RI}\alpha_{\Delta\text{Linker}}$ (**E**) and stimulated with 50 µM Forskolin (Fsk). (**F**) Comparison of the number of RIα puncta per cell in 293-RIα cells with or without PKA_{cat} overexpression and stimulated with 50 µM Fsk. Overexpressing PKA_{cat} decreases the basal RIα puncta number. (**G** and **H**) Comparison of the number of RIα (**G**) and PKA_{cat} puncta (**H**) per cell in HEK293T cells expressing EGFP-RIα and mCherry-PKA_{cat} and treated with 50 µM Fsk, 10 µM isoproterenol (Iso), or 20 µM myrisotylated-PKI (Myr-PKI) 20 min after 50 µM Fsk addition. Fsk and Iso dynamically increase the numbers of both RIα and PKA_{cat} puncta while Myr-PKI treatment following Fsk stimulation has no effect. Horizontal lines in **B-F** indicate mean ± SEM. Bars in **G** and **H** indicate mean ± SEM.

domain and linker region is both necessary and, to some extent, sufficient for RIα phase separation. The inhibitory sequence and a portion of the linker region become disordered when cAMP-bound RIα is dissociated from PKA_{cat}[155]. Because this region is involved in RIα phase separation, we hypothesized that PKA_{cat} and cAMP may directly influence this process. Indeed, increasing concentrations of purified PKA_{cat} increased the minimal RIα concentration required for liquid droplet formation *in vitro* (Figure 3.3C). Moreover, overexpression of PKA_{cat} in GFP_{1-10}-expressing 293-RIα cells decreased the number of endogenous RIα puncta per cell by 67% ± 5.8% (*P* = 0.001) in the basal state (Figure 3.4F).

On the other hand, cAMP directly enhances RIα phase separation in the presence of PKA_{cat}, as addition of cAMP attenuated the inhibitory effect of PKA_{cat} on RIα liquid droplet formation *in vitro* and allowed liquid droplet formation at lower RIα concentrations (Figure 3.3C). In 293-RIα cells expressing GFP_{1-10}, stimulation with the AC activator forskolin (Fsk) to elevate cAMP induced an acute increase in endogenous RIα puncta (70% ± 12%, n = 32 cells) (Figures 3.3D and 3.3F). Furthermore, increasing cAMP levels through the β-adrenergic receptor agonist isoproterenol transiently increased the number of endogenous RIα puncta per cell (Figure 3.3F), consistent with the cAMP dynamics induced by this GPCR agonist[148,156]. These data suggest that cAMP-bound RIα is more prone to undergo liquid-liquid phase separation, consistent with an increase in disorder within the inhibitory sequence and linker region when cAMP-bound RIα dissociates from PKA_{cat}. To observe the localization of PKA_{cat} in this process, we stimulated HEK293T cells overexpressing both RIα and PKA_{cat} with Fsk and observed a 164% ± 32% increase in the number of RIα puncta per cell, with PKA_{cat} co-localizing with RIα puncta (Figures 3.3E and 3.4G-H, n = 22 cells). Consistent with this observation, PKA_{cat} (1%

GFP-tagged) formed liquid droplets *in vitro* when mixed with RIα and cAMP (Figure 3.3G), but did not form liquid droplets on its own. These results suggest that cAMP dynamics dictate the formation and dissolution of RIα phase-separated bodies and that PKA_{cat} co-phase separates with RIα.

RIα condensates actively recruit and retain high cAMP levels and PKA activity

The observed enrichment of PKA_{cat} in RIα phase-separated bodies prompted us to directly probe PKA activity in these bodies. To perform these measurements at the endogenous level, we designed a new class of fluorescent biosensors called Fluorescent Sensors Targeted to Endogenous Proteins (FluoSTEPs). FluoSTEPs contain sensing domains sandwiched between mRuby2 (acceptor) and $\text{GFP}_{1\text{-}10}$ (partial donor). The FRET donor fully reconstitutes in the presence of GFP_{11} fused to an endogenous protein of interest, resulting in the assembly of functional biosensors only at endogenous protein loci. We designed a FluoSTEP A kinase Activity Reporter (FluoSTEP-AKAR) based on a previously established PKA activity sensing domain consisting of a surrogate PKA substrate (PKAsub) sequence (LRRA**T**LVD) and forkhead associated domain 1 (FHA1) as the phosphoamino acid-binding domain (Figure 3.5A)[157]. When PKA is active, phosphorylation of the PKA substrate and its subsequent binding to FHA1 are expected to induce a conformational change and an increase in the red/green emission ratio (Figure 3.6A).

In 293-RIα cells expressing FluoSTEP-AKAR, Fsk induced a 4.7% ± 0.35% increase in the red/green emission ratio (raw emission ratios (R): $R_{t=0}$ to $R_{t=\text{end}}$: 0.82 to 0.86; n = 35 cells) in diffuse RIα regions (Figure 3.5B) but no detectable changes within RIα puncta ($R_{t=0}$ to $R_{t=\text{end}}$:

Figure 3.5: Endogenous RIα condensates form cAMP/PKA compartments and enable PDE-mediated cAMP compartmentation. (**A**) Left: Fluorescent Sensors Targeted to Endogenous Proteins (FluoSTEPs) utilize split-GFP complementation to recruit a biosensor (e.g., FluoSTEP-AKAR) to a protein of interest (POI) expressed at endogenous levels. Right: Domain structures of RIα-GFP$_{11}$, FluoSTEP-AKAR, and FluoSTEP-ICUE. (**B-F**) Basal PKA activity and cAMP levels within RIα phase-separated bodies are high enough to saturate FluoSTEP biosensors prior to stimulation. (**B** and **C**) Left: Red/green (R/G) emission ratio changes in 293-RIα cells transfected with FluoSTEP-AKAR and stimulated with either 50 µM Fsk (**B**) or 20 µM myristoylated-PKI (Myr-PKI) (**C**). RIα puncta (blue curve) and non-puncta regions (red curve) were analyzed separately. Right: Response to Fsk (**B**) (n = 32 puncta and 35 diffuse regions from 32 cells) or Myr-PKI (**C**) treatment. (**D**) Raw starting emission ratios for FluoSTEP-AKAR and FluoSTEP-AKAR T/A. RIα puncta and non-puncta regions were analyzed separately (WT AKAR: n = 19 puncta and 17 diffuse regions from 17 cells; AKAR T/A: n = 25 puncta and 25 diffuse regions from 25 cells). (**E**) Left: Green/red (G/R) emission ratio changes in 293-RIα cells transfected with FluoSTEP-ICUE and stimulated with 50 µM Fsk. RIα puncta (blue curve) and non-puncta regions (red curve) were analyzed separately. Right: Response to Fsk stimulation. (**F**) Raw starting emission ratios for FluoSTEP-ICUE and FluoSTEP-ICUE R279E (WT ICUE: n = 32 puncta and 37 diffuse regions from 32 cells; ICUE R279E: n = 42 puncta and 43 diffuse regions from 42 cells). (**G** and **H**) Left: R/G (**G**) or G/R (**H**) emission ratio changes in 293-RIα cells transfected with FluoSTEP-AKAR (**G**) or FluoSTEP-ICUE (**H**) plus mTagBFP2-PKA$_{cat}$ and stimulated with 50 µM Fsk. Newly formed RIα puncta regions (blue curve) and non-puncta regions (red curve) were analyzed separately (FluoSTEP-AKAR: n = 12 new puncta and 12 diffuse regions from 12 cells; FluoSTEP-ICUE: n = 11 new puncta and 12 diffuse regions from 11 cells). Right: Responses to Fsk stimulation (FluoSTEP-AKAR: n = 27 new puncta and 27 diffuse regions from 27 cells; FluoSTEP-ICUE: n = 35 new puncta and 36 diffuse regions from 35 cells). Solid lines in **B-C**, **E**, **G**, and **H** indicate representative average time courses of either R/G (**B**, **C**, and **G**) or G/R (**D** and **H**) emission ratio changes; shaded areas, SEM. Bar graphs in **B-C**, **E**, **G**, and **H** show maximum emission ratio changes upon drug addition, with bars indicating mean ± SEM. Violin plots in **D** and **F** show the median and quartiles as solid and dashed lines, respectively.

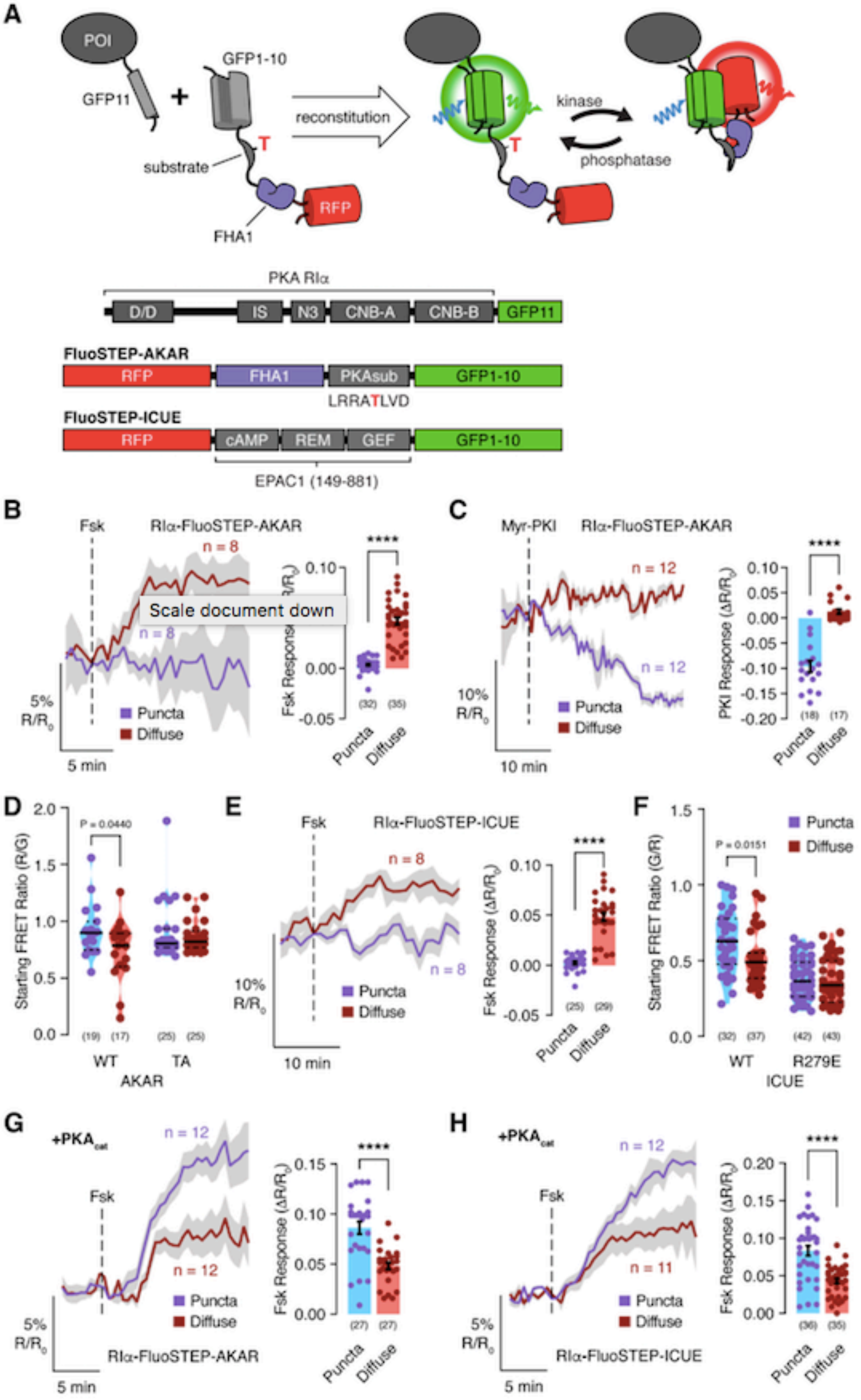
A
POI
GFP11
+
GFP1-10
T
substrate
FHA1
RFP
reconstitution
kinase
phosphatase
PKA RIα
D/D
IS
N3
CNB-A
CNB-B
GFP11
FluoSTEP-AKAR
RFP
FHA1
PKAsub
GFP1-10
LRRATLVD
FluoSTEP-ICUE
RFP
cAMP
REM
GEF
GFP1-10
EPAC1 (149-881)
B
Fsk
RIα-FluoSTEP-AKAR
n = 8
n = 8
5% R/R$_0$
5 min
Puncta
Diffuse
****
Fsk Response (ΔR/R$_0$)
0.10
0.00
-0.05
(32)
(35)
Puncta
Diffuse
C
Myr-PKI
RIα-FluoSTEP-AKAR
n = 12
n = 12
10% R/R$_0$
10 min
Puncta
Diffuse
****
PKI Response (ΔR/R$_0$)
0.10
0.05
0.00
-0.05
-0.10
-0.15
-0.20
(18)
(17)
Puncta
Diffuse
D
Starting FRET Ratio (R/G)
2.0
1.5
1.0
0.5
0.0
P = 0.0440
(19)
(17)
(25)
(25)
WT
TA
AKAR
E
Fsk
RIα-FluoSTEP-ICUE
n = 8
n = 8
10% R/R$_0$
10 min
Puncta
Diffuse
****
Fsk Response (ΔR/R$_0$)
0.10
0.05
0.00
-0.05
(25)
(29)
Puncta
Diffuse
F
Starting FRET Ratio (G/R)
1.5
1.0
0.5
0.0
P = 0.0151
Puncta
Diffuse
(32)
(37)
(42)
(43)
WT
R279E
ICUE
G
+PKA$_{cat}$
n = 12
Fsk
n = 12
Puncta
Diffuse
5% R/R$_0$
5 min
RIα-FluoSTEP-AKAR
****
Fsk Response (ΔR/R$_0$)
0.15
0.10
0.05
0.00
(27)
(27)
Puncta
Diffuse
H
+PKA$_{cat}$
n = 12
Fsk
n = 11
Puncta
Diffuse
5% R/R$_0$
5 min
RIα-FluoSTEP-ICUE
****
Fsk Response (ΔR/R$_0$)
0.20
0.15
0.10
0.05
0.00
(36)
(35)
Puncta
Diffuse

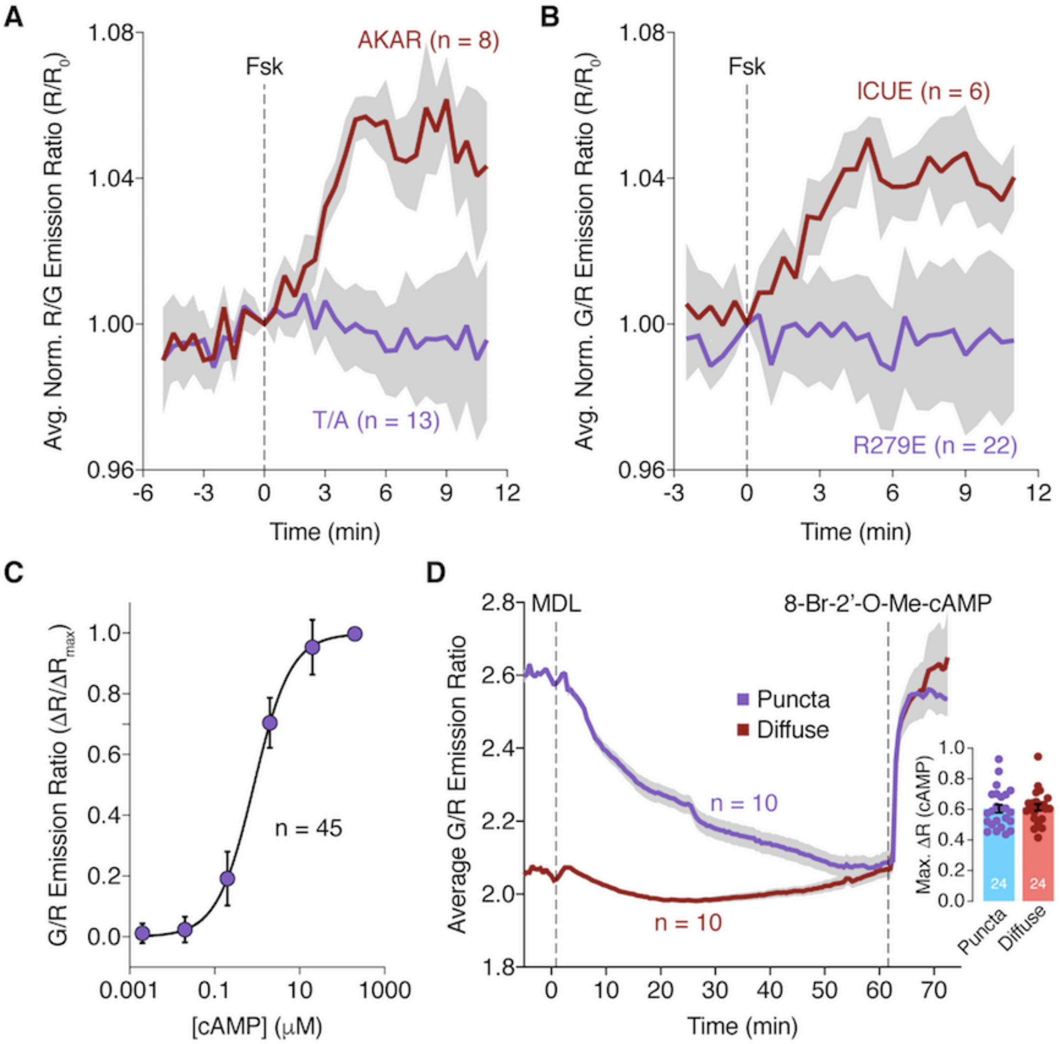

Figure 3.6: Additional characterization of FluoSTEP-AKAR and FluoSTEP-ICUE. (**A** and **B**) Testing the specificity of FluoSTEP-AKAR and FluoSTEP-ICUE. Representative whole-cell average time courses showing (**A**) the red/green (R/G) emission ratio of either FluoSTEP-AKAR (red curve) or FluoSTEP-AKAR T/A (blue curve) or (**B**) the green/red (G/R) emission ratio of either FluoSTEP-ICUE (red curve) or FluoSTEP-ICUE R279E (blue curve) in 293-RIα cells stimulated with 50 μM Fsk. Solid lines indicate the mean; shaded areas, SEM. (**C**) Characterizing the dose-response behavior of green/red ICUE. HEK293T cells were pretreated with 100 μM MDL-12330A followed by the indicated concentrations of 8-Br-2'-O-Me-cAMP-AM. Points indicate mean ± SEM. (**D**) Investigating the effect of puncta localization on the green/red ICUE response. Left: Representative average time courses of G/R emission ratio changes in HEK293T cells transfected with RIα-green/red ICUE and stimulated with 100 μM MDL-12330A (MDL) followed by 200 μM 8-Br-2'-O-Me-cAMP-AM (n = 10 puncta and 10 diffuse regions from 10 cells). RIα puncta regions (blue curve) and non-puncta regions (red curve) were analyzed separately. Right: Maximum raw emission ratio changes upon 8-Br-2'-O-Me-cAMP-AM treatment (n = 24 puncta and 24 diffuse regions from 24 cells).

0.88 to 0.86; n = 32 cells), thus indicating clear differences in PKA activity despite the limited dynamic range of this first-generation technology. Conversely, the cell-permeable PKA inhibitor myristoylated-PKI induced no detectable ratio changes in diffuse RIα regions ($R_{t=0}$ to $R_{t=end}$: 0.79 to 0.81; n = 17 cells) under these same conditions but induced a 9.6% ± 1.1% ($R_{t=0}$ to $R_{t=end}$: 0.89 to 0.81; n = 18 cells) decrease in the red/green emission ratio in RIα puncta (Figure 3.5C), suggesting that basal PKA activity within RIα phase-separated bodies is high enough to saturate FluoSTEP-AKAR prior to stimulation. Indeed, prior to any stimulation, the initial red/green emission ratio was higher in RIα puncta regions compared with diffuse RIα regions (Figure 3.5D). As a control, 293-RIα cells transfected with FluoSTEP-AKAR T/A, which contains a non-phosphorylatable PKA substrate[157], showed no significant red/green ratio difference between RIα puncta and diffuse regions (Figure 3.5D).

To similarly probe cAMP dynamics within RIα puncta, we utilized a FluoSTEP Indicator of cAMP Using Epac (FluoSTEP-ICUE) designed based on the same split biosensor approach (Figure 3.5A). Following reconstitution of the donor fluorophore, cAMP binding to a truncated fragment of Epac1, a previously established cAMP sensing domain[156] which includes the cAMP binding domain (cAMP), Ras exchange motif (REM), and guanine exchange factor domain (GEF), induces a conformational change and an increase in the green/red emission ratio (Figure 3.6B-C). In 293-RIα cells transfected with FluoSTEP-ICUE, Fsk induced no detectable changes in RIα puncta regions ($R_{t=0}$ to $R_{t=end}$: 0.61 to 0.61; n = 25 cells) but induced a 4.9% ± 0.4% increase in the green/red emission ratio in diffuse RIα regions ($R_{t=0}$ to $R_{t=end}$: 0.57 to 0.59; n = 29 cells) (Figure 3.5E), suggesting that basal cAMP levels in RIα phase-separated bodies are also able to saturate FluoSTEP ICUE prior to stimulation. As an indication of basal cAMP levels, the initial green/red emission ratio for FluoSTEP-ICUE was higher in RIα puncta regions compared with diffuse RIα regions, while introducing an R279E mutation to inhibit cAMP binding[158] abolished this difference (Figure 3.5F). Importantly, the dynamic range of our cAMP biosensor was not affected by localization to RIα puncta, as demonstrated by identical green/red emission ratio increases both inside and outside puncta in cells expressing RIα-tethered green/red-ICUE and treated with the AC inhibitor MDL-12330A followed by a cAMP analogue (Figure 3.6D). In addition, the gradual decrease in the emission ratio of the puncta-localized sensor upon MDL addition further supports the high basal cAMP levels within these puncta (Figure 3.6D).

Next, we examined how PKA activity and cAMP dynamics changed during the formation of RIα puncta. In PKA_{cat}-expressing 293-RIα cells that showed Fsk-induced puncta formation (Figure 3.4F), Fsk induced a larger increase in the FluoSTEP-AKAR red/green emission ratio (8.6% ± 0.63%; $R_{t=0}$ to $R_{t=end}$: 0.8 to 0.87; n = 27 cells) in newly formed RIα puncta compared with the constantly diffuse RIα regions (4.8% ± 0.35%; $R_{t=0}$ to $R_{t=end}$: 0.8 to 0.82; n = 27 cells) (Figure 3.5G). Similarly, Fsk-induced FluoSTEP-ICUE responses were larger in newly formed RIα puncta (8.4% ± 0.66%; $R_{t=0}$ to $R_{t=end}$: 0.55 to 0.59; n = 35 cells) compared with the constantly diffuse RIα regions (4.3% ± 0.34%; $R_{t=0}$ to $R_{t=end}$: 0.55 to 0.57; n = 36 cells) (Figure 3.5H). These results suggest that RIα phase-separated bodies recruit and retain active PKA_{cat} and cAMP.

Active cAMP buffering by RIα condensates drives cAMP compartmentation

While cAMP degradation by PDEs has been shown to help create cAMP compartments inside cells, mathematical modeling suggests that PDE activity alone is insufficient to restrict cAMP, given the current understanding of cAMP diffusion characteristics[26,119,159]. Key mechanisms that enable cAMP compartmentation therefore await discovery. Given the high level of cAMP observed in RIα condensates, we hypothesized that these bodies help compartmentalize cAMP by serving as a dynamic buffering system. Using an improved cAMP sensor (ICUE4; Figure 3.7A-B) fused to the catalytic portion of PDE4D2 (PDE4D2$_{cat}$) (PDE4D2$_{cat}$-ICUE4; Figure 3.7C and 3.8A-B) to monitor local cAMP within PDE compartments as a direct assay for cAMP compartmentation, we found that Fsk induced a small increase in the normalized cyan/yellow emission ratio of only 6.2% ± 0.23% (n = 55 cells), whereas blocking PDE activity using the PDE4-selective inhibitor rolipram and a general PDE inhibitor IBMX rescued the response, suggesting that PDE4D2$_{cat}$ can form a cAMP sink under control conditions when the cAMP compartmentation system in intact (Figure 3.8B). However, when RIα phase separation was disrupted with 2.5% 1,6-hexanediol pretreatment (Figure 3.7E, 3.8B, and 3.8D), Fsk induced much greater cAMP accumulation around PDE4D2, indicated by a larger increase in the normalized cyan/yellow emission ratio (30% ± 0.76%, $P < 0.0001$; n = 50 cells) of the PDE4D2$_{cat}$-ICUE4 probe, suggesting that disrupting RIα condensates leads to decreased cAMP buffering and loss of effective cAMP compartmentation. In cells with no RIα phase separation as RIα is homozygously knocked out, Fsk induced similar changes with and without 1,6-hexanediol pretreatment (Figure 3.8C), suggesting the effect on cAMP compartmentation is mediated by RIα. The effect of disrupting RIα condensates was even stronger when RIα was overexpressed. In control cells, Fsk induced no detectable changes in the normalized PDE4D2$_{cat}$-ICUE4 emission ratio (-0.40% ± 0.055%, n = 72 cells), suggesting that RIα overexpression further

Figure 3.7: RIα phase separation plays a crucial role in maintaining PDE-mediated cAMP compartmentation.

(**A** and **B**) Characterizing the improved cAMP sensor ICUE4. (**A**) Domain structures of ICUE3 and ICUE4. (**B**) Representative average time-courses of the cyan/yellow (C/Y) emission ratio in HEK293T cells expressing either ICUE3 (blue curve) or ICUE4 (red curve) and stimulated with 25 μM Fsk. Inset: Comparison of the maximum C/Y emission ratio responses of ICUE3 and ICUE4 after 25 μM Fsk stimulation. (**C**) PDE4D2 tethering does not affect the ICUE4 response. HEK293T cells expressing ICUE4 (blue curve) or PDE4D2-ICUE4 (red curve) were stimulated with different doses of forskolin (Fsk) in the absence (ICUE4) or presence (PDE4D2-ICUE4) of the PDE4 inhibitor rolipram. Points indicate mean ± SEM. (**D** and **E**) Representative average time courses of the C/Y emission ratio in HEK293T cells expressing ICUE4 (**D**) or ICUE4 plus mRuby2-RIa (**E**) with (red curve) and without (blue curve) 1,6-hexanediol treatment (added at t = 0 in the red curve) followed by 50 mM Fsk and then 100 mM IBMX. Hexanediol treatment induces a gradual increase in the ICUE4 C/Y emission ratio compared with control (blue curve) but has little effect on the maximum stimulated ICUE4 responses (see insets showing responses normalized to Fsk addition). (**F**) Left: Comparison of the raw initial C/Y emission ratios of PDE4D2$_{cat}$-ICUE4 in HEK293T cells with endogenously expressed RIα (endo RIα), RIα overexpression (RIα OX), or RIα knockout (RIα KO). Right: Comparison of the raw initial C/Y emission ratios of PDE4D2$_{cat}$-ICUE4 in RIα knockout HEK293T cells expressing wild-type RIα, RIα$_{D/D+Linker}$, or RIα$_{\Delta D/D+Linker}$. (**G-I**) Left: Representative average time courses of the C/Y emission ratio (normalized to max) of PDE4D2$_{cat}$-ICUE4-transfected RIα KO HEK293T cells co-expressing mRuby2-RIα (+RIα) (**G**), mRuby2-RIα$_{D/D+Linker}$ (+RIα$_{D/D+Linker}$) (**H**), or mRuby2-RIα$_{\Delta D/D+Linker}$ (+RIα$_{\Delta D/D+Linker}$) (**I**) with (red curve) and without (blue curve) hexanediol pretreatment and stimulation with 50 μM Fsk, 1 μM rolipram (Rol), and 100 μM IBMX. Right: Bar graphs showing the average normalized-to-max PDE4D2$_{cat}$-ICUE4 (C/Y) emission ratio after Fsk stimulation for each condition. (**J** and **K**) Additional examination of cAMP levels inside and outside RIα droplets. RIα KO HEK293T cells expressing ICUE4 tethered to either full-length RIα (RIα-ICUE4) (left) or RIα$_{D/D+Linker}$ (RIα$_{D/D+Linker}$-ICUE4) (right), which phase separates but does not bind to cAMP, were stimulated with 50 μM Fsk and then 100 μM IBMX. RIα puncta (red curve) and diffuse regions (blue curve) were analyzed separately. Representative average time courses of C/Y emission ratio (**J**) and maximum Fsk-stimulated ratio changes (**K**) are shown. Consistent with FluoSTEP imaging, these results suggest that cAMP levels are substantially higher in RIα droplets, which depends on the cAMP-binding capabilities of RIα. Solid lines in (**B**), (**D**), (**E**), and (**H**)-(**K**) indicate the mean; shaded areas, SEM. Error bars in (**C**), (**G**), (**H**)-(**J**), and (**L**) depict mean ± SEM. Violin plots in (**B**) and (**F**) show the median and quartiles as solid and dashed lines, respectively.

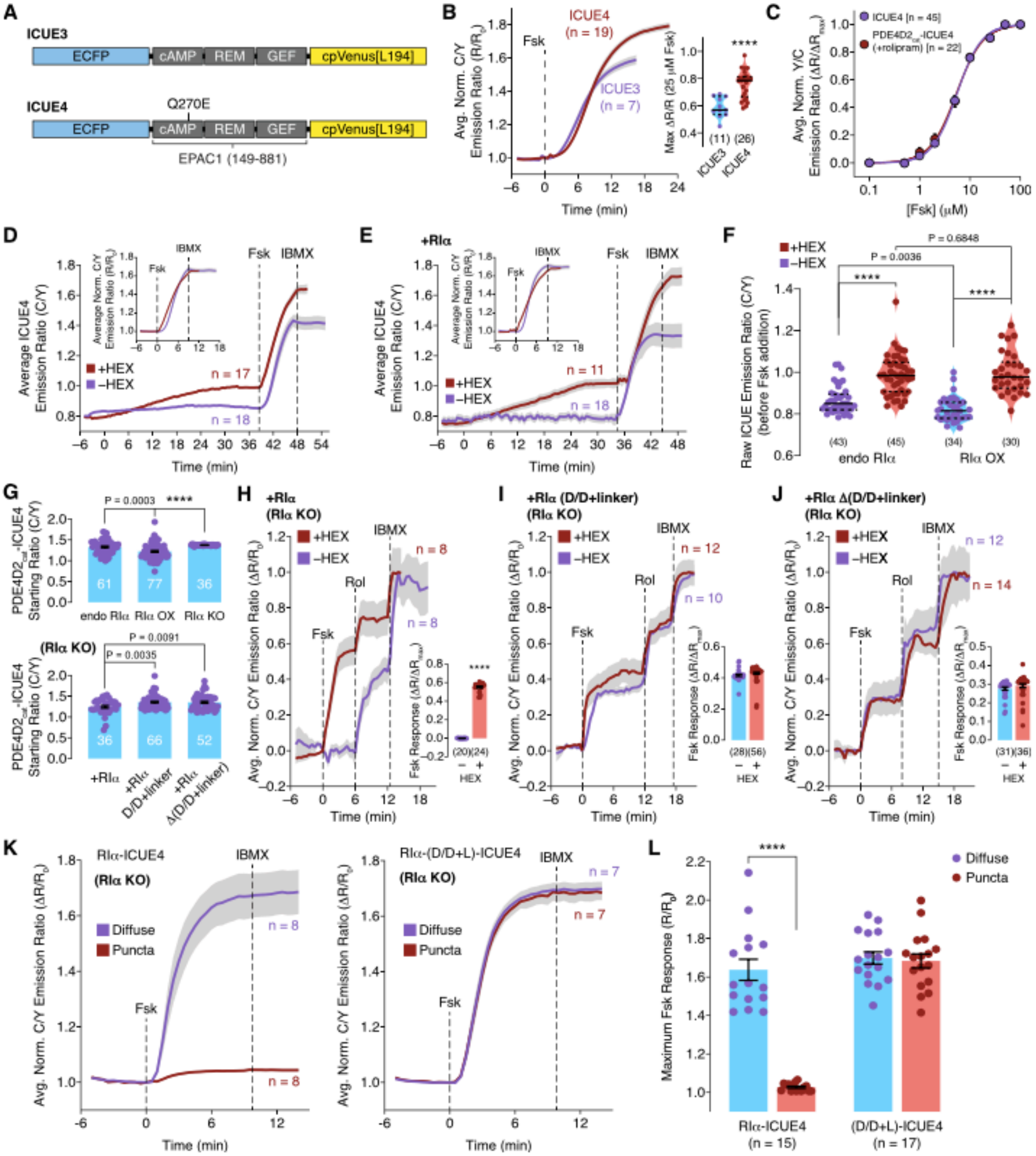
A
ICUE3
ECFP
cAMP
REM
GEF
cpVenus[L194]
ICUE4
Q270E
EPAC1 (149-881)
B
Avg. Norm. C/Y Emission Ratio (R/R$_0$)
Fsk
ICUE4 (n = 19)
ICUE3 (n = 7)
Time (min)
Max ΔR/R (25 μM Fsk)
****
(11) (26)
ICUE3
ICUE4
C
Avg. Norm. Y/C Emission Ratio (ΔR/ΔR$_{max}$)
ICUE4 [n = 45]
PDE4D2$_{cat}$-ICUE4 (+rolipram) [n = 22]
[Fsk] (μM)
D
Average ICUE4 Emission Ratio (C/Y)
Average Norm. C/Y Emission Ratio (R/R$_0$)
Fsk
IBMX
+HEX
−HEX
n = 17
n = 18
Time (min)
E
+RIα
Average ICUE4 Emission Ratio (C/Y)
Fsk
IBMX
+HEX
−HEX
n = 11
n = 18
Time (min)
F
+HEX
−HEX
P = 0.6848
P = 0.0036
****
****
Raw ICUE Emission Ratio (C/Y) (before Fsk addition)
(43) (45) (34) (30)
endo RIα
RIα OX
G
P = 0.0003
****
PDE4D2$_{cat}$-ICUE4 Starting Ratio (C/Y)
61 77 36
endo RIα
RIα OX
RIα KO
(RIα KO)
P = 0.0091
P = 0.0035
36 66 52
+RIα
+RIα D/D+linker
+RIα Δ(D/D+linker)
H
+RIα (RIα KO)
+HEX
−HEX
IBMX
n = 8
Rol
Fsk
n = 8
Avg. Norm. C/Y Emission Ratio (ΔR/R$_0$)
Fsk Response (ΔR/ΔR$_{max}$)
****
(20)(24)
− +
HEX
Time (min)
I
+RIα (D/D+linker) (RIα KO)
+HEX
−HEX
IBMX
n = 12
Rol
n = 10
Fsk
(28)(56)
− +
HEX
Time (min)
J
+RIα Δ(D/D+linker) (RIα KO)
+HEX
−HEX
IBMX
n = 12
Rol
n = 14
Fsk
(31)(36)
− +
HEX
Time (min)
K
RIα-ICUE4 (RIα KO)
IBMX
Diffuse
Puncta
n = 8
Fsk
n = 8
Avg. Norm. C/Y Emission Ratio (ΔR/R$_0$)
Time (min)
RIα-(D/D+L)-ICUE4 (RIα KO)
IBMX
n = 7
Diffuse
Puncta
n = 7
Fsk
Time (min)
L
****
Diffuse
Puncta
Maximum Fsk Response (R/R$_0$)
RIα-ICUE4 (n = 15)
(D/D+L)-ICUE4 (n = 17)

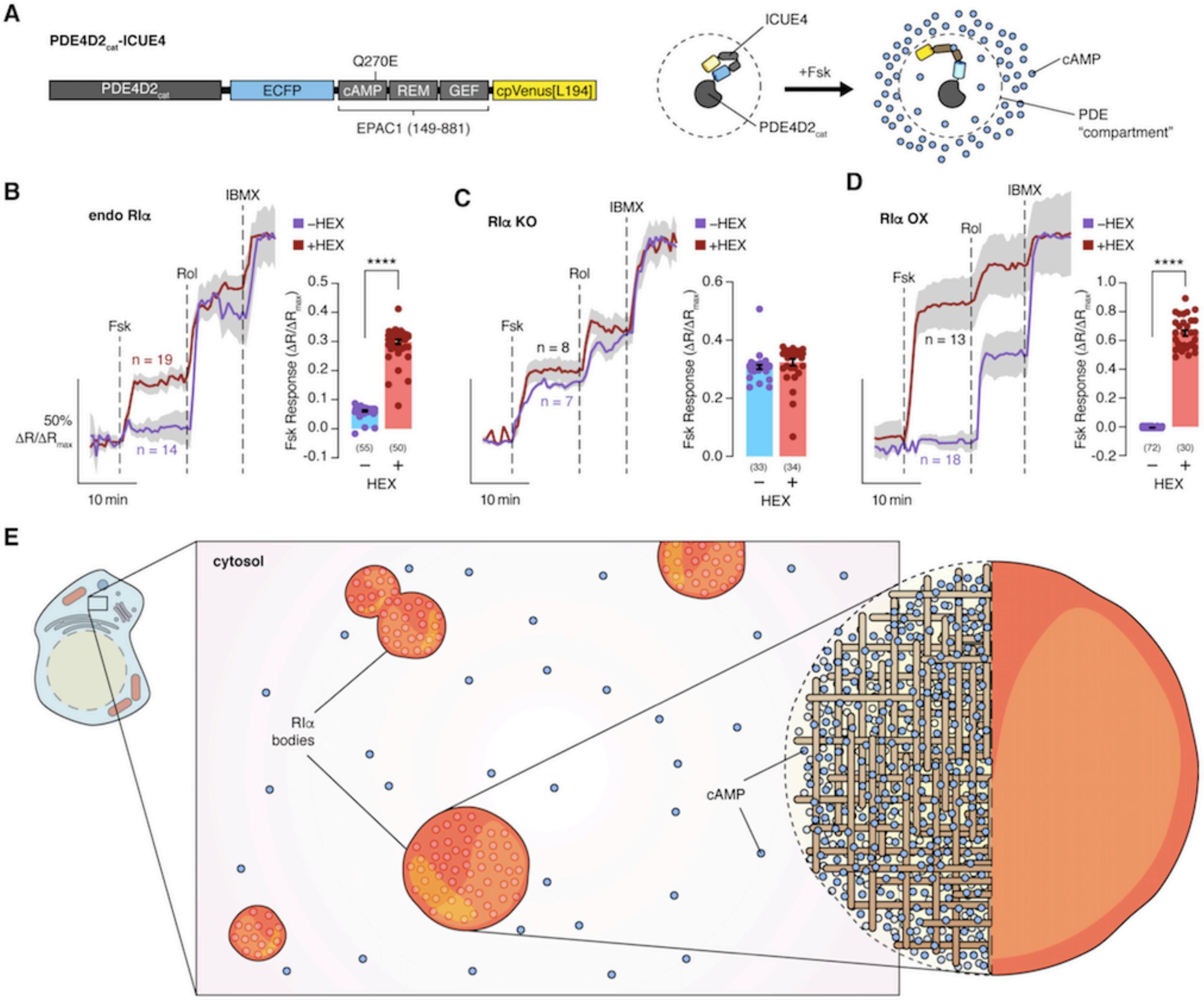

Figure 3.8: Active cAMP buffering by RIα condensates drives cAMP compartmentation. (**A**) Domain structure of the PDE4D2$_{cat}$-ICUE4 sensor, which is used to measure cAMP levels within the PDE4D2 compartment. (**B-D**) Investigating the formation of PDE-mediated cAMP sinks with and without RIα phase separation. Left: Representative average time courses of cyan/yellow (C/Y) emission ratio changes (normalized to maximum) in wild-type HEK293T cells transfected with PDE4D2$_{cat}$-ICUE4 (endo RIα) (**B**), RIα knock-out HEK293T cells transfected with PDE4D2$_{cat}$-ICUE4 (RIα KO) (**C**), or HEK293T cells co-transfected with PDE4D2$_{cat}$-ICUE4 and mRuby2-RIα (RIα OX) (**D**). Cells with (red curve) or without (blue curve) 2.5% 1,6-hexanediol pretreatment were stimulated with 50 µM Fsk, 1 µM rolipram (Rol), and 100 µM IBMX. Right: Maximum normalized emission ratio upon Fsk stimulation. Solid lines in **B-D** indicate the mean; shaded areas, SEM. Bars in **B-D** indicate mean ± SEM. (**E**) Schematic illustration of cAMP buffering via RIα phase separation. RIα droplets actively sequester cAMP, effectively buffering cAMP in the cytosol. On a biophysical level, our modeling results suggest that the internal geometry of RIα droplets functions to trap cAMP within these biomolecular condensates.

enhances cAMP compartmentation. In sharp contrast, when RIα phase separation was disrupted by 1,6-hexanediol pretreatment, Fsk stimulation induced a large 65% ± 2.0% (n = 30 cells) increase in the normalized emission ratio (Figure 3.8D, $P < 0.0001$). Moreover, RIα phase separation decreased basal cAMP levels around the PDE4D2 compartment, as the initial cyan/yellow emission ratios for PDE4D2$_{cat}$-ICUE4 were lower when RIα was present versus when RIα was knocked out (Figure 3.7F).

To identify the key determinants of RIα-mediated cAMP compartmentation, we expressed mRuby2-tagged RIα$_{D/D+linker}$, which can phase separate but does not bind cAMP, and mRuby2-tagged RIα$_{\Delta D/D+linker}$, which can bind to cAMP but cannot phase separate, in RIα null cells and measured cAMP levels around PDE4D2$_{cat}$. In both cases, Fsk treatment induced significant increases in cAMP levels around PDE4D2$_{cat}$ irrespective of 1,6-hexanediol pretreatment, while basal cAMP levels around the PDE4D2 compartment were also elevated, as the initial cyan/yellow emission ratios for PDE4D2$_{cat}$-ICUE4 were higher for both mutants compared with wild-type RIα (Figures 3.7F-K). These data suggest that both the formation of RIα condensates and the ability of RIα to sequester cAMP are required for effective cAMP compartmentalization. Moreover, experiments using dye-labeled cAMP suggest that cAMP is essentially "trapped" inside the RIα condensates (Figure 3.8E and 3.9). Overall, these results highlight a novel mechanism of cAMP compartmentation wherein RIα condensates enable PDEs to function as local cAMP sinks to drive cAMP signaling specificity.

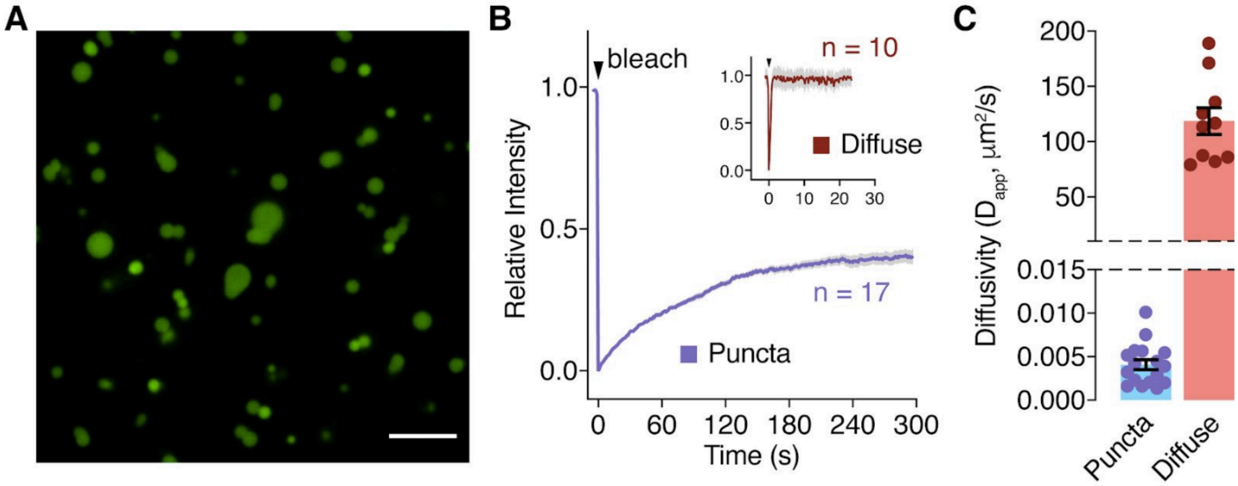

Figure 3.9: cAMP in RIα droplets *in vitro*.

(**A**) When added to 50 μM purified RIα, 10 μM dye-labeled cAMP analogue (8-Φ-450-cAMP) preferentially localized within RIα droplets, with 99% ± 0.33% of cAMP in the droplets. Scale bar, 10 μm. (**B**) cAMP FRAP experiments using dye-labeled cAMP reveal much slower fluorescence recovery within RIα droplets (Puncta) versus when cAMP is alone in solution (Diffuse; inset). Solid lines indicate the mean; shaded area, SEM. (**C**) Apparent diffusion coefficients of puncta-localized or diffuse cAMP calculated from FRAP experiments.

An oncogenic PKA fusion abolishes RIα phase separation

Disruption of RIα phase-separation leads to defective cAMP compartmentation, and the aberrant cAMP/PKA signaling caused by altered cAMP compartmentation is linked to various diseases[135,160,161]. FLC is an atypical liver cancer that primarily affects young adults with no pre-existing liver conditions[162], making the etiology of this cancer enigmatic. While the DnaJB1-PKA_{cat} fusion oncogene is detected in nearly all FLC patients, the mechanism by which this fusion protein drives FLC is completely unknown[51,53]. Intriguingly, we observed an almost complete absence of RIα puncta formation in HEK293T cells overexpressing DnaJB1-PKA_{cat} and RIα compared with cells overexpressing wild-type PKA_{cat} and RIα (Figures 3.10A-B and 3.11A). A kinase-dead, ATP-binding deficient mutant of DnaJB1-PKA_{cat}, DnaJB1-PKA_{cat}^{K72H}, which does not induce FLC in animal models[53], restored RIα phase separation when co-expressed (Figure 3.10A-B), presumably due to a reduced affinity for RIα[163]. Fsk also failed to induce any significant increases in RIα phase separation when DnaJB1-PKA_{cat} or DnaJB1-PKA_{cat}^{K72H} were co-expressed with RIα, in contrast to wild-type PKA_{cat} (Figures 3.10C and 3.11C), with little RIα phase separation observed in the case of DnaJB1-PKA_{cat} and many RIα puncta observed in the case of DnaJB1-PKA_{cat}^{K72H}.

N-terminal fusion of the J-domain abolishes PKA_{cat} myristoylation[164] and recruits the Hsp70 chaperone to the fusion protein[165]. Therefore, we next tested the effect of PKA_{cat} myristoylation and Hsp70 recruitment by the J-domain on RIα phase separation. Mutating the myristoylation site in wild-type PKA_{cat} (PKA_{cat}^{G1A}) significantly decreased the numbers of RIα puncta under both basal and Fsk-stimulated conditions (Figure 3.10D). Intriguingly, adding an N-terminal fragment to restore myristoylation to DnaJB1-PKA_{cat} partially reversed the

Figure 3.10: The FLC oncoprotein DnaJB1-PKA$_{\text{cat}}$ disrupts RIα phase separation and cAMP compartmentation, resulting in increased cell proliferation and transformation. (**A**) Representative fluorescence images of HEK293T cells transfected with EGFP-tagged RIα and either mTagBFP2-tagged DnaJB1-PKA$_{\text{cat}}$ (left) or DnaJB1-PKA$_{\text{cat}}^{\text{K72H}}$ (right). Scale bars, 40 µm. (**B**) Average number of RIα puncta per cell in HEK293T cells co-transfected with EGFP-RIα and mTagBFP2-tagged PKA$_{\text{cat}}$ (Cat), DnaJB1-PKA$_{\text{cat}}$ (J-Cat), or DnaJB1-PKA$_{\text{cat}}^{\text{K72H}}$ (J-Cat$^{\text{K72H}}$). (**C**) Average time course of the number of RIα puncta per cell following 5 µM Fsk addition to HEK293T cells transfected with EGFP-RIα alone (blue curve) or EGFP-RIα plus mTagBFP2-tagged PKA$_{\text{cat}}$ (red curve), DnaJB1-PKA$_{\text{cat}}$ (blue curve), or DnaJB1-PKA$_{\text{cat}}^{\text{K72H}}$ (green curve). (**D**) Comparison of RIα puncta number between cells expressing RIα plus DnaJB1-PKA$_{\text{cat}}$ (J-Cat), wild-type PKA$_{\text{cat}}$ with no myristoylation (Cat$^{\text{G1A}}$), DnaJB1-PKA$_{\text{cat}}$ with myristoylation consensus sequence at N-terminus (Myr-J-Cat), DnaJB1-PKA$_{\text{cat}}$ which cannot bind to Hsp70 (J$^{\text{H33Q}}$-Cat), or DnaJB1-PKA$_{\text{cat}}$ with both myristoylation and no Hsp70 binding (Myr-J$^{\text{H33Q}}$-Cat). Cells were then stimulated with 50 µM Fsk. (**E**) Representative average time courses of cyan/yellow (C/Y) emission ratio changes (normalized to maximum) in HEK293T cells transfected with PDE4D2$_{\text{cat}}$-ICUE4 and mTagBFP2-RIα plus mCherry-tagged PKA$_{\text{cat}}$ (Cat), DnaJB1-PKA$_{\text{cat}}$ (J-Cat), or DnaJB1-PKA$_{\text{cat}}^{\text{K72H}}$ (J-Cat$^{\text{K72H}}$). Cells with (red curves) or without (blue curves) 2.5% 1,6-hexanediol pretreatment were stimulated with 50 µM Fsk, 1 µM rolipram (Rol), and 100 µM IBMX. Solid lines indicate the mean; shaded areas, SEM. Inset: Maximum normalized emission ratio change upon Fsk stimulation for each condition. (**F-H**) Dysfunctional RIα phase promotes tumorigenic phenotypes in AML12 hepatocytes. RIα phase separation was achieved by knocking out RIα or expressing either RIα$_{\text{D/D+Linker}}$, which permits RIα phase separation but lacks cAMP binding, or RIα$_{\Delta\text{(D/D+Linker)}}$, which retains cAMP binding but lacks phase separation, in RIα null cells. (**F**) Average time courses of the cell count for AML12 cells under different conditions. Error bars indicate SEM. (**G**) Average percentage of BrdU+ AML12 cells. (**H**) Average number of colonies larger than 500 µm^2 grown in soft agar. Bars in **B**, **E**, **G**, and **H** indicate mean ± SEM. Violin plot in **D** show the median and quartiles as solid and dashed lines, respectively.

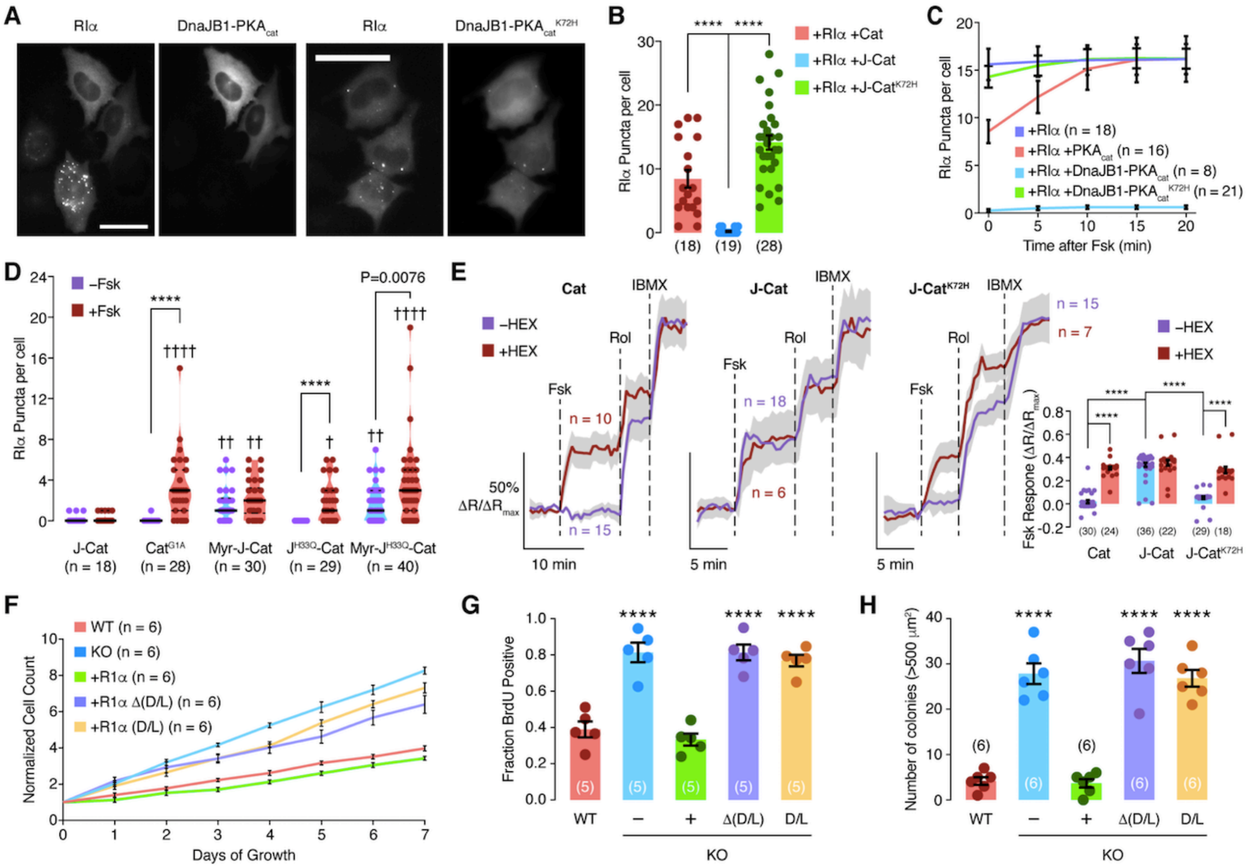
A
RIα
DnaJB1-PKAcat
RIα
DnaJB1-PKAcat K72H
B
****
****
+RIα +Cat
+RIα +J-Cat
+RIα +J-CatK72H
RIα Puncta per cell
(18)
(19)
(28)
C
RIα Puncta per cell
+RIα (n = 18)
+RIα +PKAcat (n = 16)
+RIα +DnaJB1-PKAcat (n = 8)
+RIα +DnaJB1-PKAcat K72H (n = 21)
Time after Fsk (min)
D
–Fsk
+Fsk
RIα Puncta per cell
****
††††
††
††
****
†
P=0.0076
††
††††
J-Cat (n = 18)
CatG1A (n = 28)
Myr-J-Cat (n = 30)
JH33Q-Cat (n = 29)
Myr-JH33Q-Cat (n = 40)
E
Cat
J-Cat
J-CatK72H
–HEX
+HEX
Fsk
Rol
IBMX
n = 10
n = 15
n = 18
n = 6
n = 15
n = 7
50% ΔR/ΔRmax
10 min
5 min
5 min
Fsk Respone (ΔR/ΔRmax)
****
****
****
****
(30) (24) (36) (22) (29) (18)
Cat
J-Cat
J-CatK72H
F
WT (n = 6)
KO (n = 6)
+R1α (n = 6)
+R1α Δ(D/L) (n = 6)
+R1α (D/L) (n = 6)
Normalized Cell Count
Days of Growth
G
Fraction BrdU Positive
****
****
****
(5)
WT
–
+
Δ(D/L)
D/L
KO
H
Number of colonies (>500 μm²)
****
****
****
(6)
WT
–
+
Δ(D/L)
D/L
KO

Figure 3.11: DnaJB1-PKA$_{cat}$ abolishes RIα phase separation, and loss of RIα phase separation leads to tumorigenic phenotypes.
(**A**) Representative *in vitro* phase diagram of RIα liquid droplet formation as a function of RIα and DnaJB1-PKA$_{cat}$ concentration in the absence (top) or presence (bottom) of 10 µM cAMP, showing that DnaJB1-PKA$_{cat}$ disrupts RIα phase separation. Each condition was assessed at least twice. (**B**) Purified RIα, PKA$_{cat}$, PKA type II regulatory subunit (RIIβ), or DnaJB1-PKA$_{cat}$ at the indicated concentrations were incubated in liquid droplet buffer to assess *in vitro* liquid droplet formation. Only RIα showed droplet formation. Scale bars, 10 µm. (**C**) DnaJB1-PKA$_{cat}$ disrupts RIα puncta formation in cells. Representative fluorescence images of HEK293T cells transfected with EGFP-RIα and either mTagBFP2-tagged DnaJB1-PKA$_{cat}$ (upper images) or DnaJB1-PKA$_{cat}^{K72H}$ (JB1-Cat^{K72H}, lower images) before (t = 0 min, top) or after (t = 20 min; bottom) 50 µM Fsk addition. Scale bars, 10 µm. (**D**) Representative photographs of AML12 cell (top) or mouse embryonic fibroblast (MEF) colonies (bottom) embedded in soft-agar in 6-well plates for each condition. Mutations that disrupt RIα phase separation also promote anchorage independent cell growth. (**E-G**) Dysfunctional RIα phase separation promotes tumorigenic phenotypes in MEFs. RIα phase separation was achieved by knocking out RIα or expressing either RIα$_{D/D+Linker}$, which permits RIα phase separation but lacks cAMP binding, or RIα$_{\Delta(D/D+Linker)}$, which retains cAMP binding but lacks phase separation, in RIα null cells. (**E**) Average fold-change in cell count for MEFs under different conditions after 1 week of growth. Data were analyzed using ordinary one-way ANOVA followed by Dunnett's multiple comparisons test. (**F**) Average percentage of BrdU+ MEFs. Data were analyzed using the Kruskal-Wallis test followed by Dunn's multiple comparisons test (vs. WT). (**G**) Average number of colonies larger than 500 µm^2 grown in soft agar. Bars in **E-G** indicate mean ± SEM.

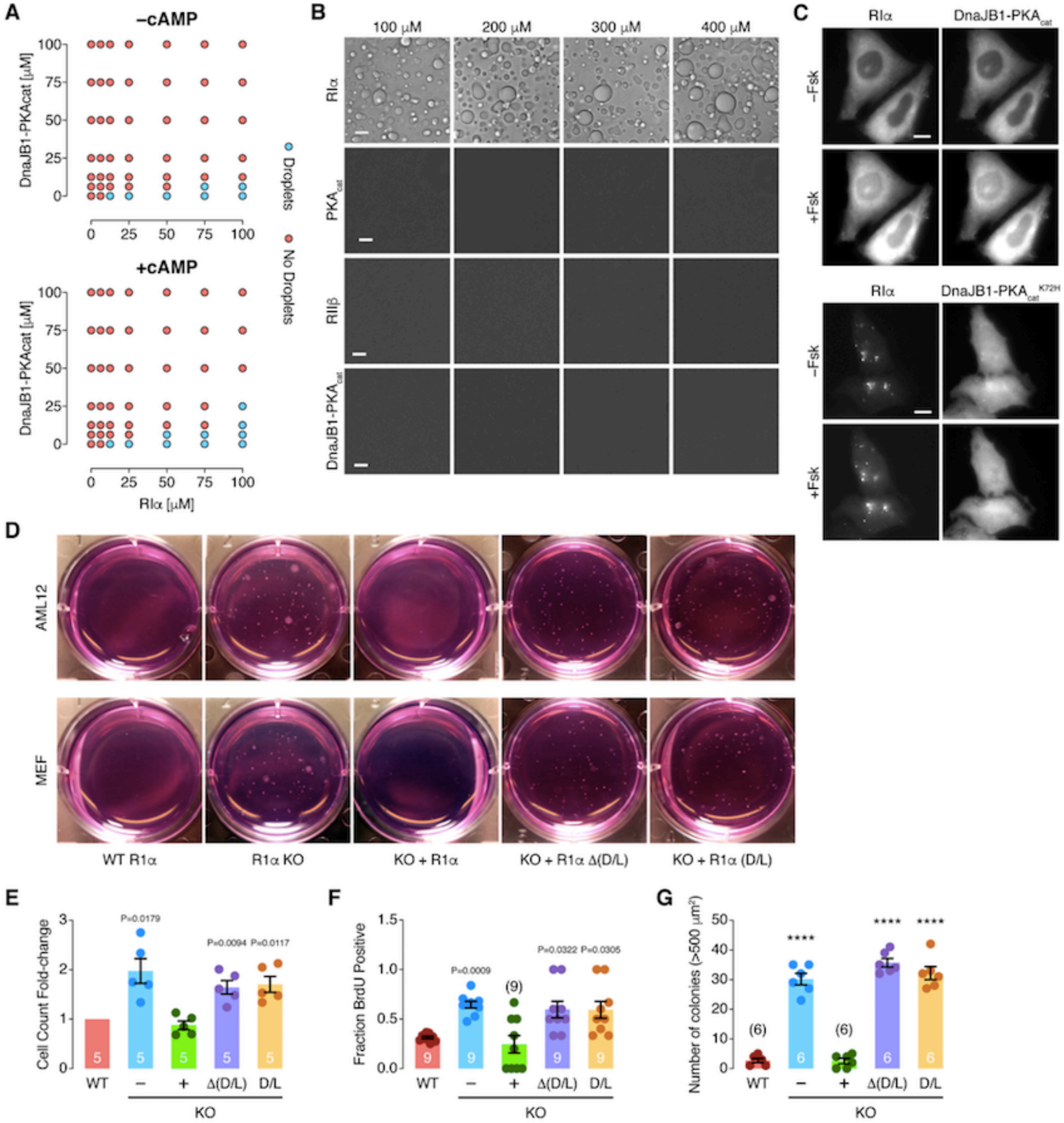
A
−cAMP
DnaJB1-PKAcat [μM]
100
75
50
25
0
0
25
50
75
100
+cAMP
DnaJB1-PKAcat [μM]
100
75
50
25
0
0
25
50
75
100
RIα [μM]
● Droplets
● No Droplets
B
100 μM
200 μM
300 μM
400 μM
RIα
PKA$_{cat}$
RIIβ
DnaJB1-PKA$_{cat}$
C
RIα
DnaJB1-PKA$_{cat}$
−Fsk
+Fsk
RIα
DnaJB1-PKA$_{cat}^{K72H}$
−Fsk
+Fsk
D
AML12
MEF
WT R1α
R1α KO
KO + R1α
KO + R1α Δ(D/L)
KO + R1α (D/L)
E
Cell Count Fold-change
3
2
1
0
P=0.0179
P=0.0094
P=0.0117
5
5
5
5
5
WT
−
+
Δ(D/L)
D/L
KO
F
Fraction BrdU Positive
1.5
1.0
0.5
0.0
P=0.0009
(9)
P=0.0322
P=0.0305
9
9
9
9
WT
−
+
Δ(D/L)
D/L
KO
G
Number of colonies (>500 μm²)
50
40
30
20
10
0
(6)
****
(6)
****
****
6
6
6
WT
−
+
Δ(D/L)
D/L
KO

abolishing effect of DnaJB1-PKA$_{cat}$ on basal RIα phase separation (Figure 3.10D). Furthermore, disrupting the ability of the J-domain to recruit the Hsp70 chaperone by introducing an H33Q mutation[165] in DnaJB1-PKA$_{cat}$ restored the cAMP-responsive formation of RIα biomolecular condensates (Figure 3.10D). Combining these two alterations partially restored both basal and Fsk-stimulated puncta formation (Figure 3.10D). Collectively, these results show that DnaJB1-PKA$_{cat}$ strongly suppresses both basal and cAMP-responsive RIα phase separation, which are partly mediated by the loss of myristoylation and binding to Hsp70, respectively.

Loss of RIα phase separation disrupts cAMP compartmentation and leads to increased cell proliferation and transformation

Given that RIα phase separation is essential to enable cAMP compartmentation, we expect that the DnaJB1-PKA$_{cat}$-induced loss of RIα phase separation should lead to defective cAMP compartmentation. We therefore tested the effect of DnaJB1-PKA$_{cat}$ using our PDE4D2$_{cat}$-ICUE4 cAMP compartmentation assay. In cells expressing wild-type PKA$_{cat}$ and RIα, Fsk induced no detectable changes in the normalized cyan/yellow emission ratio of PDE4D2$_{cat}$-ICUE4 (2.0% ± 1.5%, n = 30 cells), but induced a large 31% ± 1.3% (n = 24 cells) increase in the normalized cyan/yellow emission ratio under these same conditions when RIα phase separation was disrupted by 1,6-hexanediol pretreatment (Figure 3.10E, $P < 0.0001$). On the other hand, cells overexpressing DnaJB1-PKA$_{cat}$ showed similar Fsk-induced PDE4D2$_{cat}$-ICUE4 responses regardless of 1,6-hexanediol pretreatment (Figure 3.10E). However, in the presence of DnaJB1-PKA$_{cat}^{K72H}$, which restores RIα phase separation, Fsk again induced only a small increase in the normalized PDE4D2$_{cat}$-ICUE4 emission ratio (5.4% ± 1.2%, n = 29 cells) versus a much larger 29% ± 2.8% (n = 18 cells) increase when RIα phase separation was disrupted by 1,6-hexanediol pretreatment (Figure 3.10E, *P* < 0.0001). Altogether, these data show that the disruption of RIα phase separation by DnaJB1-PKA$_{\text{cat}}$ dramatically impairs cAMP compartmentation, providing the first mechanistic clue for aberrant signaling caused by this oncoprotein fusion.

A critical question is whether loss of RIα phase separation and subsequent disruption of cAMP compartmentation could have any functional impact on cellular processes, particularly with respect to tumorigenesis. To test the functional consequences of loss of RIα phase separation, we therefore generated an RIα null cell line using non-tumorigenic hepatocytic AML12 cells in which we then stably expressed wild-type or various mutant forms of RIα and measured their proliferation rates and transformation capabilities. Strikingly, loss of RIα increased cell proliferation and DNA synthesis by 2-fold compared with wild-type cells. In RIα null cells, re-expressing wild-type RIα rescued the wild-type phenotype, whereas stably expressing RIα mutants that were defective in either phase separation or cAMP binding failed to rescue (Figure 3.10F-G, *P* < 0.0001). Moreover, loss of RIα led to the formation of detectable colonies on soft agar (Figure 3.10H and 3.11D, *P* < 0.0001), suggesting that loss of RIα leads to anchorage-independent growth, a hallmark for cancer cells. Similar to what was observed for cell proliferation, the restoration of wild-type RIα in RIα null cells inhibited colony formation, whereas RIα null cells expressing RIα mutants that were defective in either phase separation or cAMP binding continued to exhibit anchorage-independent growth (Figure 3.10H and 3.11D, *P* < 0.0001). These results suggest that loss of RIα phase separation and disrupted cAMP compartmentation lead to tumorigenic phenotypes in hepatocytes. Similar results were also observed with mouse embryonic fibroblasts (Figure 3.11E-G), suggesting that the tumor-suppressive nature of RIα phase separation has broad implications.

Discussion

cAMP compartmentation is crucial for our understanding of how this pathway achieves signaling specificity[135,145]; however, the mechanisms responsible for compartmentalizing this ubiquitous second messenger were elusive[26,166]. Local degradation of cAMP has been suggested as a key mechanism in spatially constraining cAMP and forming cAMP compartments[167,168], yet the discrepancy between the modest catalytic capabilities of these enzymes[169,170] and the reportedly rapid diffusion of cAMP in cells[28–30] calls into question the dominant role assigned to PDEs[26]. For instance, work investigating PDE4A1-mediated cAMP compartmentalization found that only reducing cAMP diffusivity by two orders of magnitude versus measured values[171] or supplying supraphysiological levels of PDEs enabled PDE4A1 to create a cAMP sink[26]. Nevertheless, while several additional mechanisms have been suggested to restrict cAMP, including both external[30,172] and internal cellular geometry[149,151] as well as cAMP buffering[150], there is no direct experimental evidence supporting their role in restricting cAMP[26,166]. Furthermore, computational models that include these and other proposed constraints still fail to explain the generation of PKA activity gradients by localized uncaging of cAMP in cardiomyocytes, suggesting additional unknown mechanisms that restrict cAMP action[121]. Our study thus fills a key gap in our understanding of this fundamental process by identifying a novel mechanism to enable cAMP compartmentation. RIα biomolecular condensates act as a dynamic "sponge" in recruiting and retaining cAMP and active PKA_{cat}, processes that are required for cAMP compartmentation, as disruption of these condensates leads to the loss of PDE-mediated cAMP sinks. In contrast to cAMP buffering by individual PKA molecules, a role for RIα phase separation in cAMP compartmentation is especially attractive given that RIα biomolecular condensates likely enhance cAMP retention through balancing of chemical potential and physical trapping of cAMP molecules in these highly dense, polymeric condensates (Figure 3.9). This discovery of a new cAMP compartmentation system mediated by phase separation may ultimately redefine our understanding of how cAMP compartmentation shapes the cAMP/PKA signaling landscape to achieve functional diversity.

Increasing evidence suggests that phase separation acts as a principal organizer of numerous cellular processes such as actin polymerization[16], transcription[173–175], and stress responses[1,21,176]. Meanwhile, emerging studies have shown that many signaling molecules also undergo liquid-liquid phase separation[35,177]. Although many macromolecules have been shown to undergo phase separation in cells, how phase separation impacts their biochemical activities and functions is often unclear. By engineering a novel class of fluorescent biosensors (FluoSTEPs) that can reconstitute at endogenous loci, we can measure enzyme activity and small molecule dynamics directly within biomolecular condensates without perturbing the expression levels of their individual constituents. Here, we targeted FluoSTEPs to endogenous RIα and measured high cAMP levels and PKA activity in RIα bodies. cAMP levels and PKA activity were particularly enriched and retained in newly formed RIα bodies, suggesting that these condensates dynamically buffer cAMP. These live-cell activity measurements were essential for generating our hypothesis, which led us to discover the cellular function of RIα bodies as a key cAMP compartmentation system, critical for signaling specificity in the cAMP/PKA pathway. Because FluoSTEPs share the same modular design as all FRET-based sensors[31,178], their application is expandable to monitor other signaling activities and should thus aid in further elucidating the organizing principles of cellular activity architectures, including the role of phase-separated enzymatic assemblies in other systems.

FLC is atypical among liver cancers as it is not correlated with age, cirrhosis, or common markers of liver disease[162]. Although the DnaJB1-PKA$_{cat}$ fusion oncoprotein is reported to be present in the majority of FLC patients[51,179], the pathological mechanisms of this oncogenic fusion are completely unknown. From a structural and biochemical standpoint, DnaJB1-PKA$_{cat}$ is largely indistinguishable from wild-type PKA$_{cat}$ with respect to interaction interface and binding affinity for PKA regulatory subunits[54,56], cAMP activation[54], and catalytic activity[51,54,55]. Furthermore, although DnaJB1-PKA$_{cat}$ is expressed at approximately 10-fold higher levels than wild-type PKA$_{cat}$ due to promoter alterations[55], overexpressing wildtype PKA$_{cat}$ does not induce tumor formation in mice[53], suggesting that expression differences alone are not likely the determining factor. Our study provides the first mechanistic link between DnaJB1-PKA$_{cat}$ and tumorigenesis. DnaJB1-PKA$_{cat}$ abolishes RIα phase separation, disrupting cAMP compartmentation and deregulating cAMP/PKA signaling. Furthermore, loss of RIα phase separation in non-tumorigenic hepatocytes and fibroblasts leads to tumorigenic phenotypes such as increased cell proliferation and anchorage-independent growth. Interestingly, a subset of FLC patients lack the DnaJB1-PKA$_{cat}$ oncogene but exhibit loss of RIα protein expression[180], corroborating our model that loss of RIα phase separation is a key driver of FLC. Mechanistically, loss of myristylation and gain of Hsp70 binding[165] by DnaJB1-PKA$_{cat}$ are partially responsible for blocking RIα phase separation, though other mechanisms may also be involved. Intriguingly, both DnaJB1-PKA$_{cat}$ and the related fusion oncoprotein ATP1B1-PKA$_{cat}$

have been detected in intraductal oncocytic papillary neoplasms[181]; thus, our findings that loss of cAMP compartmetnation drives tumorigenic signaling may be applicable to other cancers. While multiple studies have shown that the emergence or enhancement of phase separation is linked to stress conditions or neurological disease states[12,21,22,62,176], our work provides a distinct example of phase separation being necessary for normal cellular function, with the loss of phase separation leading to disease phenotypes, where only a limited number of examples exist[182].

In summary, we have discovered a new membraneless organelle that shapes the PKA signaling landscape. Our results represent a conceptual leap forward in understanding how the cAMP/PKA pathway is dynamically organized. Given the universal nature of cAMP/PKA signaling and the ubiquitous expression of RIα[152], our findings have far-reaching physiological implications for various biological systems such as cardiomyocytes[134,138,183,184] and neurons[136,185,186], in which the cAMP/PKA pathway plays diverse roles and RIα puncta formation can be observed (Figure 3.2). Furthermore, we have identified a new link between spatially dysregulated cAMP/PKA signaling and cancer. Overall, our findings showcase the intricacies of signaling activity architectures and the importance of biomolecular condensates in their construction.

Materials and Methods

REAGENT or RESOURCE	SOURCE	IDENTIFIER
Bacterial and Virus Strains		
DH5α competent bacteria	NEB	C2987I
RIα-EGFP lentivirus	This study	N/A
RI$\alpha_{D/D+Linker}$-EGFP lentivirus	This study	N/A
RI$\alpha_{\Delta(D/D+Linker)}$-EGFP lentivirus	This study	N/A
BL21(DE3) competent bacteria	Agilent	200131
Rosetta (DE3) pLysS competent bacteria	Millipore Sigma	70956
Biological Samples		
Sprague-Dawley rat pups	Charles River	400
Chemicals, Peptides, and Recombinant Proteins		
BbsI	NEB	R3539
Q5 High Fidelity Polymerase	NEB	M0491S
HiFi DNA Assembly Kit	NEB	E5520S

HindIII	NEB	R0104S
EcoRI	NEB	R0101S
XbaI	NEB	R0145S
Q5 Site Directed Mutagenesis Kit	NEB	E0554
DMEM	Gibco	11885-084
FBS	Sigma Aldrich	F2442
Penicillin-Streptomycin	Sigma Aldrich	P7539
DMEM:F12	ThermoFisher	12634010
ITS Liquid Media Supplement	Sigma Aldrich	I3146
Dexamethasone	Sigma Aldrich	D1159
Polyjet	Signagen	SL100688
Hank's Buffered Salt Solution	Gibco	14025076
DNase I	ThermoFisher	EN0525
Neurobasal media	ThermoFisher	21103049
SM1 Supplement	STEMCELL Technologies	05711

Poly-D-Lysine	Sigma Aldrich	P6407
Lipofectamine LTX	Invitrogen	15338500
Puromycin	Sigma Aldrich	P8833
DPBS	Gibco	14040133
BSA	Roche	10738328103
HEPES	Sigma Aldrich	H3375
EDTA	Sigma Aldrich	E6758
DAPI	ThermoFisher	D21490
Noble Agar	ThermoFisher	AAJ1090722
Powdered DMEM	ThermoFisher	12800017
IPTG	Sigma Aldrich	I6758
Ampicillin	Sigma Aldrich	A1593
MES	Sigma Aldrich	M3671
NaCl	Sigma Aldrich	S9888
EGTA	Sigma Aldrich	E3889

DTT	Sigma Aldrich	D0632
Protease inhibitors	Roche	11873580001
kanamycin	Sigma Aldrich	K1637
cGMP	Sigma Aldrich	G7504
Tris	Sigma Aldrich	93362
β-mercaptoethanol	Sigma Aldrich	M6250
Imidazole	Sigma Aldrich	1336500
$MgCl_2$	Sigma Aldrich	208337
ATP	Sigma Aldrich	A26209
KCl	Sigma Aldrich	P3911
cAMP	Sigma Aldrich	A9501
PEG4000	Sigma Aldrich	1546569
Forskolin	CalBioChem	344281
IBMX	Sigma Aldrich	I7018
Rolipram	Alexis	61413-54-5

1,6-hexanediol	Sigma Aldrich	240117
Myr-PKI	Tocris	2546
Isoproterenol	Sigma Aldrich	1351005
Critical Commercial Assays		
BrdU kit	Invitrogen	B23151
MDL-12330A	Sigma Aldrich	M182
8-Br-2’-O-Me-cAMP-AM	Biolog	B028-01
8-[Φ-450]-cAMP	Biolog	P024-001
Experimental Models: Cell Lines		
HEK293T	ATCC	CRL-11268
MEF	GS McKnight Lab, University of Washington, Seattle, WA, USA	N/A
AML12	ATCC	CRL-2254
293-RIα	This study	N/A

293T-RIα KO	This study	N/A
MEF-RIα KO	This study	N/A
AML12-RIα KO	This study	N/A
AML12-RIα KO-RIα-EGFP	This study	N/A
AML12-RIα KO$_{D/D+Linker}$-RIα-EGFP	This study	N/A
AML12-RIα KO$_{\Delta(D/D+Linker)}$-RIα-EGFP	This study	N/A
MEF-RIα KO-RIα-EGFP	This study	N/A
MEF-RIα KO-RIα$_{D/D+Linker}$-EGFP	This study	N/A
MEF-RIα KO-RIα$_{\Delta(D/D+Linker)}$-EGFP	This study	N/A
HEK293A	ThermoFisher	R70507
Oligonucleotides		
RIα-FP$_{11}$ HDR ssDNA	IDT, for this study	N/A
Recombinant DNA		
pS458 mouse RIα gRNA	This study	N/A
pS459 human RIα gRNA	This study	N/A

pcDNA3.1 GFP_{1-10}	Bo Huang lab, UCSF, San Francisco, CA, USA	N/A
pcDNA3.1 EGFP-RIα	[154]	N/A
pcDNA3.1 mCherry-PKA_{cat}	[154]	N/A
pcDNA3.1 mRuby2-RIα	This study	N/A
pcDNA3.1 mTagBFP2-RIα	This study	N/A
pcDNA3.1 $RIα_{D/D+Linker}$-EGFP	This study	N/A
pcDNA3.1 $RIα_{D/D}$-EGFP	This study	N/A
pcDNA3.1 $RIα_{Linker}$-EGFP	This study	N/A
pcDNA3.1 $RIα_{\Delta(D/D+Linker)}$-EGFP	This study	N/A
pcDNA3.1 $RIα_{\Delta D/D}$-EGFP	This study	N/A
pcDNA3.1 $RIα_{\Delta Linker}$-EGFP	This study	N/A
pcDNA3.1 mTagBFP2-PKA_{cat}	This study	N/A
pcDNA3.1 FluoSTEP-AKAR	This study	N/A
pcDNA3.1 FluoSTEP-ICUE	This study	N/A

pcDNA3.1 FluoSTEP-AKAR(T/A)	This study	N/A
pcDNA3.1 FluoSTEP-ICUE(R279E)	This study	N/A
pcDNA3.1 ICUE4	This study	N/A
pcDNA3.1 PDE4D2$_{cat}$-ICUE4	This study	N/A
pcDNA3.1 mCherry-DnaJB1-PKA$_{cat}$	This study	N/A
pcDNA3.1 mCherry-DnaJB1-PKA$_{cat}^{K72H}$	This study	N/A
pcDNA3.1 mCherry-PKA$_{cat}^{K72H}$	This study	N/A
pcDNA3.1 mCherry-PKA$_{cat}^{G1A}$	This study	N/A
pcDNA3.1 mCherry-Myr-DnaJB1-PKA$_{cat}$	This study	N/A
pcDNA3.1 mCherry-DnaJB1-PKA$_{cat}$	This study	N/A
pcDNA3.1 mCherry-DnaJB1^{H33Q}-PKA$_{cat}$	This study	N/A
pcDNA3.1 mCherry-Myr-DnaJB1^{H33Q}-PKA$_{cat}$	This study	N/A
pcDNA3.1 RIα-ICUE4	This study	N/A

pcDNA3.1 RIα$_{\text{D/D+Linker}}$-ICUE4	This study	N/A
pLentibRIα-EGFP	This study	N/A
pLenti RIα$_{\text{D/D+Linker}}$-EGFP	This study	N/A
pLenti RIα$_{\Delta\text{(D/D+Linker)}}$-EGFP	This study	N/A
pRSET B sfGFP	This study	N/A
pRSET B GR-ICUE	This study	N/A
pcDNA3.1 GR-ICUE	This study	N/A
pcDNA3.1 RIα-GR-ICUE	This study	N/A
pMD2.G	Didier Trono lab, EPFL, Switzerland	N/A
psPAX2	Didier Trono lab, EPFL, Switzerland	N/A
pET-His6-SUMO-TEV-LIC-PKA$_{\text{cat}}$	This study	N/A
pET-His6-SUMO-TEV-LIC-DnaJB1-PKA$_{\text{cat}}$	This study	N/A
pET-His6-EGFP-PKA$_{\text{cat}}$	This study	N/A

pRSET B His-sfGFP	This study	N/A
Software and Algorithms		
MATLAB	MathWorks	https://www.mathworks.com/products/matlab.html
PRISM	Graphpad	https://www.graphpad.com/scientific-software/prism/
Adobe Illustrator	Adobe	https://www.adobe.com/products/illustrator
ImageJ	NIH	https://imagej.nih.gov

Plasmid construction

All plasmids are in the pcDNA3.1 backbone unless specified. The vector expressing both gRNA and Cas9 in the px459 v2.0 backbone (px459)[187] (gift of Feng Zhang, Addgene plasmid #62988) was generated using Golden Gate cloning as previously described[188]. To construct gRNA expression vectors, the 20-bp target sequence was sub-cloned into px459 using oligonucleotides (lowercase letters indicate gRNA sequences) 5’-CACCGacacaaaactgttgtactgc-3’ and 5’-AAACgcagtacaacagttttgtgtC-3’ to generate 293-RIα cells. To generate RIα null HEK293T cells, two designed guide sequences (5’-TGGCAGTACCGCCGCCAGTG-3’ and 5’-AGAGACCCATGGCATTCCTC-3’) that specifically target the human RIα gene were each cloned into the sgRNA scaffold in px458[187] (gift of Feng Zhang, Addgene plasmid #48138). For RIα null AML12 cells and MEFs, two designed guide sequences (5’-

GCACGATGGAGTCCTTCAGCA-3’ and 5’-GTATTCCCGAAGGAATGCCAT-3’) that specifically target the mouse RIα gene were each cloned into the sgRNA scaffold in px458. pcDNA3.1-GFP$_{1-10}$[32] was a gift from Bo Huang (Addgene plasmid #70219). EGFP-RIα and mCherry-PKA$_{cat}$ were generated previously[154]. mRuby2-RIα was generated via PCR amplification of mRuby2 from pcDNA3-AKAR-CR[189] (gift of Michael Lin, Stanford University, Palo Alto, CA) using primers (lowercase letters are Gibson assembly overhangs and uppercase letters are priming regions) 5’-gttttgtgtcactgtctgtcgGATCCCCACCGGTCGCCACCATGGTGTCTAAGGGCGAAGA-3’ and 5’-CTTGTACAGCTCGTCCATCCCACCACC-3’ and RIα from the RIα-EGFP plasmid backbone using primers 5’-ggatggacgagctgtacaagtgaGAATTCTGCAGATATCCAGCACAGTGG-3’ and 5’-GACAGACAGTGACACAAAACTGTT-3’, followed by Gibson assembly using the NEBuilder Hi-Fi DNA Assembly Cloning Kit (New England Biolabs). mTagBFP2-RIα was generated by Gibson assembly of PCR products amplified from pBAD-mTagBFP2[190] (gift of Vladislav Verkusha, Addgene plasmid #34632) using the primers 5’-gttttgtgtcactgtctgtcggatccccaccggtcgccaccATGAGCGAGCTGATTAAGGAG-3’ and 5’-gctggatatctgcagaattcTTAATTAAGCTTGTGCCCCAGT-3’. RIα mutants C-terminally tagged with either EGFP or mRuby2 were generated via Gibson assembly of PCR products amplified from RIα-EGFP or RIα-mRuby2 using the following primers: RIα$_{D/D+Linker}$ (forward 5’-ctatagggagacccgccaccatgGCACGCAGCCTTCGAGAAT-3’, reverse 5’-gtggcgaccggtggggatccGGATGCCGCATCTTCCTC-3’), RIα$_{D/D}$ (forward 5’-ctatagggagacccgccaccatgGCACGCAGCCTTCGAGAAT-3’, reverse 5’-gtggcgaccggtggggatccCTCCTCCTTCTCCAACCTCTCA-3’), RIα$_{Linker}$ (forward 5’-

ctatagggagacccgccaccatgGCAAAACAGATTCAGAATCTGCAGAAA-3’, reverse 5’-gtggcgaccggtggggatccGGATGCCGCATCTTCCTC-3’), $\text{RI}\alpha_{\Delta\text{D/D+Linker}}$ (forward 5’-gtaccgccgccagtgaggagTATGTTAGAAAGGTTATACCAAAAGATTACAAGAC-3’, reverse 5’-ggtataacctttctaacataCTCCTCACTGGCGGCGGTA-3’), $\text{RI}\alpha_{\Delta\text{D/D}}$(forward 5’-gtaccgccgccagtgaggaggctaagcaGATTCAGAATCTGCAGAAAGCA-3’, reverse 5’-agattctgaatctgcttagcCTCCTCACTGGCGGCGGTA-3’), $\text{RI}\alpha_{\Delta\text{Linker}}$ (forward 5’-agaggttggagaaggaggagTATGTTAGAAAGGTTATACCAAAAGATTACAAGAC-3’, reverse 5’-ggtataacctttctaacataCTCCTCCTTCTCCAACCTCTCA-3’). mTagBFP2-PKA_{cat} was constructed by Gibson assembly of PCR products amplified from pBAD-mTagBFP2 using the forward primers 5’-agacccaagctggctagcgtttaaacttaagcttgggccaccATGAGCGAGCTGATTAAGGAG-3’ and 5’-aactggggcacaagcttaatGGACTCAGATCCGGTTCAAT-3’ and the reverse primer 5’-ATTAAGCTTGTGCCCCAGT-3’. To construct FluoSTEP-AKAR, mRuby2 was PCR-amplified from AKAR-CR using the primers 5’-cccaagctggctagcgtttaaacttaagcttggATGGTGTCTAAGGGCGAAGAGCTGATC-3’ and 5’-gatctgttcttgagaaaacttatgcatgcgCTTGTACAGCTCGTCCATCCCACC-3’, and the FHA1 and PKA substrate from AKAR4[191] were PCR-amplified using primers 5’-ggtgggatggacgagctgtacaagCGCATGCATAAGTTTTCTCAAGAACAGATC-3’ and 5’-tcctttggacatagatctgttaacgaattcGAGCTCGCTGCCGCCGGTGCCGCCGTCC-3’. The resulting PCR fragments were Gibson assembled into HindIII- and EcoRI-digested pcDNA3.1 $\text{GFP}_{1\text{-}10}$. FluoSTEP-ICUE was constructed similarly, except that $\text{Epac1}^{149\text{-}881}$ was PCR-amplified from ICUE3 [156] using primers 5’-ggtggtgggatggacgagctgtacaagGAGGAGAAGAAGGAGTGTGATGAAGAA-3’ and 5’-

ggtaaacagttcttctcctttggacatCTCAACGTCCCTCAAAATCCGATTGAA-3’. FluoSTEP-AKAR (T/A) was constructed by Gibson assembly of PCR products amplified from FluoSTEP-AKAR using primers 5’-CTGCGTCGCGCCGCCCTGGTTGAC-3’and 5’-GTCAACCAGGGCGGCGCGACGCAG-3’. FluoSTEP-ICUE R279E was constructed by Gibson assembly of PCR products amplified from FluoSTEP-ICUE using primers 5’-gatgcaccccggGCAGCCACCATCATCCTG-3’ and 5’-ggtggctgcccgGGGTGCATCATTCACCAGAG-3’. To construct ICUE4, the Q270E point mutation was introduced using site-directed mutagenesis of ICUE3[156] with primers 5’-GAGGGAGATGATTTTGGAGAGCTGGCTCTGGTGAATGAT-3’ and 5’-GAGGGAGATGATTTTGGAGAACTGGCTCTGGTGAATGAT-3’. To construct PDE4D2$_{cat}$-ICUE4, PDE4D2$^{86-418}$ was PCR-amplified from PDE4D2 cDNA (gift from Hengming Ke, UNC, Chapel Hill, NC) using primers 5’-ACTGAACAAGAAGATGTCCTTGCC-3’ and 5’-CTGAGGGATTGTGCTCTGGT-3’, and the ICUE4 backbone was PCR-amplified using the forward primers 5’-tcctcgcccttgctcaccatggaaccaccagtaccgccAGATCCACCGGTACCTCCTGAA-3’ and 5’-accagagcacaatccctcagGGTGGAACAGGAGGTTCAGG-3’ and the reverse primer 5’-aggacatcttcttgttcagtcatGGTGGCGGGTCTCCCTATA-3’. The resulting PCR fragments were Gibson assembled. mCherry-DnaJB1-PKA$_{cat}$ was generated using DNA gBlock segments designed and synthesized with extra sequences (5’-CTGGCTAGCGTTTAAACTTAAGCTT-3’) at the 5’ ends, extra sequences (5’-TCTAGAGGGCCCGTTTAAACC-3’) at the 3’ ends, and -GSGS- linkers (5’-GGATCCGGGAGC-3’) in between PKA$_{cat}$/DnaJB1-PKA$_{cat}$ and mCherry, which were Gibson assembled into HindIII- and XbaI-digested pcDNA3.1. mCherry-tagged DnaJB1-PKA$_{cat}^{K72H}$ and PKA$_{cat}^{K72H}$ were constructed by Gibson assembly of PCR products amplified from mCherry-tagged DnaJB1-PKA$_{\text{cat}}$ or PKA$_{\text{cat}}$ using primers 5’-tacgccatgcatATCTTAGACAAGCAGAAGGTGGTG-3’ and 5’-tctaagatatgCATGGCGTAGTGGTTCCCACTCT-3’. mTagBFP2-tagged DnaJB1-PKA$_{\text{cat}}^{\text{K72H}}$ and PKA$_{\text{cat}}^{\text{K72H}}$ plasmids were constructed by Gibson assembly of PCR products amplified from mCherry-tagged DnaJB1-PKA$_{\text{cat}}^{\text{K72H}}$ or PKA$_{\text{cat}}^{\text{K72H}}$ using primers 5’-tacgccatgcatATCTTAGACAAGCAGAAGGTGGTG-3’ and 5’-tctaagatatgCATGGCGTAGTGGTTCCCACTCT-3’ and from pBAD-mTagBFP2 using the forward primers 5’-agacccaagctggctagcgtttaaacttaagcttgggccaccATGAGCGAGCTGATTAAGGAG-3’ and 5’-aactggggcacaagcttaatGGACTCAGATCCGGTTCAAT-3’ and the reverse primer 5’-ATTAAGCTTGTGCCCCAGT-3’. mCherry-tagged PKA$_{\text{cat}}^{\text{G1A}}$ was generated via Q5 site-directed mutagenesis (New England Biolabs) using the primers 5’-AAGCTTATGGCCAACGCCGCC-3’ and 5’-AAGTTTAAACGCTAGCCAGC-3’. mCherry-tagged myristoylated-DnaJB1-PKA$_{\text{cat}}$, which contains only the first 8 amino acids of wild-type PKA$_{\text{cat}}$ (first 8 amino acids of Cα1, an isoform of PKA$_{\text{cat}}$, aligns with the consensus myristoylation sequence[192,193]), was constructed by Gibson assembly of PCR products amplified from PKA$_{\text{cat}}$ by using primers 5’-acgccgccgccgccaagaagGGTAAAGACTACTACCAGACGTTGGG-3’ and 5’-CTTCTTGGCGGCGGC-3’. mCherry-tagged DnaJB1$^{\text{H33Q}}$-PKA$_{\text{cat}}$[165] was constructed by Gibson assembly of PCR products amplified from mCherry-DnaJB1-PKA$_{\text{cat}}$ using primers 5’-tgcgctaccagCCGGACAAGAACAAGGAGC-3’ and 5’-cttgtccggcTGGTAGCGCAGCGCCT-3’. mCherry-myristoylated DnaJB1$^{\text{H33Q}}$-PKA$_{\text{cat}}$ was constructed by Gibson assembly of PCR products amplified from mCherry-tagged myristoylated DnaJB1-PKA$_{\text{cat}}$ using the same primers described above for the H33Q J-domain mutation. RIα-ICUE4 was constructed by Gibson assembly of PCR products amplified from RIα-EGFP using primers 5’-ctatagggagacccgccaccATGGAGTCTGGCAGTACCG-3’ and 5’-atggaaccaccagtaccgccGACAGACAGTGACACAAAACTGTT-3’ and from ICUE4 using primers 5’-GGCGGTACTGGTGGTTCCAT-3’ and 5’-GGTGGCGGGTCTCCCTAT-3’. RI$\alpha_{D/D+Linker}$-ICUE4 was constructed similarly using PCR products amplified from RI$\alpha_{D/D+Linker}$-EGFP with primers 5’-ctatagggagacccgccaccATGGCACGCAGCCTTCGAGAAT-3’ and 5’-atggaaccaccagtaccgccGGATGCCGCATCTTCCTC-3’. pLenti backbone versions of RIα mutants tagged with EGFP were constructed by Gibson assembly of PCR products amplified from pLenti-puro[194] (gift of Ie-Ming Shih, Addgene plasmid #39481) using the forward primer 5’-gaattctgcagatatccatcaca-3’ and reverse primer 5’-gggatccttatcgtcatcgtc-3’ and the respective pcDNA3.1 versions of mutants using the reverse primer 5’-GATGGATATCTGCAGAATTCttacttgtacagctcgtccatgc-3’ and the following forward primers: (pLenti RIα-EGFP: 5’-ACGATGACGATAAGGATCCCatggagtctggcagtaccg-3’; pLenti RI$\alpha_{D/D+Linker}$-EGFP: 5’-ACGATGACGATAAGGATCCCatggcacgcagccttcgagaat-3’; pLenti RI$\alpha_{\Delta(D/D+Linker)}$-EGFP: 5’-ACGATGACGATAAGGATCCCatggagtctggcagtaccg-3’). sfGFP in pRSET B was constructed by Gibson assembly of PCR products amplified from pEvolvR-enCas9-PolI3M-TBD[195] (gift from John Dueber & David Schaffer, Addgene plasmid #113077) using the forward primer 5’-ATGCGGGGTTCTCATCATCATCATCATCATatgcgtaaaggcgaagagc-3’ and the reverse primer 5’-CCAGTCATGCTAGCCATACCttatttgtacagttcatccataccatgc-3’ to amplify sfGFP and the forward primer 5’- GGTATGGCTAGCATGACTGGTG-3’ and the reverse primer 5’-

TGATGATGAGAACCCCGcatatgtatatctccttcttaaagttaaacaaaatta-3’ to amplify pRSET B. All constructs were verified by Sanger sequencing (Genscript).

Cell culture and transfection

HEK293A, HEK293T, and MEF cells were cultured in Dulbecco’s modified Eagle medium (DMEM, Gibco) containing 1 g L^{-1} glucose and supplemented with 10% (v/v) fetal bovine serum (FBS, Sigma) and 1% (v/v) penicillin–streptomycin (Pen-Strep, Sigma-Aldrich). AML12 cells were cultured in DMEM:F12 medium (Thermo Fisher) containing 10% FBS, 10 μg mL^{-1} insulin, 5.5 μg mL^{-1} transferrin, 5 ng mL^{-1} selenium (ITS liquid media supplement, Sigma-Aldrich), and 40 ng mL^{-1} dexamethasone (Sigma-Aldrich). All cells were maintained in a 37°C incubator with a humidified 5% CO_2 atmosphere. Before transfection, HEK293A and HEK293T were plated onto sterile poly-D-lysine coated 35-mm glass-bottomed dishes and grown to 50–70% confluence. HEK293A and HEK293T were then transfected using Polyjet (Signagen) and grown for an additional 16-24 h before imaging.

Neonatal rat ventricular myocytes were isolated from cardiac ventricles of 1- to 2-day-old Sprague-Dawley rat pups as described previously[196]. Neonatal myocytes were plated at a density of 3.0×10^4 cm^{-2} on laminin-coated 35-mm glass-bottomed dishes and maintained in DMEM with 15% FBS overnight. Cells were transfected 24 h later using Polyjet for 48 h, with the media changed 24 h after transfection. Primary rat hippocampal neurons and glial cells were harvested from E19 Sprague-Dawley rat pups (Charles River) in ice-cold Hank’s Balanced Salt Solution (HBSS, Gibco) and were dissociated using the Papain Dissociation System with $MgSO_4$ and DNase I according to the manufacturer’s instructions. Dissociated neurons and glial cells were diluted to 200,000 cells mL^{-1} and resuspended in Neurobasal medium (Thermo Fisher) with 2% SM1 supplement (STEMCELL Technologies). Cells were plated onto 35-mm glass-bottom dishes coated with 100 μg mL^{-1} poly-D-lysine (Sigma) and cultured in a 37°C incubator with a humidified 5% CO_2 atmosphere. At 1 or 3 days *in vitro*, cells were transfected with Lipofectamine LTX (Invitrogen) according to the manufacturer's instructions in Neurobasal media and imaged after 48 h. All animals were treated in accordance with the UC San Diego Animal Care and Use Committee guidelines.

Generation of stable cell lines

To generate 293-RIα cells, HEK293A cells were plated in 6-well plates. After 24 h, 1 μg of px459 plasmid (encoding Cas9 and gRNA) and 20 pmol of ssDNA ultramer HDR template (Integrated DNA Technologies) were transfected using Polyjet following the manufacturer's protocol. Cells were passaged 1 day after transfection into a 60-mm dish, and 1 μg mL^{-1} puromycin was added 24 h later. When no viable cells remained in the untransfected dish (around 2-3 days), the media was replenished without puromycin. Cells were passaged 24 h later and resuspended in sorting buffer (1 x DPBS with 0.5% BSA, 25 mM HEPES, 1 mM EDTA, pH 7, 2.5 μg mL^{-1} of DNase I (Thermo Fisher)) with 0.1μg mL^{-1} DAPI (Thermo Fisher). Cells were sorted for DAPI-negative staining and plated as single cells in a 96-well plate using a BD FACS Aria II Cell Sorter. After 3 weeks of incubation, wells containing single-cell colonies were passaged, and DNA was extracted for genotyping using the DNeasy Blood & Tissue Kit (Qiagen). Genomic PCR was performed using the Q5 High-Fidelity Kit (New England Biolabs) with primers 5'-TTTGTTGAAGTGGGAAGATTGG-3' and 5'-TCAATAGGTGCTGGGATCTGC-3'. To evaluate the copy number of correct gene edits, PCR products were gel extracted using PureLink Quick Gel Extraction kit (Invitrogen), cloned into TOPO PCR vectors (Invitrogen), and subjected to Sanger sequencing (Genscript).

RIα null HEK293T cells were generated as described[187], but with slight modifications. When cells reached 70% confluency, cells were co-transfected with two px458 plasmids (Cas9 and gRNA) that target RIα. After 24 h of transfection, the cells were aspirated, washed with DPBS, and filtered through a 35-µm cell strainer. Cells with GFP signals were sorted into single cells in a 96-well plate using a BD FACSJazz™ cell sorter. After single cells had grown into colonies, the cells were transferred to 60-mm cell culture plates. The corresponding genomic DNA segment was PCR-amplified using primers 5'-GAGGGAGAACTGAATGAAATT-3' and 5'-GTCAGATTCCTTTTCTTCC-3' to verify correct gene editing. Each colony was validated via western blotting and DNA sequencing.

RIα null MEF and AML12 (ATCC) cells were generated similarly to RIα knock-out HEK293T cells, except the gRNAs differ, and the corresponding genomic DNA segment to verify correct gene editing was PCR amplified using primers 5'-TGAAATCTCCAGAGGGCTTG-3' and 5'-TTAGCCACACAAGCAGCATC-3'. To generate stable RIα null MEF and AML12 cells with exogenously expressed RIα mutants, lentiviruses were made by transfection of pLenti backbone versions of RIα mutants with the packaging vectors pMD2.G (gift of Didier Trono, Addgene plasmid #12259) and psPAX2 (gift of Didier Trono, Addgene plasmid #12260)[197] into HEK293T cells. At 24 h after transfection, HEK293T cells were replenished with fresh media. After an additional 2 days, supernatant was collected and sterile-filtered through a 0.45 µm filter. RIα null MEF and AML12 cells were infected with lentiviruses and underwent FACS.

Disorder and charge predictions

Disorder of full-length human RIα was predicted using PONDR (http://www.pondr.com/), which predicted that residues 63-105 and 264-320 are intrinsically disordered regions. The single-amino-acid and average (sliding window of 10 AA) charge distribution along the primary sequence were analyzed using EMBOSS (http://www.bioinformatics.nl/cgi-bin/emboss/charge), which predicted various regions to have high charge imbalance, such as the highly positively charged region of residues 81-96.

Cell proliferation assay

MEF and AML12 stable cell lines were seeded in 6-wells plates at 10,000 cells/well. Cell numbers were quantified using a Countess II cell counter (Life Technologies) each day for 7 days.

BrdU staining

MEF and AML12 stable cell lines were seeded on 35-mm glass-bottomed dishes at 10,000 cells/dish. At 48 h after plating, cells were treated with 10 μM BrdU (Invitrogen) for 4 h. Cells were washed twice with PBS and fixed with 3.7% formaldehyde in PBS. MEF and AML12 cells were imaged following application of standard immunofluorescence protocols: Triton X-100 permeabilization, 1 N and 2 N HCl addition, anti-BrdU primary antibody addition (1:100, Invitrogen), anti-mouse Alexa Fluor 647 (1:1000, Invitrogen), and 100 ng mL^{-1} DAPI nuclear staining.

Soft agar colony formation assay

Soft agar colony formation assays were performed as described previously[198]. Briefly, 6-well plates were prepared containing 0.5% Noble Agar (Thermo Fisher) and 2X concentration of the respective cell media. After the agar solidified, 0.3% Noble Agar containing 5000 cells was applied on top of the 0.5% Noble Agar layer. MEF s and AML12 cells in soft agar were cultured in a 5% CO_2 incubator for several weeks with 200 µL of the respective culture media added on top of the gel twice per week. Visible colonies appeared after 3 (MEFs) to 4 weeks (AML12 cells) and were photographed using a Canon EOS 5D Mark III DSLR camera (Canon USA).

Protein purification

Recombinant RIα and RIIβ were purified as described previously[164,199] with slight modifications. Constructs were transformed into *Escherichia coli* BL21 (DE3) cells and inoculated in LB media with 100 µg mL^{-1} ampicillin. Cultures were induced at OD_{600} = 0.6-0.8. After 16 h of expression under 0.5 mM IPTG at 16°C, the cell pellets were collected and then re-suspended and lysed in lysis buffer (20 mM MES, pH 6.5, 100 mM NaCl, 2 mM EDTA, 2 mM EGTA, and 5 mM DTT plus protease inhibitors and 10 µM 3-isobutyl-1-methylxanthine (IBMX)). The supernatant was collected after high-speed centrifugation (13,000 rpm, 1 h) and incubated overnight with cAMP-resin at 4°C. After centrifugation (3,000 rpm, 10 min) and removal of the supernatant, the resin was then washed sequentially with lysis buffer, wash buffer (20 mM MES, pH 6.5, 600 mM NaCl, 2 mM EDTA, 2 mM EGTA, and 5 mM DTT), and lysis buffer again. The proteins were eluted using elution buffer (20 mM MES, pH 5.5, 100 mM NaCl, 30 mM cGMP, 2 mM EDTA, 2 mM EGTA, and 5 mM DTT). The eluted proteins were then concentrated and further purified on an S-200 gel filtration column in 50 mM MES, pH 5.8, 200 mM NaCl, and 5 mM DTT.

PKA_{cat} and DnaJB1-PKA_{cat} were each cloned into pET-His_6-SUMO TEV LIC (gift of Scott Gradia, Addgene plasmid #29659). The constructs were transformed into Rosetta pLysS (DE3) cells and inoculated in LB media with 50 µg mL^{-1} kanamycin. Cultures were induced at OD_{600} = 0.6-0.8. After 16 h of expression under 0.5 mM IPTG at 18°C, the pellets were collected and the re-suspended and lysed in lysis buffer (20 mM Tris-Cl, pH 8.0, 300 mM NaCl, and 5 mM β-mercaptoethanol (BME)). The supernatant was collected after high-speed centrifugation (13,000 rpm, 1 h) and then passed through Ni-resin. The resin was then washed with 3 column volumes (CVs) of wash buffer (20 mM Tris-Cl, pH 8.0, 300 mM NaCl, 10 mM imidazole, and 5 mM BME), and the proteins were eluted by adding 3 CVs of elution buffer (20 mM Tris-Cl, pH 8.0, 300 mM NaCl, 500 mM imidazole, and 5 mM BME). The eluent was collected and supplemented with His_6-tagged Ulp1 [200] (gift of Hideo Iwai, Addgene plasmid #64697), Ubiquitin-like-specific protease 1 (molar ratio SUMO-PKA_{cat} or SUMO-DnaJB1-PKA_{cat}:Ulp1 = 200:1). The solution was dialyzed (20 mM Tris-Cl, pH 8.0, 300 mM NaCl, and 5 mM BME) overnight at 4°C. The cleaved tag, His_6-tagged Ulp1, and uncleaved protein were removed by passing the solution back through the Ni-resin. After collection of the flow-through, the proteins were further purified by S-75 gel filtration in 20 mM MES, pH 6.5, 300 mM NaCl, and 5 mM BME.

To purify EGFP-PKA_{cat}, we constructed pET-His_6-EGFP-PKA_{cat}, which fuses EGFP to His_6 with a -GSS- linker and EGFP to PKA_{cat} with a -GSAGSAAGSGEF- linker . The plasmid was transformed into Rosetta pLysS (DE3) cells and inoculated in LB media with 50 µg mL^{-1} kanamycin. Cultures were induced at OD_{600} = 0.6-0.8. After 16 h of expression under 0.5 mM

IPTG at 18°C, the pellets were collected, re-suspended, and lysed in lysis buffer (20 mM Tris-Cl, pH 8.0, 300 mM NaCl, and 5 mM BME). The supernatant was collected after high-speed centrifugation (13,000 rpm, 1 h) and then passed through Ni-resin. The resin was then washed with 3 CVs of wash buffer (20 mM Tris-Cl, pH 8.0, 300 mM NaCl, 10 mM imidazole, and 5 mM BME), and proteins were eluted by adding 3 CVs of each elution buffer (20 mM Tris-Cl, pH 8.0, 300 mM NaCl, 50 – 500 mM imidazole, and 5 mM BME). After collection of the eluent, the protein was further purified via S-75 gel filtration in 20 mM MES, pH 6.5, 300 mM NaCl, 5 mM BME.

After purification, all proteins were dialyzed into liquid droplet preparation buffer (150 mM KCl, 1 mM $MgCl_2$, 20 mM HEPES, pH 7.0, 1 mM EGTA, 1 mM DTT, 0.5 mM ATP, final pH 7.0) and concentrated using Amicon Ultra-15 centrifugal filters (Millipore). Protein concentrations were measured using the Pierce BCA protein assay kit (Thermo Fisher).

To purify superfolder GFP (sfGFP), the pRSET B sfGFP construct was transformed into *Escherichia coli* BL21 (DE3) cells and inoculated in LB media with 100 μg mL^{-1} ampicillin. Cultures were induced at $OD_{600} = 0.6\text{-}1.0$. After 6 h of expression under 0.5 mM IPTG at 37°C, the cell pellets were collected, re-suspended in lysis buffer (50 mM Tris, pH 7.4, 300 mM NaCl) containing 1 mM PMSF and Complete EDTA-free Protease Inhibitor Cocktail (Roche), and lysed by sonication. Following centrifugation at 25,000 x *g* for 30 min at 4°C, the clarified lysate was loaded onto an Ni-NTA column, washed with wash buffer (50 mM Tris, pH 7.4, 300 mM NaCl, 10 mM imidazole), and then eluted using an imidazole gradient (20-200 mM in lysis buffer). The eluted proteins were then concentrated, and the sfGFP protein concentration was measured via BCA assay and absorbance.

In vitro liquid droplet assays

All liquid droplet formation assays were performed in 150 mM KCl (unless specified), 5 mM $MgCl_2$, 10 μM cAMP (as indicated), 20 mM HEPES, pH 7.0, 1 mM EGTA, 1 mM DTT, 0.5 mM ATP, 100 mg/ml Polyethylene Glycol 4000 (unless specified), and a final pH of 7.0. Purified proteins were incubated at different stoichiometries and at various concentrations at room temperature for 1 h and imaged under DIC and/or fluorescence microscopy.

Fluorescent protein intensity calibration to estimate RIα concentrations

Puncta RIα concentrations were estimated based on calibration of fluorescent protein intensity on the same imaging system used to generate the data shown in Figures 3.1A, 3.1B, and 3.3-3.11. Briefly, known concentrations of purified sfGFP were loaded in glass capilary tubes and imaged under the same illumination conditions used for live-cell imaging experiments. The resulting intensity images were used to construct a standard curve and calculate a calibration constant (i.e., number of sfGFP molecules per camera count) for the system. Using this value, we then estimated the RIα concentration in each fluorescent puncta in each cell based on the measured area and the mean intensity value, assuming spherical puncta.

Fluorescence recovery after photobleaching

Cells were imaged using a Nikon A1R HD confocal with a four-line (405 nm, 488 nm, 561 nm, and 640 nm) LUN-V laser engine and DU4 detector using bandpass and long-pass filters for each channel (450/50, 525/50, 595/50 and 700/75) mounted on a Nikon Ti2 using an Apo 100x 1.49 NA objective and operated using NIS Elements software. Image stacks were acquired in Galvano mode with unidirectional scanning with a 488 nm laser at 1.5% power with a frame size of 512x512 at scan zoom, 1 frame per second (fps), and 97.1 µm pinhole size. Small regions of interest (ROIs) for stimulation were drawn over the punctate structures and in the cytosol. The total FRAP series contained 3 images before bleaching (obtained at 2 s intervals), 2 cycles of ROI bleaching with the 488 nm laser at 100% laser power (5 frames at 1 fps), and 2 min of continuous acquisition to monitor fluorescence recovery.

Time-lapse epifluorescence imaging

Cells were washed twice with HBSS and subsequently imaged in HBSS in the dark at 37°C. Forskolin (Fsk; Calbiochem), 3-isobutyl-1-methylxanthine (IBMX; Sigma), rolipram (Rol; Alexis), myristoylated PKI 14–22 amide (Myr-PKI; Tocris), isoproterenol (Iso; Sigma), and 1,6-hexanediol (Hex; Sigma-Aldrich) were added as indicated. Epifluorescence imaging was performed either on a Zeiss Axiovert 200M microscope (Carl Zeiss) equipped with a xenon lamp, a 40x/1.3 NA objective and a cooled CCD or on a Zeiss AxioObserver Z1 microscope (Carl Zeiss) equipped with a 40x/1.3 NA objective and a Photometrics Evolve 512 EMCCD (Photometrics), both controlled by METAFLUOR 7.7 software (Molecular Devices). For the Zeiss Axiovert 200M, the following excitation/emission filter combinations (center/bandwidth in nm) were used: BFP - EX380/10, EM475/25; CFP - EX420/20, EM475/25; GFP - EX480/30, EM535/45; YFP - EX495/10, EM535/25; RFP - EX568/55, EM653/95; CFP/YFPFRET - EX420/20, EM535/25; GFP/RFPFRET - EX480/30, EM653/95. For the Zeiss AxioObserver Z1, the following excitation/emission filter combinations were used: GFP - EM480/30, EX535/45.

All filter sets were alternated using a Lambda 10-2 filter-changer (Sutter Instruments). Exposure times were 50 (for acceptor direct channel) and 500 ms (for all other channels), with the EM gain set to 20 for the AxioObserver Z1 microscope, and images were acquired every 30 s. All epifluorescence experiments were subsequently analyzed using METAFLUOR 7.7 software. DIC images were acquired on the Zeiss Axiovert 200M microscope. Brightfield images were acquired on an eVos FL cell imaging system (Thermo Fisher).

FRET biosensor analysis

Raw fluorescence images were corrected by subtracting the background fluorescence intensity of a cell-free region from the emission intensities of biosensor-expressing cells. Green/red, red/green, or cyan/yellow emission ratios were then calculated at each time point (R). For some curves, the resulting time courses were normalized by dividing the emission ratio at each time point by the basal ratio value at time zero (R/R_0), which was defined as the emission ratio at the time point immediately preceding drug addition (R_0). Normalized-to-time-zero ratio changes (R/R_0) from drug stimulation ($\Delta R/R_0$ (drug)) were reported for some of the bar graphs and were calculated as ($R_{\mathrm{drug}} - R_0/R_0$), where R_{drug} is the emission ratio at the last time point after the corresponding drug addition. For PDE4D2$_{\mathrm{cat}}$-ICUE4 curves, the resulting time courses were normalized to the maximum ratio change ($\Delta R/\Delta R_{\mathrm{max}}$) by calculating $(R - R_0)/(R_{\mathrm{max}} - R_0)$, where R_{max} is the maximum emission ratio value recorded after all stimulations. Maximum normalized-to-max ratio changes ($\Delta R/\Delta R_{\mathrm{max}}$) from Fsk stimulation (Max $\Delta R/\Delta R_{\mathrm{max}}$ (Fsk)) were reported for the PDE4D2$_{\mathrm{cat}}$-ICUE4 bar graphs and were calculated as $(R_{\mathrm{max\ from\ Fsk}} - R_0)/(R_{\mathrm{max}} - R_0)$, where $R_{\mathrm{max\ from\ Fsk}}$ is the maximum emission ratio value recorded after Fsk addition. Graphs were plotted using GraphPad Prism 7 (GraphPad).

Quantification of puncta

For analysis of puncta number, cell images were individually thresholded and underwent particle analysis with circularity and size cut-offs in Image J.

Apparent diffusivity calculations from fluorescence recovery after photobleaching

The circular FRAP regions were saved and the radius (*r*) was calculated from the area. Time-to-half maximum values ($t_{1/2}$) were acquired from Image J data processing tools. Since the FRAP regions were circular, the apparent diffusivity (D_{app}) is calculated from the following equation [201]:

$$D_{app} = 0.224 \frac{r^2}{t_{1/2}}$$

Statistics and reproducibility

Statistical analyses were performed in GraphPad Prism 7 (GraphPad). All data were assessed for normality. For normally distributed data, pairwise comparisons were performed using unpaired two-tailed Student's t-tests, with Welch's correction for unequal variances used as indicated. Comparisons between three or more groups were performed using ordinary one-way analysis of variance (ANOVA). For data that were not normally distributed, pairwise comparisons were performed using the Mann-Whitney U test, and comparisons between multiple groups were performed using the Kruskal-Wallis test. Statistical significance was set at $P < 0.05$. Average time courses shown in Figures 3.1C, 3.2A, 3.5B-C, 3.5E (curves), 3.5G-H (curves), 3.6A, 3.6B, 3.6D (curve), 3.7B-D (curves), 3.7G-J (curves), 3.8B-D (curves), 3.9, and 3.10E (curves) are representative of at least 3 independently repeated experiments. Average time courses and bar graphs shown in Figures 3.1D, 3.3B, 3.3F, 3.4B-H, 3.5B-H (bar graphs), 3.6C, 3.6D (bar), 3.7B (bar graph), 3.7E, 3.7F-K (bar graphs), 3.8C-D (bar graphs), 3.10B-H (bar graphs), and 3.11E-G combined data sets from at least 3 independent experiments, unless otherwise stated.

Throughout the paper, ****$P < 0.0001$ and ††††$P < 0.0001$. Kruskal-Wallis test followed by Dunn's multiple comparisons test was performed for Figures 3.3B (* vs. wild-type RIα and † vs. Δ(D/D+linker)), 3.10D (†, vs. the corresponding DnaJB1-PKA_{cat} + RIα column), 3.4B (vs. wild-type RIα), and 3.11F (vs. WT). Unpaired two-tailed Student t-tests were performed for Figures 3.5D, 3.5F, 3.6D, 3.7B, 3.7K, and 3.10E, and Welch's correction was applied for Figures 3.5B, 3.5C, 3.5E, 3.5G, 3.5H, 3.7G-I, 3.8B-D, and 3.10B. Unpaired two-tailed Mann-Whitney U-tests were performed for Figures 3.4D, 3.4F, and 3.10D (*, –Fsk vs. +Fsk). Ordinary one-way ANOVA followed by Dunnett's multiple comparisons test was performed for Figures 3.10G, 3.10H, and 3.11G (all vs. WT) and followed by Tukey's multiple comparisons test for Figure 3.7F. A one-sample t-test versus a hypothetical value of 1 was performed for Figure 3.11E. In Figure 3.3B, †$P = 0.0258$. In Figure 3.10D, †$P = 0.0198$, J^{H33Q}-Cat +Fsk vs. J-Cat +Fsk; ††$P = 0.0012$, Myr-J-Cat -Fsk vs. J-Cat -Fsk; ††$P = 0.0021$, Myr-J-Cat +Fsk vs. J-Cat +Fsk; ††$P = 0.0039$, Myr-J^{H33Q}-Cat -Fsk vs. J-Cat -Fsk; ††††$P<0.0001$ vs. J-Cat +Fsk.

Acknowledgments

Chapter 3, in part, has been submitted for publication of the material as it may appear in Cell 2020. Lu, Tsan-Wen; Stolerman, Lucas M; Tenner, Brian; Yang, Jessica; Zhang, Jin-Fan; Falcke, Martin; Rangamani, Padmini; Taylor, Susan S; Mehta, Sohum; Zhang, Jin, Cell 2020.

Jason Zhaoxing Zhang was the first-author of this paper. We thank A. Hong, K.L. Guan, and S. Banerjee for their guidance with CRISPR; E. Griffis and D. Bindels for their confocal microscopy expertise; D.L. Schmitt for help with neuron and glial experiments; C. Brand for help with cardiomyocyte experiments; Y.L. Ma and M. Falcke for insightful discussion; and A. Nguyen and M. Tong for help with cloning.

Chapter 4: FluoSTEPs: Fluorescent biosensors for monitoring compartmentalized signaling within endogenous microdomains

Abstract

Growing evidence suggests many essential intracellular signaling events are compartmentalized within kinetically distinct microdomains in cells. Genetically encoded fluorescent biosensors are powerful tools to dissect compartmentalized signaling, but current approaches to probe these microdomains typically rely on biosensor fusion and overexpression of critical regulatory elements. Here we present a novel class of FRET-based biosensors named FluoSTEPs (Fluorescent Sensors Targeted to Endogenous Proteins) to study compartmentalized signaling dynamics *in situ* using a split biosensor approach. By combining a self-complementing split GFP approach, CRISPR-mediated knock-in, and FRET biosensor technology, we designed these FluoSTEPs for simultaneously highlighting endogenous microdomains and reporting domain-specific, real-time signaling events including kinase activities, GTPase activation, and second messenger dynamics in live cells. A FluoSTEP for 3',5'-cyclic adenosine monophosphate (cAMP) revealed distinct cAMP dynamics within clathrin microdomains in response to stimulation of G-protein coupled receptors (GPCRs), showcasing the utility of FluoSTEPs in probing spatiotemporal regulation within endogenous signaling architectures.

Introduction

Compartmentalization of intracellular signals by macromolecular complexes can reshape the kinetics of cellular processes and provide diversity and specificity in signaling. Our understanding of such microdomain architecture of signaling networks has greatly benefited from the design of genetically encoded fluorescent biosensors[31]. By attaching such sensors to proteins of interest and introducing these fusions to living cells, researchers can monitor compartmentalized signals in real time[26,202–204]. Despite the utility of such biosensors, this fusion strategy has drawbacks primarily stemming from unintended effects from the concomitant overexpression of the proteins of interest. Overexpression of enzymes or scaffolds can disrupt native signaling pathways by causing mislocalization, artificially enhancing/weakening certain biochemical reactions, and imbalancing the stoichiometry of macromolecular interactions. In addition, some biosensors themselves contain enzymatic components known to affect global signaling within the cell. For example, the DORA RhoA sensor for measuring activity of the GTPase RhoA contains active RhoA within a conformational switch[79]; however, overexpression of RhoA is a hallmark of several cancers with associated, downstream signaling effects[205,206]. Strategies have been developed to address the overexpression concerns such as utilizing nanobodies for highlighting endogenous, active receptors and using intrabodies to recruit biosensors to endogenous compartments[207,208]. However, perturbations in trafficking and signaling due to nanobody binding as well as issues of compartment specificity are still ever-present[207,209,210]. Ideally, an approach that combined the strength of quantitative biosensing, specificity of genetic fusions, and minimal perturbation of endogenous proteins of interest would be valuable for dissecting compartmentalized signaling within living cells.

In a recent study of cAMP signaling[24], we introduced a pair of fluorescent biosensors engineered based on a new strategy for probing endogenous microdomains. Here we present the design and characterization of a suite of novel fluorescent biosensors based on this strategy. By utilizing a self-complementing split GFP as a FRET donor, we designed ratiometric sensors that can be recruited and reconstituted at a tagged protein of interest (POI)[211,212], giving rise to Fluorescent Sensors Targeted to Endogenous Proteins, or FluoSTEPs. Generation of the functional biosensors only at a protein of interest ensures compartment specificity, and the self-complementing split GFP donor facilitates endogenous protein tagging. We demonstrate the generalizability of FluoSTEPs by applying the modular design to measure kinase activities, GTPase activation, and second messenger dynamics. We showcase the applicability of FluoSTEPs by deploying the new sensors to uncover mechanisms governing sustained 3'5'-cyclic adenosine monophosphate (cAMP) dynamics at clathrin membrane microdomains after GPCR stimulation.

Results

FluoSTEP-AKAR is reconstituted and functional at microdomains of interest

Our goal with the FluoSTEP design was to construct a logic-gated FRET sensor which exists predominantly in a non-functional (i.e., FRET-incapable) state except when localized to the desired protein target. In order to install a FRET-based sensor with such control logic, we adopted the robust and bright split super-folder GFP (sfGFP) as the FRET donor and an RFP as the FRET acceptor. Split sfGFP is divided between the 10th and 11th β-strands into a pair of non-fluorescent components ($GFP_{1\text{-}10}$ and GFP_{11}) capable of undergoing spontaneous fragment complementation to reconstitute intact, fluorescent sfGFP[212]. Thus, when the small GFP_{11} fragment (16 amino acids) is fused to a POI and expressed in the presence of $GFP_{1\text{-}10}$, reconstitution of the donor fluorophore should occur and give rise to a functional FRET-based sensor only at the POI (Figure 4.1A). This domain-specific logic control allows ratiometric FRET measurements of compartmentalized signaling activities at endogenous protein loci.

We initially applied this concept to generate a FluoSTEP A-kinase Activity Reporter (FluoSTEP-AKAR), in which Protein Kinase A (PKA)-mediated phosphorylation of a kinase-specific substrate domain causes intramolecular binding to the phospho-amino acid binding domain (PAABD) FHA1, resulting in a conformational change that increases FRET between the donor and acceptor fluorescent proteins (FPs) (Figure 4.1A). Specifically, we exchanged the Cerulean (cyan) donor and cpVenus (yellow) acceptor FPs in AKAR4[191] with GFP_{1-10} and mRuby2[189], respectively, to make a complementation-dependent green-red FRET probe (G_{1-10}-R-FluoSTEP-AKAR, Figure 4.1B). Given that FRET efficiency is determined not only by the distance between the donor and acceptor fluorescence transition dipole moments but also by their relative orientation[213], and because the repositioned C-terminus of $sfGFP_{1-10}$ may alter the orientation of the donor analogous to the effect of circular permutation[214], we also tested a variant in which the GFP_{1-10} donor and mRuby2 acceptor were swapped (R-G_{1-10}-FluoSTEP-AKAR; Figure 4.1B).

In HEK293T cells transiently expressing actin C-terminally tagged with GFP_{11} (actin-GFP_{11}), both sensor variants demonstrated the spontaneous reconstitution of GFP fluorescence. Interestingly, however, only the R-G_{1-10}-FluoSTEP-AKAR sensor produced a robust increase in the red/green emission ratio (sensitized acceptor RFP emission due to FRET / direct donor GFP emission) after the addition of the transmembrane adenylyl cyclase (AC) activator forskolin (Fsk, 50 μM) and the phosphodiesterase (PDE) inhibitor IBMX (100 μM) (normalized ratio

Figure 4.1: FluoSTEP-AKAR is reconstituted and functional at microdomains of interest (**A**) Fluorescent Sensors Targeted to Endogenous Proteins (FluoSTEPs) utilize the spontaneous fragment complementation of split sfGFP to reconstitute a functional FRET-based biosensor at a protein of interest (POI) expressed at endogenous levels, as shown here with a kinase activity reporter. Probe species that fail to reconstitute contain a non-fluorescent donor and thus do not contribute to the FRET signal. (**B**) Domain structures of actin-GFP$_{11}$, G$_{1\text{-}10}$-R-FluoSTEP-AKAR (V1), and R-G$_{1\text{-}10}$-FluoSTEP-AKAR (V2). (**C**) Average red/green (R/G) emission ratio time courses (left) and maximum emission ratio changes (right) in HEK293T cells expressing actin-GFP$_{11}$ plus either G$_{1\text{-}10}$-R-FluoSTEP-AKAR (V1, teal, n = 12 cells) or R-G$_{1\text{-}10}$-FluoSTEP-AKAR (V2, green, n = 18 cells) following stimulated with 50 μM Fsk and 100 μM IBMX (Fsk/IBMX). (**D** and **E**) Top: Average R/G emission ratio time courses (left) or maximum emission ratio change (right) in HeLa cells expressing actin-GFP$_{11}$ (**D**) or clathrin-GFP$_{11}$ (**E**) plus either FluoSTEP-AKAR (green curves; actin: n = 13 cells; clathrin: n = 8 cells) or FluoSTEP-AKAR (T/A) negative control (gray curves; actin: n = 15 cells; clathrin: n = 21 cells) upon stimulation with Fsk/IBMX followed by 10 μM H89. Bottom: Representative confocal fluorescence images depicting the localization of biosensor fluorescence in the GFP (left) and RFP (middle) channels. Insets are enlarged from the outlined regions. Line-profile intensity plots (right) highlight co-localization of the fluorescence signals along the indicated region. ****$P < 0.0001$; unpaired two-tailed Student's t-test. Solid lines in time-courses indicate average responses; shaded areas, SEM. Horizontal lines in scatter plots indicate mean ± SEM. Scale bars, 10 μm (inset, 1 μm).

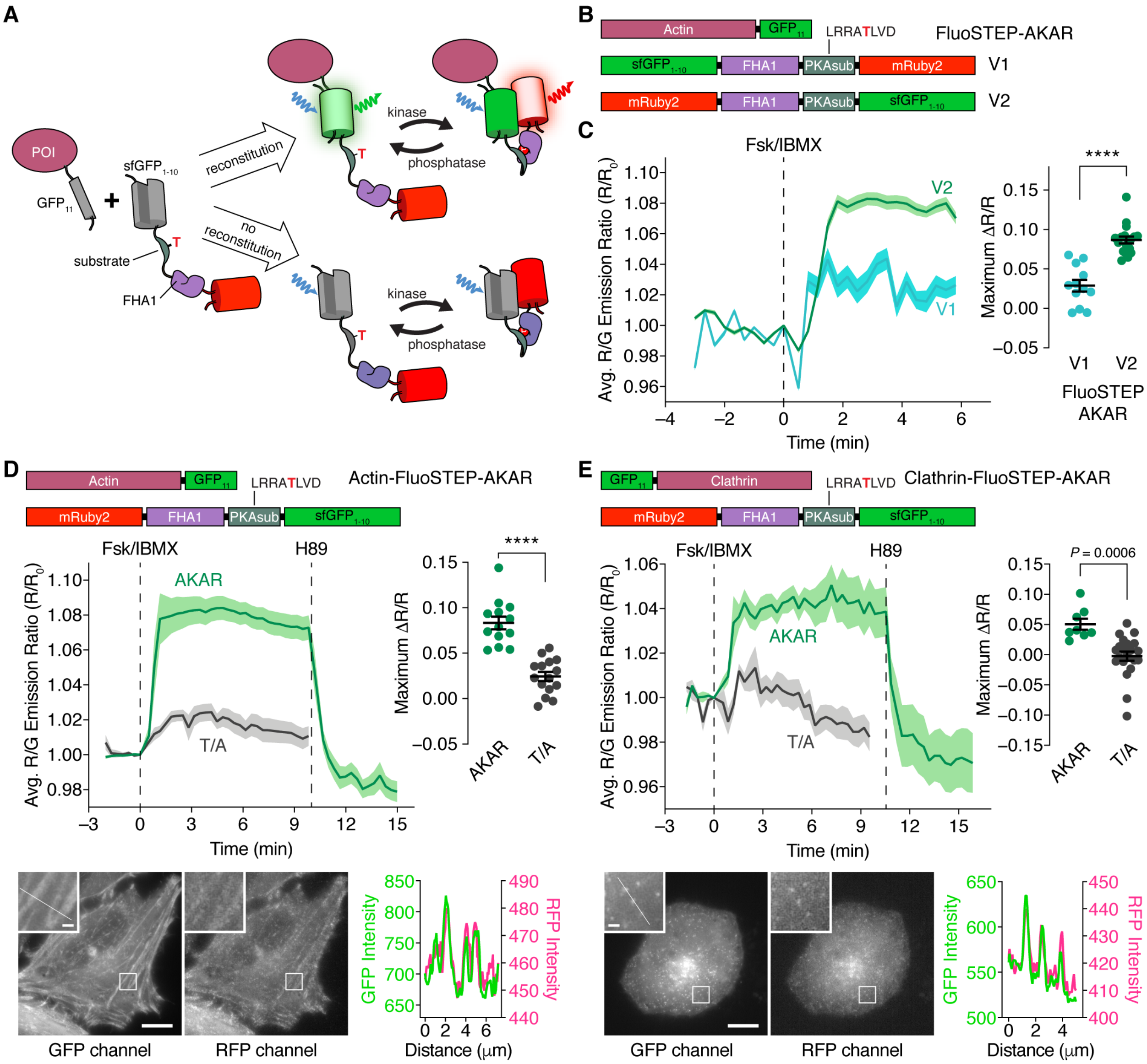
A
POI
GFP_{11}
+
$sfGFP_{1-10}$
T
substrate
FHA1
reconstitution
no reconstitution
kinase
phosphatase
kinase
phosphatase
T
T
B
Actin
GFP_{11}
LRRATLVD
FluoSTEP-AKAR
$sfGFP_{1-10}$
FHA1
PKAsub
mRuby2
V1
mRuby2
FHA1
PKAsub
$sfGFP_{1-10}$
V2
C
Fsk/IBMX
Avg. R/G Emission Ratio (R/R_0)
1.10
1.08
1.06
1.04
1.02
1.00
0.98
0.96
V2
V1
–4
–2
0
2
4
6
Time (min)
****
Maximum ΔR/R
0.15
0.10
0.05
0.00
–0.05
V1
V2
FluoSTEP AKAR
D
Actin
GFP_{11}
LRRATLVD
Actin-FluoSTEP-AKAR
mRuby2
FHA1
PKAsub
$sfGFP_{1-10}$
Fsk/IBMX
H89
AKAR
T/A
Avg. R/G Emission Ratio (R/R_0)
1.10
1.08
1.06
1.04
1.02
1.00
0.98
–3
0
3
6
9
12
15
Time (min)
****
Maximum ΔR/R
0.15
0.10
0.05
0.00
–0.05
AKAR
T/A
GFP channel
RFP channel
GFP Intensity
850
800
750
700
650
RFP Intensity
490
480
470
460
450
440
0
2
4
6
Distance (μm)
E
GFP_{11}
Clathrin
LRRATLVD
Clathrin-FluoSTEP-AKAR
mRuby2
FHA1
PKAsub
$sfGFP_{1-10}$
Fsk/IBMX
H89
AKAR
T/A
Avg. R/G Emission Ratio (R/R_0)
1.06
1.04
1.02
1.00
0.98
0.96
–3
0
3
6
9
12
15
Time (min)
P = 0.0006
Maximum ΔR/R
0.15
0.10
0.05
0.00
–0.05
–0.10
–0.15
AKAR
T/A
GFP channel
RFP channel
GFP Intensity
650
600
550
500
RFP Intensity
450
440
430
420
410
400
0
2
4
Distance (μm)

change [ΔR/R] = 8.7% ± 0.44% [mean ± SEM], n = 18 cells) (Figure 4.1C). The $G_{1\text{-}10}$-R-FluoSTEP-AKAR sensor generated a smaller Fsk/IBMX-induced response compared to its counterpart (ΔR/R = 2.9% ± 0.74%, n = 12 cells, $P < 0.0001$). This observation is consistent with the critical role of the relative orientations of the donor/acceptor fluorescence transition dipole moments in the performance of FRET-based biosensors[215].

To further characterize R-$G_{1\text{-}10}$-FluoSTEP-AKAR, which we renamed FluoSTEP-AKAR, in another cell type, we co-expressed the sensor with actin-GFP_{11} in HeLa cells. Confocal fluorescence imaging revealed proper targeting of the biosensor to actin, as shown by the actin cytoskeletal structure visible in both the GFP and RFP channels (Figure 4.1D). After Fsk/IBMX stimulation, FluoSTEP-AKAR also produced a robust increase in red/green emission ratio in these cells (ΔR/R = 8.3% ± 0.70% increase, n = 13 cells). Subsequent addition of the PKA inhibitor H89 (10 μM) acutely reversed the emission ratio change, while mutating the phospho-acceptor threonine residue in FluoSTEP-AKAR to alanine (T/A) largely abolished the emission ratio change induced by Fsk/IBMX stimulation (ΔR/R = 2.4% ± 0.50%, n = 15 cells, $P < 0.0001$), highlighting the specificity of the response (Figure 4.1D). To test recruitment and functioning at a different POI, we co-expressed FluoSTEP-AKAR with GFP_{11}-tagged clathrin (clathrin-GFP_{11}) in HeLa cells and observed GFP reconstitution via confocal fluorescence microscopy, which highlighted clathrin microdomains along the plasma membrane (Figure 4.1E). Similar to the actin-targeted sensor, Fsk/IBMX stimulation triggered a robust increase in the FluoSTEP-AKAR red/green emission ratio (ΔR/R = 5.1% ± 0.92%, n = 8 cells), which was acutely reversed upon H89 addition, while the FluoSTEP-AKAR (T/A) negative control construct showed no response to Fsk/IBMX treatment (ΔR/R = –0.24 ± 0.76%, n = 21 cells)

(Figure 4.1E). Our complementation-dependent biosensor design thus enables robust activity measurements around specific POIs with minimal disruption of molecular organization.

The FluoSTEP design can be generalized to probe multiple targets

Many FRET-based biosensors are generated based on a modular design where a signal-specific conformational switch is sandwiched between a FRET pair of FPs. This modular architecture facilitates the straightforward assembly of a suite of sensors for detecting different biological activities by simply swapping out the signal-specific switch domain[216]. We therefore took advantage of this feature to expand the FluoSTEP arsenal. For instance, most sensors designed to probe 3’,5’-cyclic adenosine monophosphate (cAMP), the upstream regulator of PKA and a second messenger with diverse regulatory roles[217], utilize the conformational change induced by the binding of cAMP to a single protein domain[218,219] to modulate FRET between flanking FPs. Thus, to construct a FluoSTEP cAMP sensor, we tested two different cAMP-binding switches derived from the cAMP-binding domains of Epac isoforms, Epac2B (285-443)[29] and Epac1 (149-881)[29,220], inserted between mRuby2 and GFP_{1-10} (Figure 4.2). Only the sensor containing Epac1 (149-881) produced an increase in the green/red emission ratio ($\Delta R/R$ = 4.1% ± 0.63%, n = 15 cells) upon Fsk/IBMX addition in HEK293T cells co-expressing actin-GFP_{11} and was thus named FluoSTEP-ICUE (Indicator of cAMP using Epac) (Figures 4.2 and 4.3A). As a negative control, Epac1’s cAMP-binding site was mutated (R279E). When co-expressed with actin-GFP_{11}, FluoSTEP-ICUE (R279E) produced no change in emission ratio after Fsk/IBMX stimulation ($\Delta R/R$ = 0.52% ± 0.46%, n = 22 cells, $P < 0.0001$) (Figure 4.3A).

In addition to PKA, many kinases are organized in macromolecular complexes and

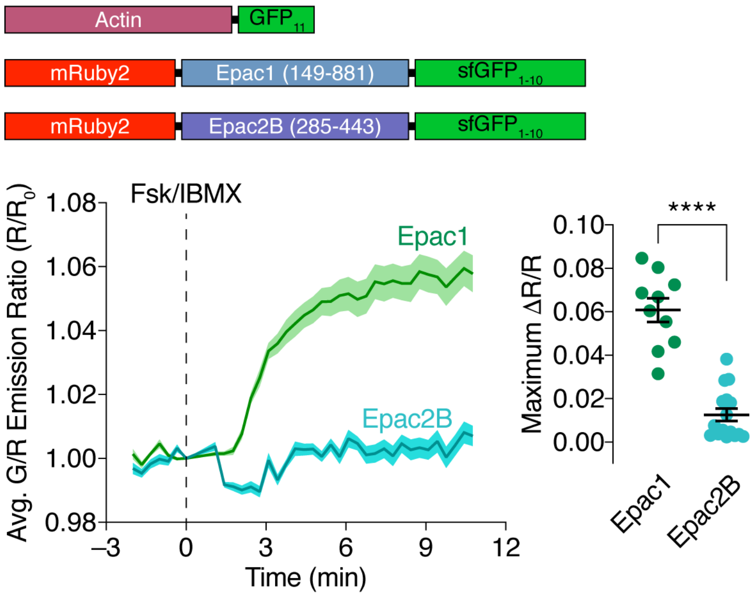

Figure 4.2: Development and testing of a FluoSTEP cAMP sensor
(top) Domain structures of actin-GFP$_{11}$, FluoSTEP-Epac1 (149-881) (also named FluoSTEP-ICUE), and FluoSTEP-Epac2B (285-443). (bottom) Representative average time courses (left) and maximum green/red emission ratio changes (right) in HEK293T cells co-expressing actin-GFP11 plus either FluoSTEP-Epac1 (149-881) (Epac1, green curve; n = 25 cells) or FluoSTEP-Epac2B (285-443) (Epac2B, teal curve; n = 16 cells) and stimulated with 50 µM Fsk and 100 µM IBMX (Fsk/IBMX). Solid lines in time courses indicate average responses; shaded areas, SEM. ****$P < 0.0001$; unpaired two-tailed Student's t-test.

Figure 4.3: The FluoSTEP design can be generalized to probe multiple targets
(**A**) (top) Domain structure of actin-targeted FluoSTEP-ICUE. (bottom) HEK293T cells expressing actin-GFP$_{11}$ plus either FluoSTEP-ICUE (green; n = 15 cells) or FluoSTEP-ICUE (R279E) negative control (gray; n = 22 cells) were stimulated 50 μM Fsk and 100 μM IBMX (Fsk/IBMX). Average green/red (G/R) emission ratio time courses (left) and maximum emission ratio changes (right) upon Fsk/IBMX stimulation are shown. (**B**) (top) Domain structure of actin-targeted FluoSTEP-AktAR. (bottom) NIH3T3 cells expressing actin-FP$_{11}$ plus either FluoSTEP-AktAR (blue; n = 31 cells) or FluoSTEP-AktAR (T/A) negative control (gray; n = 8 cells) were stimulated with 50 ng/mL PDGF. Average red/green (R/G) emission ratio time courses (left) and maximum emission ratio changes (right) upon PDGF stimulation are shown. (**C**) (top) Domain structure of actin-targeted FluoSTEP-JNKAR. (bottom) HeLa cells expressing actin-GFP$_{11}$ plus either FluoSTEP-JNKAR (orange; n = 11 cells) or FluoSTEP-JNKAR (T/A) negative control (gray; n = 5 cells) were stimulated 5 μM anisomycin. Average R/G emission ratio time courses (left) and maximum emission ratio changes (right) upon anisomycin stimulation are shown. (**D**) (top) Domain structure of actin-targeted FluoSTEP-EKAR. (bottom) HEK293T cells expressing actin-GFP$_{11}$ plus either FluoSTEP-EKAR (red; n = 71 cells) or FluoSTEP-EKAR (T/A) negative control (gray; n = 28 cells) were stimulated 100 ng/mL EGF. Average R/G emission ratio time courses (left) and maximum emission ratio changes (right) upon EGF stimulation are shown. (**E**) Schematic and domain structure of FluoSTEP-RhoA, which involves the binding of GFP$_{11}$-RhoA to cpPKN-mRuby2-GFP$_{1-10}$ to reconstitute the functional biosensor. (**F**) Average G/R emission ratio time courses (left) and maximum emission ratio change (right) in HEK293T cells expressing either FluoSTEP-RhoA (purple curve; n = 42 cells) or FluoSTEP-RhoA (L59Q) negative control (gray curve; n = 24 cells) stimulated 100 μM Histamine. $P < 0.0001$; unpaired two-tailed Student's t-test without (**A**, **B**, and **F**) or with (**C** and **D**) Welch's correction. Solid lines in time courses indicate average responses; shaded areas, SEM. Horizontal lines in scatter plots indicate mean ± SEM.

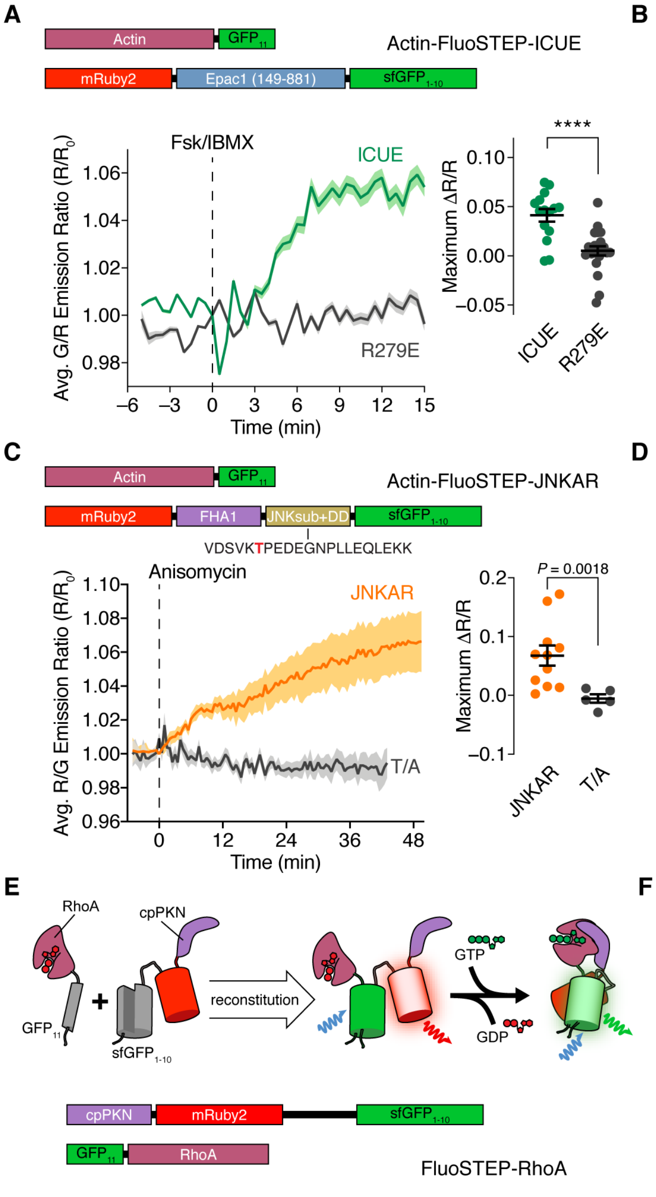
A
Actin
GFP11
Actin-FluoSTEP-ICUE
mRuby2
Epac1 (149-881)
sfGFP1-10
Fsk/IBMX
ICUE
R279E
Avg. G/R Emission Ratio (R/R0)
Time (min)
Maximum ΔR/R
****
ICUE
R279E
B
Actin
GFP11
Actin-FluoSTEP-AktAR
mRuby2
FHA1
AKTsub
sfGFP1-10
PRPRSCTWPDPRPEF
PDGF
AktAR
T/A
Avg. R/G Emission Ratio (R/R0)
Time (min)
Maximum ΔR/R
P = 0.0002
AktAR
T/A
C
Actin
GFP11
Actin-FluoSTEP-JNKAR
mRuby2
FHA1
JNKsub+DD
sfGFP1-10
VDSVKTPEDEGNPLLEQLEKK
Anisomycin
JNKAR
T/A
Avg. R/G Emission Ratio (R/R0)
Time (min)
Maximum ΔR/R
P = 0.0018
JNKAR
T/A
D
Actin
GFP11
Actin-FluoSTEP-EKAR
mRuby2
WW
ERKsub+DD
sfGFP1-10
PDVPRTPVGKFQFP
EGF
EKAR
T/A
Avg. R/G Emission Ratio (R/R0)
Time (min)
Maximum ΔR/R
P = 0.0003
EKAR
T/A
E
RhoA
cpPKN
GFP11
sfGFP1-10
reconstitution
GTP
GDP
cpPKN
mRuby2
sfGFP1-10
GFP11
RhoA
FluoSTEP-RhoA
F
Histamine
RhoA
L59Q
Avg. G/R Emission Ratio (R/R0)
Time (min)
Maximum ΔR/R
P = 0.0035
RhoA
L59Q

subcellularly targeted in order to tune signaling kinetics and target specificity[221]. For example, compartmentalization of Akt kinase and C-jun N-terminal kinase (JNK), two kinases important within cellular survival and stress pathways, has been uncovered using FRET-based biosensors[178,222,223]. By simply swapping out the PKA substrate domain for the substrate sequences corresponding to Akt and JNK, we created FluoSTEP versions of the previously published AktAR [222] (Akt Activity Reporter) and JNKAR[223] (JNK Activity Reporter), respectively. Upon activation of Akt via PDGF (50 ng/mL) in NIH3T3 fibroblasts expressing actin-GFP_{11}, FluoSTEP-AktAR produced a 6.0% ± 0.90% increase in the red/green emission ratio ($\Delta R/R$, n = 31 cells), while the non-phosphorylatable T/A mutant was nonresponsive ($\Delta R/R = -1.9\% \pm 1.2\%$, n = 8 cells, $P = 0.0002$) (Figure 4.3B). Similarly, upon stimulation of JNK activity with anisomycin (5 μM), HeLa cells expressing actin-GFP_{11} and FluoSTEP-JNKAR showed a 6.8% ± 1.7% increase in the red/green emission ratio ($\Delta R/R$, n = 11 cells), in contrast to cells expressing actin-GFP_{11} plus the non-phosphorylatable T/A mutant ($\Delta R/R = -0.54\% \pm 0.73\%$, n = 5 cells, $P = 0.0018$) (Figure 4.3C). Other FRET-based kinase sensors utilize different substrate and PAABD pairs for the conformational switch. A FluoSTEP-EKAR (Erk Kinase Activity Reporter) for Erk, a kinase essential in cell growth and differentiation, was also created by utilizing an Erk substrate/docking domain sequence, phospho-amino acid binding WW domain, and extended linker (EV)[224]. In HEK293T cells co-expressing actin-GFP_{11} and stimulated with EGF to activate Erk (100 ng/mL), FluoSTEP-EKAR produced a 5.6% ± 0.99% increase in the red/green emission ratio ($\Delta R/R$, n = 71 cells) (Figure 4.3D). As a negative control, the non-phosphorylatable T/A mutant version, FluoSTEP EKAR (T/A), showed no response ($\Delta R/R = 1.5\% \pm 0.49\%$, n = 28 cells, $P = 0.0003$).

Enzyme activation biosensors often incorporate the targets of interest within their design architecture[225], which can cause side effects from overexpression[89]. Thus, we hypothesize FluoSTEPs could help untangle this dependence by uncoupling the expression of the target of interest from the rest of the sensor. As a prototype, we used the DORA RhoA sensor which measures the activation of RhoA, a small GTPase important in cytoskeletal regulation, by transducing a binding event between GTP-bound RhoA and the interactor domain cpPKN into an increase in FRET[79]. We created a FluoSTEP version of this RhoA activation sensor by splitting the sensor into two parts: one part containing the cpPKN interactor domain and the two FPs (split sfGFP and mRuby2), with an EV linker separating the FPs, and the other containing full-length RhoA tagged with GFP_{11} at its N-terminus, similar to the organization of DORA RhoA (Figure 4.3E). Expression of both parts reconstitutes the donor GFP to engage in FRET (Figure 4.3E). Interestingly, the FluoSTEP architecture for this sensor reversed the activity-induced FRET change, therefore we plotted the FluoSTEP-RhoA response as the increase in green/red emission ratio. Upon stimulation of RhoA activity with histamine (100 μM) in HeLa cells, FluoSTEP-RhoA exhibited a 4.4% ± 0.95% increase in the green/red emission ratio ($\Delta R/R$, n = 42 cells). In comparison, a FluoSTEP-RhoA (L59Q) negative control in which the cpPKN interactor domain was mutated to prevent binding to RhoA-GTP showed no response to histamine stimulation ($\Delta R/R = -0.20\% \pm 1.2\%$, n = 24 cells, $P = 0.0035$; Figure 4.3E). The design of FluoSTEP-RhoA could potentially be adapted for endogenous tagging of RhoA with GFP_{11} and thus offer a strategy for monitoring RhoA activation at the endogenous level.

Variants of FluoSTEP to increase dynamic range and brightness

Having established the FluoSTEP design as a general approach for probing localized signaling activities, we next explored various strategies to improve biosensor performance, using FluoSTEP-AKAR as a template. We first exchanged the split sfGFP donor for a brighter, split version of mNeonGreen with an orthogonal FP_{11} tag attached to clathrin[226] and tested the variant in HEK293T cells; however, we observed a smaller dynamic range (mNeonGreen: 4.1% ± 0.30%, n = 9 cells; sfGFP: 11% ± 1.4%, n = 6 cells; $P < 0.0001$) (Figure 4.4A). We also replaced the mRuby2 acceptor in FluoSTEP-AKAR with brighter RFPs such as mRuby3[227] or mScarlet-I[228] and tested these variants with actin-$GFP_{11.}$ While the mRuby3-containing construct failed to produce a discernable response ($\Delta R/R$ = 2.2% ± 0.98%, n = 7 cells) (Figure 4.4A), mScarlet-I did yield a sensor with an approximately 2-fold increased dynamic range versus the mRuby2 version ($\Delta R/R$ = 19% ± 0.38%, n = 27 cells, $P < 0.0001$) (Figures 4.4A and 4.5A) However, we observed that the mScarlet-I sensor exhibited a strong, diffuse green signal even in the absence of GFP donor reconstitution (Figures 4.4B and C) possibly due to direct excitation of the bright mScarlet-I FP or incomplete fluorophore maturation[228], which could be mitigated by applying calibration or choosing alternative imaging conditions.

We then tested whether different FluoSTEP color variants can be developed for multiplexed applications. The donor $GFP_{1\text{-}10}$ was exchanged for two previously described sfGFP color variants[229]: $YFP_{1\text{-}10}$ and $CFP_{1\text{-}10}$. We created a yellow-red version of FluoSTEP-AKAR by using $YFP_{1\text{-}10}$ as the donor and mRuby2 as the acceptor and a cyan-yellow version of FluoSTEP-AKAR by using $CFP_{1\text{-}10}$ as the donor and cpVenus from AKAR4 as the acceptor. In HEK293T cells co-expressing actin-GFP_{11} and stimulated with Fsk/IBMX, cyan-yellow FluoSTEP-AKAR yielded a robust response ($\Delta R/R$ = 9.1% ± 1.2%, n = 17 cells), while the response from the

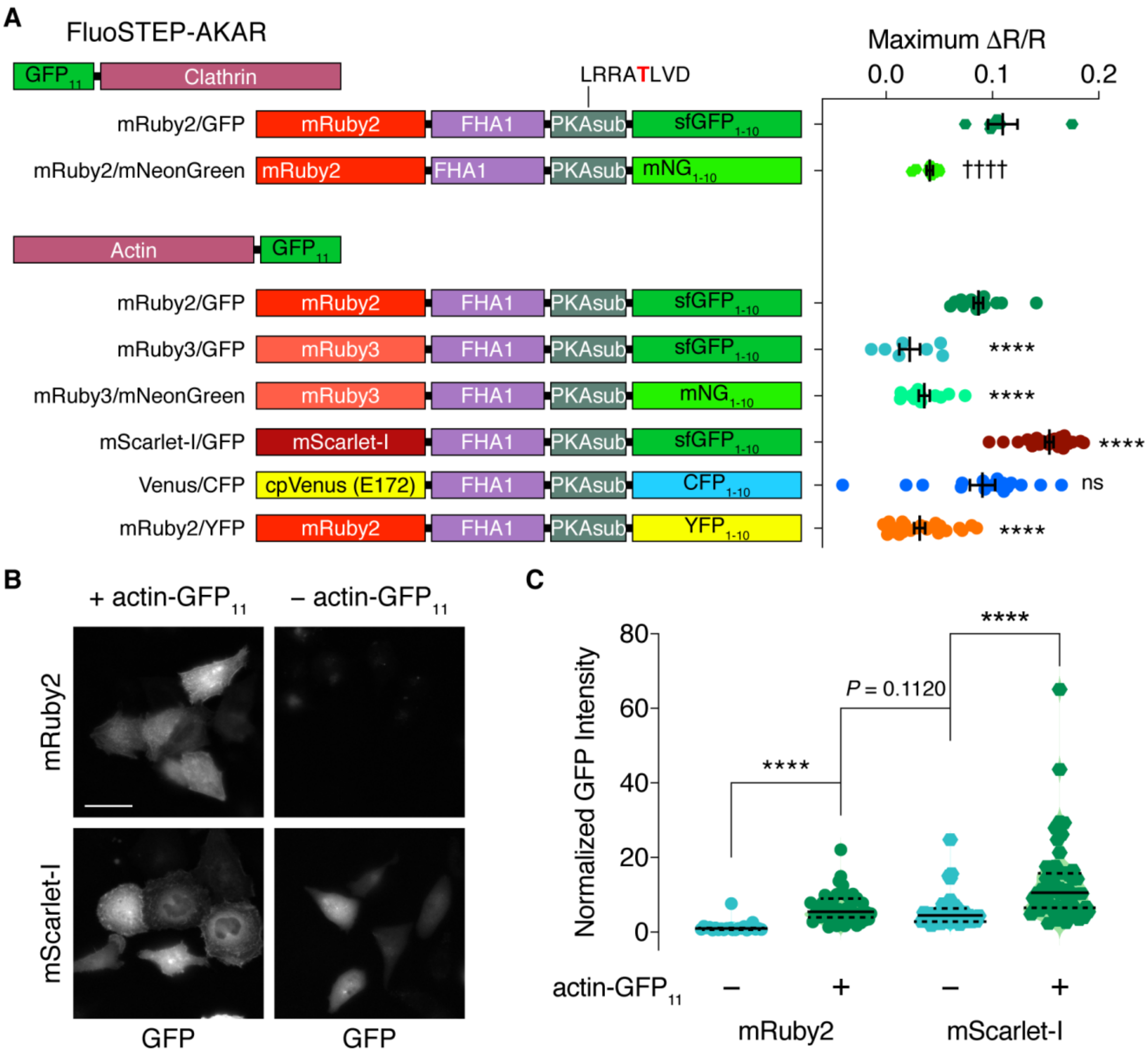

Figure 4.4: FluoSTEP-AKAR performance using various donor and acceptor FPs
(**A**) Domain structure of FluoSTEP-AKAR variants (left) and maximum emission ratio changes (right) in HEK293T cells co-expressing or clathrin-GFP$_{11}$ plus FluoSTEP-AKAR mRuby2/GFP (n = 6 cells) or mRuby2/mNeonGreen (n = 9 cells) or co-expressing actin-GFP$_{11}$ plus FluoSTEP-AKAR mRuby2/GFP (n = 18 cells), mRuby3/GFP (n = 7 cells), mRuby3/mNeonGreen (n = 12 cells), mScarlet-I/GFP (n = 27 cells), Venus/CFP (n = 17 cells), or mRuby2/YFP (n = 26 cells) and stimulated with 50 µM Fsk and 100 µM IBMX. $^{\dagger\dagger\dagger\dagger}P < 0.0001$; unpaired two-tailed Student’s t-test. *****P* < 0.0001 vs. FluoSTEP-AKAR mRuby2/GFP with actin-GFP$_{11}$; ordinary one-way ANOVA followed by Dunnet’s test for mulitple comparisons. ns, not significant. (**B**) Representative GFP fluorescence images and (**C**) normalized GFP fluorescence intensity of HEK293T cells expressing FluoSTEP-AKAR mRuby2/GFP or mScarlet-I/GFP in either the presence or absence of actin-FP$_{11}$. FluoSTEP-AKAR mRuby2/GFP: + actin-GFP$_{11}$, n = 44; −actin-GFP$_{11}$, n = 23; FluoSTEP-AKAR mScarlet-I/GFP: + actin-GFP$_{11}$, n = 51; −actin-GFP$_{11}$, n = 36. Scale bar, 40 µm. *****P* < 0.0001; unpaired, two-tailed Mann-Whitney U-test.

Figure 4.5: Variants of FluoSTEP to improve dynamic range
(**A**) (top) Domain structures of actin-GFP$_{11}$ and FluoSTEP-AKAR containing either mRuby2 (Ruby) or mScarlet-I (Scarlet) as the FRET acceptor. Average R/G emission ratio time courses (left) and maximum emission ratio changes (right) in HEK293T cells co-expressing actin-GFP$_{11}$ plus either FluoSTEP-AKAR "Ruby" (red; n = 14 cells) or FluoSTEP-AKAR "Scarlet" (dark red; n = 27 cells) upon Fsk/IBMX stimulation. Solid lines in time courses indicate average responses; shaded areas, SEM. Horizontal lines in scatter plots indicate mean ± SEM. (**B**) Tagging a POI with multiple tandem copies of GFP$_{11}$ to recruit multiple copies of GFP$_{1\text{-}10}$. (**C**) Comparison of normalized GFP intensity in HeLa cells co-expressing FluoSTEP-AKAR (left) or FluoSTEP-ICUE (right) plus either actin-GFP$_{11}$(×1) (teal) or actin-GFP$_{11}$(×7) (green). AKAR: n = 25 cells each; ICUE: n = 10 (×1) and 17 (×7). Solid and dashed lines indicate the median and quartiles, respectively. Raw fluorescence intensity values were normalized to the median intensity of the GFP$_{11}$(×1) group. (**D**) (top) Domain structures of actin-GFP$_{11}$(×n) and FluoSTEP-AKAR. Average red/green (R/G) emission ratio time courses (left) and maximum emission ratio changes (right) in HeLa cells co-expressing FluoSTEP-AKAR plus either actin-GFP$_{11}$(×1) (teal; n = 13 cells) or actin-GFP$_{11}$(×7) (green; n = 5 cells) after stimulation with 50 μM Fsk and 100 μM IBMX (Fsk/IBMX). (**E**) (top) Domain structures of actin-GFP$_{11}$(×n) and FluoSTEP-ICUE. Average green/red (G/R) emission ratio time courses (left) and maximum emission ratio changes (right) in HEK293T cells co-expressing FluoSTEP-ICUE plus either actin-GFP$_{11}$(×1) (teal; n = 10 cells) or actin-GFP$_{11}$(×7) (green; n = 17 cells) upon Fsk/IBMX stimulation. ****$P < 0.0001$; unpaired two-tailed Student's t-test (**A**, **D**, and **E**) or Mann-Whitney U-test (**C**).

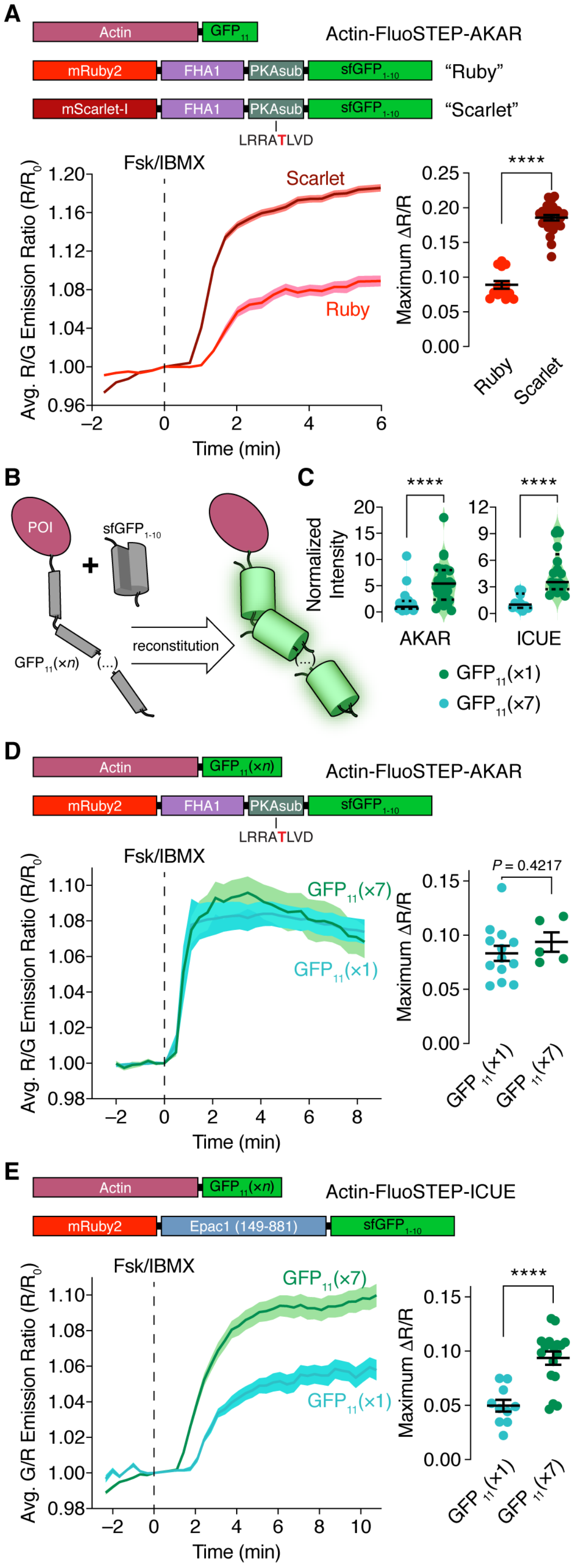
A
Actin
GFP11
Actin-FluoSTEP-AKAR
mRuby2
FHA1
PKAsub
sfGFP1-10
"Ruby"
mScarlet-I
FHA1
PKAsub
sfGFP1-10
"Scarlet"
LRRATLVD
Fsk/IBMX
Scarlet
Ruby
Avg. R/G Emission Ratio (R/R0)
1.20
1.16
1.12
1.08
1.04
1.00
0.96
−2
0
2
4
6
Time (min)
****
Maximum ΔR/R
0.25
0.20
0.15
0.10
0.05
0.00
Ruby
Scarlet
B
POI
sfGFP1-10
+
GFP11(×n)
(...)
reconstitution
C
Normalized Intensity
20
15
10
5
0
12
9
6
3
0
****
****
AKAR
ICUE
● GFP11(×1)
● GFP11(×7)
D
Actin
GFP11(×n)
Actin-FluoSTEP-AKAR
mRuby2
FHA1
PKAsub
sfGFP1-10
LRRATLVD
Fsk/IBMX
GFP11(×7)
GFP11(×1)
Avg. R/G Emission Ratio (R/R0)
1.10
1.08
1.06
1.04
1.02
1.00
0.98
−2
0
2
4
6
8
Time (min)
P = 0.4217
Maximum ΔR/R
0.15
0.10
0.05
0.00
GFP11(×1)
GFP11(×7)
E
Actin
GFP11(×n)
Actin-FluoSTEP-ICUE
mRuby2
Epac1 (149-881)
sfGFP1-10
Fsk/IBMX
GFP11(×7)
GFP11(×1)
Avg. G/R Emission Ratio (R/R0)
1.10
1.08
1.06
1.04
1.02
1.00
0.98
−2
0
2
4
6
8
10
Time (min)
****
Maximum ΔR/R
0.15
0.10
0.05
0.00
GFP11(×1)
GFP11(×7)

yellow-red FluoSTEP-AKAR variant was weaker ($\Delta R/R = 3.2\% \pm 0.51\%$, n = 26 cells) (Figure 4.4A). Fluorescence intensity is particularly important for targeted biosensing at endogenous proteins expressed at low levels; thus, we set out to increase the brightness of our sensors. The split GFP system offers a unique approach for boosting the fluorescent signal by fusing multiple copies of the small GFP_{11} tag in tandem[229]. We hypothesized that a similar strategy could be utilized to recruit multiple FluoSTEP copies and thus amplify the fluorescence intensity[219] (Figure 4.5B). Indeed, we found that co-expressing actin fused to a seven-copy array of GFP_{11} (actin-GFP_{11}(×7)) along with FluoSTEP-AKAR in HeLa cells yielded an over 5-fold increase in the brightness of the GFP channel versus actin-GFP_{11}(×1) ($P < 0.0001$, n = 25 cells) (Figure 4.5C), without affecting the Fsk/IBMX-induced response (actin-GFP_{11}(×1): $\Delta R/R = 8.3\% \pm 0.70\%$, n = 13 cells; actin-$GFP_{11}$(×7): $\Delta R/R = 9.4\% \pm 0.90\%$, n = 5 cells, $P = 0.4217$; Figure 4.5D). The same strategy was applied to FluoSTEP-ICUE. By using an array of GFP_{11} tags, we achieved a 3.6-fold enhancement in the brightness of the GFP channel ($P < 0.0001$, n = 17) (Figure 4.5C). Interestingly, we also observed a 1.9-fold enhancement in the dynamic range of FluoSTEP-ICUE when co-expressed with the GFP_{11} array (actin-GFP_{11}(×1): $\Delta R/R = 6.1\% \pm 0.54\%$, n = 10 cells; actin-$GFP_{11}$(×7): $\Delta R/R = 10\% \pm 0.64\%$, n = 17 cells; $P < 0.0001$) (Figure 4.5E). Together, these data indicate that recruiting an array of biosensors to a POI can be used to enhance the brightness of FluoSTEPs without degrading probe sensitivity.

Endogenous signaling compartments are accessible by FluoSTEPs

In order to test the compartment-specific FluoSTEPs in an endogenous context, we sought to knock-in GFP_{11} at a specific genomic locus in HEK293T cells. Due to the small size of GFP_{11}, knock-in via CRISPR and HDR with a single-stranded oligonucleotide donor is efficient and versatile and can theoretically be extended to multiple genomic loci of interest[229,230]. We previously used FluoSTEP-AKAR and FluoSTEP-ICUE to measure the PKA activities and cAMP levels in endogenous RIα phase-separated bodies[24], highlighting the utility of our FluoSTEP sensors. To showcase the versatility of our FluoSTEP sensors at endogenous POIs, we chose to measure cAMP and PKA dynamics around clathrin, which has a role in regulating cAMP/PKA signaling as this scaffold protein is important in the early steps of endocytosis of receptors such as G-protein coupled receptors (GPCR). During endocytosis, clathrin coated pits form at the plasma membrane[231], which appear visually as discrete puncta[232]. When we expressed either FluoSTEP-AKAR or FluoSTEP-ICUE in CLTA-FP11[229], a HEK293T cell line in which the GFP_{11} tag is knocked-in to the gene for the clathrin light chain A (CLTA), the donor GFP was reconstituted and distinct clathrin-containing microdomains were observed, indicating correct probe localization (Figures 4.6 A and E). The dynamic range of FluoSTEP-AKAR localized at endogenous clathrin was not negatively impacted compared to the overexpression case, as Fsk/IBMX treatment reliably induced a rapid 16% ± 0.91% increase in the red/green emission ratio ($\Delta R/R$, n = 33 cells), which completely returned to baseline levels upon subsequent addition of H89 (Figure 4.6 B and D). Similarly, treating FluoSTEP-ICUE-expressing CLTA-FP11 cells with Fsk/IBMX successfully triggered a rapid 12% ± 1.1% increase in the green/red emission ratio ($\Delta R/R$, n = 19 cells), demonstrating the utility of FluoSTEPs to monitor cAMP levels at clathrin microdomains (Figures 4.6 C and D). Taken together, these results confirm the utility of FluoSTEPs as a platform for monitoring compartmentalized signaling dynamics near specific target proteins expressed at endogenous levels from their native loci.

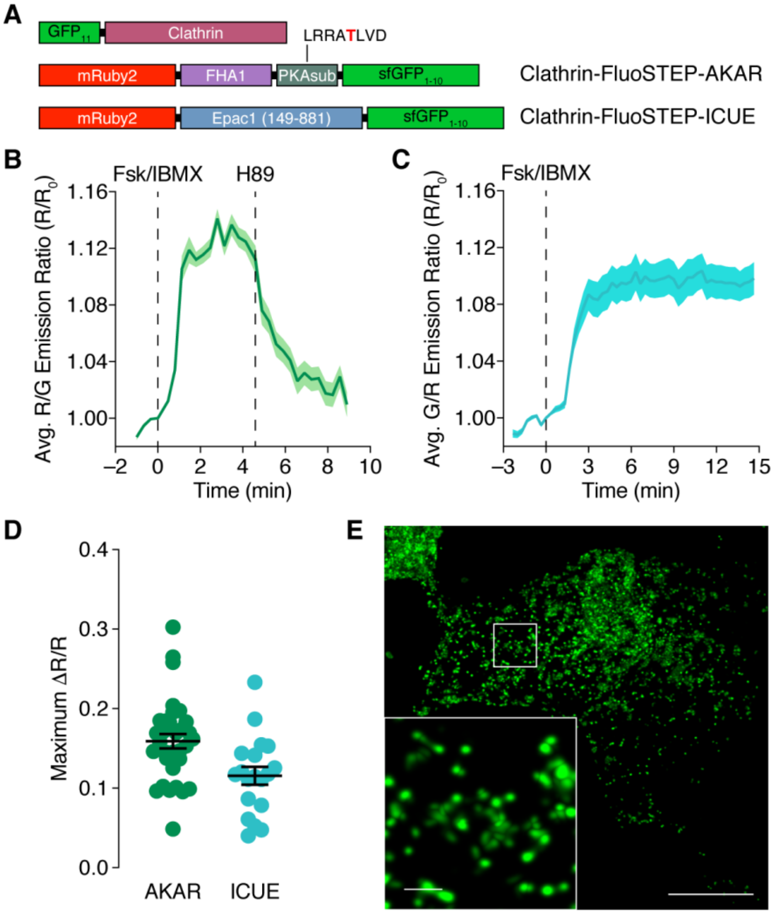

Figure 4.6: FluoSTEP sensors deployed at endogenously expressed clathrin
(**A**) Domain structures of clathrin-targeted FluoSTEP-AKAR and FluoSTEP-ICUE. (**B-D**) Average time course of the (**B**) red/green emission (R/G) ratio time course from FluoSTEP-AKAR (n = 33 cells) or (**C**) the green/red (G/R) emission ratio time course from FluoSTEP-ICUE (n = 19 cells) expressed in CTLA-FP11 cells and stimulated either with (**B**) 50 µM Fsk and 100 µM IBMX (Fsk/IBMX) followed by 10 µM H89 or (**C**) Fsk/IBMX alone. Solid lines in time courses indicate average responses; shaded areas, SEM. (**D**) Summary of the maximum emission ratio changes from FluoSTEP-AKAR and FluoSTEP-ICUE in CTLA-FP11 cells following Fsk/IBMX stimulation. Horizontal lines in indicate mean ± SEM. (**E**) Representative fluorescence image depicting the localization of biosensor fluorescence in the GFP channel in CTLA-FP11 cells, which are HEK293T cells in which the GFP_{11} tag is stably expressed at the clathrin N-terminus via CRISPR-mediated knock-in at the endogenous CLTA gene locus. Punctate clathrin structures are seen in zoomed-in inset. Scale bars, 10 µm (inset, 1 µm).

Transmembrane adenylyl cyclases regulate sustained cAMP production at long-lived clathrin microdomains following β-adrenergic receptor stimulation

After activation, GPCRs at the plasma membrane undergo desensitization, endocytosis and trafficking to endosomes, and eventual recycling back to the plasma membrane[231]. Evidence suggests that this process of GPCR endocytosis governs prolonged cAMP signaling from endosomes[233]. Clathrin plays a central role in the spatiotemporal regulation of cAMP signaling by promoting GPCR internalization and trafficking[234]. However, little is known about the receptor-mediated signaling within clathrin microdomains.

To probe clathrin-specific cAMP dynamics after GPCR stimulation, we expressed FluoSTEP-ICUE in CLTA-FP11 cells and stimulated them with the β-adrenergic receptor (β-AR) agonist isoproterenol (10 μM), followed by Fsk/IBMX to maximally induce cAMP production. Tagging with FluoSTEP-ICUE had little effect on endogenous clathrin dynamics, as assessed via TIRF imaging of CLTA-FP11 cells transfected with either $GFP_{1\text{-}10}$ or FluoSTEP-ICUE (Figures 4.7 A and B). Interestingly, while the median puncta lifetime observed via TIRF imaging was <1 min (Figures 4.7 A and B), the isoproterenol-induced response from clathrin-targeted FluoSTEP-ICUE was largely sustained over 20 min (Sustained Activity Metric[235] 20 min after stimulation [SAM20] = 0.90 ± 0.019, n = 55 cells; see Methods) (Figure 4.8A). Clathrin microdomains are known to exhibit heterogeneous dynamics and can be roughly divided among smaller structures that are only transiently present (1-2 min) at the membrane surface and other, longer-lived structures known as clathrin plaques[236,237]. Analysis of the cAMP dynamics within these different types of clathrin structures suggests that the sustained cAMP increases occur primarily in the longer-lived clathrin structures (Figures 4.7 C and D).

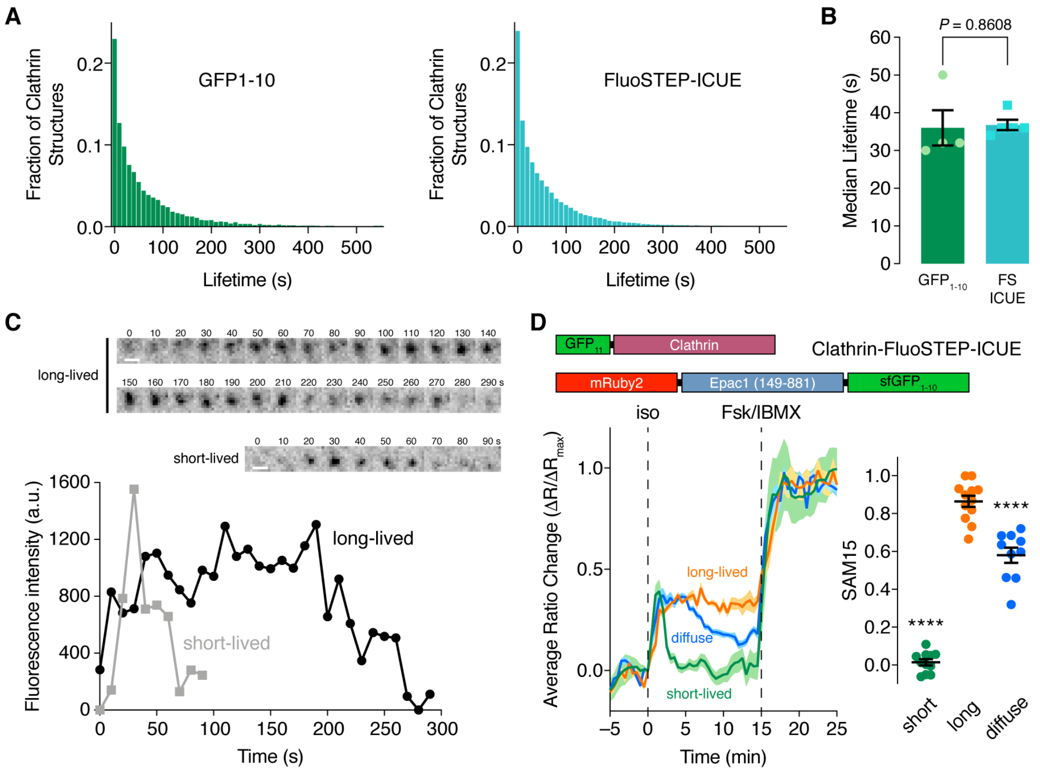

Figure 4.7: Dynamics of endogenous clathrin labeled with split fluorescent proteins
(**A**) Lifetime distribution of clathrin punctate structures imaged via TIRF for CLTA-FP11 cells expressing either GFP$_{1-10}$ (left) or FluoSTEP-ICUE (right). (**B**) Analysis of the median lifetime of clathrin structures observed in CLTA-FP11 cells expressing either GFP$_{1-10}$ or FluoSTEP-ICUE shows no effect of FluoSTEP-ICUE expression on endogenous clathrin dynamics (unpaired two-tailed Student's t-test). (**C**) Representative image sequences (top) and fluorescence intensity time courses (lower) depicting short- and long-lived (lower) clathrin structures. These trajectories are from FluoSTEP-ICUE-expressing CLTA-FP11 cells. Scale bar, 1 μm. (**D**) (top) Domain structure of clathrin-targeted FluoSTEP-ICUE. (left) Representative average time courses of the green/red emission ratio from CLTA-FP11 cells expressing FluoSTEP-ICUE and stimulated with 10 μM isoproterenol (iso) followed by 50 μM Fsk and 100 μM IBMX (Fsk/IBMX). Epifluorescence imaging revealed sustained cAMP increases upon iso treatment only in long-lived clathrin punctate regions (orange curve, n = 4 puncta from 4 cells) compared with short-lived puncta (green curve, n = 5 puncta from 4 cells) or diffuse, cytosolic regions (blue curve, n = 4 regions from 4 cells). Solid lines indicate average responses; shaded areas, SEM. (right) Summary of the cAMP dynamics in FluoSTEP-ICUE-expressing CTLA-FP11 cells recorded from short- (short: n = 11 puncta from 10 cells) and long-lived puncta (long: n = 12 puncta from 12 cells), as well as cytosolic regions (diffuse: n = 10 regions from 10 cells), and plotted as the sustained activity metric at 15 min (SAM15) following iso stimulation. Horizontal lines in indicate mean ± SEM. *****P* < 0.0001 vs. "long"; ordinary one-way ANOVA followed by the Holm-Sidak multiple comparisons test.

Figure 4.8: Transmembrane adenylyl cyclases regulate sustained cAMP production at clathrin after β-adrenergic receptor stimulation
(**A**) (top) Domain structures of clathrin-FP11 (from CTLA-FP11 cells) and FluoSTEP-ICUE, as well as plasma membrane-targeted ICUE3 (PM-ICUE3). (bottom) CLTA-FP11 cells expressing either FluoSTEP-ICUE (clathrin) or PM-ICUE3 (PM) were stimulated with 10 μM isoproterenol (iso) followed by 50 μM Fsk and 100 μM IBMX (Fsk/IBMX) as indicated. Representative average time courses (left) showing the green/red (clathrin, orange; n = 15 cells) or cyan/yellow (PM, blue; n = 28 cells) emission ratio change normalized to the maximum Fsk/IBMX-stimulated ratio change ($\Delta R/\Delta R_{max}$). (right) Summary of the sustained activity metric at 20 min (SAM20) following iso stimulation in CTLA-FP11 cells expressing FluoSTEP-ICUE (CLTA-FP11; n = 55 cells), diffusible ICUE3 (ICUE3; n = 40 cells), or plasma membrane-targeted ICUE3 (PM-ICUE3; n = 42 cells), or HEK293T cells expressing Lyn-FRB-GFP$_{11}$ plus FluoSTEP-ICUE (PM-GFP11; n = 45 cells). ****$P < 0.0001$ vs. CTLA-FP11; Kruskal-Wallis test followed by Dunn's multiple comparisons test. (**B**) CLTA-FP11 cells expressing either FluoSTEP-ICUE or PM-ICUE3 were stimulated with 10 μM iso, 10 μM propranolol, and Fsk/IBMX as indicated. (left) Representative average time courses showing the maximum-response-normalized green/red (clathrin, orange; n = 13 cells) or cyan/yellow (PM, blue; n = 18 cells) emission ratio changes ($\Delta R/\Delta R_{max}$). (right) Normalized ratio change ($\Delta R/\Delta R_{max}$) upon propranolol addition. n = 104 (clathrin) and 33 (PM) cells. (**C**) CLTA-FP11 cells expressing either FluoSTEP-ICUE or PM-ICUE3 were stimulated with 10 μM iso, 100 μM IBMX, and 50 μM Fsk as indicated. (left) Representative average time courses showing the maximum-response-normalized green/red (clathrin, orange; n = 21 cells) or cyan/yellow (PM, blue; n = 23 cells) emission ratio changes ($\Delta R/\Delta R_{max}$). (right) Maximum-response-normalized emission ratio change ($\Delta R/\Delta R_{max}$) upon IBMX addition. n = 32 (clathrin) and 36 (PM) cells. (**D**) CLTA-FP11 cells expressing either FluoSTEP ICUE or PM-ICUE3 were stimulated with 10 μM iso, 100 μM ddAdo, and Fsk /IBMX as indicated. (left) Representative average time courses showing the maximum-response-normalized green/red (clathrin, orange; n = 25 cells) or cyan/yellow (PM, blue; n = 25 cells) emission ratio changes ($\Delta R/\Delta R_{max}$). (right) Maximum-response-normalized emission ratio ($\Delta R/\Delta R_{max}$) upon ddAdo addition. n = 46 (clathrin) and 54 (PM) cells. ****$P <$ 0.0001; unpaired two-tailed Student's t-test with Welch's correction (in **B**-**D**). Solid lines in time courses indicate average responses; shaded areas, SEM. Horizontal lines in scatter plots indicate mean ± SEM.

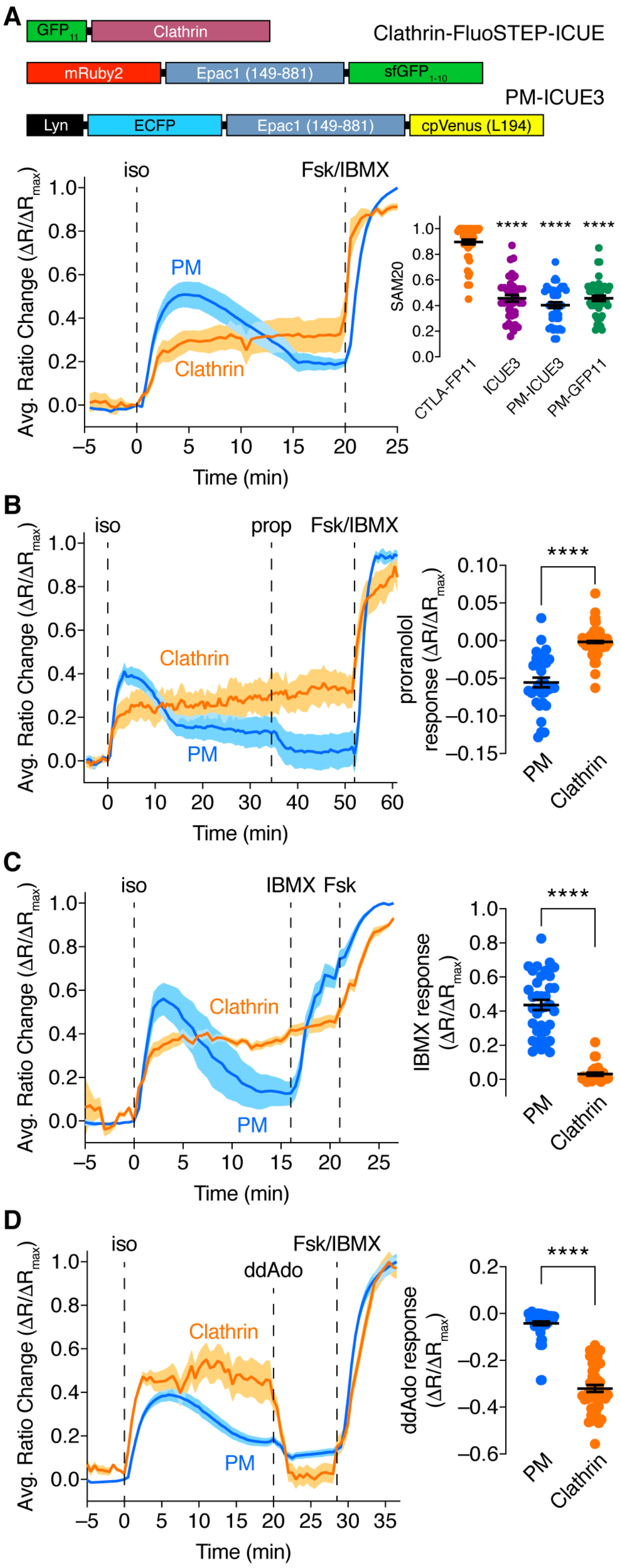

A
GFP11
Clathrin
Clathrin-FluoSTEP-ICUE
mRuby2
Epac1 (149-881)
sfGFP1-10
PM-ICUE3
Lyn
ECFP
Epac1 (149-881)
cpVenus (L194)
iso
Fsk/IBMX
Avg. Ratio Change (ΔR/ΔRmax)
1.0
0.8
0.6
0.4
0.2
0.0
PM
Clathrin
–5
0
5
10
15
20
25
Time (min)
SAM20
****
****
****
CTLA-FP11
ICUE3
PM-ICUE3
PM-GFP11
B
iso
prop
Fsk/IBMX
Clathrin
PM
0
10
20
30
40
50
60
Time (min)
proranolol response (ΔR/ΔRmax)
0.10
0.05
0.00
–0.05
–0.10
–0.15
****
PM
Clathrin
C
iso
IBMX
Fsk
Clathrin
PM
Time (min)
IBMX response (ΔR/ΔRmax)
****
PM
Clathrin
D
iso
ddAdo
Fsk/IBMX
Clathrin
PM
–5
0
5
10
15
20
25
30
35
Time (min)
ddAdo response (ΔR/ΔRmax)
0.2
0.0
–0.2
–0.4
–0.6
****
PM
Clathrin

To compare the dynamics of clathrin microdomain-specific cAMP signaling with those of bulk cAMP signals, we transfected CTLA-FP11 cells with a cyan-yellow FRET-based cAMP probe that utilizes the same switch domain[218] as FluoSTEP-ICUE, either diffusely (ICUE3) or targeted to the general plasma membrane (PM) via the myristoylation-palmitoylation sequence from Lyn kinase (PM-ICUE3). Both ICUE3 and PM-ICUE3 reported transient cAMP accumulation upon isoproterenol stimulation, exhibiting sharp increases in the normalized ratio that gradually decayed to a sub-maximum steady-state (ICUE3: SAM20 = 0.46 ± 0.026, n = 40 cells; PM-ICUE3: SAM20 = 0.40 ± 0.022, n = 42 cells) (Figures 4.8A and 4.9A), consistent with previous reports of cAMP clearance due to desensitization and internalization during canonical β-AR signaling[218]. Reconstituting FluoSTEP-ICUE at the PM by co-expressing GFP_{11} fused to a Lyn-tagged protein (Lyn-FRB-GFP_{11}) similarly revealed a transient response upon isoproterenol treatment (SAM20 = 0.46 ± 0.21, n = 45 cells) (Figure 4.9B), indicating that the sustained cAMP responses observed with clathrin-targeted FluoSTEP-ICUE were not an artifact of the complementation-based targeting strategy.

We next set out to investigate the molecular mechanisms responsible for driving the unique compartmentalized cAMP dynamics that we observed within these endogenous clathrin microdomains. We hypothesized that the presence of sustained cAMP signaling might be driven by continuous signaling by active β-ARs[238]. To test this, we treated isoproterenol-stimulated CTLA-FP11 cells expressing either FluoSTEP-ICUE or PM-ICUE3 with the β-AR antagonist 2-propranolol (10 μM). Interestingly, whereas propranolol treatment yielded an acute decrease in the normalized ratio of PM-ICUE3 ($\Delta R/\Delta R_{max} = -5.6\% \pm 0.64\%$, n = 33 cells) to almost basal levels, propranolol addition had no effect on the isoproterenol-induced response of clathrin-

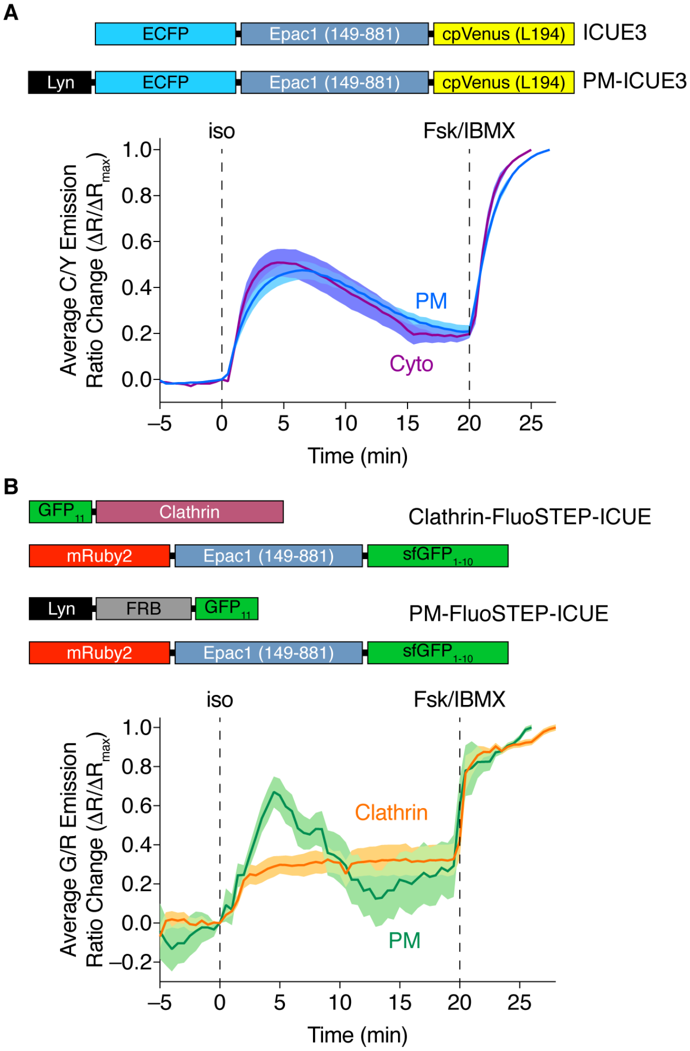

Figure 4.9: Isoproterenol induces sustained cAMP increases only in the clathrin microdomain

(**A**) (top) Domain structures of ICUE3 and plasma membrane-targeted ICUE3 (PM-ICUE3). (bottom) Representative average time courses showing cyan/yellow emission ratio changes normalized to the maximum Fsk/IBMX-stimulated ratio change ($\Delta R/\Delta R_{max}$) for PM-ICUE3 (PM, blue; n = 28 cells) and ICUE3 (cyto, purple; n = 25 cells) expressed in CTLA-FP11 cells upon stimulation with 10 µM isoproterenol (iso), followed by 50 µM Fsk and 100 µM IBMX (Fsk/IBMX). (**B**) (top) Domain structures of GFP_{11}-tagged Clathrin with FluoSTEP-ICUE to generate Clathrin-FluoSTEP-ICUE and Lyn-tagged GFP_{11}-tethered FRB with FluoSTEP-ICUE to generate PM-FluoSTEP-ICUE. (bottom) Representative average time courses showing the green/red emission ratio changes normalized to the maximum Fsk/IBMX-stimulated ratio change ($\Delta R/\Delta R_{max}$) for FluoSTEP-ICUE (clathrin, orange curve; n = 15 cells) expressed in CTLA-FP11 cells or FluoSTEP-ICUE co-expressed with Lyn-FRB-FP_{11} (PM, green curve; n = 8 cells) in HEK293T cells upon stimulation with iso followed by Fsk/IBMX. Solid lines in time courses indicate average responses; shaded areas, SEM.

targeted FluoSTEP-ICUE ($\Delta R/\Delta R_{max} = -0.18\% \pm 0.14\%$, n = 104 cells, $P < 0.0001$), indicating that this sustained cAMP response does not require active receptors (Figure 4.8B).

Local variations in cAMP accumulation within the cell can be controlled by the spatial organization of ACs and PDEs, which synthesize and degrade cAMP, respectively[217], and the compartmentalized cAMP dynamics observed using clathrin-targeted FluoSTEP-ICUE may be due to the differential distribution of these enzymes. For instance, AC3 and AC9 have been shown to undergo internalization after GPCR stimulation and traffic to endosomes containing the receptors[233,239]. Thus, to test the role of these enzymes in regulating the sustained cAMP accumulation detected by clathrin-targeted FluoSTEP-ICUE, we treated isoproterenol-stimulated CTLA-FP11 cells expressing FluoSTEP-ICUE or PM-ICUE3 with IBMX (100 μM) to acutely inhibit PDE activity or 2',3'-dideoxyadenosine (ddAdo, 100 μM) to acutely inhibit transmembrane AC (tmAC) activity. Interestingly, whereas PDE inhibition induced a large increase in the normalized ratio of PM-ICUE ($\Delta R/\Delta R_{max} = 44\% \pm 3.0\%$, n = 36 cells), the response from clathrin-targeted FluoSTEP-ICUE was largely unaffected ($\Delta R/\Delta R_{max} = 3.1\% \pm 0.89\%$, n = 32 cells, $P < 0.0001$) (Figure 4.8C). On the other hand, tmAC inhibition using ddAdo induced a sharp reversal of the normalized ratio of clathrin-targeted FluoSTEP-ICUE back to baseline levels ($\Delta R/\Delta R_{max} = -32\% \pm 1.5\%$, n = 46 cells) but had a minimal effect on the PM-ICUE3 response ($\Delta R/\Delta R_{max} = -4.2\% \pm 0.80\%$, n = 54 cells, $P < 0.0001$) (Figure 4.8D). Taken together, these data suggest that the compartmentalized cAMP dynamics associated with long-lived clathrin microdomains result from a combination of low PDE activity and high tmAC activity leading to sustained cAMP accumulation following β-AR stimulation.

Discussion

Here, we present FluoSTEPs, an adaptable biosensor framework for monitoring compartmentalized signaling at endogenous cellular locations, and deploy them to study a specific cAMP/PKA signaling microdomain. Complementation and functional reconstitution of the biosensors at endogenously tagged proteins relies on a logic gate, and thus confers domain specificity. Efficient knock-in of GFP_{11} at a specific genomic locus via CRISPR-mediated HDR[229] precludes overexpression of the protein of interest while also bypassing the need for knocking in an entire FRET-based sensor. Additionally, the ratiometric readout further strengthens the utility of this biosensor collection by allowing quantitative comparisons of localized signaling.

Despite the demonstrated advantages of this platform, potential obstacles such as low sensor dynamic range and the dependence on the level of endogenous protein expression must be considered. While we have demonstrated the ability to enhance FP reconstitution at an endogenous POI and amplify biosensor dynamic range using an array of GFP_{11} tags, future development and engineering of FluoSTEPs will include linker optimization and additional FP screening. For example, mScarlet-I incorporation into FluoSTEP-AKAR increased the dynamic range. Certain applications, such as measuring signaling dynamics in a heterogeneous cell population, might benefit from the enhanced dynamic range of the mScarlet-I-based sensor variant. Furthermore, by extending the FluoSTEP toolkit to utilize orthogonal, multicolored FP variants, several sensors may be multiplexed to simultaneously report differential compartmentalized signaling in the same cell.

GPCR endocytosis starts a cascade of intricate signaling events such as activating a second wave of cAMP signaling[240] and is implicated in pathological processes such as opioid addiction[241]. While the kinetics of bulk cAMP accumulation during GPCR endocytosis have been characterized[242], the dynamics of cAMP accumulation within the specific microdomains important in this process are elusive. Here, by deploying FluoSTEP-ICUE to probe cAMP dynamics at an endogenous signaling compartment, we were able to detect sustained cAMP accumulation within clathrin microdomains following β-AR activation. We show that this sustained cAMP accumulation primarily arises from a subset of long-lived clathrin structures known as plaques, a recently discovered class of clathrin structures that persist in the membrane for longer periods than clathrin-coated pits[236,238]. Initially, clathrin plaques were thought be biologically inert structures[237,243]; however, recent work has shed light on their functional importance[244–246]. Clathrin plaques can recruit various GPCRs such as the β_2-AR[238] and also undergo typical scission events[236,238,247]. Furthermore, these longer-lasting clathrin structures are implicated in various cellular processes such as mechanotransduction[246,248] and sarcomere organization and function[244,245].

Our results shed more light onto the signaling role of long-lived clathrin structures such as plaques by suggesting that they play an important role in shaping cAMP signaling by regulating local cAMP dynamics. The sustained cAMP elevations within clathrin plaques are likely achieved by the exclusion or inhibition of PDEs, as well as by the recruitment of ACs with the endocytosed receptor, consistent with previous reports of $G\alpha_s$ and AC co-internalization with GPCRs[233,239,249]. Compared with canonical, plasma membrane GPCR signaling, other sources of GPCR signaling, including from endosomes, produce distinct signaling profiles and dictate different cellular processes, such as cAMP-dependent transcription [250–252]. Future studies of the distinct cAMP dynamics originating within different clathrin microdomains and the general plasma membrane (Figures 4.7-4.9) may thus reveal unique downstream signaling effects and cellular functions regulated by these closely juxtaposed membrane compartments. We envision that FluoSTEPs can be further used to probe many specific GPCR compartments and habitats, thus adding to the existing toolkit[253,254] to enable a better understanding of the intricate spatiotemporal organization of GPCR signaling.

In summary, FluoSTEPs provide a strategy for observing microdomain-specific signaling at endogenous protein expression levels. Using FluoSTEPs to elucidate a unique cAMP compartment associated with clathrin microdomains uncovers new aspects of cAMP regulation during GPCR internalization and highlights the utility of FluoSTEPs to advance our understanding of the spatiotemporal regulation of biochemical networks in endogenous biological contexts.

Materials and Methods

Biosensor Construction

All assembly of constructs was performed using Gibson Assembly (NEB 2x High Fidelity Master Mix). To construct FluoSTEP-AKAR, mRuby2 was PCR-amplified from pcDNA3 AKAR-CR (gift of Michael Lin, Stanford University, Palo Alto, CA) using the primers (lowercase is Gibson overlap region, uppercase is priming region) 5’-cccaagctggctagcgtttaaacttaagcttggATGGTGTCTAAGGGCGAAGAGCTGATC-3’ and 5’-gatctgttcttgagaaaacttatgcatgcgCTTGTACAGCTCGTCCATCCCACC-3’, and the FHA1 and PKA substrate from AKAR4[191] using primers 5’-ggtgggatggacgagctgtacaagCGCATGCATAAGTTTTCTCAAGAACAGATC-3’ and 5’-tcctttggacatagatctgttaacgaattcGAGCTCGCTGCCGCCGGTGCCGCCGTCC-3’. The resulting PCR fragments were Gibson assembled into HindIII- and EcoRI-digested pcDNA3.1 GFP$_{1\text{-}10}$. GFP$_{1\text{-}10}$-FHA1-PKAsub-mRuby2 (version 1 of FluoSTEP-AKAR in Fig. 1B) was constructed similarly by Gibson Assembly using primers 5’-agcaaagatccaaatgaaaaaCGCATGCATAAGTTTTCTCAAGAACAGATCGGCGAAAAC-3’ and 5’-ccagtgtgatggatatctgcaGAATTCTTACTTGTACAGCTCGTCCATCCCACC-3’ to amplify FHA1-PKA substrate-mRuby2 from AKAR-CR, and primers 5’-gttttcgccgatctgttcttgagaaaacttatgcatgcgTTTTTCATTTGGATCTTTGCT-3’ and 5’-GAATTCTGCAGATATCCATCACACTGGCGG-3’ to amplify the GFP$_{1\text{-}10}$ pcDNA3.1 backbone. FluoSTEP-AKAR (T/A) was constructed by Gibson assembly of PCR products amplified from FluoSTEP-AKAR using primers 5’-CTGCGTCGCGCCGCCCTGGTTGAC-3’ and 5’- GTCAACCAGGGCGGCGCGACGCAG-3’. FluoSTEP-ICUE was constructed similarly, except that the Epac1 (149-881) fragment from ICUE3[220] was PCR-amplified using primers 5’-ggtggtgggatggacgagctgtacaagGAGGAGAAGAAGGAGTGTGATGAAGAA-3’ and 5’-ggtaaacagttcttctcctttggacatCTCAACGTCCCTCAAAATCCGATTGAA-3’. FluoSTEP ICUE R279E was constructed by Gibson assembly of PCR products amplified from FluoSTEP-ICUE using primers 5’-gatgcaccccggGCAGCCACCATCATCCTG-3’ and 5’-ggtggctgcccgGGGTGCATCATTCACCAGAG-3’. FluoSTEP-Epac2B (285-443) was constructed via Gibson assembly of the Epac2B (285-443) fragment PCR amplified from the Epac2camps biosensor (gift from M. Lohse) using the forward primer 5’-ggtggtgggatggacgagctgtacaagGAGGAGAAGAAGGAGTGTGATGAAGAA-3’ and the reverse primer 5’-ggtaaacagttcttctcctttggacatCTCAACGTCCCTCAAAATCCGATTGAA-3’. FluoSTEP-AktAR was constructed similarly to FluoSTEP-AKAR, except the FHA1 and Akt substrate domains were amplified from pcDNA3 AktAR[222] using the forward primer 5’-ggatggacgagctgtacaagCGCATGCATAAGTTTTCTCAA-3’ and the reverse primer 5’-agttcttctcctttggacatAAGTTCACTGCCGCCGGTACCTC-3’. FluoSTEP-AktAR (T/A) was made by Gibson assembly of a PCR product amplified from FluoSTEP-AktAR using the forward primer 5’-gtgcgcatggcctgatCCCAGGCCGGAGTTTGG-3’ and the reverse primer 5’-tgggatcaggccatgcGCACGAGCGCGGACGA-3’. FluoSTEP-JNKAR was constructed similarly to FluoSTEP-AKAR, except the FHA1 and JNK substrate domains were amplified from pcDNA3-JNKAR1[223] using the forward primer 5’-ggatggacgagctgtacaagCGCATGCATAAGTTTTCTCAA-3’ and the reverse primer 5’-agttcttctcctttggacataagttctgaacctcctgtacctccCTTCTTCTCGAGCTGCTC-3’. FluoSTEP-JNKAR (T/A) was made by Gibson assembly of a PCR fragment amplified from FluoSTEP-JNKAR using the forward primer 5’-agtgtcaaggcCCCCGAGGATGAAGGCAAC-3’ and the reverse primer 5’-tcctcgggggcCTTGACACTGTCGACcaggc-3’. FluoSTEP-EKAR was constructed by

Gibson assembly of an SphI/SacI-digested fragment of pcDNA3-Rab-EKARev[109] encoding the WW domain, EV linker, and Erk substrate sequence with a PCR fragment amplified from FluoSTEP-AKAR using the forward primer 5’-tcccccgcgcacgggagctcATGTCCAAAGGAGAAGAACTGTTTACCGGTGTT-3’ and the reverse primer 5’-tcgtccgccatgtgcatgcgCTTGTACAGCTCGTCCATCCCACCACC-3’. FluoSTEP-EKAR (T/A) was constructed similarly to FluoSTEP-EKAR, except that an SphI/SacI-digested fragment from pcDNA3-Rab-EKARev (T/A)[109] was used. GFP11-RhoA was constructed by Gibson assembly of the PCR-amplified fragment of DORA RhoA[79] to add GFP$_{11}$ onto the N-terminus of RhoA using the forward primers 5’-AGACCCAAGCTGGCTAGCGTTTAAACTTAAGCTTGGGCCACCATGCGTGACCACAT-3’, 5’-CACCATGCGTGACCACATGGTCCTTCATGAGTATGTAAATGCTGCTGGGATTA-3’, 5’-GAGTATGTAAATGCTGCTGGGATTACAGGTGGAACAGGAGGTTCA-3’, 5’-AGGTGGAACAGGAGGTTCAATGGCTGCCATCCGGAAGA-3’ and the reverse primer 5’-ggactagtggatccgagctcggtaTCACAAGACAAGGCAACCAG-3’ into pcDNA3.1 backbone (Invitrogen). cpPKN-mRuby2-EV-GFP$_{1\text{-}10}$ was constructed by Gibson assembly of cpPKN PCR-amplified from DORA RhoA[79] using the forward primer 5’-agacccaagctggctagcgtttaaacttaagcttggatgAGCCTGGGCCCCGTAG-3’ and the reverse primer 5’-tcttcgcccttagacaccattgaacctcctgttccaccGCGGCCCAGGTCAGT-3’, mRuby2 PCR-amplified from FluoSTEP-AKAR using the forward primer 5’-ATGGTGTCTAAGGGCGAAGA-3’ and the reverse primer 5’-gcactggttcctccggagccCTTGTACAGCTCGTCCATCC-3’, a Kpn2I/KpnI-digested fragment of FluoSTEP EKAR encoding theEV linker, and GFP$_{1\text{-}10}$ PCR-amplified from FluoSTEP-AKAR using the forward primer 5’-

gtggtagtgctggtggtaccATGTCCAAAGGAGAAGAACTGTTT-3’ and the reverse primer 5’-gtttaaacgggccctctagaCTATTTTTCATTTGGATCTTTGCTC-3’.

FluoSTEP-AKAR color variants were made similarly by PCR amplification of the FP to swap in and the remainder of the FluoSTEP-AKAR minus FP to swap out.

ICUE3 and PM-ICUE3 were described previously[220]. Lyn-FRB-FP_{11} was generated via Gibson assembly of an NheI/BamHI-digested fragment encoding the N-terminal targeting sequence from PM-ICUE3[220], a PCR fragment encoding FRB amplified from AKAP95-FRB[203] using the forward primer 5’-aagcgcaaggacaaggatccATCCTCTGGCATGAGATGTG-3’ and the reverse primer 5’-ACTAGTCTTTGAGATTCGTC-3’, and a PCR fragment encoding GFP_{11} along with the pcDNA3.1 backbone amplified from FluoSTEP-AKAR using the forward primer 5’-aactggggcacaagcttaatGGTGGAACAGGAGGTTCACG-3’ and the reverse primer 5’-ACGCTAGCCAGCTTGGGTCT-3’.

Cell Culture and Transfection

HeLa and HEK293T cells were cultured in Dulbecco modified Eagle medium (DMEM; Gibco) containing 1 g/L glucose and supplemented with 10% (v/v) fetal bovine serum (FBS, Sigma) and 1% (v/v) penicillin-streptomycin (Pen-Strep, Sigma-Aldrich). NIH3T3 cells were cultured in DMEM (Gibco) containing 1 g/L glucose and supplemented with 10% (v/v) fetal calf serum (FCS) and 1% (v/v) Pen-Strep (Sigma-Aldrich). All cells were maintained in a humidified incubator at 37°C with a 5% CO_2 atmosphere. Prior to transfection, cells were plated onto sterile 35-mm glass-bottomed dishes and grown to 50–70% confluence. Cells were then transfected using Lipofectamine 2000 (Invitrogen) or PolyJet (SignaGen Laboratories) and grown an additional 24 h (HeLa, HEK293T) before imaging. NIH3T3 cells were changed to serum-free DMEM immediately prior to transfection and serum-starved for 24 h before imaging.

Generation of stable GFP$_{11}$ cell lines via CRISPR-mediated knock-in

For knock-in experiments, 200 ng of Cas9+sgRNA vector (designed with px330) and 400 ng of an oligonucleotide donor DNA were transfected to HEK293FT cells per 24-well plate (Eppendorf). For CLTA, transient transfection of GFP$_{1\text{-}10}$ and FACS enrichment for GFP+ cells were performed, followed by a negative sort two weeks later to select against stable incorporation of GFP$_{1\text{-}10}$. Genomic DNA was extracted from cells and sequenced to confirm knock-in.

Time-lapse fluorescence imaging

Cells were washed twice with Hank’s balanced salt solution (HBSS, Gibco) and subsequently imaged in HBSS in the dark at 37°C. Forskolin (Fsk; Calbiochem), 3-isobutyl-1-methylxanthine (IBMX; Sigma), platelet-derived grwoth factor (PDGF; Sigma-Aldrich), anisomycin (Sigma-Aldrich), epidermal growth factor (EGF; Sigma-Aldrich), histamine (Sigma-Aldrich), isoproterenol (Sigma), 2-propranolol (Sigma-Aldrich), and 2’,3’-dideoxyadenosine (ddAdo, Cayman Chemical) were added as indicated. Epifluorescence imaging was performed either on a Zeiss Axiovert 200M microscope (Carl Zeiss) equipped with a xenon lamp, a 40x/1.3 NA objective and a cooled CCD or on a Zeiss AxioObserver Z1 microscope (Carl Zeiss) equipped with a 40x/1.3 NA objective and a Photometrics Evolve 512 EMCCD (Photometrics), both controlled by METAFLUOR 7.7 software (Molecular Devices). For the Zeiss Axiovert 200M, the following excitation/emission filter combinations (center/bandwidth in nm) were used: CFP -

EX420/20, EM475/25; GFP - EX480/30, EM535/45; YFP - EX495/10, EM535/25; RFP - EX568/55, EM653/95; CFP/YFPFRET - EX420/20, EM535/25; GFP/RFPFRET - EX480/30, EM653/95. For the Zeiss AxioObserver Z1, the following excitation/emission filter combinations were used: GFP - EM480/30, EX535/45. All filter sets were alternated using a Lambda 10-2 filter-changer (Sutter Instruments). Exposure times were 50 (for acceptor direct channel) and 500 ms (for all other channels), with the EM gain set to 20 for the AxioObserver Z1 microscope, and images were acquired every 30 s. All filter sets were alternated by a Lambda 10–2 filter-changer (Sutter Instruments). All epifluorescence experiments were subsequently analyzed using METAFLUOR 7.7 software.

Raw fluorescence images were corrected by subtracting the background fluorescence intensity of a cell-free region from the emission intensities of biosensor-expressing cells at each time point. Emission ratios or fluorescence intensities were then calculated at each time point. Biosensor response time courses shown in Figures 4.1-4.3, 4.5, and 4.6 were subsequently plotted as the normalized emission ratio with respect to time zero (e.g., R/R_0), where R is the ratio value at a given time point, and R_0 is the initial ratio value at the time point immediately preceding drug addition or the average emission ratio (−5 to 0 min) prior to drug addition. Biosensor responses shown in Figures 4.7D, 4.8, and 4.9 were plotted as the normalized-to-max emission ratio change ($\Delta R/\Delta R_{max}$), calculated as $(R-R_0)/(R_{max}-R_0)$, where R and R_0 are defined as above, and R_{max} is the maximum ratio value recorded after Fsk/IBMX stimulation. Maximum ratio ($\Delta R/R$) changes shown in Figures 4.1-4.6 were calculated as $(R_{max}-R_{min})/R_{min}$, where R_{max} and R_{min} are the maximum and minimum ratio value recorded after stimulation, respectively. Sustained activity levels in Figures 4.7D and 4.8A were assessed using the Sustained Activity Metric at 20 min (SAM20) or at 15 min (SAM15), calculated as $(R_t-R_0)/(R_{max,t}-R_0)$, where R_t is the ratio value recorded either 20 min after stimulation for SAM20 or 15 min after stimulation for SAM15, $R_{max,t}$ is the maximum ratio value recorded within either the 20 min window for SAM20 or 15 min window for SAM15, and R_0 is the ratio value at t = 0. Graphs were plotted using GraphPad Prism 8 (GraphPad Software).

TIRF Imaging and Analysis

CLTA-FP_{11} cells were plated onto glass-bottom 35-mm dishes coated with 100 μg/mL poly-D-lysine (Sigma). Cells were transfected 24 h after plating, and then incubated an additional 24 h after transfection. Cells were imaged using a 488 nm laser on a Nikon A1R TIRF microscope using a 100x objective at an 1840 TIRF angle with 20% laser power, gain multiplier of 300, and 2 sec interval time. TIRF image for single-particle tracking of the clathrin-coated structure was analyzed via Fiji plugin TrackMate[255]. Single clathrin-coated structures in each frame were detected using LoGdetector with 3 pixels of estimated blob diameter. Detected clathrin-coated structures were linked to get the trajectory by LAP tracker with the gap closing after arbitrary thresholding of dot detection for each sample. The lifetime of single clathrin-coated structure was estimated by the duration of the trajectories.

Statistics and reproducibility

Statistical analyses were performed in GraphPad Prism 8 (GraphPad). All data were assessed for normality. For normally distributed data, pairwise comparisons were performed using Student's t-tests or Welch's unequal variance test as indicated, and comparisons among three or more groups were performed using ordinary one-way analysis of variance (ANOVA) followed by

Dunnett's test for multiple comparisons. Non-Gaussian data were analyzed using the Mann-Whitney U test for pairwise comparisons or the Kruskal-Wallis test followed by Dunn's multiple comparisons test for analyses of three or more groups. Statistical significance was set at $P < 0.05$. Average time courses and summary bar graphs shown in Figures 4.1, 4.3-4.6, 4.7A-B, and 4.7D (bar graph only), and 4.8 (bar graphs only) are pooled from at least 3 independent experiments, and average time courses shown in Figures 4.2, 4.7D (time courses only), 4.8 (time courses only), and 4.9 are representative of at least 3 independently repeated experiments.

Acknowledgements

Chapter 4, in part, is currently being prepared for submission for publication of the material. Tenner, Brian; Huang, Bo; Mehta, Sohum; Zhang, Jin. Jason Zhaoxing Zhang was the co-first-author of this paper. The authors are grateful to W. Lin for their help in TIRF imaging. This work was supported by R01 DK073368 (to J.Z.); R21 EB022798, R01 GM124334, and R01 GM131641 (to B.H.); and a National Science Foundation predoctoral fellowship DGE-1650112 (to J.Z.Z.).

Chapter 5: Concluding Remarks

Cells must dynamically respond to a multitude of external stimuli to ensure proper functions. The coordination of linking specific stimuli to the correct cellular response is through signal transduction. Aberrations in signaling lead to miscommunication within the cell, which often times is responsible for pathological conditions such as cancer. Thus, it is of utmost importance for signaling to be precise, efficient, and dynamic. Spatiotemporal regulation of intercellular and intracellular signaling is an emerging theme that has been shown to be necessary for signaling specificity. To study spatiotemporal signaling, traditional biochemical assays such as Western blots, which are highly utilized in studies on signal transduction as they can capture specific information such as the protein state (e.g. phosphorylation), are not ideal as they are lacking in either spatial or temporal resolution. Fluorescence-based technologies such as FRET-based biosensors are useful in measuring spatiotemporal signaling in live cells with micron-level spatial resolution and seconds-level temporal resolution. Throughout this dissertation, we employed traditional molecular biology techniques with FRET-based probes to investigate the temporal regulation of RhoA activation (Chapter 2) and the spatial regulation of cAMP/PKA signaling (Chapter 3), and engineered new biosensors to measure signaling dynamics around proteins of interest expressed at endogenous levels (Chapter 4).

Using biochemical assays and a FRET-based biosensor to measure RhoA activity, we revealed that stimulation of $G\alpha_q$-coupled receptors induces biphasic activation of RhoA with the first phase dependent on p63 RhoGEF and the second phase dependent on the Ca^{2+}/PKC/p115 RhoGEF signaling axis. Critically, we identified Serine 240 on p115 to be the PKC-phosphorylation site necessary for $G\alpha_q$-coupled receptor-mediated p115 activation. Interestingly, the two pathways responsible for biphasic RhoA activation differed in regulation and function. With the help of computational modeling of these pathways, we found that the Ca^{2+}/PKC/p115 signaling axis is not turned off by receptor deactivation, thus leading to persistent RhoA "memory" and increased RhoA-mediated transcription. Overall, this study provides a striking example where specific wiring of signaling networks enables complex temporal dynamics of a signaling molecule that encode diverse functional information.

In the second study, we discovered that the PKA regulatory subunit RIα undergoes liquid-liquid phase separation, which was due to intrinsic disorder from the linker region in RIα and multivalent interactions from the D/D domain in RIα. RIα phase-separated droplets contained around 20-fold more RIα (compared to diffuse, cytosolic regions), 100-fold more cAMP, and sequesters PKA_{cat}, thus allowing for increased cAMP/PKA activity in the droplets. We demonstrated that this supra-stoichiometric buffering of cAMP by RIα condensates was necessary for maintaining PDE-mediated cAMP "sinks", thus providing a novel mechanism in enabling cAMP compartmentation. We further showcased that the fusion oncoprotein DnaJB1-PKA_{cat}, which is seen in the majority of patients with the rare liver cancer fibrolamellar carcinoma, disrupted RIα phase separation, which was mediated through DnaJB1-PKA_{cat}'s loss of myristoylation and gain of Hsp70 binding. Furthermore, DnaJB1-PKA_{cat}-mediated inhibition of RIα phase separation resulted in loss of cAMP compartmentation, thus providing the first mechanistic hint into how this fusion oncoprotein can induce aberrant signaling. Importantly, loss of RIα phase separation induced tumorigenic phenotypes in normal liver cells, suggesting that RIα phase separation is tumorsuppressive. As cAMP is a ubiquitous biochemical regulator and has served as a model pathway for understanding signaling architecture transducing multiple signaling inputs into numerous outputs, these discoveries represent a conceptual leap forward in the field of cell signaling as they highlight phase separation as a novel principle organizer for signal transduction.

In the last study, we further developed the FRET-based probes utilized in the previous study. Using split fluorescent protein technology and FRET-based biosensors, the fluorescent sensors targeted to endogenous proteins (FluoSTEP) platform enables measurement of signaling activity around proteins of interest expressed at endogenous levels. First focusing on the development of the PKA sensor FluoSTEP-AKAR, we generalized the design and created sensors for more kinases such as Akt, Erk, and Jnk, small molecules such as cAMP, and GTPases such as RhoA. We deployed the cAMP sensors to endogenous clathrin and recorded prolonged cAMP increases at the long-lasting clathrin plaques after GPCR stimulation, while plasma membrane localized and cytosolic cAMP dynamics were transient. Mechanistically, the sustained cAMP increases in the clathrin plaques were due to increased transmembrane adenylyl cyclase activity and not from prolonged GPCR activity. With the design of these sensors we have enhanced the molecular toolkit to detect various signaling activities at proteins of interest without perturbing endogenous protein levels, thus allowing researchers to track signal transduction within signaling microdomains in their native contexts.

Throughout this dissertation, we have expanded the toolkit to measure spatiotemporal signaling and demonstrated the role of spatiotemporal signaling in coordinating various cellular processes. Understanding how signaling specificity can be achieved is a central question in both a basic and translational science standpoint. Identifying the differences in signaling between the diseased and normal state is necessary for unveiling the etiology of various pathologies. Moreover, application of this knowledge is crucial in developing more targeted and efficacious therapeutics, which is the ultimate goal for biomedical research.

References

1. Brangwynne, C. P., Eckmann, C. R., Courson, D. S., Rybarska, A., Hoege, C., Gharakhani, J., Julicher, F. & Hyman, A. A. Germline P granules are liquid droplets that localize by controlled dissolution/condensation. *Science* **324**, 1729–1732 (2009).

2. Courchaine, E. M., Lu, A. & Neugebauer, K. M. Droplet organelles? *EMBO J.* **35**, 1603–1612 (2016).

3. Hyman, A. A., Weber, C. A. & Julicher, F. Liquid-liquid phase separation in biology. *Annu. Rev. Cell Dev. Biol.* **30**, 39–58 (2014).

4. Banani, S. F., Lee, H. O., Hyman, A. A. & Rosen, M. K. Biomolecular condensates: Organizers of cellular biochemistry. *Nat. Rev. Mol. Cell Biol.* **18**, 285–298 (2017).

5. Banani, S. F., Rice, A. M., Peeples, W. B., Lin, Y., Jain, S., Parker, R. & Rosen, M. K. Compositional Control of Phase-Separated Cellular Bodies. *Cell* **166**, 651–663 (2016).

6. Mateju, D., Franzmann, T. M., Patel, A., Kopach, A., Boczek, E. E., Maharana, S., Lee, H. O., Carra, S., Hyman, A. A. & Alberti, S. An aberrant phase transition of stress granules triggered by misfolded protein and prevented by chaperone function. *EMBO J.* **36**, 1669–1687 (2017).

7. Nair, S. J., Yang, L., Meluzzi, D., Oh, S., Yang, F., Friedman, M. J., Wang, S., Suter, T., Alshareedah, I., Gamliel, A., Ma, Q., Zhang, J., Hu, Y., Tan, Y., Ohgi, K. A., Jayani, R. S., Banerjee, P. R., Aggarwal, A. K. & Rosenfeld, M. G. Phase separation of ligand-activated enhancers licenses cooperative chromosomal enhancer assembly. *Nat. Struct. Mol. Biol.* **26**, 193–203 (2019).

8. Chong, P. A. & Forman-Kay, J. D. Liquid–liquid phase separation in cellular signaling systems. *Curr. Opin. Struct. Biol.* **41**, 180–186 (2016).

9. Mitrea, D. M., Chandra, B., Ferrolino, M. C., Gibbs, E. B., Tolbert, M., White, M. R. & Kriwacki, R. W. Methods for Physical Characterization of Phase-Separated Bodies and Membrane-less Organelles. *J. Mol. Biol.* **430**, 4773–4805 (2018).

10. Alberti, S., Gladfelter, A. & Mittag, T. Considerations and Challenges in Studying Liquid-Liquid Phase Separation and Biomolecular Condensates. *Cell* **176**, 419–434 (2019).

11. Perdikari, T. M., Murthy, A. C., Ryan, V. H., Watters, S., Naik, M. T. & Fawzi, N. L. SARS-CoV-2 nucleocapsid protein undergoes liquid-liquid phase separation stimulated by RNA and partitions into phases of human ribonucleoproteins. *bioRxiv* 2020.06.09.141101 (2020) doi:10.1101/2020.06.09.141101.

12. Markmiller, S., Soltanieh, S., Server, K. L., Mak, R., Jin, W., Fang, M. Y., Luo, E. C., Krach, F., Yang, D., Sen, A., Fulzele, A., Wozniak, J. M., Gonzalez, D. J., Kankel, M. W., Gao, F. B., Bennett, E. J., Lécuyer, E. & Yeo, G. W. Context-Dependent and Disease-

Specific Diversity in Protein Interactions within Stress Granules. *Cell* **172**, 590-604.e13 (2018).

13. Sheu-Gruttadauria, J. & MacRae, I. J. Phase Transitions in the Assembly and Function of Human miRISC. *Cell* **173**, 946-957.e16 (2018).

14. Bracha, D., Walls, M. T., Wei, M. T., Zhu, L., Kurian, M., Avalos, J. L., Toettcher, J. E. & Brangwynne, C. P. Mapping Local and Global Liquid Phase Behavior in Living Cells Using Photo-Oligomerizable Seeds. *Cell* **175**, 1467-1480.e13 (2018).

15. Mitrea, D. M. & Kriwacki, R. W. Phase separation in biology; functional organization of a higher order. *Cell Commun. Signal.* **14**, 1 (2016).

16. Li, P., Banjade, S., Cheng, H.-C., Kim, S., Chen, B., Guo, L., Llaguno, M., Hollingsworth, J. V, King, D. S., Banani, S. F., Russo, P. S., Jiang, Q.-X., Nixon, B. T. & Rosen, M. K. Phase transitions in the assembly of multivalent signalling proteins. *Nature* **483**, 336–340 (2012).

17. Wang, J., Choi, J. M., Holehouse, A. S., Lee, H. O., Zhang, X., Jahnel, M., Maharana, S., Lemaitre, R., Pozniakovsky, A., Drechsel, D., Poser, I., Pappu, R. V., Alberti, S. & Hyman, A. A. A Molecular Grammar Governing the Driving Forces for Phase Separation of Prion-like RNA Binding Proteins. *Cell* **174**, 688-699.e16 (2018).

18. Shin, Y., Berry, J., Pannucci, N., Haataja, M. P., Toettcher, J. E. & Brangwynne, C. P. Spatiotemporal Control of Intracellular Phase Transitions Using Light-Activated optoDroplets. *Cell* **168**, 159-171.e14 (2017).

19. Gallego, L. D., Schneider, M., Mittal, C., Romanauska, A., Gudino Carrillo, R. M., Schubert, T., Pugh, B. F. & Köhler, A. Phase separation directs ubiquitination of gene-body nucleosomes. *Nature* **579**, 592–597 (2020).

20. Nott, T. J., Petsalaki, E., Farber, P., Jervis, D., Fussner, E., Plochowietz, A., Craggs, T. D., Bazett-Jones, D. P., Pawson, T., Forman-Kay, J. D. & Baldwin, A. J. Phase Transition of a Disordered Nuage Protein Generates Environmentally Responsive Membraneless Organelles. *Mol. Cell* **57**, 936–947 (2015).

21. Molliex, A., Temirov, J., Lee, J., Coughlin, M., Kanagaraj, A. P., Kim, H. J., Mittag, T. & Taylor, J. P. Phase Separation by Low Complexity Domains Promotes Stress Granule Assembly and Drives Pathological Fibrillization. *Cell* **163**, 123–133 (2015).

22. Wegmann, S., Eftekharzadeh, B., Tepper, K., Zoltowska, K. M., Bennett, R. E., Dujardin, S., Laskowski, P. R., MacKenzie, D., Kamath, T., Commins, C., Vanderburg, C., Roe, A. D., Fan, Z., Molliex, A. M., Hernandez-Vega, A., Muller, D., Hyman, A. A., Mandelkow, E., Taylor, J. P. & Hyman, B. T. Tau protein liquid–liquid phase separation can initiate tau aggregation. *EMBO J.* **37**, 1–21 (2018).

23. Rai, A. K., Chen, J.-X., Selbach, M. & Pelkmans, L. Kinase-controlled phase transition of membraneless organelles in mitosis. *Nature* **559**, 211–216 (2018).

24. Zhang, J. Z., Lu, T.-W., Stolerman, L. M., Tenner, B., Yang, J., Zhang, J.-F., Falcke, M., Rangamani, P., Taylor, S. S., Mehta, S. & Zhang, J. Phase separation of a PKA regulatory subunit controls cAMP compartmentation and oncogenic signaling. *Cell* **182**, 1531-1544.e15 (2020).

25. Brunton, L. L., Hayes, J. S. & Mayer, S. E. Functional compartmentation of cyclic AMP and protein kinase in heart. *Adv. Cyclic Nucleotide Res.* **14**, 391–397 (1981).

26. Lohse, C., Bock, A., Maiellaro, I., Hannawacker, A., Schad, L. R., Lohse, M. J. & Bauer, W. R. Experimental and mathematical analysis of cAMP nanodomains. *PLoS One* **12**, e0174856 (2017).

27. Bock, A., Annibale, P., Konrad, C., Hannawacker, A., Anton, S., Maiellaro, I., Zabel, U., Sivaramakrishnan, S., Falcke, M. & Lohse, M. J. Optical mapping of cAMP signaling at the nanometer scale. *Cell* **182**, 1519-1530.e17 (2020).

28. Chen, C., Nakamura, T. & Koutalos, Y. Cyclic AMP diffusion coefficient in frog olfactory cilia. *Biophys. J.* **76**, 2861–2867 (1999).

29. Nikolaev, V. O., Bunemann, M., Hein, L., Hannawacker, A. & Lohse, M. J. Novel single chain cAMP sensors for receptor-induced signal propagation. *J. Biol. Chem.* **279**, 37215–37218 (2004).

30. Bacskai, B. J., Hochner, B., Mahaut-Smith, M., Adams, S. R., Kaang, B. K., Kandel, E. R. & Tsien, R. Y. Spatially resolved dynamics of cAMP and protein kinase A subunits in Aplysia sensory neurons. *Science* **260**, 222–226 (1993).

31. Greenwald, E. C., Mehta, S. & Zhang, J. Genetically Encoded Fluorescent Biosensors Illuminate the Spatiotemporal Regulation of Signaling Networks. *Chem. Rev.* **118**, 11707–11794 (2018).

32. Leonetti, M. D., Sekine, S., Kamiyama, D., Weissman, J. S. & Huang, B. A scalable strategy for high-throughput GFP tagging of endogenous human proteins. *Proc. Natl. Acad. Sci. U. S. A.* **113**, E3501–E3508 (2016).

33. Kamiyama, D., Sekine, S., Barsi-Rhyne, B., Hu, J., Chen, B., Gilbert, L. A., Ishikawa, H., Leonetti, M. D., Marshall, W. F., Weissman, J. S. & Huang, B. Versatile protein tagging in cells with split fluorescent protein. *Nat. Commun.* **7**, 11046 (2016).

34. Witzel, F., Maddison, L. & Blüthgen, N. How scaffolds shape MAPK signaling: What we know and opportunities for systems approaches. *Front. Physiol.* **3 DEC**, 1–14 (2012).

35. Su, X., Ditlev, J. A., Hui, E., Xing, W., Banjade, S., Okrut, J., King, D. S., Taunton, J., Rosen, M. K. & Vale, R. D. Phase separation of signaling molecules promotes T cell receptor signal transduction. *Science* **352**, 595–599 (2016).

36. Balagopalan, L., Kortum, R. L., Coussens, N. P., Barr, V. A. & Samelson, L. E. The linker for activation of T cells (LAT) signaling hub: from signaling complexes to microclusters.

J. Biol. Chem. **290**, 26422–26429 (2015).

37. Huang, W. Y. C., Alvarez, S., Kondo, Y., Lee, Y. K., Chung, J. K., Lam, H. Y. M., Biswas, K. H., Kuriyan, J. & Groves, J. T. A molecular assembly phase transition and kinetic proofreading modulate Ras activation by SOS. *Science (80-.).* **363**, 1098 LP – 1103 (2019).

38. Lee, Y. K., Low-Nam, S. T., Chung, J. K., Hansen, S. D., Lam, H. Y. M., Alvarez, S. & Groves, J. T. Mechanism of SOS PR-domain autoinhibition revealed by single-molecule assays on native protein from lysate. *Nat. Commun.* **8**, 15061 (2017).

39. Sondermann, H., Soisson, S. M., Boykevisch, S., Yang, S.-S., Bar-Sagi, D. & Kuriyan, J. Structural Analysis of Autoinhibition in the Ras Activator Son of Sevenless. *Cell* **119**, 393–405 (2004).

40. Sweetlove, L. J. & Fernie, A. R. The role of dynamic enzyme assemblies and substrate channelling in metabolic regulation. *Nat. Commun.* **9**, 2136 (2018).

41. An, S. The Glucosome: A Metabolic Complex for Glucose Metabolism and Its Functional Contribution to Cellular Metabolism in Living Cells. *FASEB J.* **34**, 1 (2020).

42. An, S., Jeon, M., Kennedy, E. L. & Kyoung, M. Chapter One - Phase-separated condensates of metabolic complexes in living cells: Purinosome and glucosome. in *Enzyme Activity in Single Cells* (eds. Allbritton, N. L. & Kovarik, M. L. B. T.-M. in E.) vol. 628 1–17 (Academic Press, 2019).

43. Pedley, A. M. & Benkovic, S. J. A New View into the Regulation of Purine Metabolism: The Purinosome. *Trends Biochem. Sci.* **42**, 141–154 (2017).

44. Zhao, H., French, J. B., Fang, Y. & Benkovic, S. J. The purinosome, a multi-protein complex involved in the de novo biosynthesis of purines in humans. *Chem. Commun. (Camb).* **49**, 4444–4452 (2013).

45. An, S., Kumar, R., Sheets, E. D. & Benkovic, S. J. Reversible Compartmentalization of de Novo Purine Biosynthetic Complexes in Living Cells. *Science (80-.).* **320**, 103 LP – 106 (2008).

46. Zhao, A., Tsechansky, M., Ellington, A. D. & Marcotte, E. M. Revisiting and revising the purinosome. *Mol. Biosyst.* **10**, 369–374 (2014).

47. Davis, B. W., Aumiller Jr., W. M., Hashemian, N., An, S., Armaou, A. & Keating, C. D. Colocalization and Sequential Enzyme Activity in Aqueous Biphasic Systems: Experiments and Modeling. *Biophys. J.* **109**, 2182–2194 (2015).

48. Tian, H., Sparvero, L. J., Amoscato, A. A., Bloom, A., Bayır, H., Kagan, V. E. & Winograd, N. Gas Cluster Ion Beam Time-of-Flight Secondary Ion Mass Spectrometry High-Resolution Imaging of Cardiolipin Speciation in the Brain: Identification of Molecular Losses after Traumatic Injury. *Anal. Chem.* **89**, 4611–4619 (2017).

49. Pareek, V., Tian, H., Winograd, N. & Benkovic, S. J. Metabolomics and mass spectrometry imaging reveal channeled de novo purine synthesis in cells. *Science (80-.).* **368**, 283 LP – 290 (2020).

50. Parker, B. C. & Zhang, W. Fusion genes in solid tumors: an emerging target for cancer diagnosis and treatment. *Chin. J. Cancer* **32**, 594–603 (2013).

51. Honeyman, J. N., Simon, E. P., Robine, N., Chiaroni-Clarke, R., Darcy, D. G., Lim, I. I. P., Gleason, C. E., Murphy, J. M., Rosenberg, B. R., Teegan, L., Takacs, C. N., Botero, S., Belote, R., Germer, S., Emde, A.-K., Vacic, V., Bhanot, U., LaQuaglia, M. P. & Simon, S. M. Detection of a recurrent DNAJB1-PRKACA chimeric transcript in fibrolamellar hepatocellular carcinoma. *Science* **343**, 1010–1014 (2014).

52. Maniaci, V., Davidson, B. R., Rolles, K., Dhillon, A. P., Hackshaw, A., Begent, R. H. & Meyer, T. Fibrolamellar hepatocellular carcinoma: prolonged survival with multimodality therapy. *Eur. J. Surg. Oncol.* **35**, 617–621 (2009).

53. Kastenhuber, E. R., Lalazar, G., Houlihan, S. L., Tschaharganeh, D. F., Baslan, T., Chen, C. C., Requena, D., Tian, S., Bosbach, B., Wilkinson, J. E., Simon, S. M. & Lowe, S. W. DNAJB1–PRKACA fusion kinase interacts with β-catenin and the liver regenerative response to drive fibrolamellar hepatocellular carcinoma. *Proc. Natl. Acad. Sci. U. S. A.* **114**, 13076–13084 (2017).

54. Cao, B., Lu, T. W., Martinez Fiesco, J. A., Tomasini, M., Fan, L., Simon, S. M., Taylor, S. S. & Zhang, P. Structures of the PKA RIα Holoenzyme with the FLHCC Driver J-PKAcα or Wild-Type PKAcα. *Structure* **27**, 816-828.e4 (2019).

55. Riggle, K. M., Riehle, K. J., Kenerson, H. L., Turnham, R., Homma, M. K., Kazami, M., Samelson, B., Bauer, R., McKnight, G. S., Scott, J. D. & Yeung, R. S. Enhanced cAMP-stimulated protein kinase A activity in human fibrolamellar hepatocellular carcinoma. *Pediatr. Res.* **80**, 110–118 (2016).

56. Cheung, J., Ginter, C., Cassidy, M., Franklin, M. C., Rudolph, M. J., Robine, N., Darnell, R. B. & Hendrickson, W. A. Structural insights into mis-regulation of protein kinase a in human tumors. *Proc. Natl. Acad. Sci. U. S. A.* **112**, 1374–1379 (2015).

57. Furugaki, K., Mochizuki, M., Kohno, M., Shu, S., Harada, N. & Yoshimura, Y. Expression of C-terminal ALK, RET, or ROS1 in lung cancer cells with or without fusion. *BMC Cancer* **19**, 301 (2019).

58. Tulpule, A. A., Guan, J., Neel, D. S., Lin, Y. P., Heslin, A., Perati, S., Ramirez, A. D., Shi, X., Yang, B. & Feng, S. Title : Cytoplasmic protein granules organize kinase-mediated RAS signaling. 1–13 (2019).

59. Chung, C.-I., Zhang, Q. & Shu, X. Dynamic Imaging of Small Molecule Induced Protein-Protein Interactions in Living Cells with a Fluorophore Phase Transition Based Approach. *Anal. Chem.* **90**, 14287–14293 (2018).

60. Ross, C. A. & Poirier, M. A. Protein aggregation and neurodegenerative disease. *Nat. Med.* **10 Suppl**, S10-7 (2004).

61. Elbaum-Garfinkle, S. Matter over mind: Liquid phase separation and neurodegeneration. *J. Biol. Chem.* **294**, 7160–7168 (2019).

62. Peskett, T. R., Rau, F., O'Driscoll, J., Patani, R., Lowe, A. R. & Saibil, H. R. A Liquid to Solid Phase Transition Underlying Pathological Huntingtin Exon1 Aggregation. *Mol. Cell* **70**, 588-601.e6 (2018).

63. Qamar, S., Wang, G. Z., Randle, S. J., Ruggeri, F. S., Varela, J. A., Lin, J. Q., Phillips, E. C., Miyashita, A., Williams, D., Ströhl, F., Meadows, W., Ferry, R., Dardov, V. J., Tartaglia, G. G., Farrer, L. A., Kaminski Schierle, G. S., Kaminski, C. F., Holt, C. E., Fraser, P. E., Schmitt-Ulms, G., Klenerman, D., Knowles, T., Vendruscolo, M. & St George-Hyslop, P. FUS Phase Separation Is Modulated by a Molecular Chaperone and Methylation of Arginine Cation-π Interactions. *Cell* **173**, 720-734.e15 (2018).

64. Zhang, P., Fan, B., Yang, P., Temirov, J., Messing, J., Kim, H. J. & Taylor, J. P. Chronic optogenetic induction of stress granules is cytotoxic and reveals the evolution of ALS-FTD pathology. *Elife* **8**, (2019).

65. McGurk, L., Gomes, E., Guo, L., Mojsilovic-Petrovic, J., Tran, V., Kalb, R. G., Shorter, J. & Bonini, N. M. Poly(ADP-Ribose) Prevents Pathological Phase Separation of TDP-43 by Promoting Liquid Demixing and Stress Granule Localization. *Mol. Cell* **71**, 703-717.e9 (2018).

66. McGurk, L., Mojsilovic-Petrovic, J., Van Deerlin, V. M., Shorter, J., Kalb, R. G., Lee, V. M., Trojanowski, J. Q., Lee, E. B. & Bonini, N. M. Nuclear poly(ADP-ribose) activity is a therapeutic target in amyotrophic lateral sclerosis. *Acta Neuropathol. Commun.* **6**, 84 (2018).

67. Prasad, A., Bharathi, V., Sivalingam, V., Girdhar, A. & Patel, B. K. Molecular Mechanisms of TDP-43 Misfolding and Pathology in Amyotrophic Lateral Sclerosis. *Front. Mol. Neurosci.* **12**, 25 (2019).

68. Cavallini, A., Brewerton, S., Bell, A., Sargent, S., Glover, S., Hardy, C., Moore, R., Calley, J., Ramachandran, D., Poidinger, M., Karran, E., Davies, P., Hutton, M., Szekeres, P. & Bose, S. An unbiased approach to identifying tau kinases that phosphorylate tau at sites associated with Alzheimer disease. *J. Biol. Chem.* **288**, 23331–23347 (2013).

69. Noble, W., Hanger, D., Miller, C. & Lovestone, S. The Importance of Tau Phosphorylation for Neurodegenerative Diseases . *Frontiers in Neurology* vol. 4 83 (2013).

70. Yadikar, H., Torres, I., Aiello, G., Kurup, M., Yang, Z., Lin, F., Kobeissy, F., Yost, R. & Wang, K. K. Screening of tau protein kinase inhibitors in a tauopathy-relevant cell-based model of tau hyperphosphorylation and oligomerization. *PLoS One* **15**, e0224952 (2020).

71. Giacomini, C., Koo, C.-Y., Yankova, N., Tavares, I. A., Wray, S., Noble, W., Hanger, D. P. & Morris, J. D. H. A new TAO kinase inhibitor reduces tau phosphorylation at sites associated with neurodegeneration in human tauopathies. *Acta Neuropathol. Commun.* **6**, 37 (2018).

72. Licht-Murava, A., Paz, R., Vaks, L., Avrahami, L., Plotkin, B., Eisenstein, M. & Eldar-Finkelman, H. A unique type of GSK-3 inhibitor brings new opportunities to the clinic. *Sci. Signal.* **9**, ra110 (2016).

73. Benn, C. L. & Dawson, L. A. Clinically Precedented Protein Kinases: Rationale for Their Use in Neurodegenerative Disease . *Frontiers in Aging Neuroscience* vol. 12 242 (2020).

74. Wheeler, R. J., Lee, H. O., Poser, I., Pal, A., Doeleman, T., Kishigami, S., Kour, S., Anderson, E. N., Marrone, L., Murthy, A. C., Jahnel, M., Zhang, X., Boczek, E., Fritsch, A., Fawzi, N. L., Sterneckert, J., Pandey, U., David, D. C., Davis, B. G., Baldwin, A. J., Hermann, A., Bickle, M., Alberti, S. & Hyman, A. A. Small molecules for modulating protein driven liquid-liquid phase separation in treating neurodegenerative disease. *bioRxiv* 721001 (2019) doi:10.1101/721001.

75. Selkoe, D. J. & Hardy, J. The amyloid hypothesis of Alzheimer's disease at 25 years. *EMBO Mol. Med.* **8**, 595–608 (2016).

76. Kametani, F. & Hasegawa, M. Reconsideration of Amyloid Hypothesis and Tau Hypothesis in Alzheimer's Disease. *Front. Neurosci.* **12**, 25 (2018).

77. Yu, O. M. & Brown, J. H. G protein-coupled receptor and RhoA-stimulated transcriptional responses: Links to inflammation, differentiation, and cell proliferation. *Mol. Pharmacol.* **88**, 171–180 (2015).

78. Zhang, B. & Zheng, Y. Regulation of RhoA GTP hydrolysis by the GTPase-activating proteins p190, p50RhoGAP, Bcr, and 3BP-1. *Biochemistry* **37**, 5249–5257 (1998).

79. Van Unen, J., Reinhard, N. R., Yin, T., Wu, Y. I., Postma, M., Gadella, T. W. J. & Goedhart, J. Plasma membrane restricted RhoGEF activity is sufficient for RhoA-mediated actin polymerization. *Sci. Rep.* **5**, 1–16 (2015).

80. Bhattacharyya, R., Banerjee, J., Khalili, K. & Wedegaertner, P. B. Differences in Gα12- and Gα13-mediated plasma membrane recruitment of p115-RhoGEF. *Cell. Signal.* **21**, 996–1006 (2009).

81. Lutz, S., Shankaranarayanan, A., Coco, C., Ridilla, M., Nance, M. R., Vettel, C., Baltus, D., Evelyn, C. R., Neubig, R. R., Wieland, T. & Tesmer, J. J. G. Structure of Galphaq-p63RhoGEF-RhoA complex reveals a pathway for the activation of RhoA by GPCRs. *Science* **318**, 1923–1927 (2007).

82. Siehler, S. Regulation of RhoGEF proteins by G 12/13-coupled receptors. *Br. J. Pharmacol.* **158**, 41–49 (2009).

83. Van Unen, J., Yin, T., Wu, Y. I., Mastop, M., Gadella, T. W. J. & Goedhart, J. Kinetics of recruitment and allosteric activation of ARHGEF25 isoforms by the heterotrimeric G-protein Gαq. *Sci. Rep.* **6**, 1–12 (2016).

84. Jaiswal, M., Gremer, L., Dvorsky, R., Haeusler, L. C., Cirstea, I. C., Uhlenbrock, K. & Ahmadian, M. R. Mechanistic insights into specificity, activity, and regulatory elements of the regulator of G-protein signaling (RGS)-containing Rho-specific guanine nucleotide exchange factors (GEFs) p115, PDZ-RhoGEF (PRG), and leukemia-associated RhoGEF (LARG). *J. Biol. Chem.* **286**, 18202–18212 (2011).

85. Basant, A. & Glotzer, M. Spatiotemporal Regulation of RhoA during Cytokinesis. *Curr. Biol.* **28**, R570–R580 (2018).

86. Zuckerbraun, B. S., Shapiro, R. A., Billiar, T. R. & Tzeng, E. RhoA influences the nuclear localization of extracellular signal-regulated kinases to modulate p21Waf/Cip1 expression. *Circulation* **108**, 876–881 (2003).

87. Reinhard, N. R., van Helden, S. F., Anthony, E. C., Yin, T., Wu, Y. I., Goedhart, J., Gadella, T. W. J. & Hordijk, P. L. Spatiotemporal analysis of RhoA/B/C activation in primary human endothelial cells. *Sci. Rep.* **6**, 25502 (2016).

88. Fitzsimons, C. P., Monczor, F., Fernández, N., Shayo, C. & Davio, C. Mepyramine, a histamine H1 receptor inverse agonist, binds preferentially to a G protein-coupled form of the receptor and sequesters G protein. *J. Biol. Chem.* **279**, 34431–34439 (2004).

89. Pertz, O., Hodgson, L., Klemke, R. L. & Hahn, K. M. Spatiotemporal dynamics of RhoA activity in migrating cells. *Nature* **440**, 1069–1072 (2006).

90. Momotani, K., Artamonov, M. V, Utepbergenov, D., Derewenda, U., Derewenda, Z. S. & Somlyo, A. V. p63RhoGEF couples Gα(q/11)-mediated signaling to Ca2+ sensitization of vascular smooth muscle contractility. *Circ. Res.* **109**, 993–1002 (2011).

91. Anastasiadis, P. Z., Moon, S. Y., Thoreson, M. A., Mariner, D. J., Crawford, H. C., Zheng, Y. & Reynolds, A. B. Inhibition of RhoA by p120 catenin. *Nat. Cell Biol.* **2**, 637–644 (2000).

92. Armbruster, B. N., Li, X., Pausch, M. H., Herlitze, S. & Roth, B. L. Evolving the lock to fit the key to create a family of G protein-coupled receptors potently activated by an inert ligand. *Proc. Natl. Acad. Sci. U. S. A.* **104**, 5163–5168 (2007).

93. Brancaccio, M., Maywood, E. S., Chesham, J. E., Loudon, A. S. I. & Hastings, M. H. A Gq-Ca2+ Axis controls circuit-level encoding of circadian time in the suprachiasmatic nucleus. *Neuron* **78**, 714–728 (2013).

94. Parsons, M. E. & Ganellin, C. R. Histamine and its receptors. *Br. J. Pharmacol.* **147 Suppl**, S127–S135 (2006).

95. Beekman, A., Helfrich, B., Bunn, P. A. J. & Heasley, L. E. Expression of catalytically

inactive phospholipase Cbeta disrupts phospholipase Cbeta and mitogen-activated protein kinase signaling and inhibits small cell lung cancer growth. *Cancer Res.* **58**, 910–913 (1998).

96. Holinstat, M., Mehta, D., Kozasa, T., Minshall, R. D. & Malik, A. B. Protein kinase Cα-induced p115RhoGEF phosphorylation signals endothelial cytoskeletal rearrangement. *J. Biol. Chem.* **278**, 28793–28798 (2003).

97. Kandabashi, T., Shimokawa, H., Miyata, K., Kunihiro, I., Eto, Y., Morishige, K., Matsumoto, Y., Obara, K., Nakayama, K., Takahashi, S. & Takeshita, A. Evidence for protein kinase C-mediated activation of Rho-kinase in a porcine model of coronary artery spasm. *Arterioscler. Thromb. Vasc. Biol.* **23**, 2209–2214 (2003).

98. Peng, J., He, F., Zhang, C., Deng, X. & Yin, F. Protein kinase C-α signals P115RhoGEF phosphorylation and RhoA activation in TNF-α-induced mouse brain microvascular endothelial cell barrier dysfunction. *J. Neuroinflammation* **8**, 1–10 (2011).

99. Safaei, J., Maňuch, J., Gupta, A., Stacho, L. & Pelech, S. Prediction of 492 human protein kinase substrate specificities. *Proteome Sci.* **9 Suppl 1**, S6–S6 (2011).

100. White, C. D. & Toker, A. Using phospho-motif antibodies to determine kinase substrates. *Curr. Protoc. Mol. Biol.* **Chapter 18**, Unit 18.20. (2013).

101. Aittaleb, M., Boguth, C. A. & Tesmer, J. J. G. Structure and function of heterotrimeric G protein-regulated Rho guanine nucleotide exchange factors. *Mol. Pharmacol.* **77**, 111–125 (2010).

102. Wells, C. D., Gutowski, S., Bollag, G. & Sternweis, P. C. Identification of potential mechanisms for regulation of p115 RhoGEF through analysis of endogenous and mutant forms of the exchange factor. *J. Biol. Chem.* **276**, 28897–28905 (2001).

103. Grabocka, E. & Wedegaertner, P. B. Functional consequences of G alpha 13 mutations that disrupt interaction with p115RhoGEF. *Oncogene* **24**, 2155–2165 (2005).

104. Bhattacharyya, R. & Wedegaertner, P. B. Characterization of G alpha 13-dependent plasma membrane recruitment of p115RhoGEF. *Biochem. J.* **371**, 709–720 (2003).

105. Bhattacharyya, R. & Wedegaertner, P. B. Mutation of an N-terminal acidic-rich region of p115-RhoGEF dissociates alpha13 binding and alpha13-promoted plasma membrane recruitment. *FEBS Lett.* **540**, 211–216 (2003).

106. Meyer, B. H., Freuler, F., Guerini, D. & Siehler, S. Reversible translocation of p115-RhoGEF by G(12/13)-coupled receptors. *J. Cell. Biochem.* **104**, 1660–1670 (2008).

107. Bhattacharyya, R., Banerjee, J., Khalili, K. & Wedegaertner, P. B. Differences in Galpha12- and Galpha13-mediated plasma membrane recruitment of p115-RhoGEF. *Cell. Signal.* **21**, 996–1006 (2009).

108. Carter, A. M., Gutowski, S. & Sternweis, P. C. Regulated localization is sufficient for hormonal control of regulator of G protein signaling homology Rho guanine nucleotide exchange factors (RH-RhoGEFs). *J. Biol. Chem.* **289**, 19737–19746 (2014).

109. Mehta, S., Zhang, Y., Roth, R. H., Zhang, J. fan, Mo, A., Tenner, B., Huganir, R. L. & Zhang, J. Single-fluorophore biosensors for sensitive and multiplexed detection of signalling activities. *Nat. Cell Biol.* **20**, 1215–1225 (2018).

110. Akerboom, J., Carreras Calderon, N., Tian, L., Wabnig, S., Prigge, M., Tolo, J., Gordus, A., Orger, M. B., Severi, K. E., Macklin, J. J., Patel, R., Pulver, S. R., Wardill, T. J., Fischer, E., Schuler, C., Chen, T.-W., Sarkisyan, K. S., Marvin, J. S., Bargmann, C. I., Kim, D. S., Kugler, S., Lagnado, L., Hegemann, P., Gottschalk, A., Schreiter, E. R. & Looger, L. L. Genetically encoded calcium indicators for multi-color neural activity imaging and combination with optogenetics. *Front. Mol. Neurosci.* **6**, 2 (2013).

111. Gau, D. & Roy, P. SRF'ing and SAP'ing - the role of MRTF proteins in cell migration. *J. Cell Sci.* **131**, (2018).

112. Finch-Edmondson, M. & Sudol, M. Framework to function: Mechanosensitive regulators of gene transcription. *Cell. Mol. Biol. Lett.* **21**, 1–23 (2016).

113. Sebe, A., Masszi, A., Zulys, M., Yeung, T., Speight, P., Rotstein, O. D., Nakano, H., Mucsi, I., Szaszi, K. & Kapus, A. Rac, PAK and p38 regulate cell contact-dependent nuclear translocation of myocardin-related transcription factor. *FEBS Lett.* **582**, 291–298 (2008).

114. Gupta, M., Korol, A. & West-Mays, J. A. Nuclear translocation of myocardin-related transcription factor-A during transforming growth factor beta-induced epithelial to mesenchymal transition of lens epithelial cells. *Mol. Vis.* **19**, 1017–1028 (2013).

115. Mao, J., Yuan, H., Xie, W. & Wu, D. Guanine nucleotide exchange factor GEF115 specifically mediates activation of Rho and serum response factor by the G protein alpha subunit Galpha13. *Proc. Natl. Acad. Sci. U. S. A.* **95**, 12973–12976 (1998).

116. Newton, A. C. Protein kinase C: poised to signal. *Am. J. Physiol. Endocrinol. Metab.* **298**, E395–E402 (2010).

117. Schwartz, M. Rho signalling at a glance. *J. Cell Sci.* **117**, 5457 LP – 5458 (2004).

118. Hughey, J. J., Lee, T. K. & Covert, M. W. Computational modeling of mammalian signaling networks. *Wiley Interdiscip. Rev. Syst. Biol. Med.* **2**, 194–209 (2010).

119. Boras, B. W., Kornev, A., Taylor, S. S. & McCulloch, A. D. Using Markov state models to develop a mechanistic understanding of protein kinase A regulatory subunit RIalpha activation in response to cAMP binding. *J. Biol. Chem.* **289**, 30040–30051 (2014).

120. Sample, V., Dipilato, L. M., Yang, J. H., Ni, Q., Saucerman, J. J. & Zhang, J. Regulation of nuclear PKA revealed by spatiotemporal manipulation of cyclic AMP. *Nat. Chem. Biol.*

8, 375–382 (2012).

121. Saucerman, J. J., Zhang, J., Martin, J. C., Peng, L. X., Stenbit, A. E., Tsien, R. Y. & McCulloch, A. D. Systems analysis of PKA-mediated phosphorylation gradients in live cardiac myocytes. *Proc. Natl. Acad. Sci. U. S. A.* **103**, 12923–12928 (2006).

122. Yung, B. S., Brand, C. S., Xiang, S. Y., Gray, C. B. B., Means, C. K., Rosen, H., Chun, J., Purcell, N. H., Brown, J. H. & Miyamoto, S. Selective coupling of the S1P(3) receptor subtype to S1P-mediated RhoA activation and cardioprotection. *J. Mol. Cell. Cardiol.* **103**, 1–10 (2017).

123. Sabbatini, M. E. & Williams, J. A. Cholecystokinin-mediated RhoGDI phosphorylation via PKCα promotes both RhoA and Rac1 signaling. *PLoS One* **8**, e66029–e66029 (2013).

124. Dovas, A., Choi, Y., Yoneda, A., Multhaupt, H. A. B., Kwon, S.-H., Kang, D., Oh, E.-S. & Couchman, J. R. Serine 34 phosphorylation of rho guanine dissociation inhibitor (RhoGDIalpha) links signaling from conventional protein kinase C to RhoGTPase in cell adhesion. *J. Biol. Chem.* **285**, 23296–23308 (2010).

125. Cowan, A. E., Moraru, I. I., Schaff, J. C., Slepchenko, B. M. & Loew, L. M. Spatial modeling of cell signaling networks. *Methods Cell Biol.* **110**, 195–221 (2012).

126. Schaff, J., Fink, C. C., Slepchenko, B., Carson, J. H. & Loew, L. M. A general computational framework for modeling cellular structure and function. *Biophys. J.* **73**, 1135–1146 (1997).

127. Li, M., Wang, X., Meintzer, M. K., Laessig, T., Birnbaum, M. J. & Heidenreich, K. A. Cyclic AMP promotes neuronal survival by phosphorylation of glycogen synthase kinase 3beta. *Mol. Cell. Biol.* **20**, 9356–9363 (2000).

128. Jhala, U. S., Canettieri, G., Screaton, R. A., Kulkarni, R. N., Krajewski, S., Reed, J., Walker, J., Lin, X., White, M. & Montminy, M. cAMP promotes pancreatic beta-cell survival via CREB-mediated induction of IRS2. *Genes Dev.* **17**, 1575–1580 (2003).

129. Gottesman, M. M. & Fleischmann, R. D. The role of cAMP in regulating tumour cell growth. *Cancer Surv.* **5**, 291–308 (1986).

130. Boularan, C. & Gales, C. Cardiac cAMP: production, hydrolysis, modulation and detection. *Front. Pharmacol.* **6**, 203 (2015).

131. Kandel, E. R. The molecular biology of memory: cAMP, PKA, CRE, CREB-1, CREB-2, and CPEB. *Mol. Brain* **5**, 14 (2012).

132. Kroeze, W. K., Sheffler, D. J. & Roth, B. L. G-protein-coupled receptors at a glance. *J. Cell Sci.* **116**, 4867 LP – 4869 (2003).

133. Patra, C. & Brady, M. F. *Biochemistry, cAMP*. (StatPearls Publishing, 2018).

134. Buxton, I. L. & Brunton, L. L. Compartments of cyclic AMP and protein kinase in mammalian cardiomyocytes. *J. Biol. Chem.* **258**, 10233–10239 (1983).

135. Steinberg, S. F. & Brunton, L. L. Compartmentation of G protein-coupled signaling pathways in cardiac myocytes. *Annu. Rev. Pharmacol. Toxicol.* **41**, 751–773 (2001).

136. Gorshkov, K., Mehta, S., Ramamurthy, S., Ronnett, G. V, Zhou, F.-Q. & Zhang, J. AKAP-mediated feedback control of cAMP gradients in developing hippocampal neurons. *Nat. Chem. Biol.* **13**, 425–431 (2017).

137. Lim, C. J., Kain, K. H., Tkachenko, E., Goldfinger, L. E., Gutierrez, E., Allen, M. D., Groisman, A., Zhang, J. & Ginsberg, M. H. Integrin-mediated protein kinase A activation at the leading edge of migrating cells. *Mol. Biol. Cell* **19**, 4930–4941 (2008).

138. Nikolaev, V. O., Bünemann, M., Schmitteckert, E., Lohse, M. J. & Engelhardt, S. Cyclic AMP imaging in adult cardiac myocytes reveals far-reaching β1-adrenergic but locally confined β2-adrenergic receptor-mediated signaling. *Circ. Res.* **99**, 1084–1091 (2006).

139. Zaccolo, M. & Pozzan, T. Discrete microdomains with high concentration of cAMP in stimulated rat neonatal cardiac myocytes. *Science* **295**, 1711–1715 (2002).

140. Maiellaro, I., Lohse, M. J., Kittel, R. J. & Calebiro, D. cAMP Signals in Drosophila Motor Neurons Are Confined to Single Synaptic Boutons. *Cell Rep.* **17**, 1238–1246 (2016).

141. Terrin, A., Monterisi, S., Stangherlin, A., Zoccarato, A., Koschinski, A., Surdo, N. C., Mongillo, M., Sawa, A., Jordanides, N. E., Mountford, J. C. & Zaccolo, M. PKA and PDE4D3 anchoring to AKAP9 provides distinct regulation of cAMP signals at the centrosome. *J. Cell Biol.* **198**, 607–621 (2012).

142. Cooper, D. M. F. Regulation and organization of adenylyl cyclases and cAMP. *Biochem. J.* **375**, 517–529 (2003).

143. Willoughby, D. & Cooper, D. M. F. Organization and Ca2+ regulation of adenylyl cyclases in cAMP microdomains. *Physiol. Rev.* **87**, 965–1010 (2007).

144. Zaccolo, M. Phosphodiesterases and compartmentalized cAMP signalling in the heart. *Eur. J. Cell Biol.* **85**, 693–697 (2006).

145. Baillie, G. S. Compartmentalized signalling: spatial regulation of cAMP by the action of compartmentalized phosphodiesterases. *FEBS J.* **276**, 1790–1799 (2009).

146. Houslay, M. D. Underpinning compartmentalised cAMP signalling through targeted cAMP breakdown. *Trends Biochem. Sci.* **35**, 91–100 (2010).

147. Saucerman, J. J., Greenwald, E. C. & Polanowska-Grabowska, R. Mechanisms of cyclic AMP compartmentation revealed by computational models. *J. Gen. Physiol.* **143**, 39–48 (2014).

148. Rich, T. C., Fagan, K. A., Tse, T. E., Schaack, J., Cooper, D. M. & Karpen, J. W. A uniform extracellular stimulus triggers distinct cAMP signals in different compartments of a simple cell. *Proc. Natl. Acad. Sci. U. S. A.* **98**, 13049–13054 (2001).

149. Rich, T. C., Fagan, K. A., Nakata, H., Schaack, J., Cooper, D. M. & Karpen, J. W. Cyclic nucleotide-gated channels colocalize with adenylyl cyclase in regions of restricted cAMP diffusion. *J. Gen. Physiol.* **116**, 147–161 (2000).

150. Agarwal, S. R., Clancy, C. E. & Harvey, R. D. Mechanisms Restricting Diffusion of Intracellular cAMP. *Sci. Rep.* **6**, 19577 (2016).

151. Richards, M., Lomas, O., Jalink, K., Ford, K. L., Vaughan-Jones, R. D., Lefkimmiatis, K. & Swietach, P. Intracellular tortuosity underlies slow cAMP diffusion in adult ventricular myocytes. *Cardiovasc. Res.* **110**, 395–407 (2016).

152. Cadd, G. & McKnight, G. S. Distinct patterns of cAMP-dependent protein kinase gene expression in mouse brain. *Neuron* **3**, 71–79 (1989).

153. Mavrakis, M., Lippincott-Schwartz, J., Stratakis, C. A. & Bossis, I. Depletion of type IA regulatory subunit (RIα) of protein kinase A (PKA) in mammalian cells and tissues activates mTOR and causes autophagic deficiency. *Hum. Mol. Genet.* **15**, 2962–2971 (2006).

154. Day, M. E., Gaietta, G. M., Sastri, M., Koller, A., Mackey, M. R., Scott, J. D., Perkins, G. A., Ellisman, M. H. & Taylor, S. S. Isoform-specific targeting of PKA to multivesicular bodies. *J. Cell Biol.* **193**, 347–363 (2011).

155. Kim, C., Xuong, N.-H. & Taylor, S. S. Crystal structure of a complex between the catalytic and regulatory (RIalpha) subunits of PKA. *Science* **307**, 690–696 (2005).

156. DiPilato, L. M. & Zhang, J. The role of membrane microdomains in shaping beta2-adrenergic receptor-mediated cAMP dynamics. *Mol. Biosyst.* **5**, 832–837 (2009).

157. Zhang, J., Hupfeld, C. J., Taylor, S. S., Olefsky, J. M. & Tsien, R. Y. Insulin disrupts beta-adrenergic signalling to protein kinase A in adipocytes. *Nature* **437**, 569–573 (2005).

158. DiPilato, L. M., Cheng, X. & Zhang, J. Fluorescent indicators of cAMP and Epac activation reveal differential dynamics of cAMP signaling within discrete subcellular compartments. *Proc. Natl. Acad. Sci. U. S. A.* **101**, 16513–16518 (2004).

159. Yang, P. C., Boras, B. W., Jeng, M. T., Docken, S. S., Lewis, T. J., McCulloch, A. D., Harvey, R. D. & Clancy, C. E. A Computational Modeling and Simulation Approach to Investigate Mechanisms of Subcellular cAMP Compartmentation. *PLoS Comput. Biol.* **12**, 1–23 (2016).

160. Caretta, A. & Mucignat-Caretta, C. Protein kinase a in cancer. *Cancers (Basel).* **3**, 913–926 (2011).

161. Perera, R. K. & Nikolaev, V. O. Compartmentation of cAMP signalling in cardiomyocytes in health and disease. *Acta Physiol. (Oxf).* **207**, 650–662 (2013).

162. Sergi, C. M. Hepatocellular Carcinoma, Fibrolamellar Variant: Diagnostic Pathologic Criteria and Molecular Pathology Update. A Primer. *Diagnostics (Basel, Switzerland)* **6**, 3 (2015).

163. Lu, T.-W., Wu, J., Aoto, P. C., Weng, J.-H., Ahuja, L. G., Sun, N., Cheng, C. Y., Zhang, P. & Taylor, S. S. Two PKA RIα holoenzyme states define ATP as an isoform-specific orthosteric inhibitor that competes with the allosteric activator, cAMP. *Proc. Natl. Acad. Sci.* **116**, 16347 LP – 16356 (2019).

164. Bastidas, A. C., Deal, M. S., Steichen, J. M., Keshwani, M. M., Guo, Y. & Taylor, S. S. Role of N-terminal myristylation in the structure and regulation of cAMP-dependent protein kinase. *J. Mol. Biol.* **422**, 215–229 (2012).

165. Turnham, R. E., Smith, F. D., Kenerson, H. L., Omar, M. H., Golkowski, M., Garcia, I., Bauer, R., Lau, H. T., Sullivan, K. M., Langeberg, L. K., Ong, S. E., Riehle, K. J., Yeung, R. S. & Scott, J. D. An acquired scaffolding function of the DNAJ-PKAc fusion contributes to oncogenic signaling in fibrolamellar carcinoma. *Elife* **8**, 1–27 (2019).

166. Yang, P.-C., Boras, B. W., Jeng, M.-T., Docken, S. S., Lewis, T. J., McCulloch, A. D., Harvey, R. D. & Clancy, C. E. A Computational Modeling and Simulation Approach to Investigate Mechanisms of Subcellular cAMP Compartmentation. *PLOS Comput. Biol.* **12**, e1005005 (2016).

167. Stangherlin, A. & Zaccolo, M. Phosphodiesterases and subcellular compartmentalized cAMP signaling in the cardiovascular system. *Am. J. Physiol. - Hear. Circ. Physiol.* **302**, (2012).

168. Conti, M., Mika, D. & Richter, W. Cyclic AMP compartments and signaling specificity: role of cyclic nucleotide phosphodiesterases. *J. Gen. Physiol.* **143**, 29–38 (2014).

169. Goraya, T. A., Masada, N., Ciruela, A., Willoughby, D., Clynes, M. A. & Cooper, D. M. F. Kinetic properties of Ca2+/calmodulin-dependent phosphodiesterase isoforms dictate intracellular cAMP dynamics in response to elevation of cytosolic Ca2+. *Cell. Signal.* **20**, 359–374 (2008).

170. Conti, M. & Beavo, J. Biochemistry and physiology of cyclic nucleotide phosphodiesterases: essential components in cyclic nucleotide signaling. *Annu. Rev. Biochem.* **76**, 481–511 (2007).

171. Agarwal, S. R., Clancy, C. E. & Harvey, R. D. Mechanisms Restricting Diffusion of Intracellular cAMP. *Sci. Rep.* **6**, 1–11 (2016).

172. Neves, S. R., Tsokas, P., Sarkar, A., Grace, E. A., Rangamani, P., Taubenfeld, S. M., Alberini, C. M., Schaff, J. C., Blitzer, R. D., Moraru, I. I. & Iyengar, R. Cell shape and negative links in regulatory motifs together control spatial information flow in signaling

networks. *Cell* **133**, 666–680 (2008).

173. Boija, A., Klein, I. A., Sabari, B. R., Dall'Agnese, A., Coffey, E. L., Zamudio, A. V, Li, C. H., Shrinivas, K., Manteiga, J. C., Hannett, N. M., Abraham, B. J., Afeyan, L. K., Guo, Y. E., Rimel, J. K., Fant, C. B., Schuijers, J., Lee, T. I., Taatjes, D. J. & Young, R. A. Transcription Factors Activate Genes through the Phase-Separation Capacity of Their Activation Domains. *Cell* **175**, 1842-1855.e16 (2018).

174. Gibson, B. A., Doolittle, L. K., Schneider, M. W. G., Jensen, L. E., Gamarra, N., Henry, L., Gerlich, D. W., Redding, S. & Rosen, M. K. Organization of Chromatin by Intrinsic and Regulated Phase Separation. *Cell* **179**, 470-484.e21 (2019).

175. Sabari, B. R., Dall'Agnese, A., Boija, A., Klein, I. A., Coffey, E. L., Shrinivas, K., Abraham, B. J., Hannett, N. M., Zamudio, A. V, Manteiga, J. C., Li, C. H., Guo, Y. E., Day, D. S., Schuijers, J., Vasile, E., Malik, S., Hnisz, D., Lee, T. I., Cisse, I. I., Roeder, R. G., Sharp, P. A., Chakraborty, A. K. & Young, R. A. Coactivator condensation at super-enhancers links phase separation and gene control. *Science* **361**, (2018).

176. Jain, S., Wheeler, J. R., Walters, R. W., Agrawal, A., Barsic, A. & Parker, R. ATPase-Modulated Stress Granules Contain a Diverse Proteome and Substructure. *Cell* **164**, 487–498 (2016).

177. Cai, D., Feliciano, D., Dong, P., Flores, E., Gruebele, M., Porat-Shliom, N., Sukenik, S., Liu, Z. & Lippincott-Schwartz, J. Phase separation of YAP reorganizes genome topology for long-term, YAP target gene expression. *Nat. Cell Biol.* **21**, 1578–1589 (2019).

178. Zhou, X., Herbst-Robinson, K. J. & Zhang, J. Visualizing dynamic activities of signaling enzymes using genetically encodable FRET-based biosensors from designs to applications. *Methods Enzymol.* **504**, 317–340 (2012).

179. Dinh, T. A., Vitucci, E. C. M., Wauthier, E., Graham, R. P., Pitman, W. A., Oikawa, T., Chen, M., Silva, G. O., Greene, K. G., Torbenson, M. S., Reid, L. M. & Sethupathy, P. Comprehensive analysis of The Cancer Genome Atlas reveals a unique gene and non-coding RNA signature of fibrolamellar carcinoma. *Sci. Rep.* **7**, 44653 (2017).

180. Graham, R. P., Lackner, C., Terracciano, L., Gonzalez-Cantu, Y., Maleszewski, J. J., Greipp, P. T., Simon, S. M. & Torbenson, M. S. Fibrolamellar carcinoma in the Carney complex: PRKAR1A loss instead of the classic DNAJB1-PRKACA fusion. *Hepatology* **68**, 1441–1447 (2018).

181. Singhi, A. D., Wood, L. D., Parks, E., Torbenson, M. S., Felsenstein, M., Hruban, R. H., Nikiforova, M. N., Wald, A. I., Kaya, C., Nikiforov, Y. E., Favazza, L., He, J., McGrath, K., Fasanella, K. E., Brand, R. E., Lennon, A. M., Furlan, A., Dasyam, A. K., Zureikat, A. H., Zeh, H. J., Lee, K., Bartlett, D. L. & Slivka, A. Recurrent Rearrangements in PRKACA and PRKACB in Intraductal Oncocytic Papillary Neoplasms of the Pancreas and Bile Duct. *Gastroenterology* (2019) doi:10.1053/j.gastro.2019.10.028.

182. Bouchard, J. J., Otero, J. H., Scott, D. C., Szulc, E., Martin, E. W., Sabri, N., Granata, D.,

Marzahn, M. R., Lindorff-Larsen, K., Salvatella, X., Schulman, B. A. & Mittag, T. Cancer Mutations of the Tumor Suppressor SPOP Disrupt the Formation of Active, Phase-Separated Compartments. *Mol. Cell* **72**, 19-36.e8 (2018).

183. Scholten, A., Van Veen, T. A. B., Vos, M. A. & Heck, A. J. R. Diversity of cAMP-dependent protein kinase isoforms and their anchoring proteins in mouse ventricular tissue. *J. Proteome Res.* **6**, 1705–1717 (2007).

184. Yin, Z., Jones, G. N., Towns, W. H. 2nd, Zhang, X., Abel, E. D., Binkley, P. F., Jarjoura, D. & Kirschner, L. S. Heart-specific ablation of Prkar1a causes failure of heart development and myxomagenesis. *Circulation* **117**, 1414–1422 (2008).

185. Park, A. J., Havekes, R., Choi, J. H., Luczak, V., Nie, T., Huang, T. & Abel, T. A presynaptic role for PKA in synaptic tagging and memory. *Neurobiol. Learn. Mem.* **114**, 101–112 (2014).

186. Shelly, M., Lim, B. K., Cancedda, L., Heilshorn, S. C., Gao, H. & Poo, M. Local and long-range reciprocal regulation of cAMP and cGMP in axon/dendrite formation. *Science* **327**, 547–552 (2010).

187. Ran, F. A., Hsu, P. D., Wright, J., Agarwala, V., Scott, D. A. & Zhang, F. Genome engineering using the CRISPR-Cas9 system. *Nat. Protoc.* **8**, 2281–2308 (2013).

188. Adikusuma, F., Pfitzner, C. & Thomas, P. Q. Versatile single-step-assembly CRISPR/Cas9 vectors for dual gRNA expression. *PLoS One* **12**, e0187236 (2017).

189. Lam, A. J., St-Pierre, F., Gong, Y., Marshall, J. D., Cranfill, P. J., Baird, M. A., McKeown, M. R., Wiedenmann, J., Davidson, M. W., Schnitzer, M. J., Tsien, R. Y. & Lin, M. Z. Improving FRET dynamic range with bright green and red fluorescent proteins. *Nat. Methods* **9**, 1005–1012 (2012).

190. Subach, O. M., Cranfill, P. J., Davidson, M. W. & Verkhusha, V. V. An enhanced monomeric blue fluorescent protein with the high chemical stability of the chromophore. *PLoS One* **6**, e28674 (2011).

191. Depry, C., Allen, M. D. & Zhang, J. Visualization of PKA activity in plasma membrane microdomains. *Mol. Biosyst.* **7**, 52–58 (2011).

192. Tillo, S. E., Xiong, W.-H., Takahashi, M., Miao, S., Andrade, A. L., Fortin, D. A., Yang, G., Qin, M., Smoody, B. F., Stork, P. J. S. & Zhong, H. Liberated PKA Catalytic Subunits Associate with the Membrane via Myristoylation to Preferentially Phosphorylate Membrane Substrates. *Cell Rep.* **19**, 617–629 (2017).

193. Udenwobele, D. I., Su, R.-C., Good, S. V, Ball, T. B., Varma Shrivastav, S. & Shrivastav, A. Myristoylation: An Important Protein Modification in the Immune Response. *Front. Immunol.* **8**, 751 (2017).

194. Guan, B., Wang, T.-L. & Shih, I.-M. ARID1A, a factor that promotes formation of

SWI/SNF-mediated chromatin remodeling, is a tumor suppressor in gynecologic cancers. *Cancer Res.* **71**, 6718–6727 (2011).

195. Halperin, S. O., Tou, C. J., Wong, E. B., Modavi, C., Schaffer, D. V & Dueber, J. E. CRISPR-guided DNA polymerases enable diversification of all nucleotides in a tunable window. *Nature* **560**, 248–252 (2018).

196. Miyamoto, S., Purcell, N. H., Smith, J. M., Gao, T., Whittaker, R., Huang, K., Castillo, R., Glembotski, C. C., Sussman, M. A., Newton, A. C. & Brown, J. H. PHLPP-1 negatively regulates Akt activity and survival in the heart. *Circ. Res.* **107**, 476–484 (2010).

197. Dull, T., Zufferey, R., Kelly, M., Mandel, R. J., Nguyen, M., Trono, D. & Naldini, L. A third-generation lentivirus vector with a conditional packaging system. *J. Virol.* **72**, 8463–8471 (1998).

198. Borowicz, S., Van Scoyk, M., Avasarala, S., Karuppusamy Rathinam, M. K., Tauler, J., Bikkavilli, R. K. & Winn, R. A. The soft agar colony formation assay. *J. Vis. Exp.* 1–6 (2014) doi:10.3791/51998.

199. Bruystens, J. G. H., Wu, J., Fortezzo, A., Kornev, A. P., Blumenthal, D. K. & Taylor, S. S. PKA RIalpha homodimer structure reveals an intermolecular interface with implications for cooperative cAMP binding and Carney complex disease. *Structure* **22**, 59–69 (2014).

200. Guerrero, F., Ciragan, A. & Iwai, H. Tandem SUMO fusion vectors for improving soluble protein expression and purification. *Protein Expr. Purif.* **116**, 42–49 (2015).

201. Kang, M., Day, C. A., Kenworthy, A. K. & DiBenedetto, E. Simplified equation to extract diffusion coefficients from confocal FRAP data. *Traffic* **13**, 1589–1600 (2012).

202. Surdo, N. C., Berrera, M., Koschinski, A., Brescia, M., MacHado, M. R., Carr, C., Wright, P., Gorelik, J., Morotti, S., Grandi, E., Bers, D. M., Pantano, S. & Zaccolo, M. FRET biosensor uncovers cAMP nano-domains at b-adrenergic targets that dictate precise tuning of cardiac contractility. *Nat. Commun.* **8**, 1–14 (2017).

203. Clister, T., Greenwald, E. C., Baillie, G. S. & Zhang, J. AKAP95 Organizes a Nuclear Microdomain to Control Local cAMP for Regulating Nuclear PKA. *Cell Chem. Biol.* **26**, 885-891.e4 (2019).

204. Tenner, B., Mehta, S. & Zhang, J. Optical sensors to gain mechanistic insights into signaling assemblies. *Curr. Opin. Struct. Biol.* **41**, 203–210 (2016).

205. Kamai, T., Yamanishi, T., Shirataki, H., Takagi, K., Asami, H., Ito, Y. & Yoshida, K.-I. Overexpression of RhoA, Rac1, and Cdc42 GTPases is associated with progression in testicular cancer. *Clin. Cancer Res.* **10**, 4799–4805 (2004).

206. Liu, X., Chen, D. & Liu, G. Overexpression of RhoA promotes the proliferation and migration of cervical cancer cells. *Biosci. Biotechnol. Biochem.* **78**, 1895–1901 (2014).

207. Irannejad, R., Tomshine, J. C., Tomshine, J. R., Chevalier, M., Mahoney, J. P., Steyaert, J., Rasmussen, S. G. F., Sunahara, R. K., El-Samad, H., Huang, B. & Von Zastrow, M. Conformational biosensors reveal GPCR signalling from endosomes. *Nature* **495**, 534–538 (2013).

208. Perez-Alvarez, A., Fearey, B. C., O'Toole, R. J., Yang, W., Arganda-Carreras, I., Lamothe-Molina, P. J., Moeyaert, B., Mohr, M. A., Panzera, L. C., Schulze, C., Schreiter, E. R., Wiegert, J. S., Gee, C. E., Hoppa, M. B. & Oertner, T. G. Freeze-frame imaging of synaptic activity using SynTagMA. *Nat. Commun.* **11**, 2464 (2020).

209. Menzel, S., Schwarz, N., Haag, F. & Koch-Nolte, F. Nanobody-based biologics for modulating purinergic signaling in inflammation and immunity. *Front. Pharmacol.* **9**, 266 (2018).

210. Jank, L., Pinto-Espinoza, C., Duan, Y., Koch-Nolte, F., Magnus, T. & Rissiek, B. Current approaches and future perspectives for nanobodies in stroke diagnostic and therapy. *Antibodies* **8**, 5 (2019).

211. Cabantous, S., Terwilliger, T. C. & Waldo, G. S. Protein tagging and detection with engineered self-assembling fragments of green fluorescent protein. *Nat. Biotechnol.* **23**, 102–107 (2005).

212. Pédelacq, J. D., Cabantous, S., Tran, T., Terwilliger, T. C. & Waldo, G. S. Engineering and characterization of a superfolder green fluorescent protein. *Nat. Biotechnol.* **24**, 79–88 (2006).

213. Fritz, R. D., Letzelter, M., Reimann, A., Martin, K., Fusco, L., Ritsma, L., Ponsioen, B., Fluri, E., Schulte-Merker, S., Van Rheenen, J. & Pertz, O. A versatile toolkit to produce sensitive FRET biosensors to visualize signaling in time and space. *Sci. Signal.* **6**, (2013).

214. Baird, G. S., Zacharias, D. A. & Tsien, R. Y. Circular permutation and receptor insertion within green fluorescent proteins. *Proc. Natl. Acad. Sci. U. S. A.* **96**, 11241–11246 (1999).

215. Lakowicz, J. R. *Principles of fluorescence spectroscopy*. (Second edition. New York : Kluwer Academic/Plenum, [1999] ©1999).

216. Zhang, J. & Allen, M. D. FRET-based biosensors for protein kinases: illuminating the kinome. *Mol. Biosyst.* **3**, 759–765 (2007).

217. Calebiro, D. & Maiellaro, I. cAMP signaling microdomains and their observation by optical methods. *Front. Cell. Neurosci.* **8**, 350 (2014).

218. Violin, J. D., DiPilato, L. M., Yildirim, N., Elston, T. C., Zhang, J. & Lefkowitz, R. J. beta2-adrenergic receptor signaling and desensitization elucidated by quantitative modeling of real time cAMP dynamics. *J. Biol. Chem.* **283**, 2949–2961 (2008).

219. Klarenbeek, J., Goedhart, J., van Batenburg, A., Groenewald, D. & Jalink, K. Fourth-generation epac-based FRET sensors for cAMP feature exceptional brightness,

photostability and dynamic range: characterization of dedicated sensors for FLIM, for ratiometry and with high affinity. *PLoS One* **10**, e0122513 (2015).

220. Dipilato, L. M. & Zhang, J. The role of membrane microdomains in shaping β 2-adrenergic receptor-mediated cAMP dynamics. *Mol. Biosyst.* **5**, 832–837 (2009).

221. Wang, Y., Yang, F., Fu, Y., Huang, X., Wang, W., Jiang, X., Gritsenko, M. A., Zhao, R., Monore, M. E., Pertz, O. C., Purvine, S. O., Orton, D. J., Jacobs, J. M., Camp, D. G. 2nd, Smith, R. D. & Klemke, R. L. Spatial phosphoprotein profiling reveals a compartmentalized extracellular signal-regulated kinase switch governing neurite growth and retraction. *J. Biol. Chem.* **286**, 18190–18201 (2011).

222. Gao, X. & Zhang, J. Spatiotemporal analysis of differential Akt regulation in plasma membrane microdomains. *Mol. Biol. Cell* **19**, 4366–4373 (2008).

223. Fosbrink, M., Aye-Han, N.-N., Cheong, R., Levchenko, A. & Zhang, J. Visualization of JNK activity dynamics with a genetically encoded fluorescent biosensor. *Proc. Natl. Acad. Sci. U. S. A.* **107**, 5459–5464 (2010).

224. Komatsu, N., Aoki, K., Yamada, M., Yukinaga, H., Fujita, Y., Kamioka, Y. & Matsuda, M. Development of an optimized backbone of FRET biosensors for kinases and GTPases. *Mol. Biol. Cell* **22**, 4647–4656 (2011).

225. Donnelly, S. K., Miskolci, V., Garrastegui, A. M., Cox, D. & Hodgson, L. Characterization of Genetically Encoded FRET Biosensors for Rho-Family GTPases. *Methods Mol. Biol.* **1821**, 87–106 (2018).

226. Feng, S., Sekine, S., Pessino, V., Li, H., Leonetti, M. D. & Huang, B. Improved split fluorescent proteins for endogenous protein labeling. *Nat. Commun.* **8**, 370 (2017).

227. Bajar, B. T., Wang, E. S., Lam, A. J., Kim, B. B., Jacobs, C. L., Howe, E. S., Davidson, M. W., Lin, M. Z. & Chu, J. Improving brightness and photostability of green and red fluorescent proteins for live cell imaging and FRET reporting. *Sci. Rep.* **6**, 20889 (2016).

228. Bindels, D. S., Haarbosch, L., Van Weeren, L., Postma, M., Wiese, K. E., Mastop, M., Aumonier, S., Gotthard, G., Royant, A., Hink, M. A. & Gadella, T. W. J. MScarlet: A bright monomeric red fluorescent protein for cellular imaging. *Nat. Methods* **14**, 53–56 (2016).

229. Kamiyama, D., Sekine, S., Barsi-Rhyne, B., Hu, J., Chen, B., Gilbert, L. A., Ishikawa, H., Leonetti, M. D., Marshall, W. F., Weissman, J. S. & Huang, B. Versatile protein tagging in cells with split fluorescent protein. *Nat. Commun.* **7**, 1–9 (2016).

230. Mali, P., Yang, L., Esvelt, K. M., Aach, J., Guell, M., DiCarlo, J. E., Norville, J. E. & Church, G. M. RNA-guided human genome engineering via Cas9. *Science* **339**, 823–826 (2013).

231. Luttrell, L. M., Roudabush, F. L., Choy, E. W., Miller, W. E., Field, M. E., Pierce, K. L.

& Lefkowitz, R. J. Activation and targeting of extracellular signal-regulated kinases by β-arrestin scaffolds. *Proc. Natl. Acad. Sci. U. S. A.* **98**, 2449–2454 (2001).

232. Eichel, K., Jullie, D., Barsi-Rhyne, B., Latorraca, N. R., Masureel, M., Sibarita, J.-B., Dror, R. O. & von Zastrow, M. Catalytic activation of beta-arrestin by GPCRs. *Nature* **557**, 381–386 (2018).

233. Calebiro, D., Nikolaev, V. O., Persani, L. & Lohse, M. J. Signaling by internalized G-protein-coupled receptors. *Trends Pharmacol. Sci.* **31**, 221–228 (2010).

234. Kaksonen, M. & Roux, A. Mechanisms of clathrin-mediated endocytosis. *Nat. Rev. Mol. Cell Biol.* **19**, 313–326 (2018).

235. Keyes, J., Ganesan, A., Molinar-Inglis, O., Hamidzadeh, A., Zhang, J., Ling, M., Trejo, J., Levchenko, A. & Zhang, J. Signaling diversity enabled by Rap1-regulated plasma membrane ERK with distinct temporal dynamics. *Elife* **9**, (2020).

236. Grove, J., Metcalf, D. J., Knight, A. E., Wavre-Shapton, S. T., Sun, T., Protonotarios, E. D., Griffin, L. D., Lippincott-Schwartz, J. & Marsh, M. Flat clathrin lattices: stable features of the plasma membrane. *Mol. Biol. Cell* **25**, 3581–3594 (2014).

237. Saffarian, S., Cocucci, E. & Kirchhausen, T. Distinct Dynamics of Endocytic Clathrin-Coated Pits and Coated Plaques. *PLOS Biol.* **7**, e1000191 (2009).

238. Lampe, M., Pierre, F., Al-Sabah, S., Krasel, C. & Merrifield, C. J. Dual single-scission event analysis of constitutive transferrin receptor (TfR) endocytosis and ligand-triggered beta2-adrenergic receptor (beta2AR) or Mu-opioid receptor (MOR) endocytosis. *Mol. Biol. Cell* **25**, 3070–3080 (2014).

239. Lazar, A. M., Irannejad, R., Baldwin, T. A., Sundaram, A. B., Gutkind, J. S., Inoue, A., Dessauer, C. W. & Von Zastrow, M. G protein-regulated endocytic trafficking of adenylyl cyclase type 9. *Elife* **9**, e58039 (2020).

240. Pavlos, N. J. & Friedman, P. A. GPCR Signaling and Trafficking: The Long and Short of It. *Trends Endocrinol. Metab.* **28**, 213–226 (2017).

241. Koch, T. & Hollt, V. Role of receptor internalization in opioid tolerance and dependence. *Pharmacol. Ther.* **117**, 199–206 (2008).

242. Ferrandon, S., Feinstein, T. N., Castro, M., Wang, B., Bouley, R., Potts, J. T., Gardella, T. J. & Vilardaga, J. P. Sustained cyclic AMP production by parathyroid hormone receptor endocytosis. *Nat. Chem. Biol.* **5**, 734–742 (2009).

243. Batchelder, E. M. & Yarar, D. Differential requirements for clathrin-dependent endocytosis at sites of cell-substrate adhesion. *Mol. Biol. Cell* **21**, 3070–3079 (2010).

244. Franck, A., Lainé, J., Moulay, G., Lemerle, E., Trichet, M., Gentil, C., Benkhelifa-Ziyyat, S., Lacène, E., Bui, M. T., Brochier, G., Guicheney, P., Romero, N., Bitoun, M. &

Vassilopoulos, S. Clathrin plaques and associated actin anchor intermediate filaments in skeletal muscle. *Mol. Biol. Cell* **30**, 579–590 (2019).

245. Vassilopoulos, S., Gentil, C., Lainé, J., Buclez, P.-O., Franck, A., Ferry, A., Précigout, G., Roth, R., Heuser, J. E., Brodsky, F. M., Garcia, L., Bonne, G., Voit, T., Piétri-Rouxel, F. & Bitoun, M. Actin scaffolding by clathrin heavy chain is required for skeletal muscle sarcomere organization. *J. Cell Biol.* **205**, 377–393 (2014).

246. Baschieri, F., Dayot, S., Elkhatib, N., Ly, N., Capmany, A., Schauer, K., Betz, T., Vignjevic, D. M., Poincloux, R. & Montagnac, G. Frustrated endocytosis controls contractility-independent mechanotransduction at clathrin-coated structures. *Nat. Commun.* **9**, 3825 (2018).

247. Leyton-Puig, D., Isogai, T., Argenzio, E., van den Broek, B., Klarenbeek, J., Janssen, H., Jalink, K. & Innocenti, M. Flat clathrin lattices are dynamic actin-controlled hubs for clathrin-mediated endocytosis and signalling of specific receptors. *Nat. Commun.* **8**, 16068 (2017).

248. Franck, A., Lainé, J., Moulay, G., Trichet, M., Gentil, C., Fongy, A., Bigot, A., Benkhelifa-Ziyyat, S., Lacène, E., Thao Bui, M., Brochier, G., Guicheney, P., Mouly, V., Romero, N., Coirault, C., Bitoun, M. & Vassilopoulos, S. Clathrin plaques form mechanotransducing platforms. *bioRxiv* 321885 (2018) doi:10.1101/321885.

249. Calebiro, D., Nikolaev, V. O., Gagliani, M. C., De Filippis, T., Dees, C., Tacchetti, C., Persani, L. & Lohse, M. J. Persistent cAMP-signals triggered by internalized G-protein-coupled receptors. *PLoS Biol.* **7**, (2009).

250. Bowman, S. L., Shiwarski, D. J. & Puthenveedu, M. A. Distinct G protein-coupled receptor recycling pathways allow spatial control of downstream G protein signaling. *J. Cell Biol.* **214**, 797–806 (2016).

251. Eichel, K. & von Zastrow, M. Subcellular Organization of GPCR Signaling. *Trends Pharmacol. Sci.* **39**, 200–208 (2018).

252. Tsvetanova, N. G. & von Zastrow, M. Spatial encoding of cyclic AMP signaling specificity by GPCR endocytosis. *Nat. Chem. Biol.* **10**, 1061–1065 (2014).

253. Ni, Q., Mehta, S. & Zhang, J. Live-cell imaging of cell signaling using genetically encoded fluorescent reporters. *FEBS J.* **285**, 203–219 (2018).

254. Clister, T., Mehta, S. & Zhang, J. Single-cell analysis of G-protein signal transduction. *J. Biol. Chem.* **290**, 6681–6688 (2015).

255. Tinevez, J.-Y., Perry, N., Schindelin, J., Hoopes, G. M., Reynolds, G. D., Laplantine, E., Bednarek, S. Y., Shorte, S. L. & Eliceiri, K. W. TrackMate: An open and extensible platform for single-particle tracking. *Methods* **115**, 80–90 (2017).